High Pressure Scanning Tunneling Microscopy Studies of Adsorbate Structure and Mobility during Catalytic Reactions.
Novel Design of an Ultra High Pressure, High Temperature Scanning Tunneling Microscope System for Probing Catalytic Conversions

by

David Chi-Wai Tang

B.A. (Princeton University) 2000

A dissertation submitted in partial satisfaction of the

requirements for the degree of

Doctor of Philosophy
in

Chemistry

in the

GRADUATE DIVISION

of the

UNIVERSITY OF CALIFORNIA, BERKELEY

Committee in charge:

Professor Gabor A. Somorjai, Chair
Professor A. Paul Alivisatos
Professor Kyriakos Komvopoulos

Spring 2005

The dissertation of David Chi-Wai Tang is approved:

_____

Chair Date

_____

Date

_____

Date

University of California, Berkeley

Spring 2005

High Pressure Scanning Tunneling Microscopy Studies of Adsorbate Structure and Mobility during Catalytic Reactions.
Novel Design of an Ultra High Pressure, High Temperature Scanning Tunneling Microscope System for Probing Catalytic Conversions

by

David Chi-Wai Tang

Abstract

High Pressure Scanning Tunneling Microscopy Studies of Adsorbate Structure and Mobility during Catalytic Reactions.
Novel Design of an Ultra High Pressure, High Temperature Scanning Tunneling Microscope System for Probing Catalytic Conversions

by

David Chi-Wai Tang

Doctor of Philosophy in Chemistry

University of California, Berkeley

Professor Gabor A. Somorjai, Chair

The aim of the work presented therein is to take advantage of scanning tunneling microscope's (STM) capability for operation under a variety of environments under real time and at atomic resolution to monitor adsorbate structures and mobility under high pressures, as well as to design a new generation of STM systems that allow imaging *in situ* at both higher pressures (35 atm) and temperatures (350 °C).

The design of a high pressure, high temperature scanning tunneling microscope system, that is capable of monitoring reactions *in situ* at conditions from UHV and ambient temperature up to 1 atm and 250 °C, is briefly presented along with vibrational

and thermal analysis, as this system serves as a template to improve upon during the design of the new ultra high pressure, high temperature STM.

Using this existing high pressure scanning tunneling microscope we monitored the co-adsorption of hydrogen, ethylene and carbon dioxide on platinum (111) and rhodium (111) crystal faces in the mTorr pressure range at 300 K in equilibrium with the gas phase. During the catalytic hydrogenation of ethylene to ethane in the absence of CO the metal surfaces are covered by an adsorbate layer that is very mobile on the time scale of STM imaging. We found that the addition of CO poisons the hydrogenation reaction and induces ordered structures on the single crystal surfaces. Several ordered structures were observed upon CO addition to the surfaces pre-covered with hydrogen and ethylene: a rotated ($\sqrt{19}$ x $\sqrt{19}$)R23.4° on Pt(111), and domains of c(4 x 2)-CO+C_2H_3, previously unobserved (4 x 2)-CO+3C_2H_3, and (2 x 2)-3CO on Rh(111). A mechanism for CO poisoning of ethylene hydrogenation on the metal single crystals was proposed, in which CO blocks surface metal sites and reduces adsorbate mobility to limit adsorption and reaction rate of ethylene and hydrogen.

In order to observe heterogeneous catalytic reactions that occur well above ambient pressure and temperature that more closely resemble industrial settings, a custom STM motor has been designed and constructed in-house. The new STM design features a much reduced size and a rigid coupling to the sample, and has been tested to show considerably higher resonance frequency than conventional tripod designs, providing the ability to image faster and yielding smaller susceptibility to noise. A flow reactor cell of much reduced volume for pressures up to 35 atmospheres has also been designed and

constructed to house the new STM. The small volume reduces gas consumption and sensitivity to impurities in high pressure gases, as well as maximizes product concentration and reduces response time. The ability to flow reactant gases also allows for continuous monitoring of reaction mixture by mass spectrometry or gas chromatography, and permits correlation of structural information from STM and reaction kinetics. The reactor cell containing the STM is placed inside an UHV system to allow cleaning and characterization of sample before and after experiments, as well as continuous monitoring by mass spectrometry or gas chromatography through a leak valve. The new ultra high pressure system also allows *in vacuo* sample and tip exchange through a load lock, without exposing the system to impurities in air. This new ultra high pressure, high temperature STM system has been shown to perform with major improvements over the existing high pressure, high temperature STM system. Unlike the older system which requires extensive vibration damping setup in order to operate, the new system is shown to be less susceptible to noise, and be able to image atomic steps with no vibration isolation and atomically resolve highly ordered pyrolytic graphite with only spring suspension and a cut tip. Extensive vibrational analysis of the new system is presented, as well as an appendix of AutoCAD-generated design schematics for the major components of the system is included at the end.

Dedicated to the cherished members of my First, Second, and Third Triumvirates.

Hsi-Chen and Kelly

Sunil and Mike

Rob and James

Without their support and rebuke, I would have never come this far in life.

Table of Contents

List of Figures and Tables

Acknowledgements

My long journey through graduate school could not have been as successful, in both scientific and individual growth, without the large group of people who have helped and supported me both professionally and personally. While I hold dear thanks and owe life boons to all of them, the following people have been especially dear and earnest in their efforts to give me aid and succor over the past four years.

First, I would like to thank my dissertation advisor, Professor Gabor A. Somorjai, who took me under his wings and allowed me to freely explore, both scientifically and technically, my direction in research. Without his tutelage and encouragement, without his emotional and (especially) financial support, I would never become the scientist and engineer that I am now proud to be.

Dr. Miquel Salmeron has been invaluable in his guidance and friendship during the undertaking of the new system design and construction. His seasoned experience in both scanning probe microscopy and scientific instrumental innovation is inexpendable to my graduate career, but his genuineness as a person and his acceptance of my sluggish scientific development and my immature antics has made me think of him as more than merely an advisor in scientific ventures, but also a dear friend and partner in the path of life.

I would like to thank all members of both Somorjai and Salmeron groups, especially the scanning probe section, past and present, for their constant support over the years in every way they are kind enough to offer. In particular, I would like to thank Mark Rose, both friend and unofficial project partner, for guiding me on my design plan

especially during the first year, when every one including me seemed to neither understand the magnitude of this undertaking nor find the logical thread to begin. He offered his decade of experience in both SPM experimentation and design, knowing well enough that it has never been his obligation to offer the extensive help that he managed to continue even after his departure. I have been lucky enough to have him as my benefactor and now as my good friend, even though the contrast in our life approaches verges to dichotomy.

I would also like to thank the mechanical and electronic shops at both UC Berkeley and Lawrence Berkeley National Lab. In particular, I want to thank Eric Granlund and company at the campus machine shop, for all their advice in both work and life, for all the parties and the laughs that we shared over the years.

The extensive support during the constant harsh time of the years from my dearest friends, my most treasured Triumvirates, cannot be thanked enough with words alone. However little sensible science do we discuss, Hsi-Chen, Kelly, Sunil, Mike, Rob, and James, your friendship has made the life of this maniacally depressed and pessimistic fellow more bearable. Your advice, both the supportive and the idiotic, has always offered me the comfort that I otherwise can never seek in my overly analytical self. You have constantly reminded me that my long and withering personal crusades do not always earn me strength or nobleness, and there is no weakness in accepting and proffering aid from and to whom I care for and love.

I would like to thank my parents, John and Ada, for letting me cut my own path in both my career and life, however much we have disagreed on the choices that I have

made. No matter what arguments we have voiced over the years, I just want to say I still love you two and care much about what you think of me, Mom and Dad.

Chapter 1

Scanning Tunneling Microscopy and Surface Science

1.1 Overview

The study of surfaces and interfaces is of great interest because they represent a special kind of defects in a phase, be it solid, liquid, or gas. Much of the understanding of phases is based on the fact that they are perfectly periodic in three dimensions. The introduction of an interface breaks this periodicity in one direction, often resulting in changes of physical structure and properties, as a result of stresses due to different chemical interaction of the surface atoms to the interfacial environment in comparison to the bulk atoms. It is important to recognize that surfaces often behave much differently than bulk materials, due to the two dimensional confinement of molecules on surfaces in comparison to that exists in three dimensional gaseous, liquid, and solid bulk phases.

Metals, for example, will often reconstruct at the surface and order differently from those in the bulk, due to the additional interaction with a heterogeneous environment [1]. Polymers can change their conformation to expose hydrophobic or hydrophilic groups near the phase interface, depending on the type of more energetically favorable interaction [2]. Thus, achieving an understanding of surfaces and interfaces is essential to gaining insight to everyday phenomena that involve surfaces: tribological interaction at the solid-solid interface that is responsible for both movement and the lack thereof, the nucleation of dewdrops as a resulting of gas-solid interaction and forming a new liquid-solid interface, and the evaporation of water that involves a gas-liquid interface.

One of the most common motivations for surface science studies is the goal of improving heterogeneous catalysis, oftentimes for industrial processes, by customizing catalysts to enhance performance in activity, selectivity, and lifetime. In heterogeneous catalysis, the catalyst, which is usually a solid, interacts with reactants and products in a different phase--gas or liquid. The purpose of the catalyst is not only to enhance activity and selectivity by the virtue of utilizing favorable solid faces that are otherwise unavailable in a centrosymmetric bulk, but also to both maintain separate conditional control on catalysts and ease the separation of the catalysts from reactants and products.

The problems of understanding catalytic processes on a microscopic or even atomic scale are daunting. Intrinsically, surfaces are more difficult to study than the bulk due to the lower concentration of 10^{15} atoms/cm^2 on a surface compared to 10^{24} atoms/cm^3 in the bulk. As a result, experimental techniques for surface studies must be

highly sensitive and able to detect signals associated from a relatively small number of atoms in addition to discriminating those from the bulk. In addition, industrial processes frequently operate at great conversion rates at high temperatures and pressures, and the catalysts are oftentimes highly dispersed metal particles on oxide supports. In particular, oxide-supported metal-based heterogeneous catalysts are used today for many purposes, including refining hydrocarbons from petroleum, catalytic conversion of carbon monoxide in an automobile and synthesizing ammonia. Thus, studying an actual catalyst used in industry can be complicated, as they are often metals of numerous and unknown surface structures embedded in porous oxides. These disperse and high surface area catalysts can be studied as a function of pretreatment and particle size, but these studies have ill-defined compositions and even less defined structures, thus making it difficult to draw detailed conclusions from these investigations. Model catalysts such as metal single crystals are often used instead to deconvolute the effects of different crystal surfaces and grain boundaries as a result of a comparably uncontrolled catalyst surface. These model catalysts provide a uniform surface that is catalytically relevant, as industrial catalysts often contain metal particles that are not amorphous but instead have many facets that are crystalline in nature. They often insights to the roles of different crystal faces and interfaces during a reaction, and as a result help decipher the key to engineering more effective catalysts for industrial processes.

A range of experimental techniques exploiting physical phenomena quickly became the basis of standard tools for surface studies, and there are over 70 surface science techniques available for determining surface structure and composition before

and after a catalytic reaction [3]. Some common, often electron- and ion-based, spectroscopic and diffraction techniques that have been extensively used include low energy electron diffraction (LEED), Auger electron spectroscopy (AES), electron energy loss spectroscopy (EELS), temperature programmed desorption (TPD), ultraviolet and X-ray photoemission spectroscopy (UPS, XPS), inverse photoemission spectroscopy (IPS), field ion microscopy (FIM), scanning electron microscopy (SEM), infrared reflection absorption spectroscopy (IRAS), ion scattering, and high resolution electron energy loss spectroscopy (HREELS) [4]. With these techniques, it is possible to obtain atomic and molecular information about surface composition, structure, electronic configuration, interaction, local chemical environments, and various other physical and chemical characteristics of catalyst surfaces and adsorbates. However, these techniques are often limited by their requirement of large mean free paths and clean surfaces over a long period of time. Therefore, traditionally surface science experiments were performed in ultrahigh vacuum (UHV). This can be seen from the kinetic theory of gases:

$$F = \frac{N_A P}{\sqrt{2\pi MRT}}$$

where F is the flux of molecules striking the surface, N_A Avogadro's number, P the pressure, M the molecular mass of incoming molecules, R the gas constant and T the temperature. Since the surface of a solid has on the order of 10^{15} atoms cm^{-2}, keeping a surface clean for an hour requires a flux of about 10^{12} molecules cm^{-2} s^{-1}. Calculating for typical molecules such as CO at room temperature, a pressure less than 10^{-9} Torr is necessary. Consequently, it is not possible to carry out *in situ* studies using such techniques and approach, since model catalysts and reactions can only be studies at low

pressures. In some cases, the "pressure gap" between traditional surface science technique and industrial process condition of high pressure and temperature can be bridged and data can be extrapolated from that under low pressure (albeit across more than seven orders of magnitude) and low temperature (which helps induce high coverage condition), but in these instances the surface is not in equilibrium with the gas phase and the surface molecules are kinetically arrested, which raise questions over how similar these artificial high coverage conditions are to the actual reaction conditions.

In attempt to understand how reactions proceed on catalyst surfaces at conditions closer to that of industrial processes, much effort has been directed towards the development of new techniques that combine the benefits of controlled UHV surface analysis and high pressure and temperature catalytic reaction measurements. Traditionally, for reaction studies, surface science reaction experiments have been done using a high-pressure reaction cell attached to the vacuum chamber [5], which allow samples that have been characterized by UHV techniques to be exposed intermittently to high pressure and temperature. The sample can be cleaned in UHV before being transferred to the reaction cell. During and after the reaction, the sample can be extracted and transferred back to the UHV chamber for analysis. However, the surface is not characterized *in situ*, while progress of the reaction can be monitored in real time by analyzing the gases using techniques such as gas chromatography (GC).

In recent years, surface physical chemists have developed techniques that allow one to probe the surface under reaction conditions. Sum-frequency generation (SFG) is an inherently surface sensitive vibrational spectroscopy that has been used to study

heterogeneous catalysis under reaction conditions [6], as well as biologically important systems such as contact lenses [7] and protein adsorption related to implant rejection [8]. Unlike infrared spectroscopy, SFG generates no signal from centrosymmetric media. This means that it does not suffer as much from gas phase absorption and probes only the surface, where symmetry is broken, as most materials are centrosymmetric.

Another promising technique is high-pressure XPS [9]. XPS is related to AES and also gives atomic surface composition. It is possible to differentially pump an electron analyzer, keeping the pressure it sees low while still examining a surface exposed to gas in the Torr pressure range. Preliminary results suggest this will be an important technique for studying heterogeneous catalysis.

Neither of the two previous techniques gives surface structure. It is possible to use grazing-angle x-ray diffraction to get this information on metals, but the scattering cross section of important adsorbates such as carbon and oxygen is too low for the technique to be useful for studying heterogeneous catalysis. Scanning tunneling microscopy (STM) can be used under high pressure to study surface structure at the atomic level [10]. The demonstrated capability of STM to robe the topography and electronic structure of surfaces and adsorbed layers with atomic resolution makes it a powerful tool in the study of surface chemistry where atomic interaction and local phenomena dominates: adsorption is often site-specific, reactions occur at particular active sites, and the effects of surface defects are usually localized. Since most of the conventional surface techniques mentioned above, with the exception of FIM, average over surface areas containing usually more than 10^{12} atomic sites, site-specific information are inaccessible

under such analytical methods. For example, LEED, which can detect displacement of surface atoms on the order of picometers, operates on areas larger than 10 nm and is there not sensitive to local effects produced by isolated defects or adatoms. Even the effectiveness of FIM, which can observe motion of individual atoms on a surface and interactions between a pair of atoms by applying a high field to a fashioned metal tip surface, is limited by restrictions in the selections of compatible substrate materials and adsorbates as well as the narrow field of view.

The advantages of STM in surface science studies are numerous, as it has found applications in many different scientific disciplines such as condensed matter physics, chemistry, biology, metrology, and materials science. Scanning tunneling microscopy has made dramatic advances in many areas of surface science since its introduction by Binnig and Rohrer in 1982 [11], allowing direct observation of dynamic processes such as adatom diffusion [12], chemical reactions [13], and adsorbate restructuring of surfaces [14], on both model surfaces and supported catalysts [15]. Clearly, its direct real space observation at extremely high resolution, in comparison to averaged information obtained by diffraction techniques, allows one to monitor atomic features from adsorbates, defects (vacancies, interstitials, impurities, steps, dislocations, and grain boundaries), to molecular processes such as adsorbate mobility and surface reconstruction. This local information can be obtained regardless of periodicity on the surface due to the ability of STM to perform real space observations on non-periodic features. Thus, STM has a great potential for the investigation of complex systems such as multicomponent materials, polycrystalline samples, grains and grain boundaries, composite and nanostructured

materials, all of which are important components for different supported catalysts in industrial processes. In addition, STM has been proven to work at temperatures from milliKelvin to a thousand Kelvin, and can also work in gas or liquid medium as well as theoretically at any pressures from UHV to very high pressures. There are novel applications to STM also, such as modifying surfaces and manipulating molecules using the tip and its electric field, as well as performing atomically-resolved spectroscopy.

The aim of the work presented therein is to take advantage of STM's capability for operation under a variety of environments under real time and at atomic resolution to monitor adsorbate structures and mobility under high pressures, as well as to design a new generation of STM systems that allow imaging *in situ* at both higher pressures (> 30 atm) and temperatures (> 300 °C). Chapter 1 introduces the principles, as well as capability and limitations of scanning tunneling microscopy. Chapter 2 addresses the operational theories behind the additional and complementary surface science techniques used in the studies recorded therein. Chapter 3 offers an overview of a STM system that is representative of many existing high pressure and high temperature STM systems used in STM labs other than the author's and is currently used to perform studies of pressure up to 1 atm and 250 °C, while Chapter 4 describes the study of ethylene hydrogenation and its poisoning by CO over single crystal surfaces of transition metals using the said system to monitor adsorbate ordering and mobility during reactions. Chapter 5 introduces a detailed description of the design schematic and essential considerations for a new STM system that is capable of operating at conditions closer to the elevated temperatures and pressures of industrial processes, while also provides preliminary results and performance

findings of this latest system. Finally, Chapter 6 will complete the discussion of the author's work by giving a summary of results as well as future direction. An appendix of detailed AutoCAD drawings for the system as referred to and described in Chapter 5 is included at the end.

1.2 Scanning Tunneling Microscopy

1.2.1 Operating Principles

Scanning tunneling microscopes use piezoelectric transducers to move a sharpened metal probe (tip) across a surface with sub-angstrom precision, and takes advantage of the exponential dependence of quantum mechanical tunneling current on the separation distance to produce highly detailed images of a conductive surface. Classically, electrons in two electrodes separated by a nonconductive medium are confined by the potential barrier imposed by the medium. However, when the tip-surface separation is less than about 1 nm, a purely quantum mechanical effect allows electrons to tunnel through the energy barrier in the gap between the tip and the surface. A bias voltage (typically < 1 V) applied between the tip and the surface causes a small net current to flow through the barrier. This current can be detected and measured by a sensitive current amplifier and, together with an external feedback loop and a tip-sample manipulation system usually precisely controlled (on the order of 0.1 Å) by a piezoelectric system, serves to regulate the tip-surface separation.

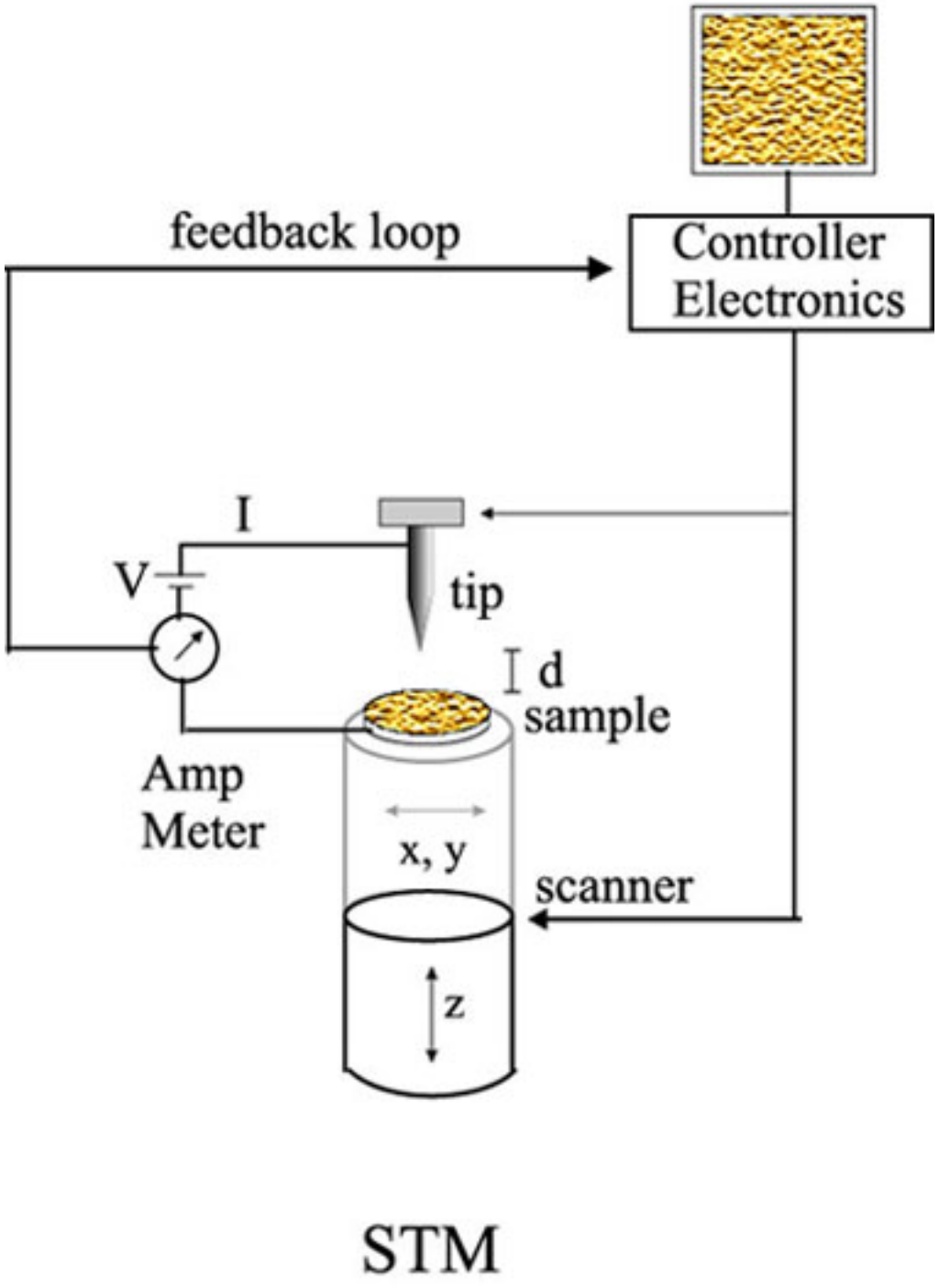

Figure 1.1. Overall schematic of a scanning tunneling microscope. A bias voltage is applied between the sample and tip while the tunneling current as a result is measured versus displacement by a computer-controlled piezoelectric system.

A simple expression for the tunneling current in one-dimension can be derived using the WKB approximation (Fowler-Nordheim tunneling) [16]:

$$I \propto \frac{\Delta E}{d} \exp(-\mathrm{K} d \sqrt{\Phi_{avg}})$$

where ΔE is the bias voltage to denote the applied potential necessary to overcome the energy difference between the barrier and the Fermi level E_F of the electrons in the electrodes, d the electrode (or tip-surface) separation, K a constant of 1.025 $\text{Å}^{-1}\ \text{eV}^{-0.5}$ for the case of electron, and Φ_{avg} the average of the effective work functions of the two electrodes. The effective work functions here are not the same as in the case of field emission or photoelectric effect. In STM, the work functions are reduced due to the interaction between tunneling electrons and electrons in local density of states within the electrodes. This interaction can be described as image potential effects, where a unit charge such as a tunneling electron induces an image charge on the metal electrode surfaces, and lead to a distance-dependant reduction of the barrier height. Since work function is the measured work required to remove an electron from the Fermi state to a macroscopic distance from the solid, and since STM operates at a much reduced distance, the tunneling barrier causes a perturbation in the effective work functions of the electrons on the electrodes involved.

The exponential variation of the current with separation is related to the rapid decay of electron wavefunctions extending into the gap between the tip and surface. This strong dependence, roughly one order of magnitude per angstrom separation for typical metals, is thus directly responsible for the high spatial resolution of STM, typically on the order of 0.01 Å. In practice, the tip used for electron tunneling in STM is

macroscopically extremely sharp, but on the molecular level it has a radius of curvature on the order of 10 Å. While the ideal tip would be a perfect apex terminating in a single atom, many tips of varying and usually unknown shapes are still able to produce images of atomic resolution. This is due to the exponential relationship between distance and tunneling described above. As long as one atom of the tip extends slightly further than any other, tunneling current will preferentially flow through that atom.

The bias voltage applied plays an important role in determining the electronic states of the electrodes (tip and surface) being probed. Referring to Figure 1.2, the sample being probed can be biased positively or negatively relative to the tip with the applied potential ΔE. In the former case, a positive bias is said to be applied by the sign convention, and the tunneling electrons flow from the filled energy states of the tip to the empty energy states of the tip. The only energy states that can participate are the ones between the Fermi levels of the sample and the tip, between $E_{F,sample}$ and $E_{F,sample} + \Delta E$ in this case. Likewise, for a negative bias applied, the tunneling electrons flow from the filled states of the sample to the empty states of the tip, and the contributing energy states are limited to $E_{F,sample}$ and $E_{F,sample} - \Delta E$. Two important features of STM result from this. First, by choosing the sign of the bias applied, the user can selectively probe empty or filled states of the sample surface interest. This technique is especially useful in distinguishing the electron-deficient and the electron-rich elemental components of a superconductor or a doped semiconductor. Second, for a small bias the density of states can be approximated to be constant with respect to energy, and the tunneling current varies nearly linearly with both bias and density of states as $\sqrt{\Phi_{avg}}$ approaches zero. As a result, the contribution to the contrast

due to the topography of a surface of homogeneous composition dominates over the electronic variation in contributing energy states, and thus the image becomes an accurate reflection of surface corrugation even though it probes only the electronic effects of the sample.

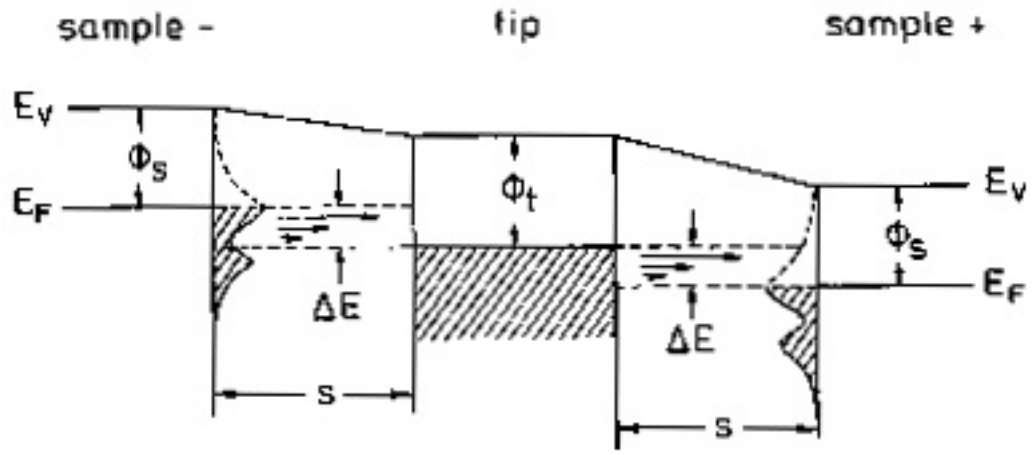

Figure 1.2. Energy diagram of tunneling for both positive (right) and negative (left) sample bias. The shaded areas represent filled energy states. In the positive bias mode, electrons flow from the filled states of the tip into the empty states of the sample. In the negative bias mode, the electrons flow from the filled states of the sample into the empty states of the tip. [14]

More complete theories of tunneling that account for the three-dimensional geometry of the tip and the detailed electronic structures of the tip and surface preserve this fundamental picture while emphasizing the importance of contribution by the local density of states [17-20].

1.2.2 Capabilities and Limitations

The scanning sharp tip probing the sample locally through quantum tunneling of electrons makes STM a unique microscopy, as it requires no lens as in the case of SEM

and thus there is no image distortion due to aberration. The electrons involved in STM have an energy of a few electron volts (eV), in contrast to electron energies of several keV to MeV in high resolution electron microscope, making radiation-induced sample changes and damages less likely. In STM, the electron energies used in imaging can be selected to be smaller than typical energies of chemical bonds to minimize destructive atomic resolution imaging, or to be larger than certain types of chemical bonds to selectively induce bond cleavage. Although the wavelength of a typical tunneling electron of 1 eV used in STM is roughly 12 Å, which is larger than typical interatomic distances in solids of about 3 Å, STM operates in the near-field regime where the distance between tip and sample surface of typically a few angstroms is comparable to or less than the electron wavelength. In this regime, the spatial resolution is no longer diffraction-limited (as in techniques such as SEM that operate in the far-field region) and is not determined by the wavelength of probing electrons.

In addition to high resolution and sensitivity, STM offers considerable versatility. Scanning tunneling microscopes can image the surfaces of metals [21], semiconductors [22], superconductors [23], and even thin oxide layers grown on conductive substrates [24]. Because the tunneling mechanism relies primarily on proximity, STM is not restricted to environments with large mean free electron paths. In addition to vacuum, common operating environments include low and high pressure gases [25] (up to several atmospheres) and liquids [26]. Especially in the case of liquid medium, tunneling current can still occur even though the intermolecular distance of the medium may be comparable or even smaller than the tip-surface separation distance, for as long as the

medium remains homogeneous on the time scale of tunneling current measurement, the medium and its molecular components serve only as a stable potential barrier for the tunneling electrons to overcome. In addition, substrate temperatures for STM studies can vary over a wide range as well, from cryogenic up to several hundred degrees centigrade [27, 28].

One intrinsic limitation of STM is the combined dependence of the tunnel current on d and Φ_{avg}, which mixes the effects of topographic and electronic variations as the tip moves across the surface to generate an image. Thus, although STM can produce images of surfaces with superb detail, care must be taken when interpreting features in these images [29-31]. For example, upon individual adsorptions onto a Pt(111) surface, CO appears as a protrusion (or region of brighter contrast) while O and H both appear as depressions (or areas of darker contrast) on the same surface. Theoretical calculations, as well as experimental techniques such as measuring the change of I with respect to d and V, are generally required to separate topographic and electronic contributions. In attempt to decouple topographical and electronic effects in imaging, many different types of scanning modes have been developed to emphasize one contrast mechanism over another in imaging the surface. The two most common measuring modes (generally for surfaces of homogeneous composition) are the topography (or constant current) mode and the current (or constant height) mode. (Figure 1.3)

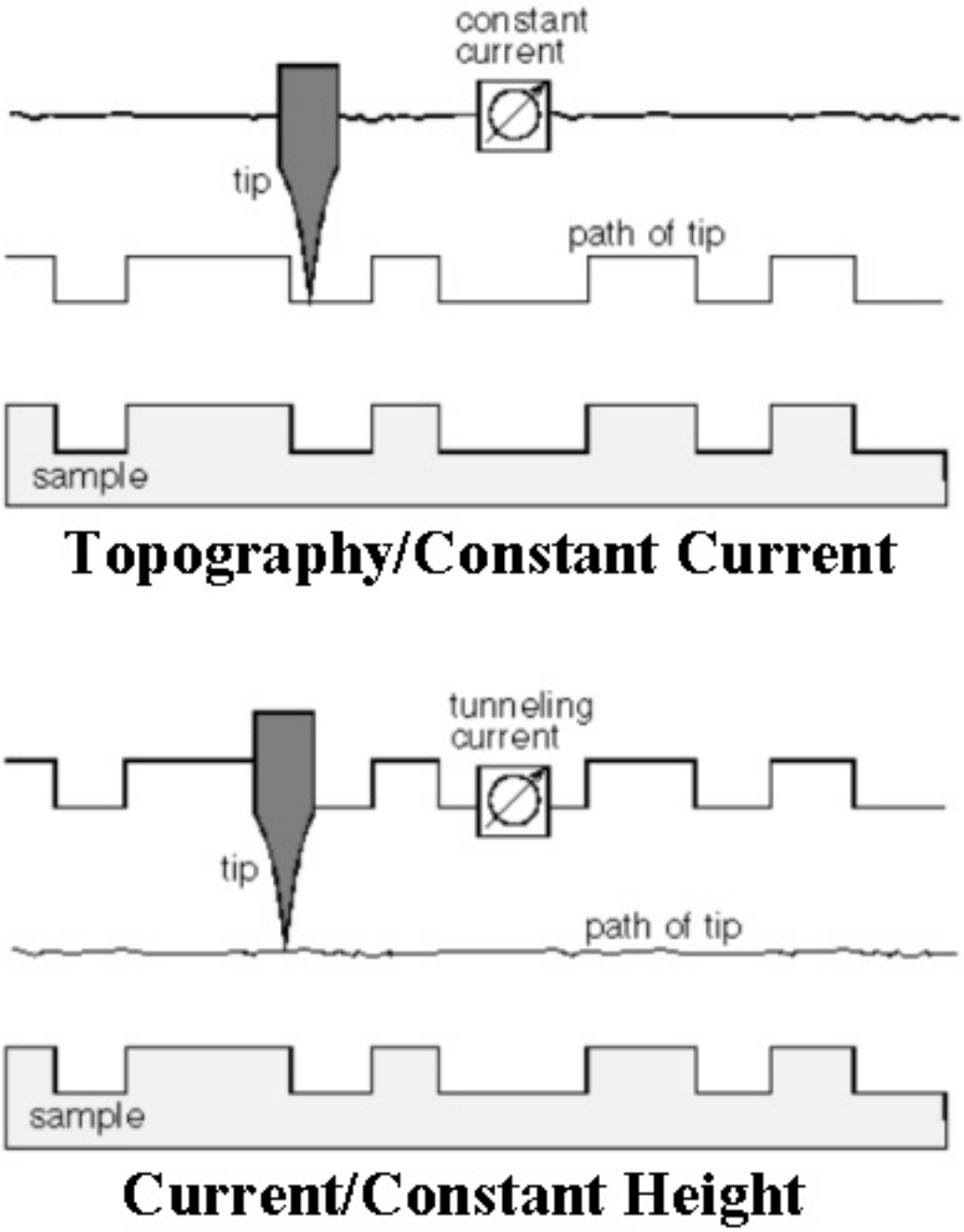

Figure 1.3. Operational principles of topography and current modes. In the former case, the tip is traced over the corrugation of the surface as a feedback loop maintains a constant current. In the latter, the tip position is constant while the variation in current is measured.

In topography mode, the tunneling current is constantly monitored by a feedback loop, which adjusts the tip height through the use of piezoelectric transducers to maintain the same current set point at a preset voltage. By measuring the change in the voltage applied to the piezoelectrics, a topographical image can be produced assuming the surface is mostly homogeneous. Such assumption in general is true for large scale and low-resolution imaging, since local defects become less significant in the tunneling contribution. Due to the careful control of a feedback control loop, the topography mode is extremely sensitive to surface changes in topographical height or local electronic states. By the same token, due to the necessary settling time for tunneling current (to minimize induced current from previous piezoelectric adjustment) before input to the feedback control and the finite time for piezoelectric regulation, the imaging time is generally long (tens of seconds to minutes per image) for this mode. However, (to a larger degree) by minimizing the size and resonance frequency of the piezoelectrics used and (to a smaller degree) by developing feedback control with faster response, while sacrificing imaging size and range, imaging time under topography mode can be reduced to several images per minute.

In contrast, the current mode images are taken by increasing the scan rate through minimizing the feedback control of the tip, by either decreasing the settling time allowed of the measured current input (and thus resulting in less accurate and responsive feedback) or disabling the feedback completely in some cases. The goal is to measure the changes in topography and electronic states on the surface through the variation in the tunneling current, while a suppressed feedback loop can continue to provide adequate

compensation for slopes and thermal drifts. As a result of the virtual absence of the feedback loop, the imaging rate under the current mode can be several orders of magnitude higher than that under the topography mode. Thus, this allows for real time monitoring of dynamic processes such as surface reconstruction as result of adsorption or reaction. At the same time, thermal drifts and distortion in the slower scan direction can be minimized due to smaller acquisition time. The rate of obtaining images is practically limited by the high speed of the data acquisition system, although the maximum scan rate (or more accurately the sweeping frequency of the scanning piezoelectric transducer) is still limited by the inherent resonance frequency of the system. In addition, since the tip needs to be positioned only a few angstroms above the surface as a result of the exponential decay of tunneling current upon increase in distance, the surface imaged under the current mode must be atomically relatively flat as a simple step edge can lead to loss of height resolution, tip-induced surface changes, or even a mechanical crash of the tip. In general, ultra fast STM constructed for rapid scanning under the current mode is especially rigid and small, to minimize mechanical instability and piezoelectric response time and nonlinearity, as well as to reduce net thermal drifts as a result of temperature control or the lack thereof.

In addition, different modes of imaging local density of states have been developed to decouple electronic structure measurements from topographic effect. By varying voltage at small amplitude and high frequency to minimize the nonlinear change of transmission coefficient and feedback compensation, measurements of $\frac{\partial I}{\partial V}$, known as scanning tunneling spectroscopy, provide information about the local density of states

and have been utilized extensively to study semiconducting surfaces [32-34], as well as metals [35], isolated atoms [36], superconductors [37, 38], and oxides [39]. Measurements of $\frac{\partial I}{\partial d}$ (known as constant barrier height mode), which is proportional to $\sqrt{\Phi_{avg}}$, can be used to map spatial variations of the work function, by modulating the tip-sample distance at a frequency higher than the feedback compensation and measuring the variation in current [40, 41]. Since the effective work function of the tip remains constant and modulation of the tip height is small, any variation in contrast is as a result of changes in the local density of states on the surface.

A further limitation of STM is a lack of chemical specificity when imaging atoms and molecules adsorbed on surfaces. This weakness is typically addressed by studying systems of predetermined chemical composition, as evidenced in Chapter 4, or by pairing STM with complementary but albeit more averaging techniques such as IRAS, AES, XPS, or TPD. In recent years, however, experiments have demonstrated the ability of STM to conduct vibrational spectroscopy on individual molecules. [42-44] In this technique, known as STM inelastic electron tunneling spectroscopy (STM-IETS), a small fraction of tunneling electrons lose energy during tunneling between tip and substrate surface to internal vibrational modes of the adsorbed molecule being monitored. By varying the bias voltage applied between the tip and sample, new inelastic tunneling channels open whenever the electron energy exceeds the energy of a molecular vibrational mode, and the resulting variation of the total tunneling current yields a vibrational spectrum of the molecule. In addition to finger-printing the chemical identity

of adsorbates, this technique opens exciting new possibilities for studying the effects of the local environment on the internal states of molecules.

STM-IETS is also closely related to the topic of manipulation of adsorbates by STM, in which energy provided by tunneling electrons to vibrational modes induces controlled translations or rotations of an adsorbed molecule [45. 46]. If sufficient energy is provided to specific vibrational modes, molecules may desorb [47] or internal chemical bonds may be selectively broken [48, 49]. Under specific conditions the reverse process of selective bond formation has also been observed, offering the potential to use STM to construct complex molecules atom by atom [49]. In general, both STM-IETS and molecular manipulation requires either low temperature or weakly adsorbed large molecules to minimize adsorbate diffusion in the former case while avoid necessitating large bias voltage that may inadvertently alter the probing tip in the latter, but the prospect of manipulating and constructing molecules atomically offers an exciting front of nanotechnology.

While there are inherent limitations in STM, new imaging modes and novel STM motor designs are continuously being developed to match the different needs required by numerous fields of science. As the field of nanometer-scale science and technology becomes more and more important, STM and its related SPM techniques can provide the crucial answers to the needs of observing and understanding the increasing role of surfaces at the atomic level in real space and time, as well as offer the satisfaction to the aspirations to create and control with similar precision. In particular, the ability to

observe reaction progress in real space and time with atomic resolution is vital in understanding reaction mechanism as well as improving catalyst design.

1.3 References and Notes

[1] Chan, C. M.; Van Hove, M. A.; Weinberg, W. H.; Williams, E. D. *Surf. Sci.* **1980**, *91*, 440.

[2] Chen, Z.; Ward, R.; Tian, Y.; Baldelli, S.; Opdahl, A.; Shen, Y. R.; Somorjai, G. A. *J. Am. Chem. Soc.* **2000**, *122*, 10615.

[3] Somorjai, G. A. *Introduction to Surface Chemistry and Catalysis*. Wiley, **1994**.

[4] Woodruff, D. P. and Delchar, T. A. *Modern Techniques of Surface Science*. Cambridge University Press, **1994**.

[5] Blakely, D. W.; Kozak, E. I.; Sexton, B. A.; Somorjai, G. A. *J. Vac. Sci. Technol.* **1976**, *13*, 1091.

[6] McCrea, K. R.; Parker, J. S.; Somorjai, G. A. *J. Phys. Chem. B* **2002**, *106*, 10854.

[7] Kim, S. H.; Opdahl, A.; Marmo, C.; Somorjai, G. A. *Biomaterials* **2002**, *23*, 1657.

[8] Kim, J.; Somorjai, G. A. *J. Am. Chem. Soc.* **2003**, *125*, 3150.

[9] Bluhm, H.; Ogletree, D. F.; Fadley, C. S.; Hussain, Z.; Salmeron, N. *J. Phys – Con. Matt.* **2002**, *14*, L227.

[10] McIntyre, B. J.; Salmeron, M.; Somorjai, G. A. *Rev. Sci. Instrum.* **1993**, *64*, 687.

[11] Binnig, G.; Rohere, H.; Gerber, C.; Weibel, E. *Phys. Rev. Lett.* **1982**, *49*, 57.

[12] Dunphy, J. C.; Sautet, P.; Ogletree, D. F.; Dabbousi, O.; Salmeron, M. B. *Phys. Rev. B* **1993**, *47*, 2320.

[13] Avouris, P.; Wolkow, R. *Phys. Rev. Lett.* **1988**, *60*, 1049.

[14] Wintterline, J. and Behm, R. J. *Scanning Tunneling Microscopy I.* Springer-Verlag, **1992**.

[15] Besenbacher, F.; Laegsgaard, E.; Stensgaard, I.; Stoltze, P.; Topsoe, H. *Catal. Lett.* **1991**, *8*, 273.

[16] Fowler, R.; Nordeim, L. W. *Proc. Roy. Soc. Lond. A* **1928**, *119*, 173.

[17] Tersoff, J.; Hamann, D. R. *Phys. Rev. B* **1985**, *31*, 805.

[18] Lang, N. D. *Phys. Rev. Lett.* **1986** , *56*, 1164.

[19] Martin-Rodero, A.; Flores, F. *Phys. Rev. B* **1988**, *38*, 10047.

[20] Jurczyszyn, L.; Mingo, N.; Flores, F. *Surf. Sci.* **1998**, *402-404*, 459.

[21] Crommie, M. F.; Lutz, C. P.; Eigler, D. M. *Nature* 1993, *363*, 524.

[22] Goldman, R. S.; Feenstra, R. M.; Briner, B. G.; O'Steen, M. L.; Hauenstein, R. J. *Appl. Phys. Lett.* **1996**, *69*, 3698.

[23] Pan, S. H.; Hudson, E. W.; Lang, K. M.; Eisaki, H.; Uchida, S.; Davis, J. C. *Nature* 2000, *403*, 746.

[24] Lai, X.; Chusuei, C. C.; Luo, K.; Guo, Q.; Goodman, D. W. *Chem. Phys. Lett.* 2000, *330*, 226.

[25] Rasmussen, P. B.; Hendriksen, B. L. M.; Zeijlemaker, H.; Ficke, H. G. *Rev. Sci. Instrum.* **1998**, *69*, 3879.

[26] Sonnenfeld, R.; Hansma, P. K. *Science* **1986**, *232*, 211.

[27] Upward, M. D.; Janssen, J. W.; Gurevich, L.; Morpurgo, A. F.; Kouwenhoven, L. P. *Appl. Phys. A* **2001**, *72*, S253.

[28] Kuipers, L.; Loos, R. W. M.; Neerings, H.; ter Horst, J.; Suwiel, G. J.; de Longh, A. P.; Frenken, J. W. M. *Rev. Sci. Instrum.* **1995**, *66*, 4557.

[29] Sautet, P.; Bocquet, M.-L. *Phys. Rev. B* **1996**, *53*, 4910.

[30] Sautet, P. *Surf. Sci.* **1997**, *374*, 406.

[31] Bocquet, M.-L.; Cerda, J.; Sautet, P. *Phys. Rev. B* **1999**, *59*, 15437.

[32] Stroscio, J. A.; Feenstra, R. M.; Fein, A. P. *Phys. Rev. Lett.* **1986**, *57*, 2579.

[33] Wolkow, R.; Avouris, P. *Phys. Rev. Lett.* **1988**, *60*, 1049.

[34] Avouris, P.; Wolkow, R. *Phys. Rev. B* **1989**, *39*, 5091.

[35] Hasegawa, Y.; Avouris, P. *Phys. Rev. Lett.* **1993**, *71*, 1071.

[36] Crommie, M. F.; Lutz, C. P.; Eigler, D. M. *Phys. Rev. B* **1993**, *48*, 2851.

[37] de Lozanne, A. L.; Elrod, S. A.; Quate, C. F. *Phys. Rev. Lett.* **1985**, *54*, 2433.

[38] Elrod, S. A.; Bryant, A.; de Lozanne, A. L.; Park, S.; Smith, D.; Quate, C. F. *IBM J. Res. Develop.* **1986**, *30*, 387.

[39] Garcia, R. ; Saenz, J. J.; Garcia, N. *Phys. Rev. B* **1986**, *33*, 4439.

[40] Binnig, G.; Roher, H. *Surf. Sci.* **1983**, *126*, 236.

[41] Khaikin, M. S.; Trojanovsky, A. M. *Pis'ma Zh. Tech. Phys.* **1985**, *11*, 1236.

[42] Stipe, B. C.; Rezaei, M. A.; Ho, W. *Science* **1998**, *280*, 1732.

[43] Lauhon, L. J.; Ho, W. *Phys. Rev. B* **1999**, *60*, R8525.

[44] Pascual, J. I.; Jackiw, J. J.; Song, Z.; Weiss, P. S.; Conrad, H.; Rust, H.-P. *Phys. Rev. Lett.* **2001**, *86*, 1050.

[45] Walkup, R. E.; Newns, D. M.; Avouris, P. *Phys. Rev. B* **1993**, *48*, 1858.

[46] Stipe, B. C.; Rezaei, M. A.; Ho, W. *Science* **1998**, *279*, 1907.

[47] Bartels, L.; Meyer, G.; Reider, K.-H. *Phys. Rev. Lett.* **1997**, *79*, 697.

[48] Stipe, B. C. ; Rezaei, M. A.; Ho, W.; Gao, S.; Persson, M.; Lundqvist, B. I. *Phys. Rev. Lett.* **1997**, *78*, 4410.

[49] Hla, S.-W.; Bartels, L.; Meyer, G.; Rieder, K.-H. *Phys. Rev. Lett.* **2000**, *85*, 2777.

Chapter 2

Experimental Techniques

2.1 Overview

The difficulties of imaging and detecting surfaces at the level of atoms, molecules, ions, or electronic structures are often formidable. Accordingly, characterization of surfaces generally involves the use of a variety of complementary techniques. While as described in the previous chapter most traditional surface science techniques are highly dependent of the electron mean free path and thus limited in their roles in high pressure *in situ* studies, they still provide valuable *ex situ* information otherwise difficult to obtain by the limited selection of high pressure surface analysis methods. The lack of chemical specificity and large sampling area in scanning tunneling microscopy (STM) studies can be alleviated by performing in addition other experimental techniques, such as Auger electron spectroscopy (AES) for chemical analysis of the

surface species, low energy electron diffraction (LEED) for observing long-ranged surface order, and mass spectrometry for identifying reaction products in the gas phase as well as providing information about reaction kinetics to correlate with structural information given by STM and LEED. The former two of these three techniques, along with proper sample preparation by ion bombardment and annealing, provide the basis of sample treatment and analysis before and after the high pressure STM studies presented in the following chapters, while mass spectrometry provides the means of identifying contaminants as well as monitoring reaction progress within the system. This chapter describes the principles behind these techniques as well as outlines their specific roles in the studies as reported in this dissertation.

2.2 Auger Electron Spectroscopy

Auger electron spectroscopy (AES) has emerged as one of the most widely used analytical techniques for obtaining the chemical composition of solid surfaces. The basic advantages of this technique are its high sensitivity for chemical analysis in the less than 20 Å deep near the surface, a rapid data acquisition speed, its ability to detect all elements above helium, and its capability of high-spatial resolution. The high-spatial resolution is achieved because the specimen is excited by an electron beam that can be focused into a fine probe. Combined with scanning tunneling microscopy (STM), AES makes a useful complement to provide the necessary chemical identification of surface species *ex situ* both before and after high pressure experimentation.

The Auger effect was discovered by Pierre Auger in 1925 while working with X-rays and using a Wilson cloud chamber. Tracks corresponding to ejected electrons were observed along a beam of X-ray [1]. He observed such electrons to have discrete energy characteristics of the emitting elements. In 1953, J. J. Lander became the first to identify Auger transitions through the use of electron bombarding in high vacuum as the means to observe Auger emission from solid surfaces. [2]

Excitation of an atom, such as by an energetic electron, photon, or ion can result in the emission of a core electron. To reduce the significant potential energy of this ionized state, an electron from the outer shell relaxes into the vacant orbital. The energy released from this relaxation process can be emitted in a radiative (usually an X-ray) or non-radiative (via a third electron, known as the Auger electron) process, as indicated in Figure 2.1 . The kinetic energy of the emitted Auger electron is approximately equal to the energy available from the relaxation process (or the energy difference between the core and the outer shell electrons) subtracting the binding energy of the final emitted electron. Thus, the Auger electron carries information concerning the electronic structure of the emitting atom. All elements, except hydrogen and helium due to insufficient electrons, exhibit the Auger effect. In the 50 to 2500 eV kinetic energy range (which forms the typical AES operating range), the Auger emission predominates X-ray emissions by approximately two orders of magnitude. [3] This energy range, in turn, translates into a typical mean escape path of less than 40 Å, or less than 20 atomic layers, for the Auger electron, making the Auger effect quite surface selective especially when

enhanced at the expense of signal strength by employing grazing angles of incidence and detection.

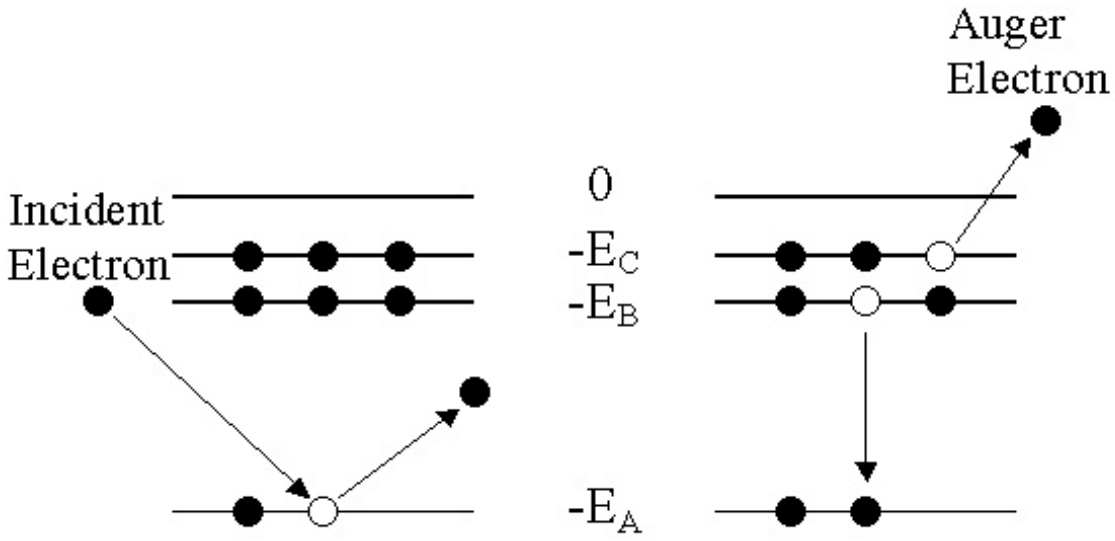

Figure 2.1. Energy level diagram showing the Auger electron process. The energy states are labeled with their one-electron binding energies. Incident excitation, in form of an electron in this case, causes an ejection of a core electron and subsequent relaxation of an outer electrons, which in turn leads to the emission of the Auger electron.

In AES the atomic core levels are typically ionized by an incident electron beam and the resulting Auger electrons are detected with an electron spectrometer. These electrons form small peaks in the total energy distribution function. The incident electrons entering a solid are scattered both elastically and inelastically. At the primary beam energy a sharp peak is observed, caused by electrons that have been elastically scattered back out of the specimen. For a crystalline specimen, these electrons carry the crystal structure information, which is exploited in techniques such as low energy electron diffraction, as will be discussed in the following section. At slightly lower energies there are smaller peaks due to electrons that have undergone characteristic

energy losses. The information contained in this region is exploited in the technique of low-energy electron loss spectroscopy. At the low-energy side of the spectrum, there is a large peak corresponding to the secondary electrons. A few hundred electron-volts above this peak is a loosely defined crossover energy, above which the distribution is dominated by backscattered primary electrons, and below which the secondary electrons form the major component. The crossover point depends on the primary beam energy and moves to higher energies with increasing incident beam energy. The peaks due to Auger electrons are superimposed on this distribution. As a result, the Auger effect was not fully taken advantage of and AES was not developed until the 1960s, when ultra high vacuum (UHV) technology became commercially available, and L. A. Harris was the first to demonstrate that differentiation of the secondary electron energy distribution was essential to obtain high contrast spectra [4], since Auger electrons are typically only a small fraction of the total number of secondary electrons detected at a given kinetic energy. Differentiation emphasizes the Auger electron distribution because the energy dependence of the Auger electrons is peaked in energy and much sharper than that of the secondary electron background, which varies gradually with incident beam energy.

In this work, an electron gun bombards the surface with energies near 3000 eV. The ejected Auger electrons are collected using a cylindrical mirror analyzer (CMA), which acts as a band pass to measure the number of electrons within a energy range set by collection aperture size and angle. The differentiation of the collected signals is achieved by modulating the voltage to the grid, then detecting the second harmonic of the signal with a lock-in amplifier. For the STM studies recorded herein, AES is mainly used

to qualitatively verify the cleanliness of the single crystal surfaces before performing experiments. Figure 2.2 shows AES spectra for a Pt(111) surface before and after sample preparation by ion bombardment and sample annealing, with the former case contaminated mainly by carbon. Our detection limit for carbon, the major contaminant for our transition metal surfaces, is about four percent of a monolayer. In addition to qualitative analysis, to some extent quantitative information can also be obtained from the spectra to determine the surface coverage of specific elements by comparing the relative intensity of the adsorbate peaks to that of the substrate peaks.

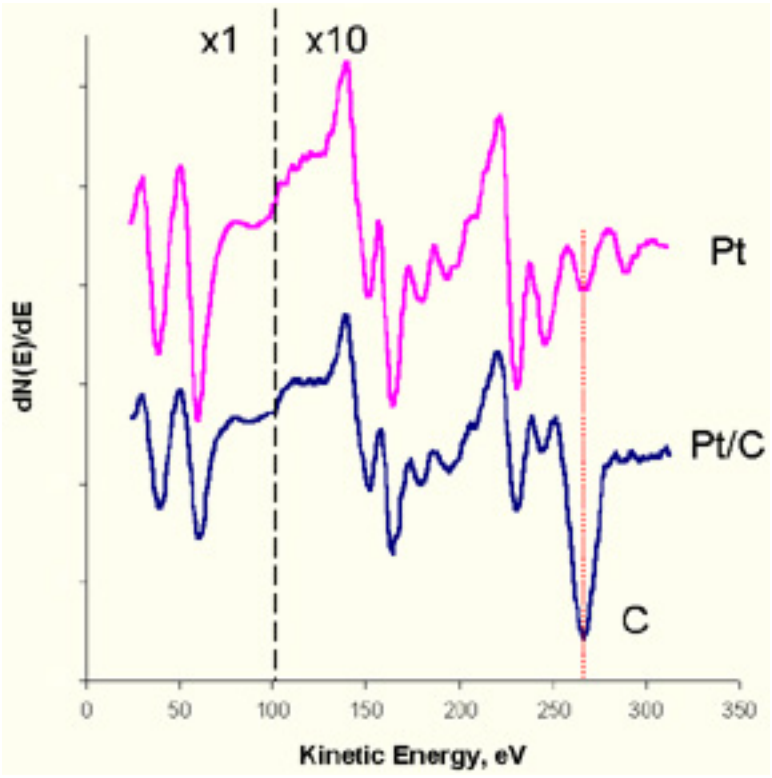

Figure 2.2. AES spectra for a Pt(111) surface before (magenta) and after (blue) sample preparation. The platinum characteristic peaks appear at 43 eV, 63 eV, 168 eV, 237 eV, and 251 eV. These peaks are attenuated, when carbon (272 eV) is present.

2.3 Low Energy Electron Diffraction

Low energy electron diffraction (LEED) provides a method to investigate surface ordered structures under ultra high vacuum conditions. The strong interaction between electrons and matter provide LEED with its surface sensitivity, and offers information about the size and shape of the unit cell of the substrate surface, the degree of order, and the atomic structure and bond angle of overlaying adsorbates. The dynamical analysis of intensities, which fully accounts for the multiple scattering of electrons, yields the structure of the surface with high precision for atomic positions. Although limited by high vacuum application and sensitivity to impurities due to its reliance on electron beam, LEED provides crucial chemical and structural information on surface ordered structures to aid the interpretation of often convoluted topographical and electronic information provided by STM: LEED experiments provide information over macroscopic sample surface areas and yield averaged interatomic distances for crystalline materials, while clear and sharp diffraction patterns can still occur on a surface that appears highly defective under STM; on the other hand, the surface area that STM typically observes is of atomic details but comparably small, where this narrow observation may sometimes be inadequate to draw representative conclusions for the whole surface.

The basis of LEED is based on the fact that electrons act both as particles and waves, which C. J. Davisson and L. H. Germer proves in 1927. [5] This relationship between the electron's wavelength and its kinetic energy can be calculated through the de Broglie relation. Above certain energy, the electron wavelength is short enough to undergo diffraction from a periodic atomic array. In the case of LEED, a monochromatic

beam of low energy electron, typically of 20 to 300 eV (or of 0.7 to 2.7 Å wavelength), is scattered elastically off the lattice of a sample. Due to the wavelength of the electron beam being on the same order of a typical lattice constant, the beam of electrons forms a diffraction pattern off an ordered surface. Due to small mean escape path of the scattered electrons, only the top 2 to 3 layers of sample atoms contribute to the diffraction pattern and this gives rise to the surface specificity of LEED.

The LEED pattern formed is related to the two dimensional surface unit cell of the sample as the X-ray diffraction pattern is to the three dimensional unit cell of a crystal, such as the LEED pattern of Pt(111) shown in Figure 2.3; the LEED diffraction is a projection in reciprocal space of the real space two dimensional unit cell. Similar to X-ray diffraction, LEED diffraction pattern follows the condition of Bragg diffraction (Figure 2.4), where each atom in the two dimensional unit cell scatters the incident wave into spherical waves, which merge into outgoing plane waves. Only the scattered waves with path difference being an integer multiple of the electron's wavelength will be constructively interfering and outgoing. Thus by tuning the energy and thus the wavelength of the incident electron beam, different unit cells on the sample surface will yield observable diffraction patterns.

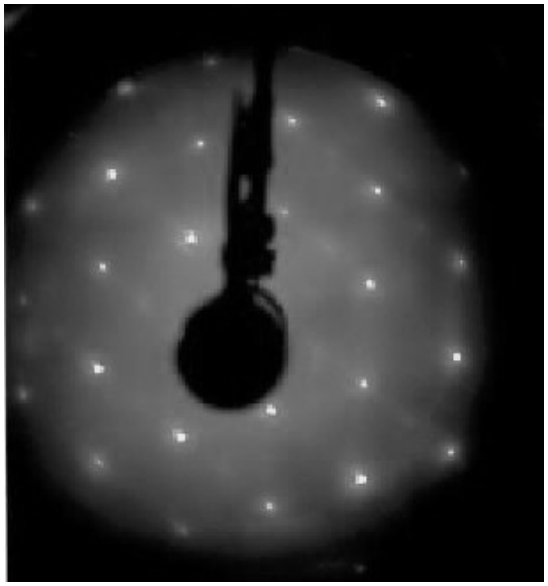

Figure 2.3. LEED pattern of a Pt(111) surface.

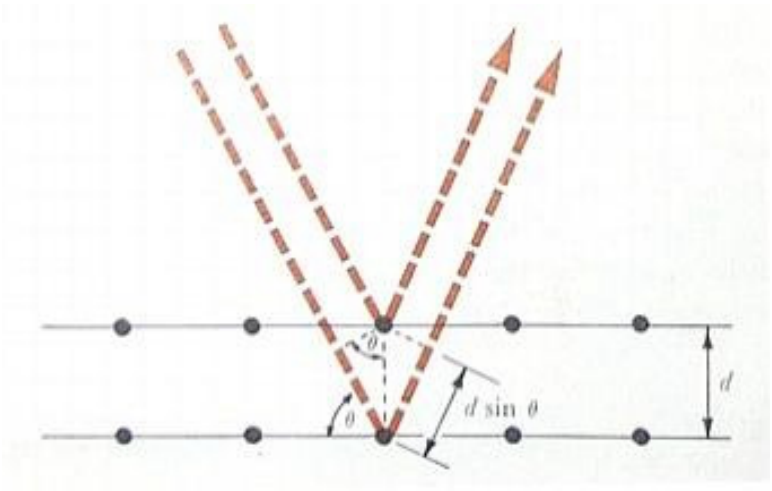

Figure 2.4. The layer of exposed balls constitutes a Bragg plane, a plane from which the incident microwave is reflected. Two such waves will interfere constructively if the path difference is equal to an integer number of wavelengths: $n\lambda = 2d\sin\theta$.

For qualitative analysis, LEED can be used to determine the symmetry of the surface and any overlayer of adsorbates through inspection of the diffraction patterns. Quantitative application can be also performed to determine the three dimensional

positions of both adsorbate and substrate atoms on the surface, to an accuracy of below tenths of an angstrom, through interpretation and calculation of both the intensity and symmetry of the scattering patterns and their relationship to incident beam energy.

However, the information obtained from LEED is limited to low coverage structures under vacuum or kinetically arrested order induced by cooling, and can only serve as a complement to STM under similar conditions. In addition, the diffraction pattern of LEED is an averaging result over many equivalent atoms, with little sensitivity to the involvement of local ordering and defects as well as molecular clusters.

Due to the high pressure nature of the studies recorded therein, LEED is used primarily to ascertain the order of the clean sample crystal surfaces prior to experiments after polishing and cleaning. Referring to Figure 2.5, a sample is irradiated by an electron beam of typically 200 to 300 eV, and the backscattered electrons are collected by a phosphorus-coated screen behind four grids that serve as a high pass filter to prevent illumination of the screen by inelastically scattered electrons. The pattern thus formed is proportional to the number of impacting electrons [6], and is inspected visually through a charge-coupled device (CCD) video camera. The cleanliness and the miscut angle of the sample are then determined by the intensity and the reciprocal lattice vectors of the diffraction pattern.

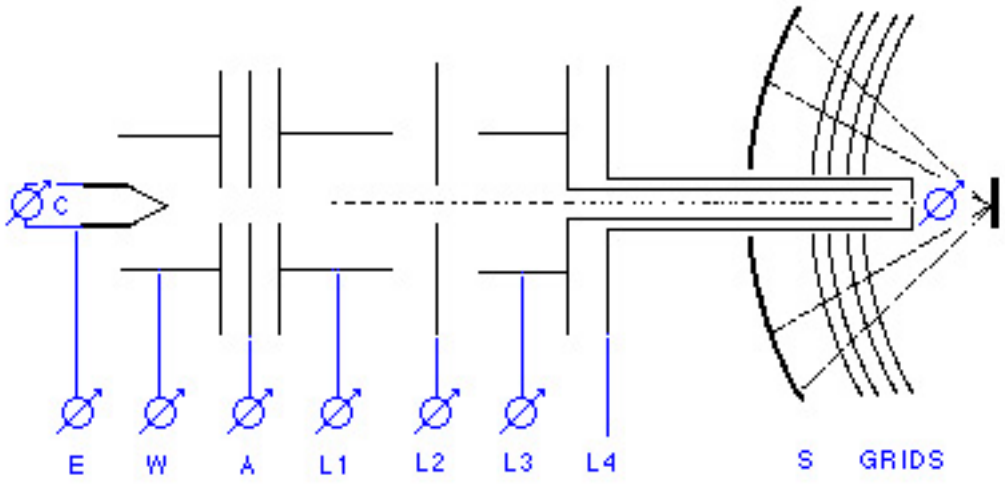

Figure 2.5. Schematics of a LEED apparatus, where electron beam from a electron source is focused and accelerated to a specific energy to impact a sample surface. The diffracted electrons illuminate the phosphorus screen after passing through differential grid filters.

2.4 Mass Spectrometry

Mass spectrometry provides a complementary technique to monitor the chemical composition of the gas phase during heterogeneous catalysis, just as AES provides a means to monitor chemical identities of the surface species albeit after high pressure *in situ* studies. By extracting a small sample of the high pressure reaction gas into a ballast, which can be as simple as a vacuum chamber of a much larger volume, that is equipped with a mass spectrometer, the reaction progress as well as the gaseous species present can be continuously examined and related to the structural information provided by the simultaneous STM observation of the catalyst surface. However, care must be taken to ensure the reaction gases are well mixed within the reactor so that the sampling is representative of the actual reaction progress near the catalyst surface.

The evolution of mass spectrometry has been marked by an ever-growing demand for its application to problems of increasing difficulty such as biomolecule analysis and the coincidental development of computer technology. New developments in the technology have created a complex array of instruments, but the basic components of all mass spectrometers are essentially the same. These components may be best understood by tracing the path of an ionized molecule within a mass spectrometer. As a general overview as indicated in Figure 2.6, an ion source first ionizes the molecule of interest, then a mass analyzer differentiates the ions according to their mass-to-charge ratio, and finally a detector measures the current induced by ion beam. Each of these elements exists in many forms and is combined to produce a wide variety of mass spectrometers with specialized characteristics.

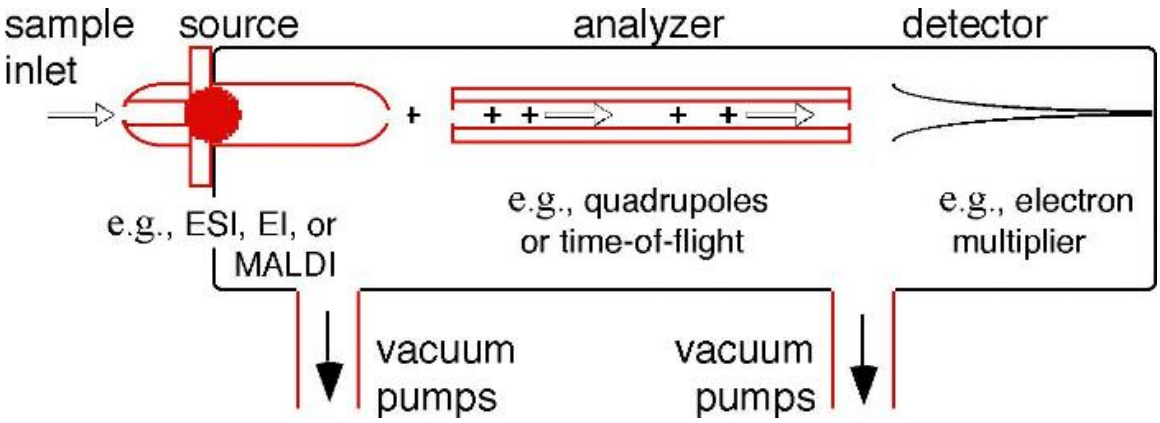

Figure 2.6. Schematics of a mass spectrometer, which can be functionally divided into three areas: source where sample is introduced and ionized, analyzer where ions are filtered and selectively fragmented, and detector where ion quantity is converted into electrical signals.

All mass spectrometers require a vacuum. A vacuum is necessary to permit ions to reach the detector without colliding with other gaseous molecules. Such collisions

would reduce the resolution and sensitivity of the instrument by increasing the kinetic energy distribution of induced fragmentations of the ions, or by simply preventing the ions from reaching the detector. When the mean free path of gas molecules in a vacuum system is on the order of a few centimeters or more (at $< 10^{-3}$ Torr), a hot filament in a mass spectrometer can provide a source of electrons through thermal emission to create mostly positive ions at a rate depending on the gas pressure, temperature and species of the individual molecules. After the electrons pass through the source grid, they continue through to the ionization gauge section, where they produce more ions. These ions will strike the collector wire and produce a current there, proportional to the total gas pressure. The stream of ions is then electrostatically focused toward the mass filter. In a lot of cases, a quadrupole mass filter, consisting of an arrangement of four metal rods with a time-varying electrical voltage of the proper amplitude and frequency applied, can be made to pass only ions of a particular mass entering along the axis at one end, through to the other end. Thus, the mass filter must be constructed very accurately to have the same pass band throughout its length. At the same time, the quadrupole mass filter can also serve an ion trap to selectively isolate ionized molecule of a particular mass for subsequent collision activation to produce a fragmentation spectrum that often serves as a fingerprint of the molecule. The ions that pass through the mass filter are then focused towards a Faraday cup, where the collision of ions onto the dynode surface generates a small current as a result of secondary electron emission, and the current is measured with a sensitive amp meter, with the resulting signal being proportional to the partial pressure of the particular ion species passed by the mass filter. The current produced by the ions is

very small. For example, at 10^{-11} Torr partial pressure at mass 28 the current at the Faraday detector is approximately 10 femtoamps. [7] This requires an extremely sensitive amplifier, usually in the form of an electron multiplier where serial collisions upon a series of dynodes generate an electron cascade and a much amplified current (typically by a factor of a million).

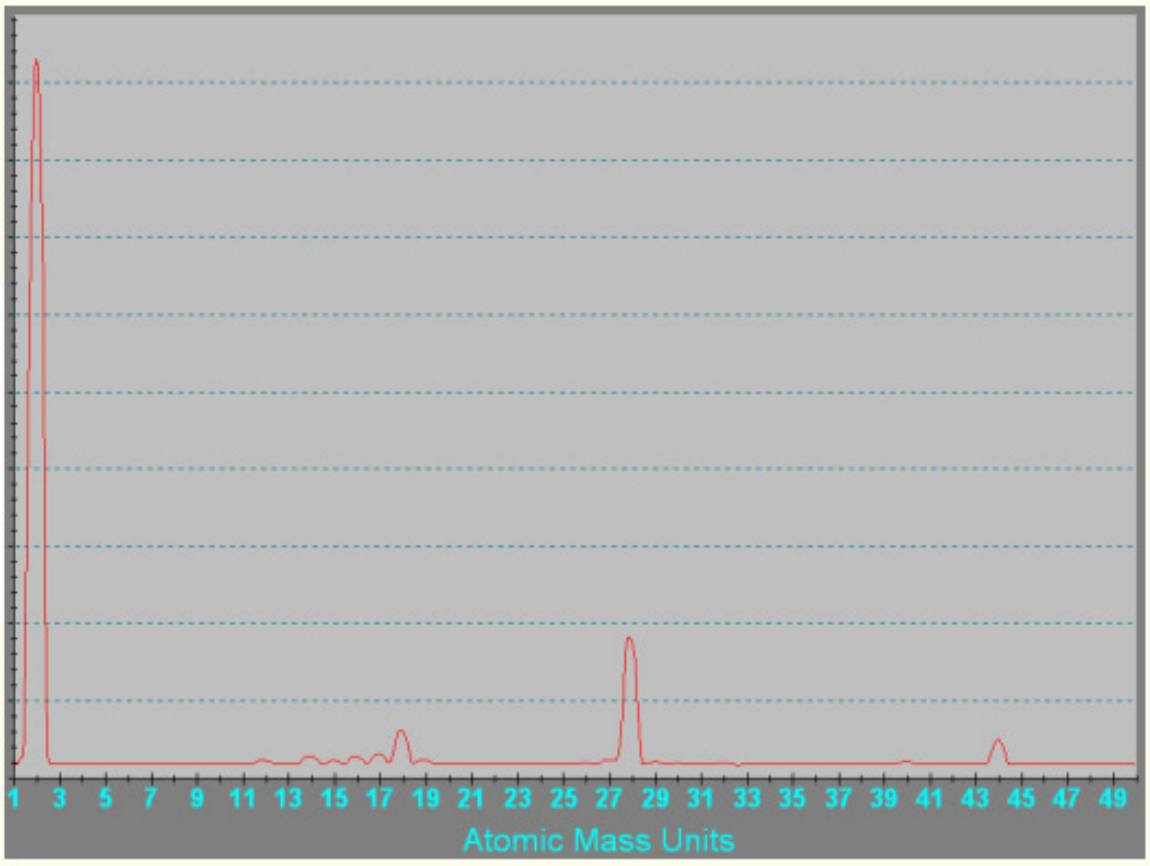

Figure 2.7. Residual gas analysis of a typical UHV system at 1 x 10^{-10}, showing main contaminants in form of hydrogen, methane, water, CO and CO_2, with hydrogen being the most dominant due to its low compression ratio in pumps.

The primary function of the mass spectrometers equipped on both of the STM systems as described in Chapter 3 and Chapter 5 is twofold. First, residual gas analysis by

mass spectrometry is regularly performed on the system background gases as a means to monitor contaminants and perform helium leak testing if necessary. A typical spectrum of residual gases is presented in Figure 2.7 and show a minor amount of atmospheric components, which include hydrogen, methane, water, carbon monoxide, and carbon dioxide. Of these, hydrogen, and occasionally carbon monoxide, is typically the dominant species. An abnormally strong presence of water and the presence of oxygen peaks oftentimes indicate improper evacuation of the system and possibly leaks, which usually warrants subsequent helium leak testing to locate offending regions. Secondly, mass spectrometry is periodically performed during *in situ* studies to provide information on the chemical composition and thus reaction progress of the reaction gases. Due to the high pressure nature of the STM studies performed, a small sample of the batch reactor gas mixture is withdrawn by a leak valve to be monitored by mass spectrometer. Due to the lack of a reactor stirring mechanism and the relatively long diffusion path from the reactor to the mass spectrometer detector, sampling is usually allowed to proceed for 5 minutes or more, until the detected values are stable, before a final figure of the gas composition is recorded. For each study, the detection sensitivities of the mass spectrometer towards different gases are calibrated using the known gas quantities added and the detected peak intensities of the initial composition.

2.5 Sample Preparation

In general, a single crystal sample of certain desired size and surface orientation is initially prepared by either growth method or selective cleavage from an existing boule of

correct orientation. Due to inherent degree of imprecision as a result of the method used, the sample oftentimes requires subsequent polishing to minimize the miscut angle and maximize the atomic terrace size of the correct orientation. The sample is usually first polished with grinding papers of high mesh level (> 400 mesh), and afterward refined using different diamond paste of decreasing grain size (from 15 μm to 0.25 μm) on wet-and-dry polishing cloths. The atomic flatness of the single crystal sample is achieved, when microscopic residues as a result of the polishing are removed by chemical etching of the single crystal in the end, usually by immersing in hot acid bath for a short period of time.

Although the sample thus prepared has good atomic flatness, the cleanliness of the crystal still needs to be maintained on a daily basis to remove impurities as a result of contamination from the UHV environments, prior reaction or adsorption studies, and surfacing impurities from the bulk due to the initial crystal growth method. Contamination as such not only occupies surface metal sites of interest during experiments, but also leads to crystallographic changes of the sample surface. As a result, the sample needs to be monitored by AES and LEED to ensure cleanliness and correct ordered orientation of the sample, respectively, before each study.

Oftentimes, contamination needs to be from the sample surface prior to experiments in form of ion bombardment followed by annealing. Ion bombardment guns are usually electrostatic devices, where inert gas ions, such as Ar^+, are generated by collisional excitation with electrons of typically 100-200 eV from a hot filament. To avoid contamination of the analysis chamber where ion bombardment is performed, the

ion gun is usually differentially pumped during operation. Highly charges ions are produced by with a high intensity electron beam (~100 A/cm^2) that strips many electrons from inert gas molecules (usually introduced at about 5 x 10^{-5} Torr to achieve high ion density) that happen to cross its path. The positive ions as a result are then accelerated to 0.5-5 keV and focused onto the sample surface. The impact of the highly energetic ions causes small clusters of atoms to be ejected indiscriminately from the surface, and the amount of materials removed from the surface can be adjusted by either energy of the ion bombardment, or, more significantly, performing the ion bombardment process at elevated temperatures. As a result, impurities as well as native sample atoms are removed, leaving behind a surface that is more pristine but no longer atomically flat for the crystal orientation of interest. In the case of STM where large atomic terraces are often desired in order to allow successful imaging, the sample needs to be annealed at elevated temperature to allow surface atoms to realign into order with the bulk orientation of the sample crystal. The sample crystal can be heated by various means, such as resistive heating by applying a differential on the sample, conductive heating by a button heater, radiative heating by a heating lamp, or electron bombardment by an electron beam heater (which operates similar to the electron source in an ion gun, but oftentimes uses a filament of lowered work function through doping to generate an increased flux of electrons). In cases where contamination is severe on the sample surface as a result of newly obtained sample or recent exposure to atmospheric environment, reductive or oxidative gases (such as carbon monoxide and oxygen, respectively) can be added in small amount (~ 10^{-7} Torr) during annealing to promote removal of contaminants. The

cleanliness and order of the sample thus prepared by the combination of ion bombardment and sample annealing can then be confirmed by AES and LEED, prior to introduction to the experimental setup.

2.6 References and Notes

[1] Auger, P. *Ann. Phys. (Paris)* **1926**, *6*, 183.

[2] Lander, J. J. *Phys. Rev.* **1953**, *91*, 1382.

[3] Cahn, R. W. and Lifshin, E., Eds. *The Concise Encyclopedia of Materials Characterization*. Pergamon, **1993**.

[4] Harris, L. A. *J. Appl. Phys.* **1968**, *39*, 1419.

[5] Davisson, C. J.; Germer, L. H. *Nature* **1927**, *119*, 558.

[6] Ertl, G. and Kuppers, J. *Low Energy Electrons and Surface Chemistry*. Weinheim, **1974**.

[7] De Hoffmann, E., Charette. D., Stroobant, V. and Trottier, J. *Mass Spectrometry: Principles and Applications*. Wiley, **1996**.

Chapter 3

High Pressure, High Temperature Scanning Tunneling Microscope System

3.1 Overview

This section describes the design of a high pressure, high temperature scanning tunneling microscope system that is capable of monitoring reactions *in situ* at conditions from UHV and ambient temperature up to 1 atm and 250 °C. Similar to many existing high pressure and high temperature STM systems in the world, the STM motor is contained in a UHV chamber that serves as a reactor cell up to 1 atm, and samples can be transferred in and out of the reactor chamber to an adjacent UHV analysis chamber for external characterization and treatment. The system was originally designed by Dr. John Jensen, and assembled by Dr. John Jensen, Dr. Keith Rider, and Dr. Yong Chen. The system continued to evolve and be maintained over a number of years through the work

of Dr. Kevin Hwang and the author. While the basic performance of the instrument was demonstrated within two years of the initial design work, years of development and modification have continued to be needed to meet the new demands of thermal requirement and reactive environment. The design presented in this chapter and the results presented in Chapter 4 are a direct product of the considerable effort that the author and many others have spent to achieve the current satisfactory performance from the system. This system also serves as a template to improve upon during the design of the new ultra high pressure, high temperature STM as described in Chapter 5.

3.2 STM Design

The microscope is a commercially available Beetle or "Johnny Walker" STM (RHK Model VT-UHV300), a popular STM design inspired originally by Besocke [1, 2], equipped with built-in sample heating and cooling ability within the sample stage, and *in vacuo* tip and sample exchange.

3.2.1 Motor

Referring to Figure 3.1, the motor consists of a metallic body, three piezoelectric tubes arranged concentrically on a bolt circle of 5/16"that support the overall body and provides inertial coarse approach for bringing the tip into scanning range as well as coarse positioning across the sample surface, and a central piezoelectric tube that is used for scanning as well as fine adjustment of scanning window and holds a receptacle for receiving an exchangeable tip holder. The placement of the four piezoelectric tubes

minimizes the mechanical loop and thus the vibration from instability felt by the central scan tube. The set of the three outer piezoelectric tubes on the STM motor is lowered by a linear manipulator onto a set of three molybdenum ramps, which are machined as three helical segments and polished to the same roughness, on top of the sample holder. Sapphire half-balls are glued to the end of each outer tube to provide a stable three-point contact (as three points determine only a single plane) with the set of ramps. Then the manipulator is retracted so that the motor decouples and rests under its own weight.

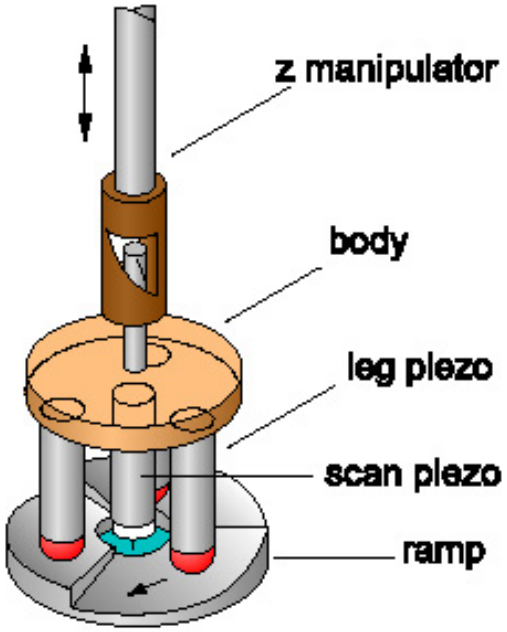

Figure 3.1. Schematic of a Beetle-style STM. The microscope consists of a metallic body (disc), piezoelectric tubes for approach and scanning (gray tubes), and sapphire ball point contacts (half-balls). The microscope can be lowered onto a set of three ramps by a manipulator until they decouple from each other. Through slip-stick motion, the tip is lowered till it is in tunneling range with the sample (center of the set of ramps).

The outer piezoelectric tubes are 0.5” long and 0.125” in diameter, while the inner tube is the same size but half as long to compensate for the length of the tip and its

holder. All tubes are attached to the microscope body with epoxy, and each is plated on both inside and outside with nickel as electrodes, with the outer electrode partitioned into four quadrants. Asymmetric voltages applied to opposite quadrants relative to the common inner electrode produce transverse deflection of the tube end, while symmetric voltages to all quadrants result in axial expansion or contraction. At room temperature the step sizes are roughly 20 nm/V and 4 nm/V for transverse and axial deformation of the outer tubes, respectively, and half the sizes for the inner tube. Calibration is performed periodically *in situ* using known periodic structures, usually CO adsorption on transition metal surfaces, or highly ordered pyrolytic graphite (HOPG).

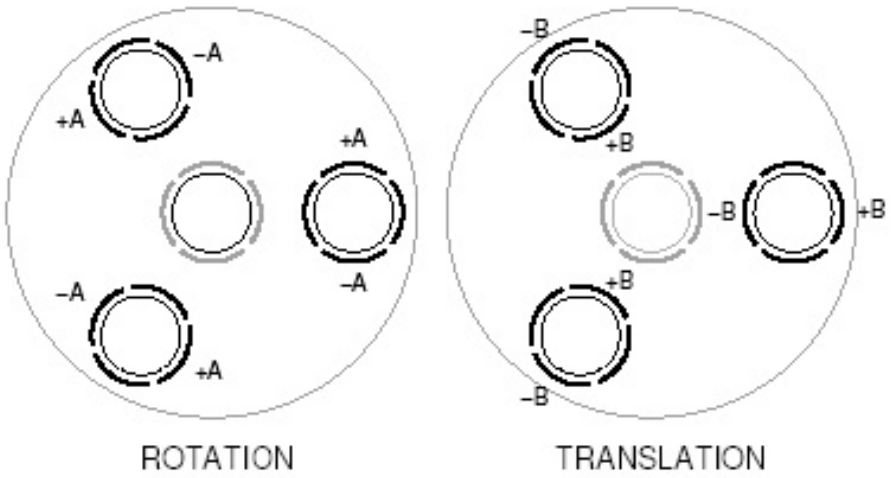

Figure 3.2. Electrode orientation of the approach and scanning piezoelectrics. Combined with the helical ramp design, voltage signals applied to electrode group A will result in vertical displacement of the tip by inertial rotation of the microscope. Signals applied to electrode group B allows coarse repositioning of the tip along the sample surface.

The outer tube quadrants are oriented for tangential and radial displacements (Figure 3.2). By applying a voltage pulse of a selected polarity, which determines the direction of the net motion, with a short rise-time (< 1 ms) followed by a slow (on the

order of milliseconds) reduction of the voltage, the inertia of the head causes the ball contacts at the end of the outer tubes to initially slip against the ramps, and subsequently stick to the ramps and relax to bring the rest of the body to the new equilibrium position. The size of each concerted set of step is determined by the amplitude of the voltage pulse applied. As the STM motor rotates, it ascends or descends the ramp segments to vary the tip-sample distance over a 1 mm range, with reproducible vertical steps from 20 to 200 nm depending on the voltage applied. During approach, the software controlling the STM generates a series of 5 steps with the central tube fully retracted to protect the tip, and then the central tube is extended toward the sample to test for tunneling current. The process repeats itself until the value of tunneling current reaches a preset threshold, after which the user can manually bring the tip into tunneling and scanning range through single coarse approach step or extending central piezoelectric tube.

Due to the small contact area between the STM motor and the ramps on the sample holder, the body and the piezoelectric tubes remain near room temperature at all times during heating and cooling. This thermal isolation of the STM from the sample, which can be improved significantly by using glass instead of sapphire for contact points, helps to protect the piezoelectric transducers, and to reduce thermal expansion transients due to temperature gradients and different equilibrating time of different materials when the sample temperature is varied. However, due to the proximity of the tip to the sample, the energy resolution of the STM is severely limited due to the thermal distribution of electrons at the tip. In addition, the intrinsic resonance modes of this design without the added mass of tip exchange mechanism are in general only moderately high (4-5 kHz),

which limit the maximum scan rate and make imaging more susceptible to thermal drifts. A further and significant disadvantage of this STM design is the tendency to exhibit undesirable vibrational resonances between 500 and 1700 Hz [3], which appear to relate to the low contact force between the half-balls and the ramps [4], and instability as a result of ball contacts resting on irregular pits on the ramps that are a result of wear from repetitive slip-stick motion of the hard sapphire balls on the molybdenum ramps.

3.2.2 Sample Holder

The design of a removable sample holder is essential to combining the benefits of sample preparation and characterization under UHV conditions and high pressure and high temperature *in situ* STM studies under equilibrium. Not only does the holder need to incorporate design that allows for easy handling methods even under the already limited *in vacuo* manipulation precision, but the holder must serve as a sufficient conduit between sample and stage to maintain good mechanical and thermal contact and stability upon insertion to the mating counterpart. Moreover, the materials chosen for the sample holder must behave similarly with each other as well as with the sample stage materials, in order to minimize discrepancies in thermal expansion that lead to loosening of components or even mechanical failures upon thermal cycles.

The basic sample holder consists of two parts: a gold-plated copper body, and a set of three molybdenum helical ramps at the top for coarse approach of the Beetle STM as briefly described in the previous section. The choice of copper for the sample holder body ascertains rapid thermal transition and equilibration during thermal adjustment. The

purpose of the soft gold plating is threefold. First, it serves as a protective barrier of the copper body against chemical erosion during reactive studies. Secondly, the good malleability of gold, especially at high temperature, ensures good mechanical and thermal contact between the copper body with the mating receptacle. Lastly, by the same token, gold serves as an inert lubricant to ease transfer under vacuum, where friction generally is higher to due to lack of carbon species and moisture commonly found in ambient environment. The side of the sample holder body contains two notches, or "necks", all the way around to allow handling by manipulation forks as well as mounting onto stages for preparation and experiments. The center of the holder body is hollowed out and lined with alumina for thermal protection of the body, to allow the insertion of a halogen light bulb through the sample holder to irradiate and heat the sample from the back side.

The molybdenum section of three ramps has a central depression with a smaller circular hole in the middle that allows seating of a sample of 10 mm in diameter. A type K thermocouple that touches the sample is isolated by a ceramic tube and extends about 4 mm away from the sample holder. These wires are positioned so that they align with matching wires on both the STM and the UHV analysis stages. Initially, the sample holder is designed to have a sample spot-welded directly or mounted by two tantalum strips spot-welded onto a tantalum disc of 10 mm in diameter, which in turn is seated mechanically onto the ledge of the central depression in the molybdenum section and held down by three leaf springs mounted through screws at the bottom of the ramps. However, this design has been found to create two serious problems. First, the mechanical stability of the sample in the holder is poor due to the lack of direct rigid

mounting of the sample onto the holder. The spot-welding of the sample onto the tantalum disc does not ensure a stable mechanical connection, while the seating of the sample ensemble onto the ledge is unstable due to large contact area. Secondly, the thermal performance of the sample holder is seriously compromised, as heat is readily transferred from the sample onto the ramps and subsequently to the entire sample holder and the stage. The thermal loss from the sample to the rest of the system prevents the sample from annealing at temperatures higher than 800 °C, and the thermal cycling of the molybdenum section causes the loosening of the screws that are controlling the tension of the leaf springs.

As a result, the sample holder has been modified to ensure better mechanical stability and thermal isolation of the sample from the holder body. (Figure 3.3) The sample is now mounted down directly by the existing three tantalum leaf springs, which are maintained by three screws accompanied by three split washers to maintain tension upon repeated heating cycles. On the other side of the sample and directly opposite the contact points of the three leaf springs, the sample is seated on three glass balls of 1 mm diameter, which serve as a three-point contact to maintain mechanical stability and thermal isolation of the sample. The glass balls are, in turn, seated in three holes of 0.25 mm diameter aligned evenly on the same bolt circle on the existing ledge. This overall modification reduces the amount of mechanical vibrations detected (especially at high gain and thus enhanced response of the feedback loop) during imaging, and allows the sample to be heated and maintained to temperatures above 900 °C repeatedly with minimal need to readjust the tension of the leaf springs.

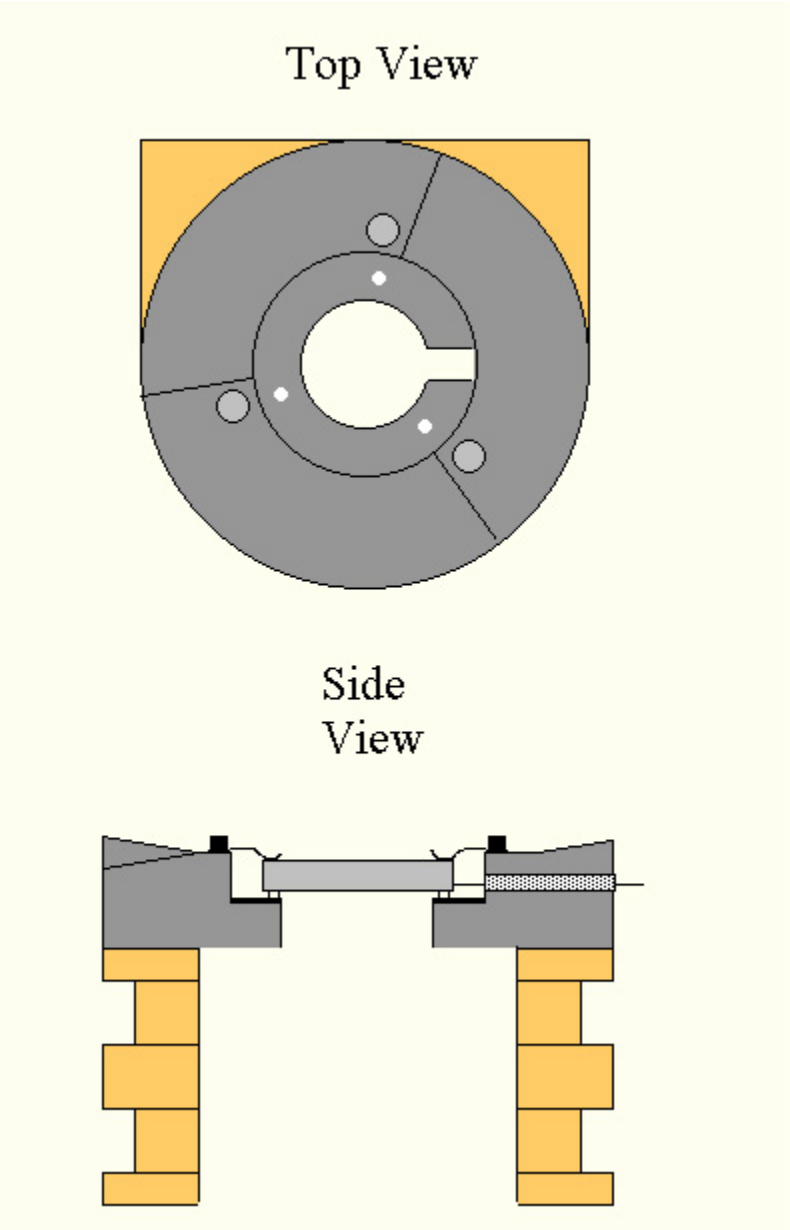

Figure 3.3. Schematic of the modified sample holder for the Beetle STM, which consists of a set of three molybdenum ramps (gray) for approach and a gold-plated copper body with two "necks" for manipulation by forks. Top view shows a set of three 2-56 screws for mounting leaf springs (gray circles) and a set of clearance holes of 0.010" diameter (white circles) for 1 mm glass balls to seat in, between both of which the sample is mounted as shown in side view. Thermocouple wires are routed through a ceramic tube (lightly shaded) spot-welded onto the sample.

3.2.3 Sample Stage

While the existence of a sample stage is simply to serve as a receptacle for the exchangeable sample and tip holders in preparation for STM studies, the design requirement of the sample stage remain stringent and similar to that of the sample holder, due to its direct mechanical path to the STM motor and the sample with no damping in-between, in which mechanical rigidity and excellent thermal properties are still principal factors during construction.

The commercial STM stage of the system described here is constructed out of stainless steel. The purpose of the stage is to secure the sample during experiments through engaging the lower neck of the sample holder body, and to house the temperature control setup necessary for heating and cooling. Heating at high pressures is not effective with an electron beam heater due to the much reduced mean free path of the electrons. Thus, a modified overhead projector light bulb (82 V, 250 W) is used, whose surrounding reflective shielding around the bulb and epoxy around the electrical leads are removed due to size and degassing. The light bulb is attached to a linear manipulator within the stage, and can be elevated by this means to within the interior hollow of the sample holder to provide radiative heating, which can be controlled externally by a variable voltage supplier. A soft copper braid is attached to the stage at one end and a reservoir at the other, to allow necessary counter-cooling during heating by means of recirculating coolant such as water or actual chilling of the sample by an external cryostat, while maintaining vibration isolation of the sample stage from the external environment. For the purpose of the STM studies currently performed in this laboratory, the cooling

mechanism of the system serves only as a counter-cooling unit during heating. Temperature of the sample can be increased to and maintained at as high as 900 K using this thermal setup in vacuum. However, heating under high pressures is not effective due to high heat loss to the gaseous environment and the sample stage, and also not advisable as the high pressure gases serve as a thermal conduit to heat up the piezoelectric transducers of the STM motor.

3.2.4 Tip Exchange

The lifetime of a tip for STM studies is highly dependent on how reactive the environment the tip is being exposed during the study. While the choice of the material for the tip plays a major role in minimizing interaction between the tip and the reactive environment that it is immersed in, occasional and unexpected adsorption of molecules onto and consequently modification of the tip is unavoidable for *in situ* studies, even during UHV experiments. Under high pressures and elevated temperatures, this situation becomes more problematic, as not only the high incoming flux of molecules at high temperature makes adsorption and reaction on the tip surface more likely and frequently, but also fashioning or reforming of the tip by controlled contact with the sample surface becomes more difficult due to the more rapid chemical and physical change of the tip apex as well as thermal drift. Furthermore, the consequently reduced lifetime of a tip translates into more frequent tip exchanges, and thus this makes an *in vacuo* tip exchange mechanism highly desirable. By designing a tip holder that can be rigidly attached to the end of the piezoelectric scan tube but yet removable to outside of the system through a

small load lock with minimal manual manipulation, one can minimize the exposure of the system to contaminants in air and the time necessary in preparing a tip for use in a controlled environment.

The tip exchanger is designed to require minimal manual input so that only wobble stick equipped with a fork is necessary to perform the exchange. The body of the exchanger is designed similarly to the sample holder, with two necks for attachment of manipulation forks and mounting onto STM and UHV analysis sample stages, and the lower central area vacated for protection of the tip and placement of the exchanger onto a special stage for thermal and field emission treatment of the tip. The exchanger has three posts identical in height to and located on the same bolt circle as the outer piezoelectric tubes of the STM motor. Evenly between each post and on the same bolt circle, there are three holes machined into the tip exchanger for receiving the outer tubes of the motor. Similarly, three holes are uniformly fashioned between the outer piezoelectrics on the STM body for mating with the alignment posts on the tip exchanger. When the tip exchanger is placed into the sample stage in the same fashion as the sample holder, the motor can be lowered onto the exchanger, where the holes on both bodies, outer piezoelectric tubes, and alignment posts collectively serve as a positioning system for ensuring the tip holder that the exchanger carries is aligned properly with repeatable precision for entry into the receptacles that the central piezoelectrics and the exchanger carry. Before uncoupling the STM motor from the exchanger through adjusting the vertical manipulator, a wire across the exchanger can be manipulated through the use of a wobble stick fork to disengage from or secure into a notch machined in the side of the tip

holder, in the case of loading or removing a tip for STM studies, respectively. The tip holder itself is a simple tube with two major diameters, with one diameter devised slightly larger than the scan tube receptacle to enhance the frictional force in holding onto the tip holder, and the other diameter minimized to reduce the weight at the end of and thus resonance frequency of the scan tube.

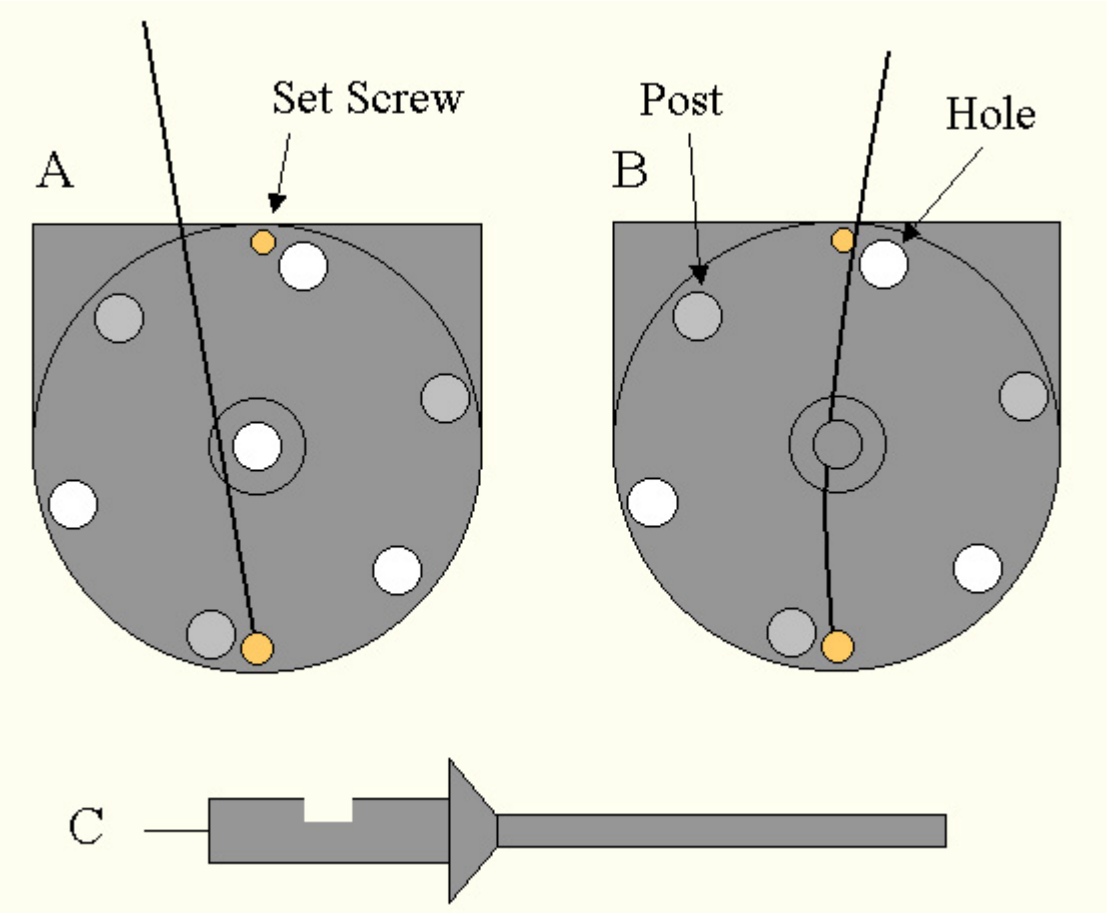

Figure 3.4. Schematics of tip exchanger (A and B) and tip holder (C). Top view of the tip exchanger reveals alternating circular placement of three posts and three holes for alignment of the STM motor for tip exchange, while a wire can be used to engage the notch machined into the side of the tip holder to secure the holder during manipulation.

3.3 System Design

3.3.1 Overall Schematic

As shown in detail in figure 3.5, the system is divided functionally into three sections separated from each other through gate valves: a load lock that allows exchange of tip and sample to and from air without exposing the rest of the system to ambient environment, a variable pressure STM chamber that houses the microscope and serves as a reactor cell for studies between 1 x 10^{-10} and 1000 Torr, and a UHV surface preparation and analysis chamber where samples can be treated and characterized by standard surface science equipments. A magnetically coupled linear rotary transfer arm of 36" in length is used to transfer the sample and tip holders between all three compartments.

The load lock segment is a simple six-way cross with 2.75" conflat flanges, to allow easy relocation of sample and tip holders between the transfer arm and a manual manipulation fork designed for use externally, while maintaining minimal evacuation volume and contamination. During introduction or extraction of a sample or a tip, the load lock is isolated from the rest of the system by gate valves and filled with dry nitrogen to atmospheric pressure to minimize contamination. Upon completion of transfer, the section is evacuated by the system turbo molecular and mechanical pumps over a minimum of 6 hours before introducing the new material to the rest of the system. Due to the nature of constant exposure to ambient environment, the load lock maintains a constant pressure of 1 x 10^{-9} Torr upon complete evacuation.

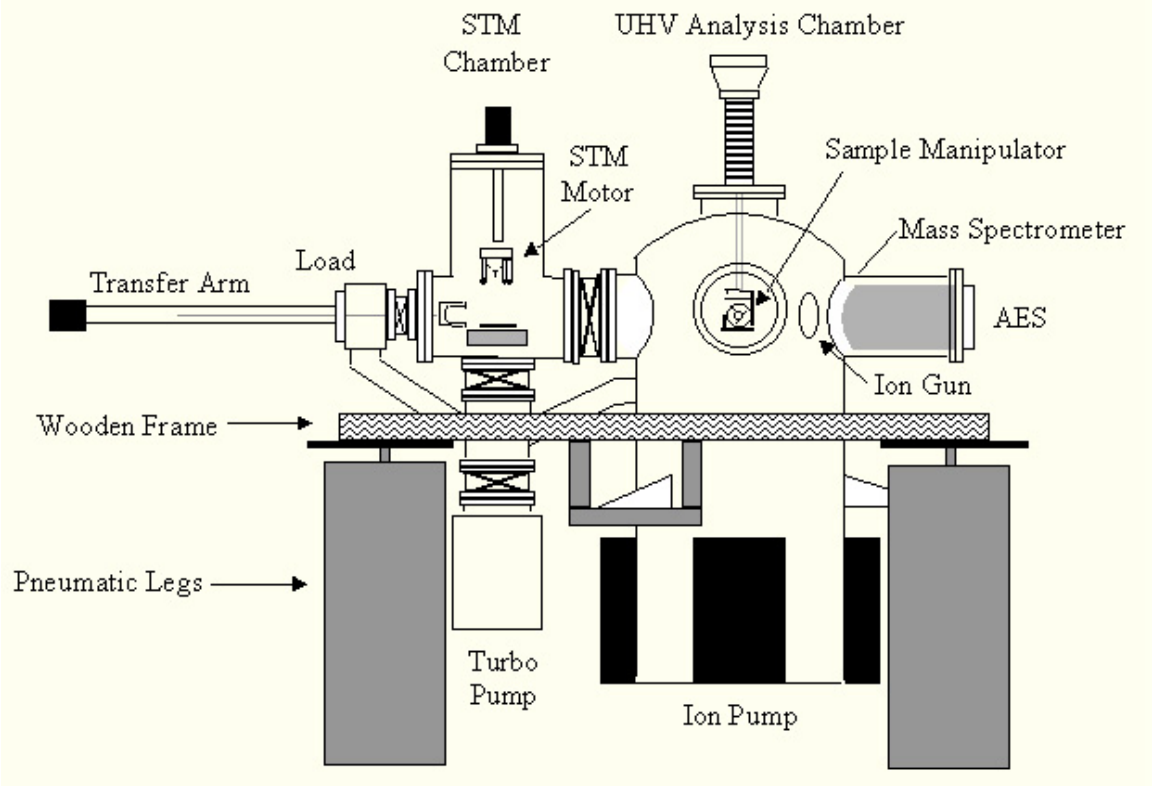

Figure 3.5. Overall schematic of the high pressure, high temperature STM system, which can be divided into three compartments: a load lock for sample and tip exchange, a STM chamber for reaction studies, and a UHV analysis chamber for sample treatment and analysis before and after high pressure *in situ* studies.

The STM portion of the system contains a chamber of 10 liters in volume and can be pressurized to as high as 1.5 atm, similar to standard UHV chambers. The STM motor with the manipulator is mounted vertically from a 6" conflat flange on top, while the sample stage is positioned through a horizontal 8" flange. Several leak valves are arranged on the chamber for controlled introduction of reaction gases, while the reaction pressure is monitored by a combination of ion gauge and capacitance barometers. Originally, a 2' long loop of stainless steel tubing of 0.25" in diameter has been attached to the chamber on one end and terminated with a rubber septum for sampling of gas by

syringe for gas chromatography analysis. In improving the base pressure of the reactor chamber and minimizing contaminants present, the loop is replaced by a stainless steel sheathed tubing of 4' in length and 0.5" in diameter to directly connect to a leak valve on the adjacent UHV analysis chamber, for periodic sampling of reaction mixture for mass spectrometry analysis. When idle, the STM section is maintained by an ion pump to a base pressure of 1 x 10^{-10} Torr, with the use of the system turbo molecular and mechanical pumps if necessary.

The UHV chamber is a Varian surface analysis chamber equipped horizontally with a collection of surface science equipment for treatment and analysis before and after *in situ* STM studies: cylindrical mirror analyzer (CMA) for Auger electron spectroscopy, mass spectrometer for residual gas analysis, sputtering gun for argon or oxygen ion bombardment to vigorously remove surface contaminants, and electron beam bombardment heater for annealing (to desorb contaminants and eliminate surface defects after ion bombardment treatment) under vacuum, or low pressures of oxygen if carbon contamination proves to be a significant problem for the sample. The placement of the sample analysis stage on a XYZΘ manipulator allows positioning of the sample to access different instruments within this section. Leak valves are equipped on this chamber for introduction of various gases for bombardment and thermal treatments of the sample, as well as for introduction of gas samples for analysis by mass spectrometry. This compartment has access to both the system turbo molecular and mechanical pumps, but is typically maintained to a base pressure of 1 x 10^{-9} Torr by the use of an ion pump when not in use, and can be further reduced in pressure to below 5 x 10^{-10} by a titanium

sublimation pump (cooled by a liquid nitrogen reservoir to improve performance) before sample annealing.

3.3.2 Sample Preparation Stage

The UHV sample analysis stage is situated on a commercial XYZθ manipulator. Referring to Figure 3.6, the stage consists of a stainless steel fork to couple and secure the lower neck of the sample holder, and a mobile carriage that contains the temperature control setup necessary for effective sample annealing. An exposed pair of type K thermocouple wires of 0.020" diameter is placed on the fork to align with those on the sample holder upon insertion. The mobile carriage contains an electron beam bombardment filament (tungsten wire of 0.010" diameter doped with thorium to lower work function) embedded in a ceramic casing, which in turn is rigidly mounted through a copper plate of 5 mm thickness. The copper plate serves as a cooling block, and is connected to through a copper braid to a stainless steel coil of 0.25" diameter that is accessible from outside the chamber. Coolant, typically cryogenically cooled nitrogen gas, can be introduced externally to chill the cooling block. The sample can be continuously cooled to and maintained at as low as 225 K if liquid nitrogen is constantly introduced externally to the cooling coil and block. The mobile carriage of this thermal control setup can be moved through a rack-and-pinion mechanism to bring the electron beam filament within 1 mm to the back of the sample, while the copper cooling block makes mechanical contact with the base of the sample holder. There are two significant advantages to this arrangement. First, the sample can be effectively heated due to the

short beam path of electron bombardment, while the surroundings (namely, the sample holder) can be kept cooled from errant electrons and by the use of a cooling block. Secondly, the cooling time to ambient temperature in vacuum after annealing cycles is significantly shortened by the cooling block, which ensures a reduced exposure to contaminants in the UHV analysis chamber before introduction to the sample stage for STM studies.

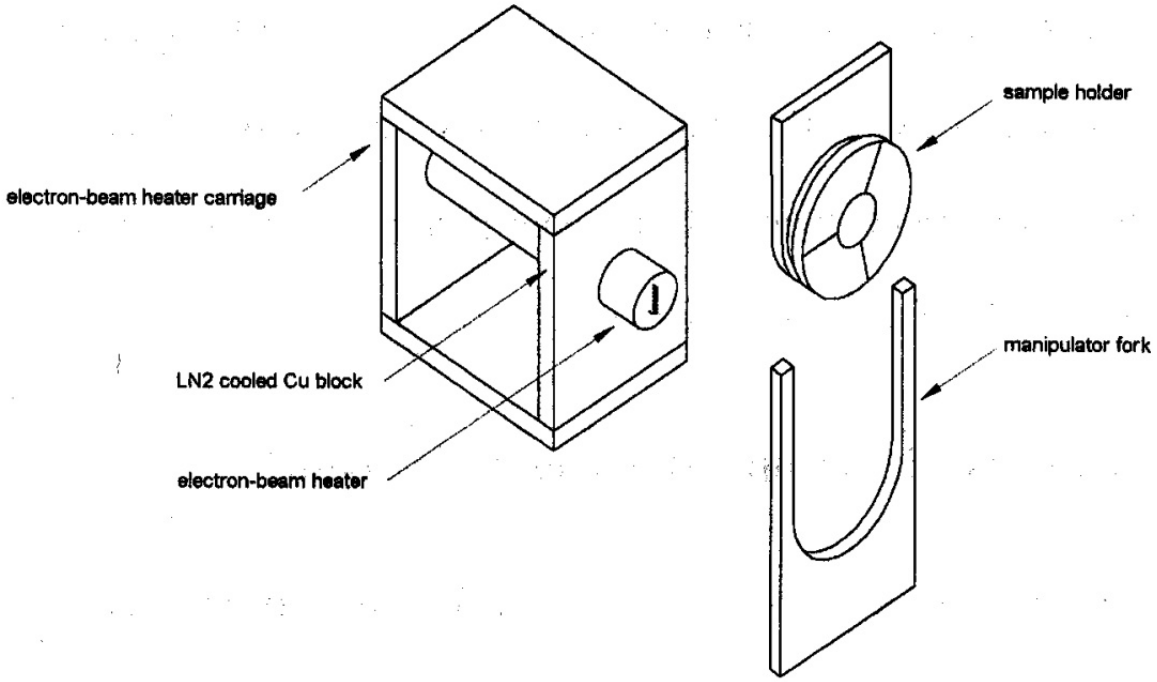

Figure 3.6. Schematic of the sample preparation stage, which consists of a fork for securing the sample holder for UHV preparation, and a carriage that brings in proximity to the sample holder an electron bombardment heater as well as a copper cooling block that is connected to a liquid nitrogen cooled coil by a copper braid not shown.

3.3.3 Vibration Isolation and Vibrational Analysis

Avoiding strong, low-frequency mechanical resonances of the STM and sample stage is essential for good STM performance. Vibrational damping systems with low

resonance frequencies serve to attenuate high frequency noise, and the stiffness of the combined mechanical system formed by the sample holder, stage, and STM head prevents low-frequency noise from coupling to the tunnel junction [5]. For a well-designed sample holder and stage in proper condition, the softest intrinsic mode of the STM often determines the overall stiffness of the junction. Furthermore, strong mechanical resonances at low frequency couple to the closed-loop feedback circuit. This may cause instability at high gain of the feedback loop when the product of mechanical gain and integrator attenuation exceeds unity. Moving the dominant mechanical resonance to higher frequency improves feedback stability, allowing higher gain and faster scanning. In some cases, specially designed filters matched to the properties of a particular STM head can also increase stability by selectively attenuating the dominant mechanical resonance.

For the STM system currently presented in this chapter, low pass filtering vibration isolation exist in three stages: damping by pneumatic air legs (1-2 Hz), wooden support framework (<5 Hz), and Viton spacers within the sample stage (<20 Hz). This filtering system has been designed in hope of damping all but the mechanical vibrations of very low frequencies, which should be far from and thus decoupled from the high intrinsic resonance frequencies of the Beetle microscope (typically 4-5 kHz).

The intrinsic response characteristics of the microscope can be measured independently by using the piezoelectric elements of the microscope as both vibration sources and detectors. (Figure 3.7) A programmable frequency generator supplies a small sine wave (typically in the range of 1-10 V_{pp}) to a particular combination of electrodes on

the piezoelectric elements. The response signal from a different set of electrodes is amplified by either a current preamplifier or a low-noise instrumentation amplifier. By imputing the same (stretching excitation) or opposite (bending excitation) voltage differential to the opposite quadrants in comparison to inner electrode, and measuring the response on the sum or difference of the perpendicular quadrants, intrinsic stretching and bending resonance frequencies of a piezoelectric tube can be measured. By the same token, the stretching and bending response of the scanning piezoelectrics to mechanical excitation of various parts of the STM motor can be measured. This amplified signal is detected by a lock-in amplifier using the excitation signal as a reference. By slowly sweeping the excitation frequency, the output of the lock-in amplifier maps the resonance response of the head. The relative intensities of the resulting peaks depend on the choice of electrodes used for excitation and detection. This dependence, along with basic modeling of the mechanical response of the head, can help to deduce which modes correspond to each set of peaks.

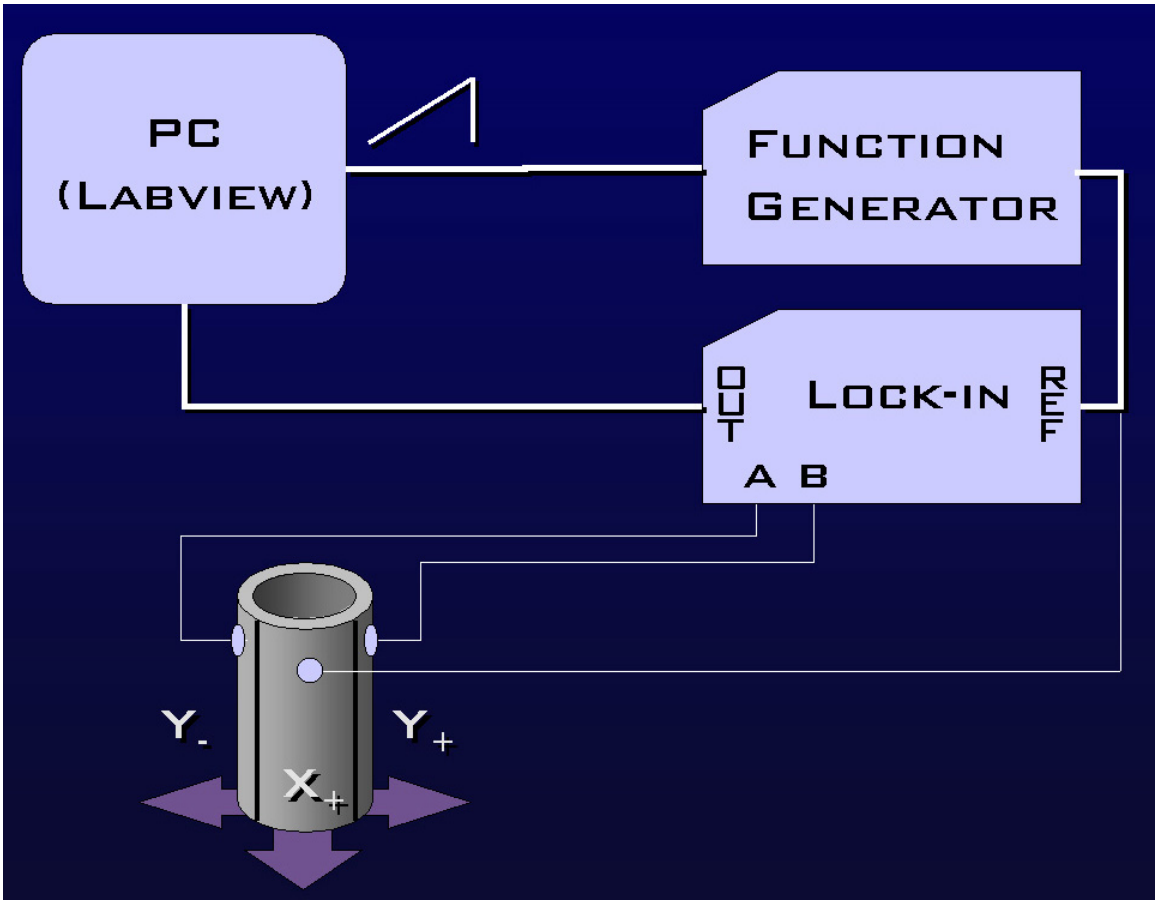

Figure 3.7. Setup for vibrational analysis of a STM motor, where a LabVIEW-driven function generator provides a sinusoidal driving frequency to sectors of one axis on the scan tube and a lock-in amplifier measures the response from the sectors of the other axis.

Modeling and theoretical calculations of various components within a STM motor can be complex and involving. However, the most important and direct contribution of mechanical vibrations lies in the response of scanning piezoelectric tube to excitation. For calculating the stretching (or parallel to the tube length) and bending (or perpendicular to the tube length) responses of the scan tube and other similar tube-like structures, we treat the tubular component as a well-behaved Newtonian spring. Thus, the parallel and vertical spring constants can be calculated as such:

$$K_{\parallel} = \frac{\pi}{4} E \frac{OD^2 - ID^2}{L}$$
$$K_{\perp} = \frac{3\pi}{64} E \frac{OD^4 - ID^4}{L^3}$$

where $K_{\parallel}$ and $K_{\perp}$ represent respectively the stretching and bending mode spring constants, E the Young's modulus of the tube material, OD and ID the outer and inner diameters of the tubular structure, and L the length. Using the springs constants thus calculated, the fundamental resonance frequency response of the particular component can be calculated using the following equation:

$$f = \frac{1}{2\pi} \sqrt{\frac{K}{M_{eff}}}$$

where f is the resonance frequency, K the spring constant of either stretching or the bending modes and M_{eff} is the effective mass of the tube. For a tube with evenly distributed mass throughout the length, the effective mass is a third of the overall mass.

For the current Beetle STM motor, modeling of the mechanical responses are severely limited, and only theoretical resonance frequencies of the three coarse approach and one scanning piezoelectric tubes are calculated, due to all motor components have been pre-assembled commercially. The weights of various components, such as the piezoelectrics and the end sapphire half-balls, have to be calculated based on the materials used or estimated due to the lack of access to dimension measurement for the same reason. In the case of attached mass at the end of a tube, as in the case of sapphire half-balls at the end of the three coarse approach piezoelectrics, the attached mass is treated as point mass at the end of the proposed spring.

The calculated and measured responses of the Beetle STM motor, although differ slightly in values, agree with each other in general. The theoretical stretching and bending modes of the scanning piezoelectrics are 43.92 kHz and 12.92 kHz, respectively, while they are 4.62 kHz and 3.92 kHz for each of the outer coarse approach tubes. While the resonance frequencies of the outer tubes are low, these tubes should be at rest during imaging and should not receive any direct excitation besides minor vibrations from the scanning motions of the central piezoelectrics.

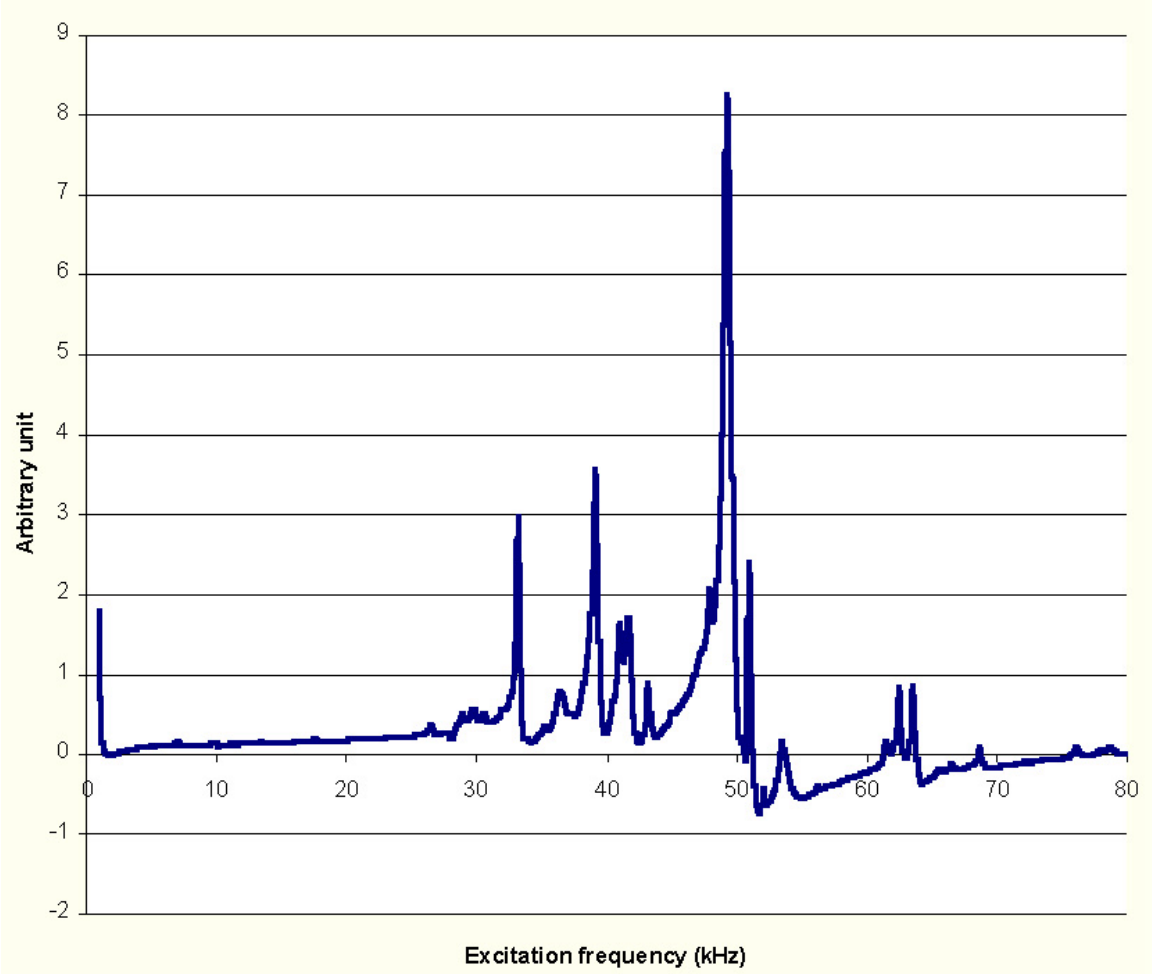

Figure 3.8. Vibrational response in the stretching mode of the Beetle STM shows strong response in 30-55 kHz and 60-65 kHz regions. Strong response in 4-10 kHz range is observed in addition for the bending mode (as shown in Figure 3.9).

The measured vibration response spectra of the stretching (Figure 3.8) and bending modes of the scan tube, under the excitation of different sectors of both inner and outer piezoelectrics while suspended and not in the presence of the tip holder and the sample holder, reveal strong excitation responses at three regions: 4-10 kHz, 30-55 kHz, and 60-65 kHz. The measured responses are in general lower than those calculated theoretically due to three major reasons. First, various additional masses at the end of the piezoelectrics, such as epoxy and silver solder for wiring and tip exchange mechanism, are treated as negligible. Secondly, attachments of different components, such as sapphire half-balls and wires, are treated as noncontributing to additional and lower resonance modes. Lastly, the attachment of the tubes to the STM body, which is significantly more massive than the attached masses on the other of the tube, is treated as attachment to a rigid and nonmoving body, thus resulting in high frequencies calculated.

While resonance frequencies above 50 kHz are likely the result of more rigid metallic body of the microscope and the harmonics of the fundamental resonances of the measured components, these frequencies are too far removed from both the scanning frequency (< 1 kHz) and the resonance frequencies of the scanning piezoelectrics produce significant relevant noises in imaging. For the same reason, the resonance response between 30 and 50 kHz, most likely the result of the stretching frequency of the scan tube and the added modes from the tip exchange mechanism at the end, do not constitute concerns for the performance of the STM motor. In the 4-10 kHz region, there are four main excitation modes at 4.1 kHz, 6.9 kHz, 7.2 kHz, and 10 kHz. The intermediate vibration response of 4.1 kHz is present as a unique bending frequency of the scan tube

during the excitation of various parts of the microscope. In comparison of the calculated bending frequency of 21.92 kHz of the scan tube, the measured response is much reduced in frequency and this closer to the imaging frequency, most likely due to the added weight of the tip holder receptacle at the end of the scan tube.

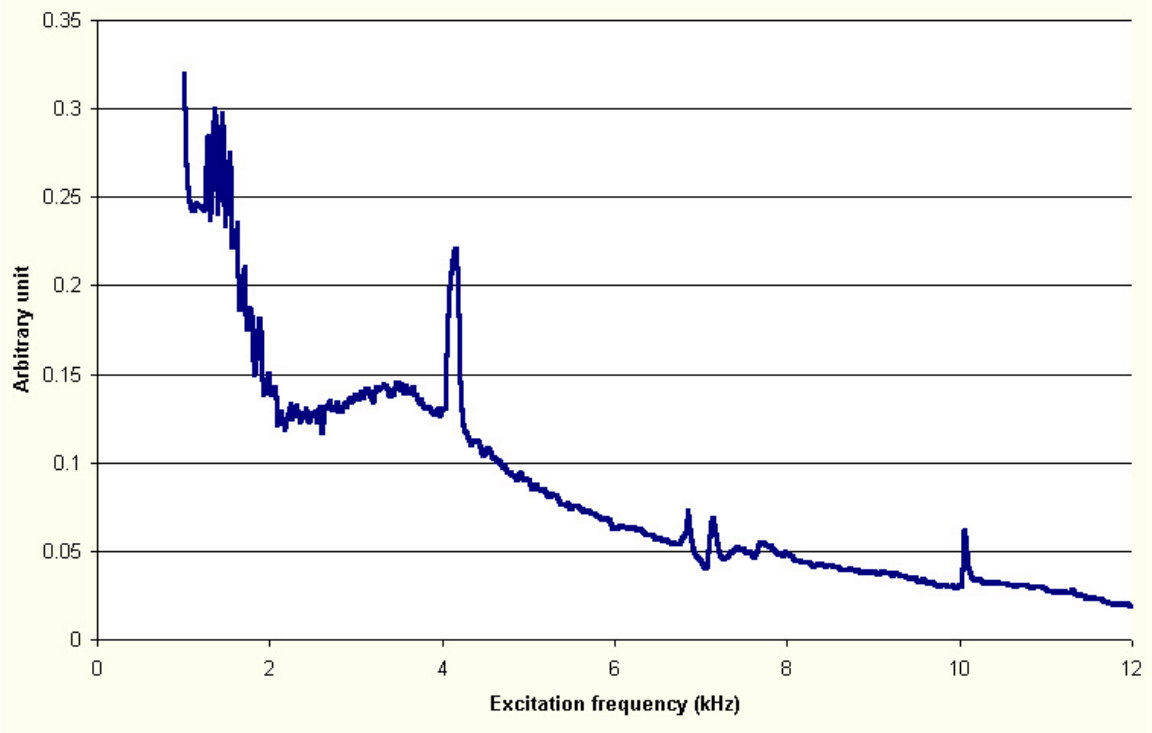

Figure 3.9. Vibrational response in the bending mode of the Beetle STM shows strong responses in the 4-10 kHz region, in addition to excitation frequencies observed in the stretching mode. Elevating baseline below 2 kHz is due to low energy resolution of the lower range of the driving signal.

Figure 3.10 shows the tunnel current and mechanical response spectra measured for the Beetle STM motor with both tip holder and its receptacle attached while suspending and not in contact of the sample holder. The motor exhibits relatively poor mechanical stability at high feedback gain. Both measurement techniques show a strong vibrational mode below 3 kHz, suggesting that an intrinsic mode of the motor was

responsible. STM heads of the same design but without the tip exchange mechanism did not show a resonance peak near this frequency. The added mass from the tip exchange mechanism decreases the intrinsic resonance frequency of the scan tube and thus increases the response of the feedback loop at high gain and the coupling to the scanning rate (< 1 kHz). Furthermore, the multi-components of the tip exchange mechanism increase the number of vibration modes of lower frequency at the end of the scanning piezoelectric, as a result of low frequency beat pattern from mechanical vibrations of different components.

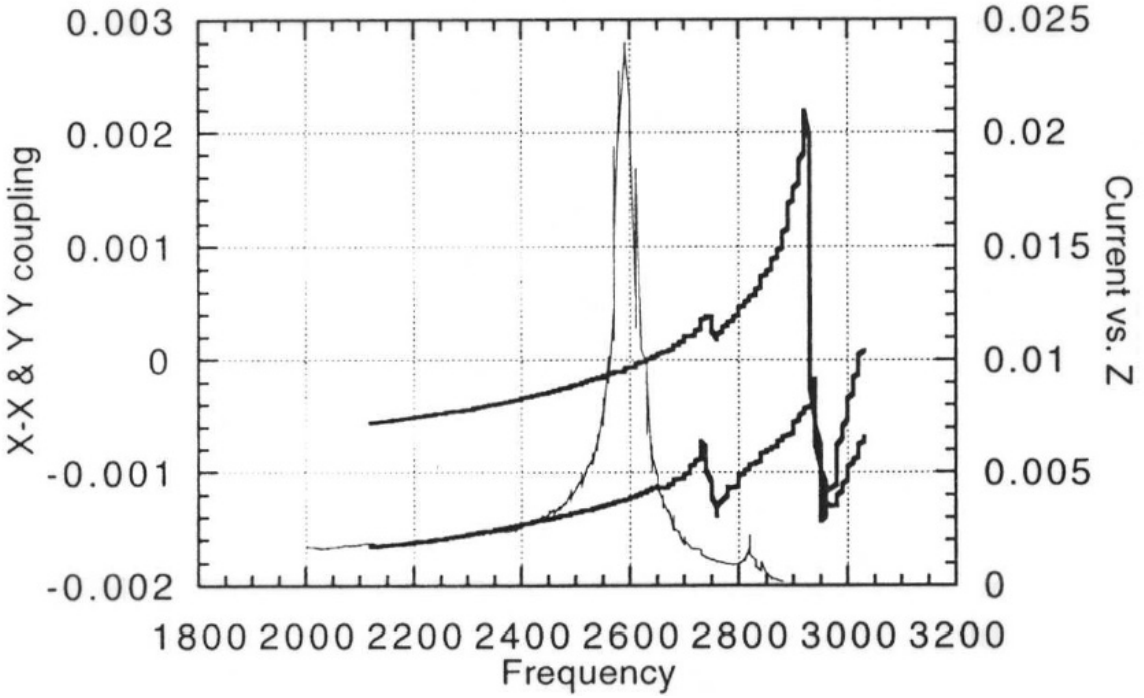

Figure 3.10. Tunnel current noise spectrum (light line) and mechanically-induced vibrational response (darker lines) of the Beetle STM reveal weak mechanical stability due to tip exchange mechanism. The shift in peaks between two methods is due to non-linearity of mechanical driving amplitude inherent in setup.

Weak contact force between the STM motor and the sample, through ball point connections by gravity between the sample holder ramps and the sapphire half-balls at the end of the three coarse approach piezoelectrics, introduces further and more serious vibration complications at low frequency. Assuming the contact between the sapphire half-balls and the molybdenum ramps is Hertzian, the contact area can be calculated as followed:

$$a = \left(\frac{3FR}{4E^*}\right)^{1/3} \quad \text{where} \quad \frac{1}{E^*} = \frac{(1-\nu_1^2)}{E_1} + \frac{(1-\nu_2^2)}{E_2}$$

where a is the radius of the Hertzian contact area, F the force applied, R the effective radius (typically on the order of 10^{-5} m for elastic contact [6]), E^* the effective Young's Modulus of the system while E_i the Young's Modulus for each of the surface materials, and υ_i the Poisson constant of each component material.

Then $K_{\|}$ and $K_{\perp}$, the shear (or parallel to the contact surfaces) and the normal (or perpendicular to the contact surfaces) spring constants of the Hertzian contact, respectively, can be calculated using the following equations.

$$K_{\|} = 8E^* a$$

$$K_{\perp} = 2E^* a$$

Using the formula given previously for calculating resonance frequency with a known spring constant, the calculated shear and normal responses of each of the sapphire-molybdenum point contacts are 813.7 Hz and 405.2 Hz, respectively.

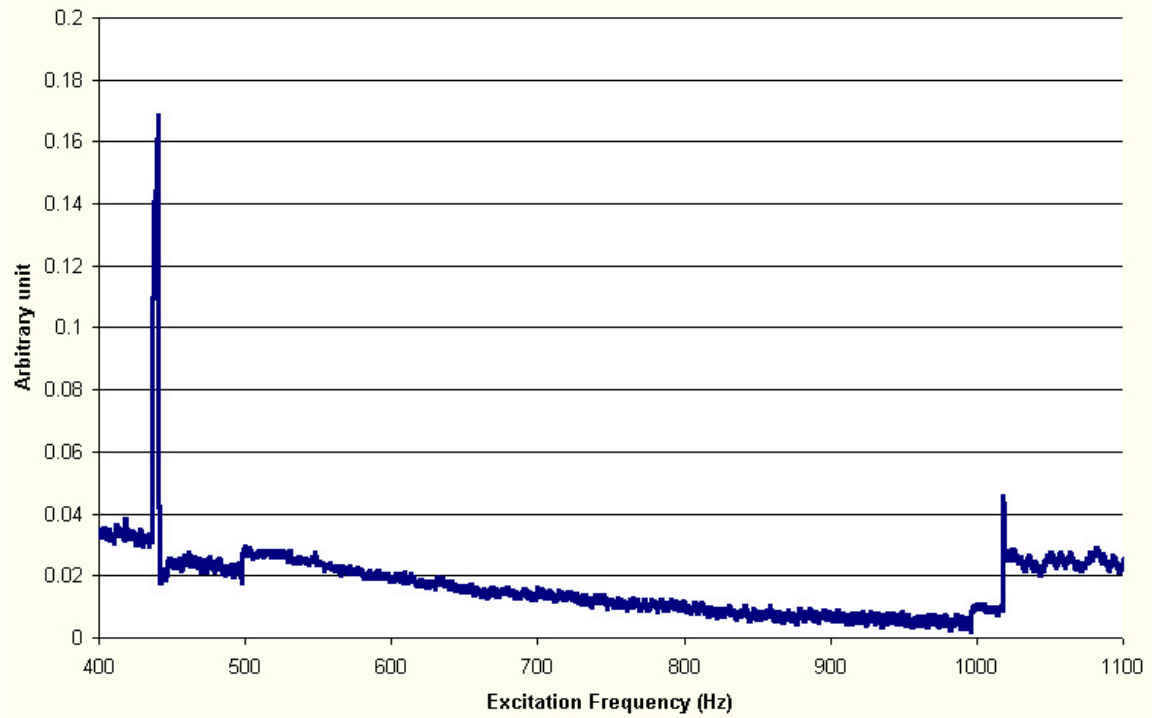

Figure 3.11. Vibrational response (bending) of the Beetle STM in contact with sample holder, shows additional low frequency response as a result of weak mechanical coupling between the motor and the sample holder.

Measured vibrational responses of the scanning piezoelectric tube to excitation reveal vibrations at 440.2 Hz and 1018.5 Hz when the motor is resting on the sample holder ramps, which agree well with the calculated values, with the shear mode much reduced in frequency probably due to the coupling to the bending mode of the attached coarse approach piezoelectrics. The lack of similar response peaks when the motor is not in contact with the sample holder further identify the two peaks as a result of mechanical contact between the two parts. The low frequency vibrations thus introduced is most probably a consequence of weak mechanical couple between motor and sample, as well as a result of unstable resting positions of the sapphire contacts on increasingly coarse molybdenum ramps from recurring approach and retraction of the hard ball contacts.

Periodic polishing of the ramps using fine grain (< 1 μm) diamond polishing pastes leads to a weaker mechanical response at those frequencies, but does not eliminate it completely.

3.4 Challenges and Limitations

Beyond the daily challenges common to most STM systems, a number of specific design weaknesses remain to be addressed in the current instrument. Foremost among these weakness is mechanical stability. While the Beetle STM is a reliable design that has been proven to obtain atomic resolution images at various temperatures and pressures, the intrinsic moderately high resonance frequency limits the imaging rate and resolution at high scan rate. However, the most significant disadvantage comes from the weak mechanical coupling between the STM motor and the sample. Although the motor is seated on a three-point contact on the sample holder, the weak contact force between the two mating surfaces mean that the rigidity of the motor-sample system can be severely compromised, as pointed out in the previous section, especially when deterioration of the originally smoothened ramp surfaces gives rise to local microscopic pits that are unstable for ball contacts to rest on. Furthermore, the current tip exchange design, while the relative ease of use is undisputable, places a much increased mass at the end of the scanning piezoelectrics mainly, due to the stainless steel tip holder receptacle therein for providing a rigid entry for and grasp on the tip holder, which in turn decreases the resonance frequency and limit the scanning rate of the inner piezoelectric tube. Lastly, the wooden support that the system rests on, while serving as a low pass filter and

providing a high damping rate for large amplitudes, has a low resonance frequency and low damping factor for small amplitude noises due to its small Young's modulus and low density. Any external excitation induced onto the frame directly thus necessitates a long equilibrium time.

Second foremost among the existing weaknesses is thermal stability. State of the art reaction studies demand extremely high thermal stability to allow the tip to remain accurately positioned above a group of molecules for extended periods of time. Radiative heating by a halogen lamp, while simple to implement, is not effective at high pressures due to high heat loss to the surroundings on the thermal path. Due to the massive design of the microscope system, which surprisingly thermally couples the sample holder to a massive sample stage (that is built out of comparatively less thermal conductive stainless steel), heating of the sample is very limited and sluggish due to large connected thermal mass and poor thermal conductivity. Furthermore, the problem is made more acute by the enhanced heat loss to the large volume of reactive gases (which is also thermally a poor conductor at near-zero convection) through conduction at high pressures. Oftentimes, the system must be heated overnight at a steady temperature in order to obtain basic large-scale images of sample step edges between terraces. Too often the drift rate as a result of sample heating is on the order of 1 nm per minute, combined with the limited scan rate (> 1 minute per image) inherent in the system, which precludes the possibility of obtaining atomically resolved images of the surface reaction at elevated temperatures.

Lastly, the large reaction volume of the chamber that houses the STM causes two considerable problems in *in situ* reaction studies. First, as mentioned above, the gas

volume serves a large but relatively poor thermal load during temperature studies of reactions. As a result, both the heating capability and the thermal equilibrating time of the system are compromised. Secondly, despite the initial assumption of adequate mixing of the reactor volume by diffusion, the use of large batch volume and a small sample causes a definite chemical gradient of product concentration in the reactor chamber, which in turn leads to non-representative sampling of the reaction mixture to correlate with the STM images, as evidenced in the study outlined in Chapter 4.

While the mechanical and thermal complications in this system have been moderately addressed by modifying the existing sample holder to a mechanically stable and thermally isolated adaptation through the use of glass point contacts, many stability issues remain to be addressed by major revisions of the present design. While it is difficult to make significant changes in the design of the current microscope to eliminate many key problems as identified above, vibrational and thermal noises can be reduced significantly by constructing a more rigid support framework (from carbon steel I-beams or square tubes filled with sand, for example, the latter of which serve as an excellent filter with a large damping factor for most amplitudes) for the system and utilizing a button heater that can be raised to be in direct contact with the sample. Furthermore, the reaction volume, while limited by the size of the microscope, can be considerably decreased by using a smaller chamber, that can as a result improve both thermal and chemical sampling performance of the system.

3.5 References and Notes

[1] Frohn, J.; Wolf, J. F.; Besocke, K.; Teske, M. *Rev. Sci. Instrum.* **1989**, *60*, 1200.

[2] Besocke, K. *Surf. Sci.* **1987**, *181*, 145.

[3] Behler, S.; Rose, M. K.; Ogletree, D. F.; Salmeron, M. *Rev. Sci. Instrum.* **1997**, *68*, 124.

[4] Miwa, J. A.; MacLeod, J. M.; Moffat, A. and McLean, A. B. *Ultramicroscopy*. In press, **2003**.

[5] Pohl, D. W. *IBM J. Res. Dev.* **1987**, *30*, 417.

[6] Private communication with Professor Robert Carpick, Department of Engineering Physics, University of Wisconsin.

Chapter 4

High Pressure Scanning Tunneling Microscopy Study of CO Poisoning of Ethylene Hydrogenation on Pt(111) and Rh(111) Single Crystals

4.1 Overview

Using the high pressure scanning tunneling microscope that is described in Chapter 3, we monitored the co-adsorption of hydrogen, ethylene and carbon dioxide under ambient catalytic condition of ethylene hydrogenation on platinum (111) and rhodium (111) crystal faces in the mTorr pressure range at 300 K in equilibrium with the gas phase. During the catalytic hydrogenation of ethylene to ethane in the absence of CO the metal surfaces are covered by an adsorbate layer that is very mobile on the time scale of STM imaging. We found that the addition of CO poisons the hydrogenation reaction and induces ordered structures on the single crystal surfaces. Several ordered structures were observed upon CO addition to the surfaces pre-covered with hydrogen and ethylene:

a rotated (√19 x √19)R23.4° on Pt(111), and domains of c(4 x 2)-CO+C_2H_3, previously unobserved (4 x 2)-CO+3C_2H_3, and (2 x 2)-3CO on Rh(111). A mechanism for CO poisoning of ethylene hydrogenation on the metal single crystals was proposed, in which CO blocks surface metal sites and reduces adsorbate mobility to limit adsorption and reaction rate of ethylene and hydrogen.

4.2 Introduction

The nature of catalyst poisoning under reaction conditions is an important and unresolved question in catalysis science. Understanding the effects of co-adsorbed species on the activity of catalysts is crucial in the development of more efficient catalysts. During reactions, the catalyst surface may be covered with undesirable adsorbates that may deactivate the catalyst, in addition to reactants, intermediates and products. These adsorbates may render the catalytic surface inactive by blocking active surface sites or impeding the diffusion of adsorbed reactants and intermediates. Other adsorbates may promote the desired reactions by reducing activation energies or blocking undesired reaction pathways. For a reaction to occur the surface should remain flexible, atomic rearrangements should be possible, and adsorbate mobility should be high enough so that favorable adsorption sites can be accessed. Understanding the roles of co-adsorbed species in catalytic reactions and their influence on catalytic surfaces at the high pressures employed in real catalysis is even more important, as the high incoming molecular flux at such conditions facilitates high adsorbate coverage even above adsorbate desorption temperatures.

Scanning tunneling microscopy (STM) is a unique surface analysis probe that permits atomically resolved imaging of adsorbed species over a broad pressure range of 10^{-10}-10^{3} Torr. High pressure environments ensure that equilibrium between adsorbate structures and gas phase is achieved. New and unexpected phenomena on catalytic surfaces have been previously reported at high pressures in comparison to what is observed under ultra high vacuum (UHV) conditions [1-4]. Furthermore, the ability of STM to image *in situ* with molecular details at high pressures makes STM a viable technique to monitor adsorbate mobility on the surface during catalytic reactions, which allows correlation between surface diffusion observed by STM and reaction rates as measured by methods such as mass spectrometry or gas chromatography.

In this chapter we report on a STM study of ethylene hydrogenation and its poisoning by carbon monoxide on the Pt(111) and Rh(111) crystal surfaces. The reaction rates are high enough on both metal surfaces at room temperature to be detectable by mass spectrometry. We find that in the mTorr pressure range of both hydrogen and ethylene, the latter of which converts to mostly ethylidyne (C_2H_3) on the surfaces, the species adsorbed on the metal surfaces are very mobile. However, when CO is introduced into the system, the catalytic reaction ceases abruptly and static ordered structures of the adsorbates are formed that can be readily imaged by STM. We interpret these results as due to the blocking of metal sites by CO that prevents both the adsorption and mobility of ethylene and hydrogen on the surface necessary for the catalytic reaction. Poisoning occurs when surface mobility is suppressed and the adsorbate species become locked into static ordered structures

4.3 Experimental Methods

All experiments were carried out with a high pressure, high temperature STM system previously reported elsewhere [5]. The system consists of an UHV chamber containing surface preparation and analysis equipment, and an adjoining smaller chamber housing a tripod STM (RHK Technology, Model VT-UHV 300) that allows experiments in UHV as well as at high pressures, with a working pressure and temperature ranges of 10^{-10}-10^{3} Torr and 300-525 K. The base pressure of the system was 5 x 10^{-10} Torr, with the background made up primarily of H_2, CO, and water.

Platinum and rhodium single crystal samples of (111) orientation were used. The crystals were cut and polished to a miscut angle of less than 1°. Before each experiment the sample was prepared by sputtering with 400 eV oxygen ions for 10 minutes, followed by annealing in vacuum at 1123 K for 10 minutes in the case of Pt(111) and 973 K for 2 minutes in the case of Rh(111). The sample cleanliness was checked with Auger electron spectroscopy. Just before the sample was transferred to the STM chamber, it was flashed to 1123 K for 2 minutes in the case of Pt(111) and 973 K for 1 minute in the case of Rh(111).

During the experiments, the STM chamber was isolated from the rest of the system by gate valves. Hydrogen, ethylene and carbon monoxide of ultra high purity grade were then introduced at room temperature in this order and allowed to equilibrate for 5 minutes before imaging under pressure after each addition. All STM images reported here were acquired using an electrochemically etched tungsten tip with the

sample at room temperature and with settings of I = 0.2 nA and V = 100 mV. The STM chamber pressure during all experiments was monitored by a pressure transducer (MKS Instrument, Baratron® 722A). The gas composition in the chamber was examined periodically by sampling gas through a leak valve to the mass spectrometer (Stanford Research Systems, RGA 200) in the UHV chamber.

4.4 Results

4.4.1 CO Poisoning of Ethylene Hydrogenation on Pt(111)

Figures 1a and 1b show images of the platinum surface after addition of 20 mTorr each of hydrogen and ethylene. No ordered structures were detected, indicating rapid diffusion of the adsorbate species, within the time scale of STM imaging (250 Å s^{-1}). The activity of the metal catalyst, and thus the presence of adsorbed reactants, was confirmed by ethane production detected by mass spectrometry. The hydrogenation rate was found to be 2.1 x 10^{-2} molecules $site^{-1}$ s^{-1} on Pt(111) at room temperature, lower than previously reported [6]. The lower measured reaction rate is due to the slow diffusion of the ethane product from the STM chamber to the UHV chamber through the sampling tubing. Upon the addition of CO, as low as 1 mTorr, to the hydrogen and ethylene mixture, production of ethane was no longer detected by mass spectrometry over the course of a week. The STM images revealed the presence of large domains of a hexagonal pattern rotated 22 ± 1° with respect to the rhodium surface **(1 0)** vector, with a periodicity of 12.2 ± 0.3 Å and a corrugation of 0.3 ± 0.02 Å (Figure 1c). Figure 1d shows two hexagonal domains

rotated by 7 ± 1°. No other ordered structures or disordered domains were observed on the surface.

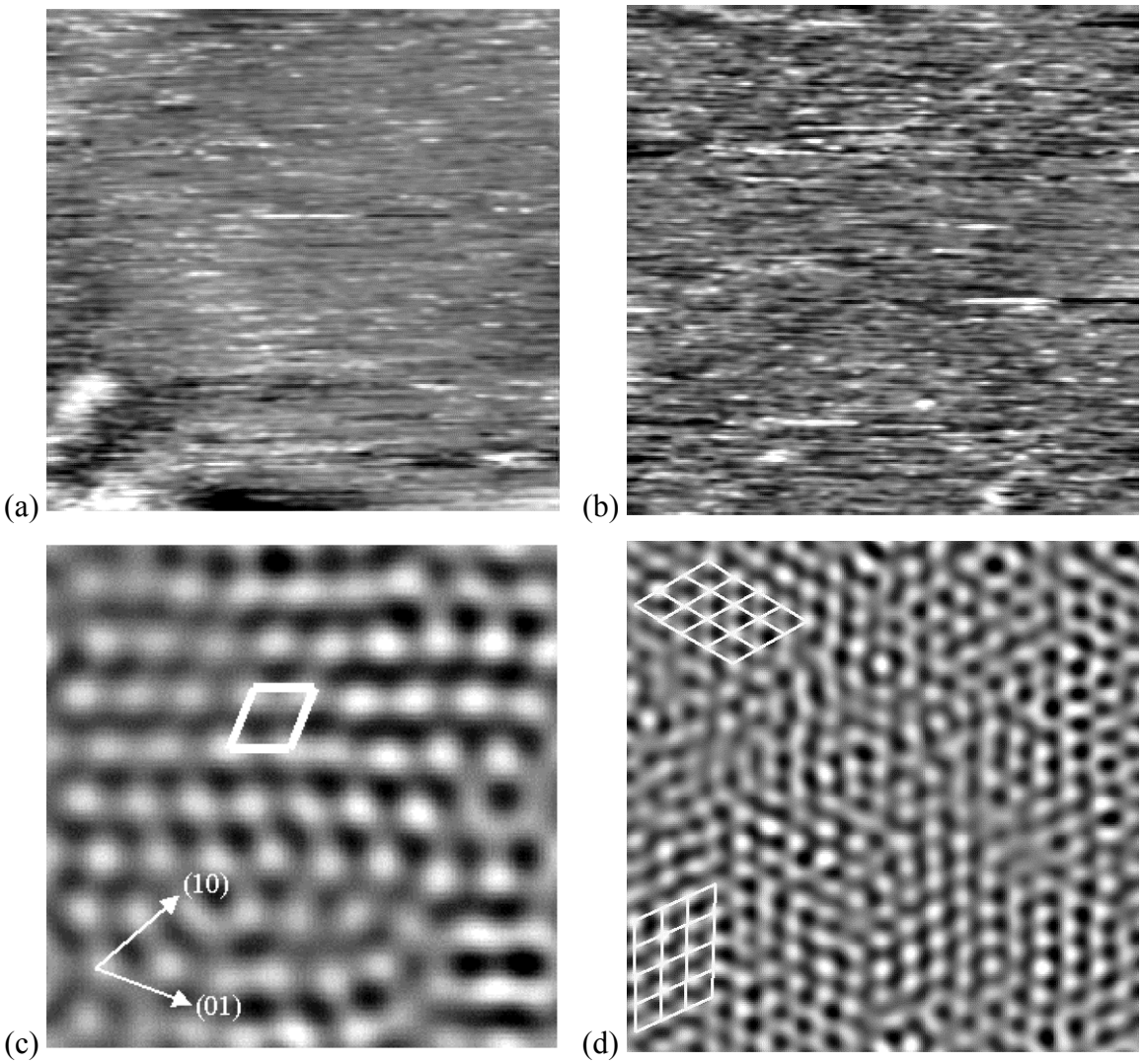

Figure 4.1. (100 x 100) $Å^2$ STM images of the Pt(111) surface under different pressures: (a) 20 mTorr H_2, (b) 20 mTorr H_2 and 20 mTorr ethylene, and (c) 20 mTorr H_2, 20 mTorr ethylene and 2.5 mTorr CO. The presence of CO induced the formation of a (√19 x √19)R23.4° structure on the surface. (d) (200 x 200) $Å^2$ STM image showing two rotational domains of (√19 x √19)R23.4°.

4.4.2 CO Poisoning of Ethylene Hydrogenation on Rh(111)

Similar to the Pt(111) case, no ordered structures could be detected by STM when the Rh(111) surface was exposed to 20 mTorr each of hydrogen and ethylene (Figures 2a and 2b). The ethylene hydrogenation rate under these conditions was found to be 1.3 x 10^{-4} molecules site^{-1} s^{-1} at room temperature by mass spectrometry. Similar to the case of Pt(111), the measured reaction rate is believed to be slower than the actual rate, due to slow diffusion rate of the product from the single crystal to the mass spectrometer as explained above. After the addition of 2 to 5.6 mTorr CO to gas phase, ethane production stopped as detected by mass spectrometry over the course of a week following the addition. STM images reveal the formation of several ordered structures, such as the c(4 x 2) structure shown in Figure 2c.

Figure 3 shows a larger STM image showing several Rh(111) terraces separated by monoatomic steps. They are covered by two visibly different domains. The brighter area, in the middle terrace in Figure 3, was found to be a mixture of c(4 x 2) and (4 x 2) structures. The darker areas consist of a (2 x 2) periodicity. Images of the c(4 x 2), (4 x 2) and (2 x 2) structures are shown in Figures 2c, 4a and 4c, and the corresponding schematics of their proposed structures in Figures 2d, 4b and 4d respectively. Large domains of c(4 x 2) and (4 x 2) structures, rotated by 120°, could be observed with small (2 x 2) islands on the surface.

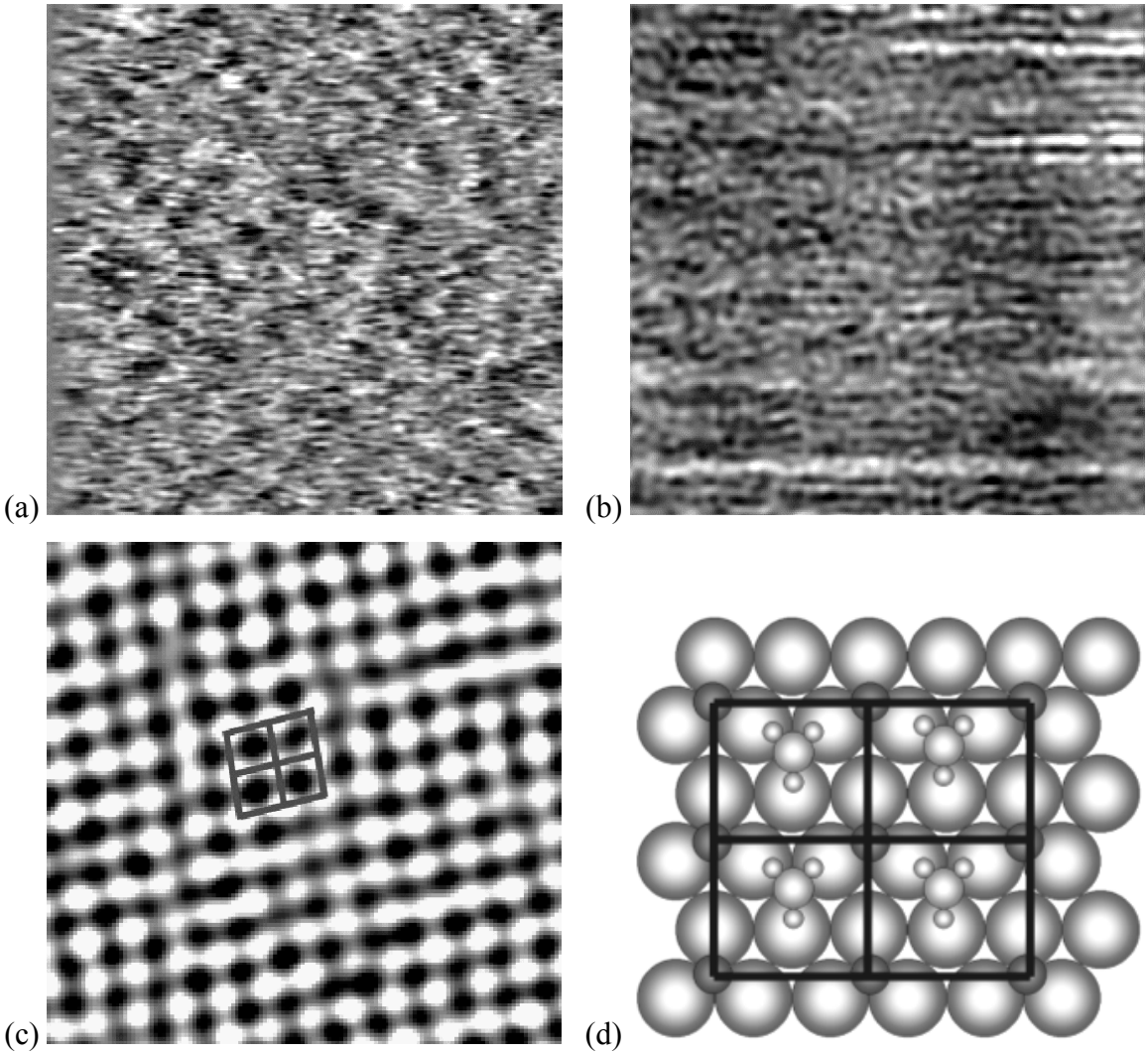

Figure 4.2. (100 x 100) $Å^2$ STM images of the Rh(111) surface under pressures of (a) 20 mTorr H_2, and (b) 20 mTorr H_2 and 20 mTorr ethylene. (c) (50 x 50) $Å^2$ STM image of c(4 x 2)-CO+C_2H_3 structure formed at 20 mTorr H_2, 20 mTorr ethylene and 5.6 mTorr CO and (d) a schematic showing the proposed structure of the corresponding unit cell as indicated in the image.

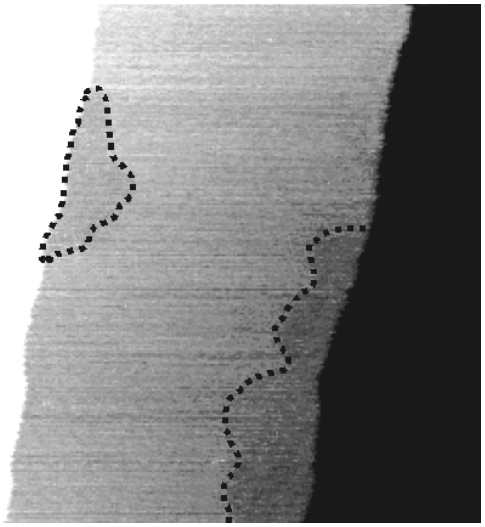

Figure 4.3. (1000 x 1000) $Å^2$ STM image of a Rh(111) terrace with two different regions at 20 mTorr H_2, 20 mTorr ethylene and 5.6 mTorr CO. Images of the bright region shows that it is a combination of c(4 x 2) and (4 x 2) periodic structures. Those of the darker contrast (small outlined areas) show a (2 x 2) periodicity.

Figure 5 shows domain boundaries between domains of (2 x 2), c(4 x 2) and (4 x 2). The c(4 x 2) structure has a corrugation of 0.21 ± 0.01 Å, and a rectangular periodicity of 4.3 ± 0.3 Å and 4.6 ± 0.2 Å. The (4 x 2) is similar to c(4 x 2) but with every other row having lower contrast, which doubles the unit cell size to a rectangular periodicity of 4.4 ± 0.3 Å and 8.9 ± 0.3 Å. The corrugation in the low contrast rows is 0.12 ± 0.02 Å, while in the higher contrast rows the corrugation is 0.19 ± 0.01 Å. The distance between each bright row and its adjacent dark row is 4.5 ± 0.3 Å. The (2 x 2) structural periodicity is 4.8 ± 0.4 Å, with a corrugation of 0.19 ± 0.03 Å.

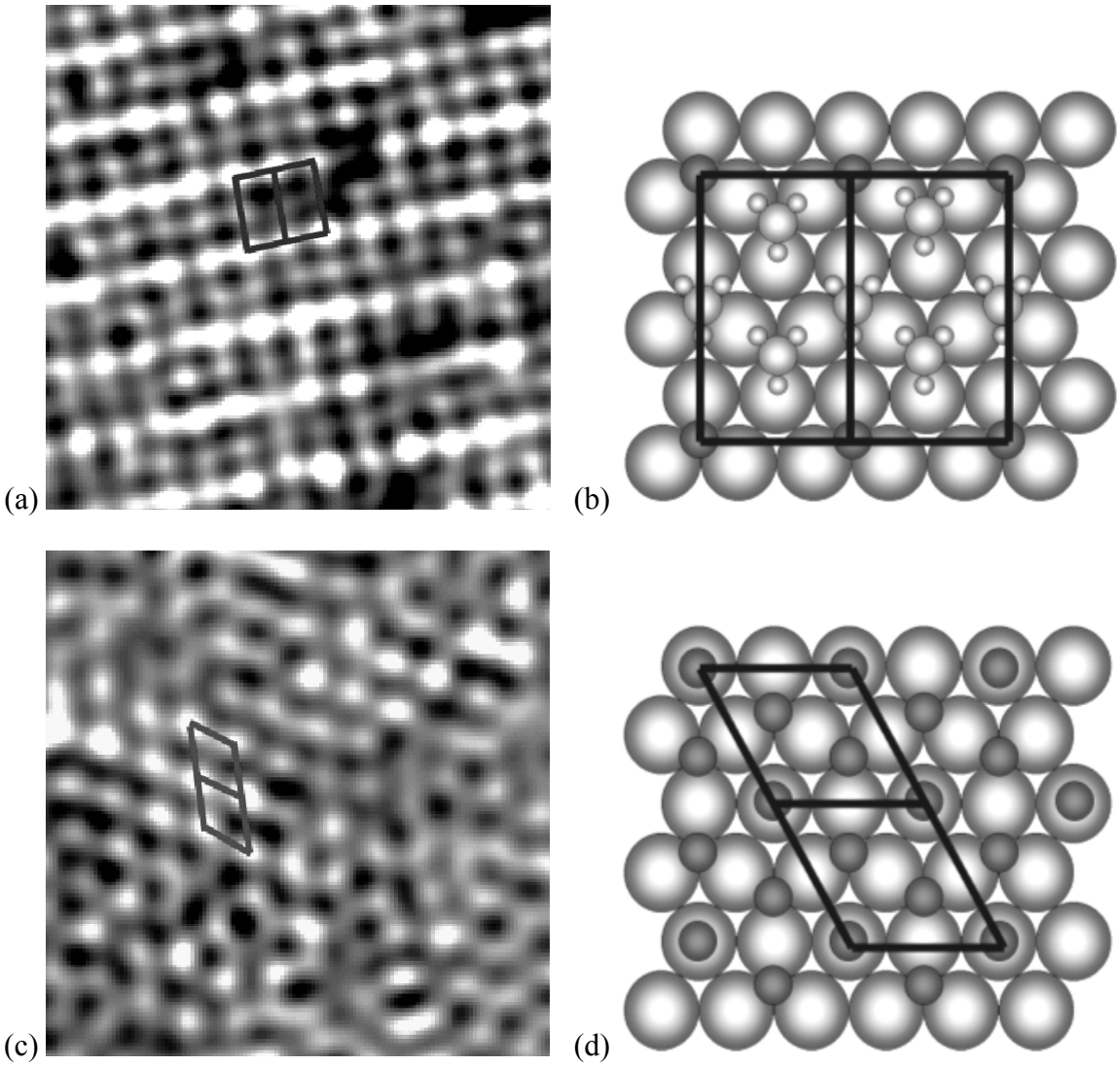

Figure 4.4. (50 x 50) $Å^2$ STM images of the (a) (4 x 2)-CO+3C_2H_3 and (b) (2 x 2)-3CO structures. Schematics (b) and (d) show the proposed structures of unit cells for the (4 x 2) and (2 x 2), respectively.

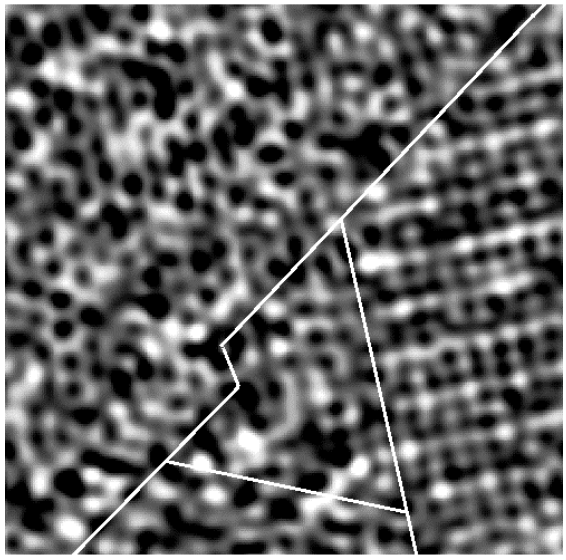

Figure 4.5. (100 x 100) $Å^2$ STM image of domains boundaries between (2 x 2), c(4 x 2) and (4 x 2) structures, from left to right, respectively.

4.5 Discussion

4.5.1 CO Poisoning of Ethylene Hydrogenation on Pt(111)

The high surface mobility and small corrugation of hydrogen, 0.03 Å on platinum [7, 8], makes hydrogen difficult to image by STM at room temperature. It has been shown by electron energy loss spectroscopy [9], helium diffraction [7] and recoil scattering [8] experiments that hydrogen adsorbs dissociatively on platinum at threefold hollow sites, with face-centered cubic (fcc) hollow sites being slightly more energetically favorable and forming (1 x 1) structure at saturation [8, 10, 11].

The adsorption of ethylene on Pt(111) is well documented [12-21]. At temperatures below 50 K, ethylene is physisorbed with its C-C bond parallel to the surface [12]. Above 60 K it rehybridizes to form a di-σ-bonded state on fcc hollow sites

[13-16]. The di-σ-bonded ethylene forms ethylidyne readily near room temperature through the loss of one hydrogen and transfer of another to the other carbon to form a methyl group [22-24]. At high pressure of ethylene or on surfaces pre-covered with hydrogen or ethylidyne, a second, more weakly adsorbed π-bonded ethylene has been shown to exist on top sites. This π-bonded species is believed to be directly involved in the catalytic hydrogenation process [17, 20]. Ethylidyne is also rehydrogenated to ethylene but only very slowly. Ethylidyne is essential in promoting the formation of the π-bonded instead of the di-σ-bonded ethylene on the surface [6, 23, 25, 26]; the former can be readily hydrogenated to ethane, while steric hindrance makes difficult hydrogen addition to the latter.

High ethylidyne mobility, with a surface diffusion barrier smaller than 0.109 eV at high pressure [27, 28], explains the difficulty in observing this species with STM at room temperature. Ethylidyne has been shown by room temperature low energy electron diffraction (LEED) [24, 29] and low temperature STM [21, 29] to form a (2 x 2) structure (θ = 0.25 ML) on Pt(111) occupying fcc hollow sites, and reaching a nearly saturated coverage of 0.22 ML at room temperature [30]. At room temperature, however, ordered structures of ethylidyne could not be observed by STM, indicating rapid mobility on the time scale of STM imaging. Ethylidyne has been shown to be a spectator adsorbate during ethylene hydrogenation at high pressure [6, 23, 25, 26], even as it competes with H for the same adsorption sites. Thus it appears that the high mobility of ethylidyne together with its open (2 x 2) structure, which allows hydrogen atoms to easily diffuse on the surface and add to a weakly adsorbed π-bonded ethylene, is very important for the

hydrogenation reaction to occur on a surface densely populated by adsorbates under high reaction pressure.

The (2 x 2) ethylidyne structure was observable by LEED but not by STM at room temperature due to the fact that in LEED the probing electron interacts with the surface on the time scale of picoseconds and therefore provides an "instantaneous" view of the structure. In contrast, in STM the interaction time between tip and surface is measured in milliseconds, and therefore cannot image molecules moving faster than such. The (100 x 100) $Å^2$ images obtained by STM in our current study were obtained at a scan rate of about 250 Å s^{-1}, indicating the surface diffusion rate of ethylidyne must be greater than this speed at room temperature since no ethylidyne was imaged. In comparison to previous STM studies of ethylidyne performed under UHV [21, 29], the current study shows that neither a high background pressure of ethylene nor pre-covering the surface with hydrogen reduces the mobility of ethylidyne.

By adding CO to the Pt(111) surface pre-covered with hydrogen and ethylidyne, which has a diffusion activation energy of 0.130 eV at saturation coverage [31], ordered structures could be resolved with STM indicating that the adsorbate mobility was notably decreased, whereas the rate of ethylene hydrogenation dropped to zero. The ordered structure formed is similar in corrugation and periodicity to the ($\sqrt{19}$ x $\sqrt{19}$)R23.4° (θ = 0.68 ML) structure previously examined under higher pressure of pure CO [32, 33]. Adsorption of pure CO on Pt(111) at similar pressures yielded the same hexagonal ordered pattern on the surface with comparable periodicity and corrugation (Figure 6). The images shown in Figure 1c and 1d show only one maximum per primitive unit cell.

In the case of pure CO this maximum was assigned to an atop CO, due to its higher tunneling probability than that of CO at a threefold hollow site [34].

(a) 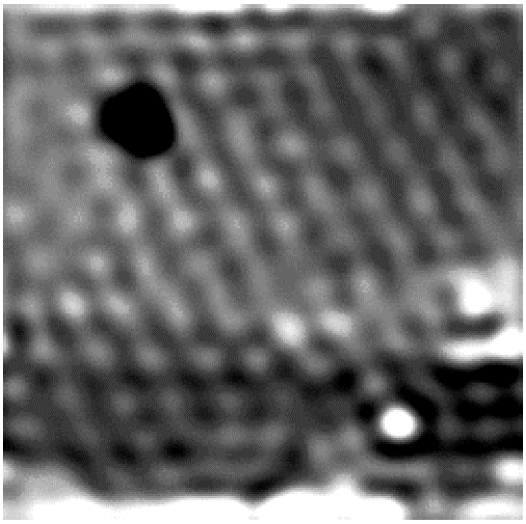 (b) 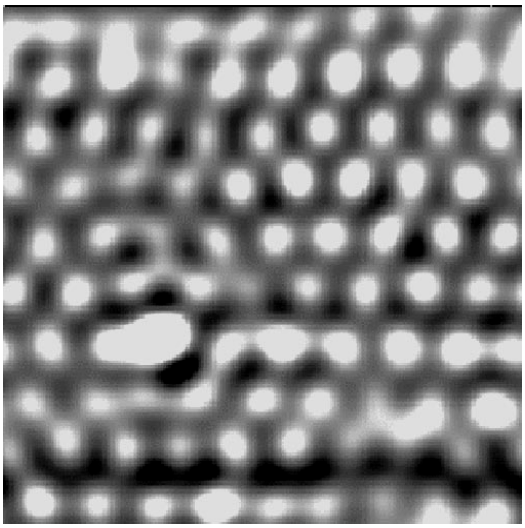

Figure 4.6. (100 x 100) $Å^2$ STM images of Pt(111) surface at (a) 5 mTorr CO and (b) 45 mTorr CO. The periodicity and corrugation is 11.4 ± 0.4 Å and 0.25 ± 0.04 Å in both cases, similar to the values found for the (√19 x √19)R23.4° structure formed by the co-adsorption of hydrogen, ethylene and CO at comparable pressure.

Sum frequency generation (SFG) [35] and infrared spectroscopic [36] studies have shown that both CO and ethylidyne are present on the Pt(111) surface and that CO does not completely displace ethylidyne from the surface at room temperature during high pressure co-adsorption. The important question of whether ethylidyne and CO are mixed or segregated during co-adsorption on Pt(111) is difficult to answer. On one hand, the observation of a (√19 x √19)R23.4° structure suggests pure domains of CO, with the ethylidyne segregating in regions between CO domains. Although we did not observe disordered patches or other domains that might indicate such segregation, this could be due to fast domain boundary mobility compared to the STM imaging time. The long-range order of the large (√19 x √19)R23.4°-13CO unit cell is a result of complex CO-CO

and CO-substrate interactions extending to several neighbors; it is therefore unlikely to replace some of the CO molecules with ethylidyne while still maintaining the same large unit cell ordered structure.

On the other hand, infrared spectroscopic studies have shown that high pressure co-adsorption of ethylene and CO yields predominantly atop CO molecules and considerable interaction between CO and ethylidyne on Pt(111) [36]. The red-shift of atop CO stretch in infrared spectroscopy for CO on Pt(111) pre-covered with ethylidyne [36], in comparison to CO on clean Pt(111) surface, would indicate mixing of CO and ethylidyne on the surface. Since only large domains of (√19 x √19)R23.4° were visible on the surface with no evidence of disorder domains or other ordered structures, we cannot exclude that this observed ordered structure contains both CO and ethylidyne. Figure 7 shows a possible model for co-adsorption of ethylene and CO within a (√19 x √19)R23.4° unit cell. This model has CO molecules occupy atop and near-atop sites and ethylidyne possibly replace CO molecules at threefold hollow sites, which could explain the infrared observation of mainly atop CO upon co-adsorption. Since pure CO at comparable pressure forms the same incommensurate pattern on Pt(111) and the current STM used could not resolve molecules in the threefold hollow sites of the observed structure, we could not discern between (√19 x √19)R23.4° domains of pure CO and of mixed ethylidyne and CO structures on the surface. Assuming a complete replacement of CO by ethylidyne at the threefold hollow sites in the mixed unit cell, ethylidyne will have a coverage of 0.31 ML within the co-adsorption domains. Thus, the coverage of ethylidyne changes from 0.22 ML initially on the surface before the addition of CO to a

higher coverage of 0.31 ML within the co-adsorption (√19 x √19)R23.4° structure. This means that both domains of pure CO and the mixed structure must be present on the surface. This agrees with previous SFG observations of two different atop CO stretches in the adsorption of CO on Pt(111) pre-covered with ethylidyne [35], which represent two atop CO species with different neighboring adsorbates.

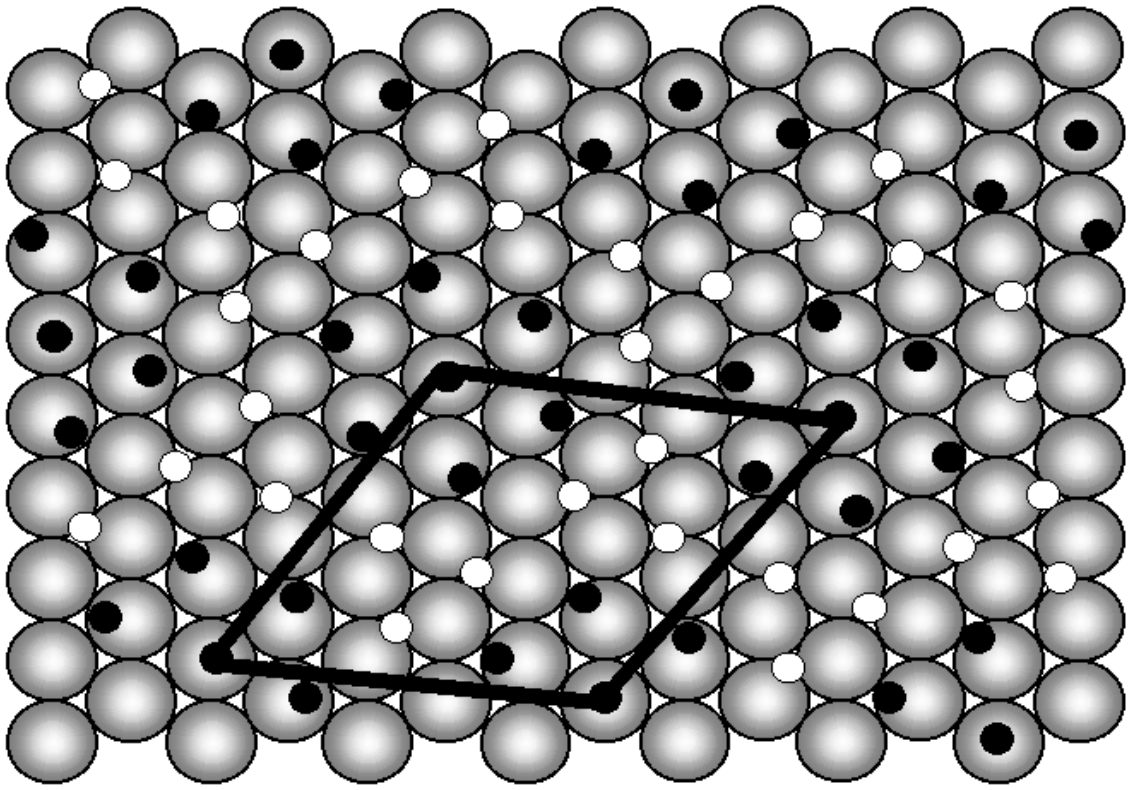

Figure 4.7. Model of (√19 x √19)R23.4° structure formed by the co-adsorption of ethylene and CO. The gray, black, and white circles represent platinum atoms, atop and near-atop CO molecules, and possible ethylidyne replacements of CO at threefold hollow sites, respectively.

To see how CO affects the two key intermediates, π-bonded ethylene and adsorbed hydrogen, in the rate-determining step of initial addition of a single hydrogen to adsorbed ethylene in ethylene hydrogenation on the catalytic Pt(111) surface, we can

estimate the desorption rates and coverage of these two adsorbates under pressure in the presence of CO. The heat of adsorption for CO at saturation coverage has been found by laser-induced thermal desorption to be 10 kcal/mol with a pre-exponential factor of $10^{7.5}$ s^{-1} [37]. By assuming the adsorption of π-bonded ethylene on a sterically hindered surface that is nearly saturated with ethylidyne and CO to resemble physisorption [21], we expect its heat of adsorption and pre-exponential factor to be on the order of 10 kcal/mol and 10^{12} s^{-1} [38]. This implies that the CO-to-ethylene ratio on the surface at high coverage in equilibrium with the gas phase is on the order of 10^4. Thus, we believe that most of the adsorbed π-bonded ethylene is replaced by CO due to the stronger binding of this species on the surface.

In comparison, we anticipate any adsorbed hydrogen on the surface to remain on the surface after CO addition, and recombine and desorb slowly at room temperature, due to slow diffusion within the compact (√19 x √19)R23.4° structure. We calculated the recombination and desorption rate of hydrogen within the less dense (2 x 2) ethylidyne structure to be 6.8 x 10^{-15} s^{-1} using the heat of adsorption and pre-exponential factor previously obtained by Zaera [39, 40]; the rate should be even lower in the denser (√19 x √19)R23.4° structure. A mass spectrometry experiment of co-adsorbate effects on H_2-D_2 exchange and recombination rate was performed. Table 1 correlates the recombination rates to reaction temperatures and adsorbing gas composition. While ethylidyne (an adsorbate predominantly formed from adsorbing ethylene at room temperature) shows a small degree of poisoning in the H_2-D_2 exchange reaction, it is very clear that CO slows down the reaction in a more pronounced manner. By monitoring the recombination rate of HD during the study,

we found that the hydrogen diffusion rate across the surface was reduced more than 5 orders of magnitude upon the addition of CO. The slow diffusion rate of hydrogen, along with the lack of available π-bonded ethylene for hydrogen addition, means that hydrogen remains unreacted on the surface.

H_2-D_2 Exchange on Pt(111)	HD Formation at 293 K (molecules/site-sec)	HD Formation at 330 K (molecules/site-sec)
20 mTorr H_2 20 mTorr D_2	7.4×10^{-1}	1.2
20 mTorr H_2 20 mTorr D_2 20 mTorr C_2H_4	1.4×10^{-2}	6.5×10^{-2}
20 mTorr H_2 20 mTorr D_2 20 mTorr C_2H_4 5 mTorr CO	$< 10^{-7}$	$< 10^{-7}$

Table 4.1. The HD formation from a H_2-D_2 exchange reaction on the Pt(111) surface was monitored at both ambient and elevated temperatures over the duration of a week., in the presence of hydrogen adsorption site competitors. Ethylidyne slightly decreased the hydrogen diffusion and recombination rate, and CO suppressed the rate in a more prominent manner.

The CO poisoning of ethylene hydrogenation on Pt(111) is thus a result of the reduction in adsorbate mobility and of the blocking of surface metal sites. The immobile and dense ordered structures induced by CO impede mobility of ethylidyne and adsorbed hydrogen. They also block adsorption of additional reactants near these adsorbates. As a

result of both decrease in adsorbate mobility and blocking of adsorption sites, the rate of ethylene hydrogenation drops to zero.

4.5.2 CO Poisoning of Ethylene Hydrogenation on Rh(111)

Adsorptions of hydrogen [41, 42] and ethylene [43-47] on Rh(111) have been determined to be quite similar to those on Pt(111) in past studies, with the noted difference of hydrogen [41] and ethylidyne [43] favoring hexagonal close-packed (hcp) hollow sites over fcc hollow sites on Rh(111) in forming (1 x 1) and (2 x 2) structures at room temperature, respectively. The conversion of ethylene to ethylidyne also occurs readily at a lower temperature of 170 K on Rh(111) [47]. However, the current STM investigation on Rh(111) shows many similarities to the Pt(111) case and provides much insight in the poisoning effects of CO. During ethylene hydrogenation on Rh(111) at room temperature, atomic hydrogen, adsorbed ethylene and ethylidyne were shown to be too mobile for STM to atomically resolve individual adsorbates.

The introduction of CO dramatically changed the situation, stopping the reaction completely as indicated by mass spectrometry. STM images of the poisoned surface showed ordered domains with large areas of c(4 x 2) and (4 x 2) periodicity and smaller regions of (2 x 2) periodicity. The formation of structures that could be imaged with molecular resolution is a consequence of the immobility of the adsorbed species in the STM time scale.

The c(4 x 2) (θ = 0.50 ML) has been previously observed and studied by LEED after co-adsorption of ethylene and CO, with a determined structure of CO occupying hcp hollow sites and ethylidyne fcc hollow sites [48]. A model is shown in the schematic of

Figure 2d. The total coverage is 0.5 monolayer (ML). This structure does not form under pressure of pure CO [49]. We propose that maxima at the corners of the rectangular unit cell observed by STM correspond to CO molecules, due to the similar corrugation of CO in rhodium threefold hollow sites previously reported [49].

In this study a new (4 x 2) periodic structure (θ = 0.50 ML) is also observed after co-adsorption of ethylene and CO. This structure has a primitive unit cell twice as large as that of c(4 x 2), containing alternating rows of different contrasts. The species in the high contrast rows have the same corrugation and periodicity along the rows as those measured in the c(4 x 2). The dark rows also have similar periodicity but only nearly half the corrugation. The distance between two adjacent rows was measured to be a $\sqrt{3}$ multiple of rhodium-rhodium interatomic distance (2.69 Å), indicating that the observed molecules in both types of rows occupy the same type of adsorption sites. Thus, we conclude that the differently contrasted rows in the (4 x 2) structure were caused by two different molecules. H atoms are unlikely candidates since in substrates where it has been imaged, they appear as depressions and their contrast is extremely small, on the order of 0.05 Å [50, 51]. This leaves ethylidyne and CO as the only candidate molecules. Following the same argument as in the case of c(4 x 2), we assign the molecules in the bright rows to CO molecules and thus those in the dim rows to ethylidyne. Since CO molecules have similar corrugations at hcp and fcc hollow sites as previously found on Pd(111) [52] and we observed similar ordered structures in the absence of H_2, the two unobserved molecules inside the (4 x 2) primitive unit cell are assigned to be ethylidyne molecules occupying different sites from those in the dim rows. Thus, (4 x 2) appears as a

unit cell with the less conductive ethylidyne replacing CO molecules at every other row of the hcp hollow sites in the c(4 x 2). The proposed structure is shown in the schematic of Figure 4b.

Both c(4 x 2) and (4 x 2) regions were observed on the surface in similar amounts, and intermixed in form of patches. The mosaic distribution of c(4 x 2) and (4 x 2) structures of same coverage density but different ethylidyne concentrations shows the formation is not thermodynamically equilibrated. This kinetically arrested configuration on the surface is most likely due to the low adsorbate mobility induced by CO co-adsorption. Successive imaging of the same area over time did not show any exchange between different domains, indicating clearly low mobility of both ethylidyne and CO.

In addition to the above structures, small islands with (2 x 2) structure were observed along step edges on the surface, which we assign to be domains of (2 x 2)-3CO (θ = 0.75 ML). Only the top site CO molecules were resolved by STM due to higher tunneling probability, similar to observations on other metals [34, 52]. The corrugation and periodicity of the observed (2 x 2) agreed with that of the (2 x 2)-3CO formed on Rh(111) under high pressure of pure CO [49]. The observed order could not be caused by (2 x 2)-C_2H_3 since the open structure would allow adsorption of CO between ethylidyne, forming such mixed structures as c(4 x 2) and (4 x 2). In contrast, the denser (2 x 2)-3CO would be too compact for ethylene to adsorb. The lack of agreement of the observed (2 x 2) corrugation with that of ethylidyne as examined in (4 x 2) further confirms that the observed structure was (2 x 2)-3CO and not immobilized (2 x 2)-C_2H_3 islands.

Imaging across the rhodium surface revealed no disordered areas. The bright regions of the c(4 x 2)-CO+C_2H_3 and (4 x 2)-CO+3C_2H_3 domains were observed to cover 77.2% of the surface, with the remaining occupied by the (2 x 2)-3CO structures in the darker areas. Within the observed bright areas, 48.8% of the surface was of c(4 x 2) and 51.2% (4 x 2). Assuming CO co-adsorption has no effects on either ethylidyne formation or rehydrogenation (and thus desorption), and using the proposed structures for the observed orders above, the initial coverage of ethylidyne on the Rh(111) surface prior to the CO addition is thus calculated to be 0.242 ML. Given that ethylidyne molecules organize into (2 x 2) order on a Rh(111) surface at room temperature, this indicates the initial Rh(111) surface prior to poisoning under the current hydrogenation condition is already covered with this inert spectator species and nearly saturated by the (2 x 2)-C_2H_3 structures.

The formation of ordered structures and the drastic decrease in reaction rate upon the addition of CO show the similarities of the poisoning mechanism by CO on ethylene hydrogenation on Pt(111) and Rh(111). The presence of c(4 x 2) and (4 x 2) on Rh(111) confirms that the introduction of CO does not completely displace ethylidyne from the surface, but reduces surface mobility by confining surface species such as ethylidyne within non-mobile CO-induced structures. This is much in contrast to the (2 x 2)-C_2H_3 structures of the active surface formed in the absence of CO that allow adsorbates to be mobile. No reaction occurs on the poisoned surface of c(4 x 2) and (4 x 2) periodicity, even though the concentration of ethylidyne in these structures is comparable to the unpoisoned (2 x 2)-C_2H_3 surface. Due to the reduced mobility induced by CO, ethylidyne

becomes a poison to the metal catalyst surface. The regions of (2 x 2)-3CO structure show no catalytic activity towards ethylene hydrogenation, due to the high density coverage of immobile adsorbates excluding additional adsorption in those areas. Like in the case of Pt(111), we propose that CO replaces weakly adsorbed ethylene and blocks ethylidyne mobility, reducing available surface metal sites for additional adsorption of hydrogen and ethylene and leading to slower diffusion of adsorbed hydrogen and ethylene across the Rh(111) surface, thus causing a termination of ethylene hydrogenation.

4.6 Conclusions

The poisoning effects of CO on ethylene hydrogenation were studied by STM on Pt(111) and Rh(111) single crystal surfaces in the mTorr range at room temperature. The rates of ethylene hydrogenation on both metal surfaces were shown to drop to zero upon the addition of CO. While adsorbed hydrogen, ethylene and ethylidyne were too mobile to be observable by STM on Pt(111) and Rh(111) surfaces, the presence of CO reduced adsorbate mobility and induced static ordered structures on the surfaces that could be imaged by STM. A (√19 x √19)R23.4° structure was found for the co-adsorption of ethylene and CO that is similar to that observed at the same pressure of pure CO. The addition of CO to the Rh(111) surface pre-covered with hydrogen and ethylene resulted in three different ordered patterns on the surface. A c(4 x 2)-CO+C_2H_3 structure was observed, along with a new, previously unobserved (4 x 2)-CO+3C_2H_3 structure. We conclude that alternating rows of this new (4 x 2) structure are the result of replacement

of CO by ethylidyne. A (2 x 2)-3CO structure was also observed on the Rh(111) surface, indicating that regions with pure CO are also formed, as in the case of Pt(111).

The present results clearly indicate that mobility of the surface species is an essential condition for catalytic action on the densely covered catalyst surfaces. The importance of adsorbate mobility for adsorption has recently been shown in the case of H_2 dissociation on Pd(111), where near saturation coverage thermally activated statistical fluctuations were found to be necessary to bring together three or more vacancies needed for the molecule to dissociate [51]. At lower temperature, when H became immobile, no aggregation of vacancies occurred and H_2 dissociative chemisorption stopped. Here we show that adsorbate mobility is necessary not only for adsorption of the reactants but also for the reaction between adsorbates to occur. We have shown that the presence of the site-blocking but mobile ethylidyne does not poison the ethylene hydrogenation reaction, even if ethylidyne occupies the same sites as H. Mobility facilitates statistical fluctuations in surface adsorbate density that open up sites for both gas phase molecules to adsorb and dissociate, as well as for adsorbed species to diffuse across the surface and react. When ethylidyne is immobilized by CO co-adsorption, ethylidyne becomes a poison to the catalyst and the reaction stops. The STM results indicate that the poisoning mechanism of CO on ethylene hydrogenation on Pt(111) and Rh(111) are similar, with CO lowering adsorbate mobility and inducing static ordered structure on both surfaces. This, in turn, prevents the statistical fluctuation necessary for availability of surface metal sites for reactant adsorption under high pressures. We propose that CO replaces most of the weakly adsorbed π-bonded ethylene and prevents further adsorption, while the dense CO-

induced ordered structure immobilizes and traps atomic hydrogen on the surface, thus preventing ethylene hydrogenation. This poisoning mechanism of CO entails that any adsorbate that has a long resident time and lowers surface mobility can become an effective poisoning reagent to a catalytic surface.

In both cases of ethylene hydrogenation on Pt(111) and Rh(111), we found that adsorbate mobility was a crucial factor. These observations extend our understanding of the mechanisms of catalysis by demonstrating that the presence of inert spectators and poison species is only a part of the catalytic process. In addition, adsorbate mobility and modifiers of this mobility are also essential factors that need to be understood as well.

4.7 References and Notes

[1] McIntyre, B. J.; Salmeron, M.; Somorjai, G. A. *J. Vac. Sci. Technol. A* **1993**, *11*, 1964.

[2] Su, X.; Cremer, P. S.; Shen, Y. R.; Somorjai, G. A. *Phys. Rev. Lett.* **1996**, *77*, 3858.

[3] Hendriksen, B. L. M.; Frenken, J. W. M. *Phys. Rev. Lett.* **2002**, *89*, 46101.

[4] Thostrup, P.; Kruse Vestergaard, E.; An, T.; Lægsgaard, E.; Besenbacher, F. *J. Chem. Phys.* **2003**, *118*, 3724.

[5] Jensen, J. A.; Rider, K. B.; Chen, Y.; Salmeron, M.; Somorjai, G. A. *J. Vac. Sci. Technol. B* **1999**, *17*, 1080-1084.

[6] Zaera, F.; Somorjai, G. A. *J. Am. Chem. Soc.* **1984**, *106*, 2288.

[7] Lee, J.; Cowin, J. P.; Wharton, L. *Surf. Sci.* **1983**, *130*, 1.

[8] Umezawa, K.; Ito, T.; Asada, M.; Nakanishi, S.; Ding, P.; Lanford, W. A.; Hjorvarsson, B. *Surf. Sci.* **1997**, *387*, 320.

[9] Baro, A. M.; Ibach, H.; Bruchmann, H. D. *Surf. Sci.* **1979**, *88*, 384.

[10] Batra, I. P.; Barker, J. A.; Auerbach, D. J. *J. Vac. Sci. Technol. A* **1984**, *2*, 943.

[11] Christmann, K. *Surf. Sci. Rep.* **1988**, *9*, 1.

[12] Cassuto, A.; Kiss, J.; White, J. M. *Surf. Sci.* **1991**, *255*, 289.

[13] Steininger, H.; Ibach, H.; Lehwald, S. *Surf Sci.* **1982**, *117*, 685.

[14] Doll, R.; Gerken, C. A.; Van Hove, M. A.; Somorjai, G. A. *Surf. Sci.* **1997**, *374*, 151.

[15] Cremer, P.; Stanners, C.; Niemantsverdriet, J. W.; Shen, Y. R.; Somorjai, G. *Surf. Sci.* **1995**, *328*, 111.

[16] Ibach, H.; Lehwald, S. *J. Vac. Sci. Technol.* **1978**, *15*, 407.

[17] Cremer, P. S.; Su, X. C.; Shen, Y. R.; Somorjai, G. A. *J. Am. Chem. Soc.* **1996**, *118*, 2942.

[18] Carlsson, A. F.; Madix, R. J. *J. Chem. Phys.* **2001**, *115*, 8074.

[19] Watson, G. J.; Wells, R. P. K.; Willock, D. J.; Hutchings, G. J. *J. Phys Chem. B* **2000**, *104*, 6439.

[20] Ofner, H.; Zaera, F. *J Am. Chem. Soc.* **2002**, *124*, 10982.

[21] Land T. A.; Michely T.; Behm R. J.; Hemminger J. C.; Comsa G. *Appl. Phys. A – Mater.* **1991**, *53*, 414.

[22] Cremer, P. S.; Somorjai, G. A. *J. Chem.. Soc. Faraday Trans.* **1995**, *91*, 3671.

[23] Zaera, F.; French, C. R. *J. Am. Chem. Soc.* **1999**, *121*, 2236.

[24] Starke, U.; Barbieri, A.; Materer, N.; Van Hove, M. A.; Somorjai, G. A. *Surf. Sci.* **1993**, *286*, 1.

[25] Ofner, H.; Zaera, F. *J. Phys. Chem. B* **1997**, *101*, 396.

[26] Zaera, F. *Langmuir* **1996**, *12*, 88.

[27] Nomikou, Z.; Van Hove, M. A.; Somorjai, G. A. *Langmuir* **1996**, *12*, 1251.

[28] The calculated value from Ref. 27 was based on single molecular diffusion. We believe the actual diffusion barrier of ethylidyne in a (2 x 2)-C_2H_3 structure to be much lower at near-saturation due to ethylidyne-ethylidyne repulsive interaction and weaker binding to the surface due to electron donation to the surface from more ethylidyne molecules.

[29] Land, T. A.; Michely, T.; Behm, R. J.; Hemminger, J. C.; Comsa, G. *J. Chem. Phys.* **1992**, *97*, 6774.

[30] Abon, M.; Billy, J.; Bertolini, J. C. *Surf. Sci.* **1986**, *171*, L387.

[31] Ma, J.; Xiao, X.; DiNardo, N. J.; Loy, M. M. T. *Phys. Rev. B* **1998**, *58*, 4977.

[32] Kruse Vestergaard, E.; Thostrup, P.; An, T.; Lægsgaard, E.; Stensgaard, I.; Hammer, B.; Besenbacher, F. *Phys Rev. Lett.* **2002**, *88*, 259601.

[33] Another high pressure CO structure has also been proposed but subsequently refuted by Ref. 32: Jensen, J. A.; Rider, K. B.; Salmeron, M.; Somorjai, G. A. *Phys. Rev. Lett.* **1998**, *80*, 1228.

[34] Chiang, S.; Wilson, R. J.; Mate, C. M.; Ohtani, H. *Vacuum* **1990**, *41*, 118.

[35] Chen, P.; Kung, K. Y.; Shen, Y. R.; Somorjai, G. A. *Surf. Sci.* **2001**, *494*, 289.

[36] Ainsworth, M. K.; McCoustra, M. R. S.; Chesters, M. A.; Sheppard, N.; De La Cruz, C. *Surf. Sci.* **1999**, *437*, 9.

[37] Seebauer, E. G.; Kong, A. C. F.; Schmidt, L. D. *Surf. Sci.* **1986**, *176*, 134.

[38] The weak adsorption of π-bonded ethylene on the surface was believed to resemble physisorption of noble gases on Pt(111), since unlike the strong binding of di-σ-bonded ethylene the weaker and longer bonding allows addition of hydrogen amidst an already crowded surface. The pre-exponential factor and heat of adsorption of the latter have been previously investigated by: Widdra, W.; Trischberger, P.; Friess, W.; Menzel, D.; Payne S. H.; Kreuzer, H. J. *Phys. Rev. B* **1998**, *57*, 4111.

[39] Zaera, F. *J. Phys. Chem.* **1990**, *94*, 8350.

[40] The "abnormally low" pre-exponential value for hydrogen desorption is due to its overall second-order nature as a result of dependence on both bimolecular recombination and desorption rates, and has been previously investigated and

explained by: (a) Poelsema, B.; Mechtersheimer, G.; Comsa, G. *Surf. Sci.* **1981**, *111*, 519., and (b) Poelsema, B.; Mechtersheimer, G.; Comsa, G. *Surf. Sci.* **1981**, *111*, L728.

[41] Payne, S. H.; Kreuzer, H. J.; Frie, W.; Hammer, L.; Heinz, K. *Surf. Sci.* **1999**, *421*, 279.

[42] Yanagita, H.; Fujioka, H.; Aruga, T.; Takagi, N.; Nishijima, M. *Surf. Sci.* **1999**, *441*, 507.

[43] Wander, A.; Van Hove, M. A.; Somorjai, G. A. *Phys Rev. Lett.* **1991**, *67*, 626.

[44] Bowker, M.; Gland, J. L.; Joyner, R. W.; Li, Y.; Slin'ko, M. M.; Whyman, R. *Catal. Lett.* **1994**, *25*, 293.

[45] Bent, B. E.; Mate, C. M.; Kao, C. T.; Slavin, A. J.; Somorjai, G. A. *J. Phys. Chem.* **1988**, *92*, 4720.

[46] Calhorda, M. J.; Lopes, P. E. M.; Friend, C. M. *J. Mol. Catal. A* **1995**, *97*, 157.

[47] Papageorgopoulos, D. C.; Ge, Q.; King, D. A. *Surf. Sci.* **1998**, *397*, 13.

[48] Blackman, G. S.; Kao, C. T.; Bent, B. E.; Mate, C. M.; Van Hove, M. A.; Somorjai, G. A. *Surf. Sci.* **1988**, *207*, 66.

[49] Cernota, P.; Rider, K.; Yoon, H. A.; Salmeron, M.; Somorjai, G. *Surf. Sci.* **2000**, *445*, 249.

[50] Lauhon, L. J.; Ho, W. *Phys. Rev. Lett.* **2000**, *85*, 4566.

[51] Mitsui, T., Rose; M. K., Fomin, E.; Ogletree, D. F.; Salmeron, M. *Nature* **2003**, *422*, 705.

[52] Rose, M. K.; Mitsui, T.; Dunphy, J.; Borg, A.; Ogletree, D. F.; Salmeron, M.; Sautet, P. *Surf. Sci.* **2002**, *512*, 48.

Chapter 5

Novel Design of an Ultra High Pressure, High Temperature Scanning Tunneling Microscope System

5.1 Overview

Considerable technical challenges must be overcome in order to perform scanning tunneling microscopy (STM) studies at the level of atomically resolving individual adsorbates on close-packed metal surfaces, especially for *in situ* reaction studies. Unlike the study presented in the previous chapter, varying temperature is generally required in chemical reaction studies to monitor the diffusion rate of adsorbed atoms and molecules, as well as measuring surface dynamics and reaction progress in response to temperature variation. To study thermally activated processes, moreover, the sample temperature must be precise and programmable so that the speed of the events of interest can be tuned to

the limited time-scale accessible to STM. Environmental vibrations (be it mechanical, electrical, or chemical) must be attenuated dramatically to provide stable imaging conditions, as to observe atomic features such as the weak periodic corrugation of the substrate lattice, the STM tip must be stabilized over the surface with a precision on the order of picometers. Since the goal of the STM studies performed in this laboratory is to observe individual reactive species bound to otherwise clean metal surfaces under high pressure and temperature, the reactor and the microscope contained therein must be designed to endure harsh conditions while maintaining stability necessary for STM imaging. Meanwhile, ultra high vacuum (UHV) conditions remain essential for such system in order to prevent contamination before the experiments perform analysis on the catalyst surfaces that is otherwise inaccessible by STM technique alone. The necessity of combining high pressure *in situ* techniques with UHV preparation methods, particularly when combined with the wide range of operating temperatures necessary for sample preparation and reaction studies, severely limits the list of materials that can be used to construct key components of the system and generally complicates both operation and maintenance.

To meet these challenges, the design and performance of a novel ultra high pressure, high temperature scanning tunneling microscope system is designed described in this chapter, which is set up as a flow reactor and is integrated in a UHV system. The flow-reactor STM is designed to allow imaging of the catalyst surface *in situ* from vacuum up to 30 atm, and simultaneous determination of the reaction gas using a mass spectrometer. In addition, the STM sample holder is designed to allow thermal control of

the sample between room temperature up to 350 °C under pressure and 1000 °C in vacuum, by the use of a custom-designed button heater. The STM is compactly and rigidly designed as a vertical slip-stick motor, and is integrated within a small pressure cell in such a way that two crucial features result: the flow of reaction gas is along the length of the tip to minimize the amount of vibration induced by turbulence, and the interior of the pressure cell can be accessed through a bayonet-sealed opening that can be opened *in vacuo* with a wobble stick to allow tip or sample exchange. The pressure cell containing the STM is housed in an ultra high vacuum system, which allows surface preparation and analysis before and after high pressure studies. The theory and design of the reactor STM and its integration into a UHV system are presented here with related detailed schematics outlined in a separate appendix, and the initial performance of the full setup is demonstrated by experiments on gold deposited on glass and high ordered pyrolytic graphite (HOPG) under ambient condition.

5.2 STM Design

Mechanically, scanning probe microscopes (SPM), which include STM, have to fulfill design specifications which are oftentimes contradictory. On one hand, the scan range of a SPM should exceed the size of the largest features on the sample. This usually implies the use of large and thin-walled piezoelectric transducers. For many applications, it is also desirable to have the ability to adjust the relative position of the tip in relation to the sample over distance on the order of micrometers, which requires additional piezoelectric control like in the case of the Beetle STM and thus increases the size of the

microscope. On the other hand, any SPM is a system of mechanical resonators with various quality factors. These resonances can be excited either by the surroundings or by the rapid movement of the tip or the sample. Especially, the microscope is affected by building vibrations and by other ambient sounds and excitation, which has comparably large amplitudes to tunneling gap size, on the order of micrometers. The frequency spectrum of such environmental excitation peaks between 10 and 100 Hz. Thus, it is important to avoid any resonating body within the STM with a resonance frequency of up to 1 kHz, since a larger difference between the driving frequency and the resonance frequency decreases the coupling and excitation, as evidenced by the following equation:

$$\Delta A_0 = 1 - 2Q^2 \left(\frac{\omega - \omega_0}{\omega_0}\right)^2$$

where ΔA_0 is the change in amplitude of the resonant body, Q the quality factor of the mechanical connection between the exciting and resonant bodies, and ω_0 and ω the excitation and resonance frequencies. In particular, quality factor Q describes the sharpness of the resonance in a vibratory system, with a large Q value represents a well-defined resonance with narrow bandwidth (which means high response near resonance). In general, a small Q value is desired in a vibration damping system to be effect.

Thus, it is of paramount importance to optimize the design of the STM for high resonance frequencies, which usually means decreasing the size of the microscope as the resonance frequency of a body scales proportionally with the diameter and the length of the body, as indicated by the following equation:

$$f = \frac{1}{2\pi} \frac{h}{l^2} \sqrt{\frac{E}{\rho}}$$

where f is the resonance frequency of the object, h the height, l the length, E the Young's modulus of the material used, and ρ the density of the material. Since the roles of height and length exchange with each other as dimensions change, the aspect ratio of the microscope generally needs to be near unity in a mechanically stable configuration. At the same time, the high resonance frequency design of the STM need to be complemented by a low pass filtering scheme with small quality factor, so that excitation of all frequencies and amplitudes is adequately damped, while only low frequency vibration modes that are hardly coupled to the STM resonance can reach the microscope.

Materials	Young's modulus E (10^{10} Pa)	Density ρ (g/cm^3)	$(E/\rho)^{0.5}$ (m/s)
PZT	6.9	7.5	3000
Molybdenum	31.7	10.2	5500
Macor	6.7	2.5	5200
Glass	6 - 8	2.3	5500
Stainless steel	19.3	8	4900
Aluminum	7.2	2.7	5200

Table 5.1. Young's modulus values and densities for materials commonly used for UHV application.

Materials chosen in the construction of a STM needs to be mechanically robust against stress (large Young's modulus) as a result of either rigid mounting or thermal expansion, while light weight in design to give rise to high intrinsic resonance frequency,

as indicated by the equation above. Table 5.1 shows the Young's modulus values and densities for materials commonly used for UHV application, and the last column indicates the contribution factor in determining the resonance frequency of an object made from indicated material. In particular, PZT ceramics is used to fashion necessary transducers for the scanning and approach motions of a STM with precision as high as on the order of picometers. In particular, both stainless steel and Macor are especially favored in construction of STM components in general, due to their low cost, excellent mechanical properties and machinability. Aluminum is sometimes preferred if weight is an important concern and electrical conduction is required, as in the case of a tip holder at the end of the scanning piezoelectric tube, though oxidation of the surface makes aluminum less favorable for dynamic electrical contacts.

In addition to mechanical properties, the materials used in the design of a STM need to behave well thermally, in response to thermal changes from both ambient environment and active temperature control. Most materials expand with changes in temperature, and thus it becomes particularly important to compensate for the thermal drift as a result by having a compact low expansion design with materials of similar thermal expansion coefficients, in addition to good temperature control (which requires small thermal load and high thermal diffusivity) and strategic thermal isolation.

A plot of the thermal conductivity values of some materials used in the construction of the new STM is shown in Figure 5.1. From this chart it is clear that glass and Macor (a machinable ceramic) are ideal low thermal conductivity materials, which can withstand relatively high temperatures (800 °C). Several alloys and pure metals

provide moderate thermal resistivity where electrical conductivity is required. Oxygen-free high conductivity (OFHC) copper can provide very high thermal conductivity. Polycrystalline sapphire (alumina) is more affordable than sapphire and provides thermal conductivity comparable to tantalum. Tungsten, although difficult to machine, offers excellent thermal conductivity with a much higher maximum working temperature than copper.

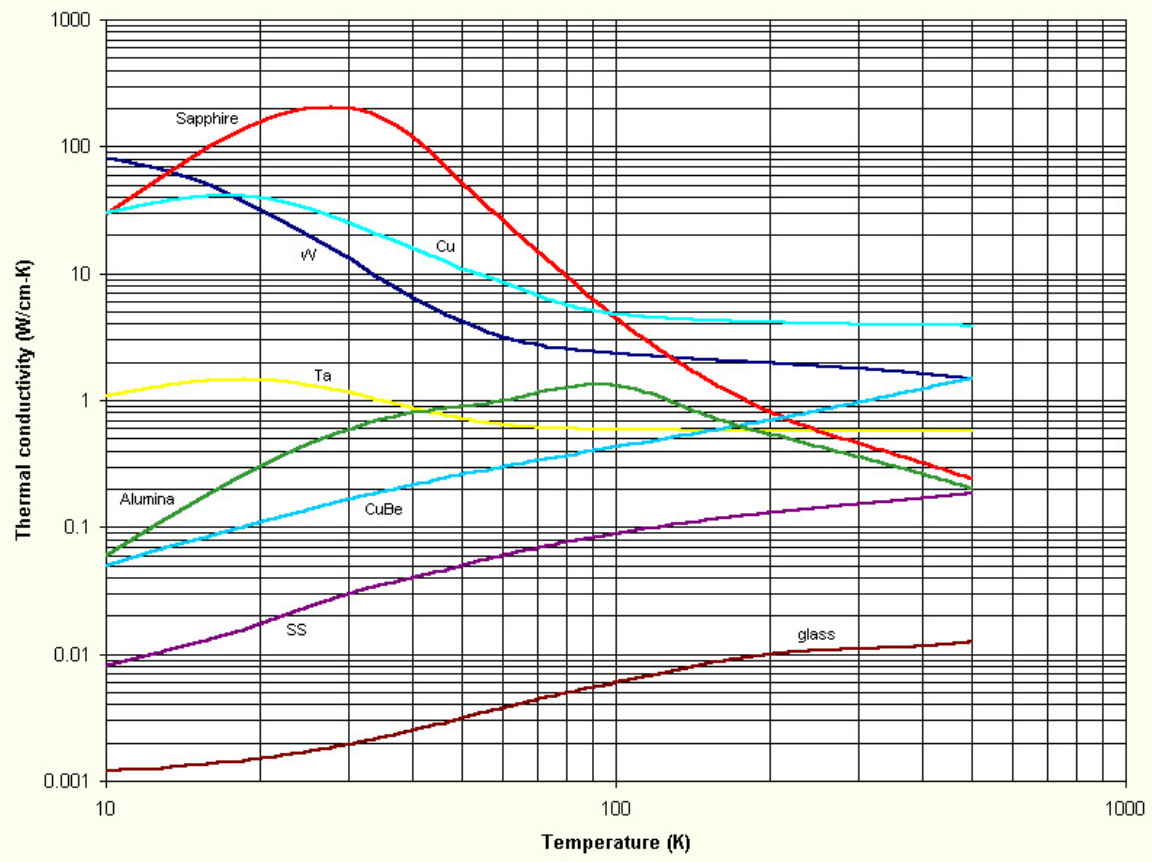

Figure 5.1. Thermal conductivity of various UHV-compatible materials as a function of temperature.

Table 5.2 outlines additional relevant thermal properties of the materials outlined above, which are selectively chosen for the current design due to their similarly low

thermal expansion coefficients to those of materials in the PZT piezoelectric family. Molybdenum and tungsten both have low thermal expansion values and excellent thermal diffusivity, the former of which is ideal for the STM body due to its machinability as well as chemical inertness towards both oxidative and reductive environments. Macor and glass are also compatible with a low thermal expansion design, and can be used when both thermal and electrical isolation are needed, though the latter of which is difficult to fashion for small components. Stainless steel can be used as a limited thermal insulator, when electrical connection needs to be maintained, and thermal expansion is less of a concern.

Materials	Thermal expansion coefficient (ppm/K)	Thermal conductivity (W/m-K)	Heat Capacity (J/g-K)
Molybdenum	4.8	138	0.255
Tungsten	4.5	174	0.13
Macor	10	1.6	2.5
Sapphire	8.8	46	0.76
Alumina	8.4	36	0.88
Glass	5 – 10	1.4	
PZT	7		0.19
Tantalum	6.3	57	0.14
Stainless steel	16	26.5	0.483
Aluminum	23	237	0.9

Table 5.2. Thermal properties of various UHV-compatible materials used in the design of the new Walker STM.

Materials	Dielectric constant	Dissipation factor (%)	Piezoelectric coefficient (nm/V)	Curie temperature (°C)	Young's modulus (10^{10} Pa)	Density (g/cm^3)
PZT-5A	1900	2	-0.18	365	6.6	7.9
BM500	1750	1.6	-0.16	360	6.5	7.65
PZT-5H	300	2	-0.27	195	6.1	7.6
BM527	2750	2	-0.25	225	6.9	7.5
PZT-4	1335	0.2	-0.12	325	7.7	8.1

Table 5.3. Physical properties of different piezoelectric materials used for fine motor movement.

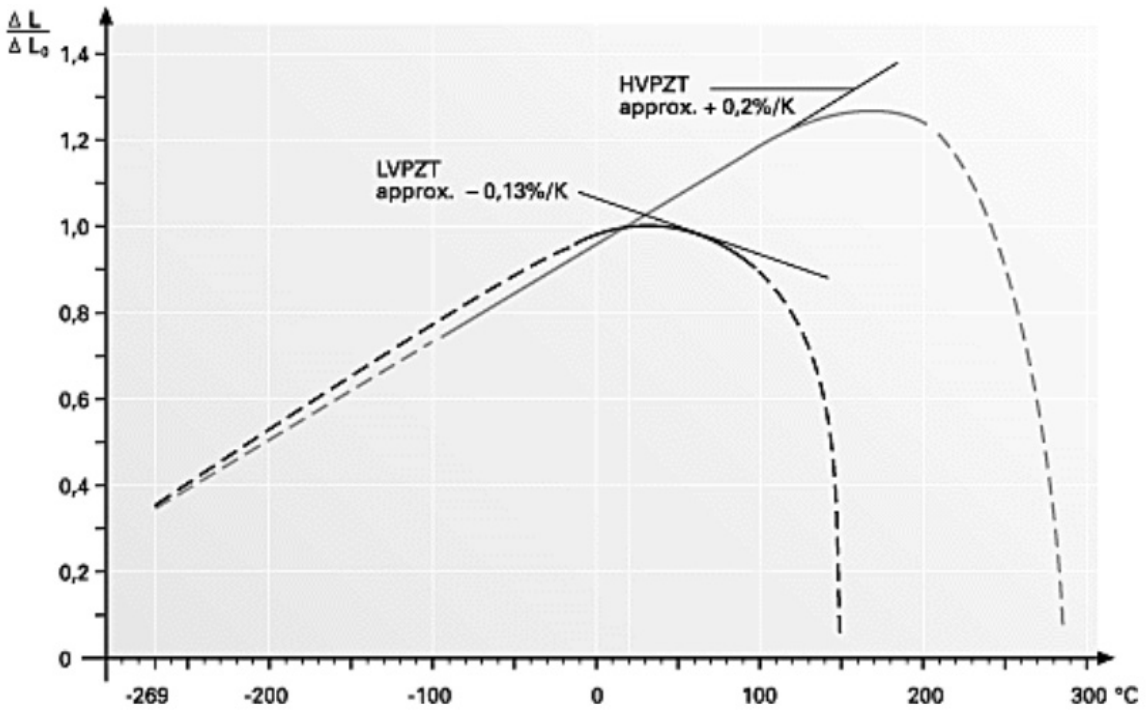

Figure 5.2. Performance of high voltage and low voltage materials of the PZT family as a function of temperature.

Lastly, the choice of piezoelectric materials for a STM motor is important in determining the service temperature range of the microscope as well as mechanical response per potential applied, in addition to mechanical and thermal properties already discussed. A variety of piezoelectric ceramics is available, which differ in their electrical, piezoelectric and mechanical properties. Table 5.3 lists a small selection of properties for four types of piezoelectric ceramics commonly used in scanning probe microscopes. A large piezoelectric coefficient d_{31} means you get large excursion per applied voltage, which is usually desirable. Large dielectric constants are undesirable, since they mean a large capacitance of the piezoelectric tube, which will limit the scanning frequency obtainable for a given drive current. The Curie temperature indicates the point at which an piezoelectric transducer is completely depolarized, but Figure 5.2 shows that the performance of an piezoelectric element is seriously degraded long before reaching the Curie temperature. In the case of a piezoelectric transducer for axial motion, the element can be re-polarized under high temperature and strong applied electric field. However, a shear-action piezoelectrics cannot be re-polarized, due to its dependence on the grain boundary formed between two oppositely aligned piezoelectric grains. A high dissipation factor means that a large part of the driving energy is converted to heat inside the piezoelectrics. All piezoelectric materials commonly used in scanning probe microscopes are "soft", optimized for high sensitivity (large d_{31}) but with rather large thermal dissipation. They cannot be driven with large amplitudes and at high frequencies, which could heat them up significantly. Soft piezoelectric ceramics also exhibits a larger hysteresis (asymmetric response to potentials of opposite polarities), with 15% to 20%

difference in pressure exerted for potentials of same magnitude but different polarities as typical for soft materials, as opposed to 3% to 5% for hard materials.

In the case of piezoelectric transducers for the new ultra high pressure, high temperature STM, PZT-5A is chosen for its high maximal service temperature.

5.2.1 Motor

From a design point of view, a practical STM must have two core capabilities in addition to the fine positioning control afforded by the piezoelectric transducers. First, the overall design must be rigid enough to prevent external vibrations from causing the tip-surface separation to vary significantly, while attenuation of vibrations through external damping is also an important and complementary requirement. High mechanical stiffness also allows faster operation of the feedback loop controlling the tip-surface separation, which in turn increases the maximum scan speed. Although specialized STM designs can acquire multiple images per second [1], common STM systems require between 10 and 100 seconds per image. To study dynamic processes at surfaces, therefore, it is generally necessary to vary the temperature of the surface. By heating and cooling the substrate temperature, the rates of chemical reactions and adsorbate diffusion can be adjusted to coincide with the timescale of STM. Systems designed specifically for variable temperature operation, especially above room temperature, contain materials of low and similar thermal expansion characteristics to minimize and accommodate mechanical stresses as a result of temperature change, and generally incorporate some form of

thermal expansion compensation in order to minimize unwanted net motion of the tip compared to the sample surface. [2, 3]

A second basic requirement is that an STM must incorporate a reliable means of approaching the tip to the surface to within the small range of the scanning piezoelectric transducer (typically 100 to 1000 nm). This coarse approach capability must not compromise the stiffness of the STM. Often the coarse approach mechanism must also operate reliably without external mechanical interaction. [4, 5]

The current STM motor design is based on the concept previously developed by Pan *et al*. [6] The idea of a piezoelectric scanner rigidly braced by six shear piezoelectrics that also provide the coarse approach mechanism remains the same, but the size of the STM body has been significantly streamlined to reduce thermal load exerted on the small button heater required in a compact high pressure and temperature STM. As evidenced at the beginning of this section, materials of low thermal expansion and similar thermal performance, such as molybdenum, Macor, alumina, sapphire and glass, are chosen to construct the new STM to minimize drift and mechanical stress as a result of variable temperature applications.

In using a braced "slip-stick" approach mechanism by shear piezoelectric "legs" instead of piezoelectric tubes as in the case of the Beetle STM, the overall lateral scan range of the STM scanner is reduced in exchange for a more mechanically stable design. Referring to Figure 5.3 and Figure 5.4, the overall blueprint of the new "Walker" STM is circular in design, where the scanner (a hexagonal sapphire slider housing the scanning piezoelectric transducer, both of which are secured on a Macor base plate) is

concentrically aligned with the circular STM body and sample, in order to minimize the lateral drift in imaging during thermal variation as a result of ambient or active changes. A more compact molybdenum STM body of 1" diameter and 1.25" long (Figure 5.5) has been designed to replace the larger Macor body in the former version, to provide the same rigidity and low thermal expansion design while sacrificing some of the coarse approach distance. The body contains a central semi-hexagonal cavity for placement of the shear piezoelectric legs and the scanner, and is plated with 1 μm thick gold for chemical passivation. Referring to Figure 5.6, the top surface of the body contains a square formation of thirty two 0.032" diameter clearance holes to be lined with alumina tubing of 0.030" outer diameter (OD) and 0.020" inner diameter (ID) for the purpose of wiring, and a circle of eleven 2-56 tapped holes for secured mounting to the high pressure flow reactor cell. The front of the circular side on the STM body is open to provide access to the inner cavity, and features a pair of vertically align 0.2" wide and 0.060" deep notches with centrally aligned 0-80 tapped holes on the top and bottom ends, for installation of a copper beryllium (CuBe) spring plate to press all shear piezoelectric legs tightly against the scanner once installed. Referring to Figure 5.7, the rear of the body contains two 0.1" wide and 0.040" deep channels, each of which can house three alumina tubing of 0.020" OD and 0.012" ID and be subsequently covered by a gold foil for the purpose of electrically shielded wiring. The bottom end of the body also has open access to the inner cavity, through which the scanner and the tip can gain access to the sample surface, and have a circular arrangement of three depressions of 0.020" diameters for

seating of three glass balls for rigid mechanical coupling and thermal installation with the sample stage (Subsection 5.2.2).

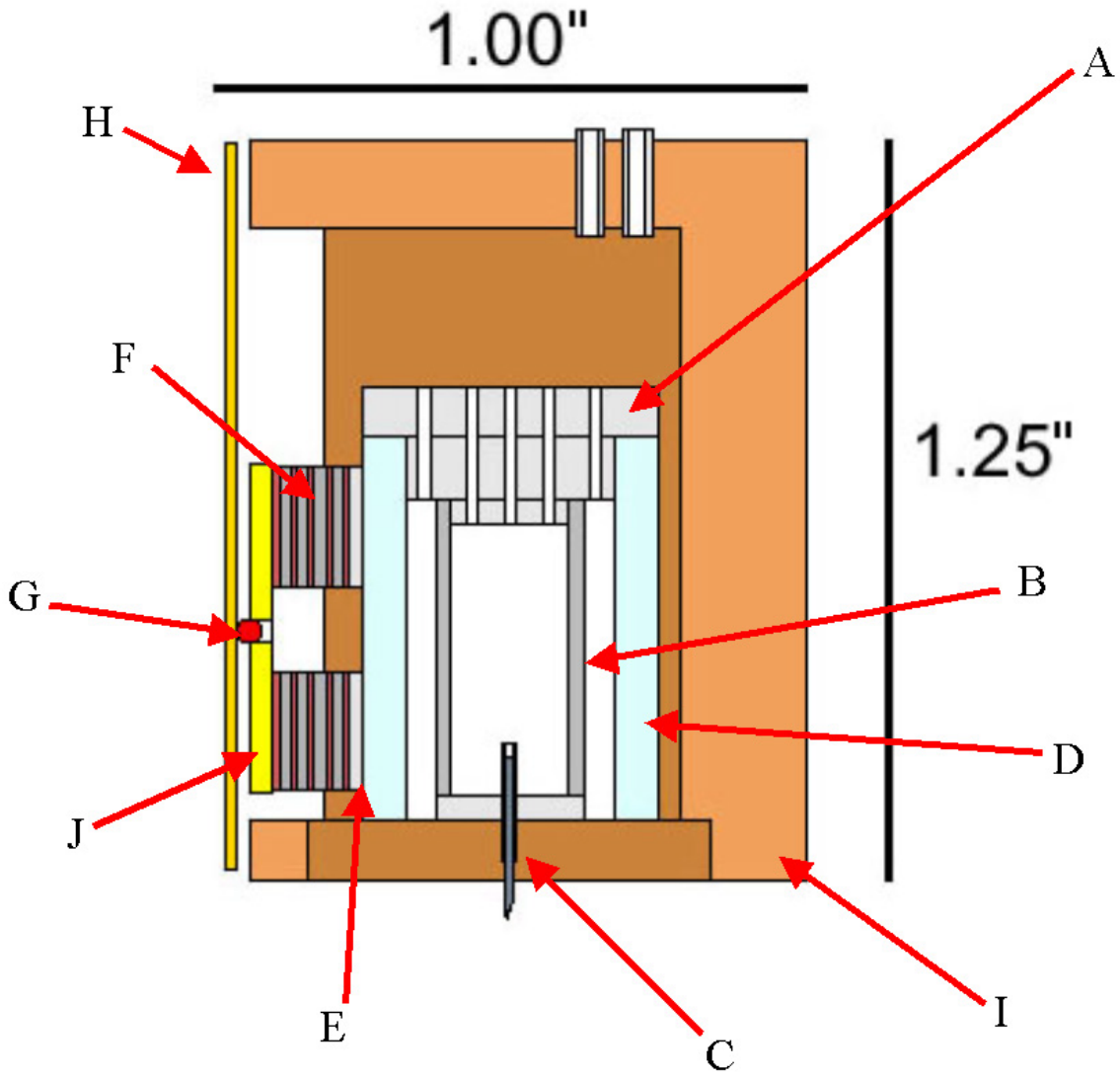

Figure 5.3. The scanner of the "Walker" STM contains a Macor base plate (**A**), on which the scanning piezoelectric tube (**B**) with the tip holder (**C**) and a hexagonal sapphire prism slider (**D**) are glued. The scanner is braced against the alumina spacers (**E**) on six shear piezoelectric stacks (**F**) by applying pressure through a glass ball (**G**) contact with a copper beryllium spring plate (**H**). Four of the stacks are glued to the inside walls of the molybdenum body (**I**), and the other two on an alumina plate.

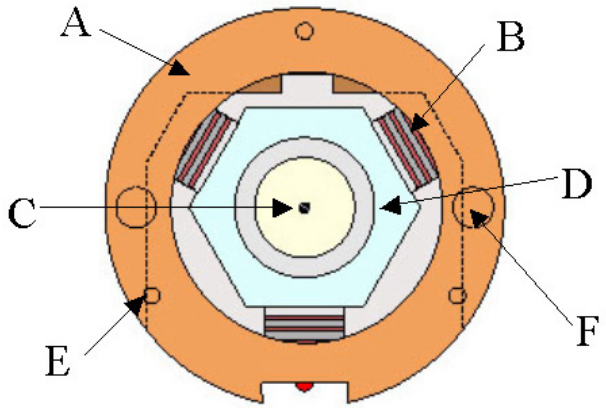

Figure 5.4. The bottom view of the Walker STM schematic reveals that the design is centrally symmetric. The circular molybdenum body (**A**) is in rigid contact and concentric, through the use of six shear piezoelectric stacks (**B**), with the scanner, which contains the scan tub equipped with a tip holder (**C**) and a sapphire slider (**D**) that are glued to a Macor base plate. The underside of the STM body contains 0.010" diameter holes (**E**) for glass ball contacts to mount a sample stage through the use of 2-56 screws (**F**).

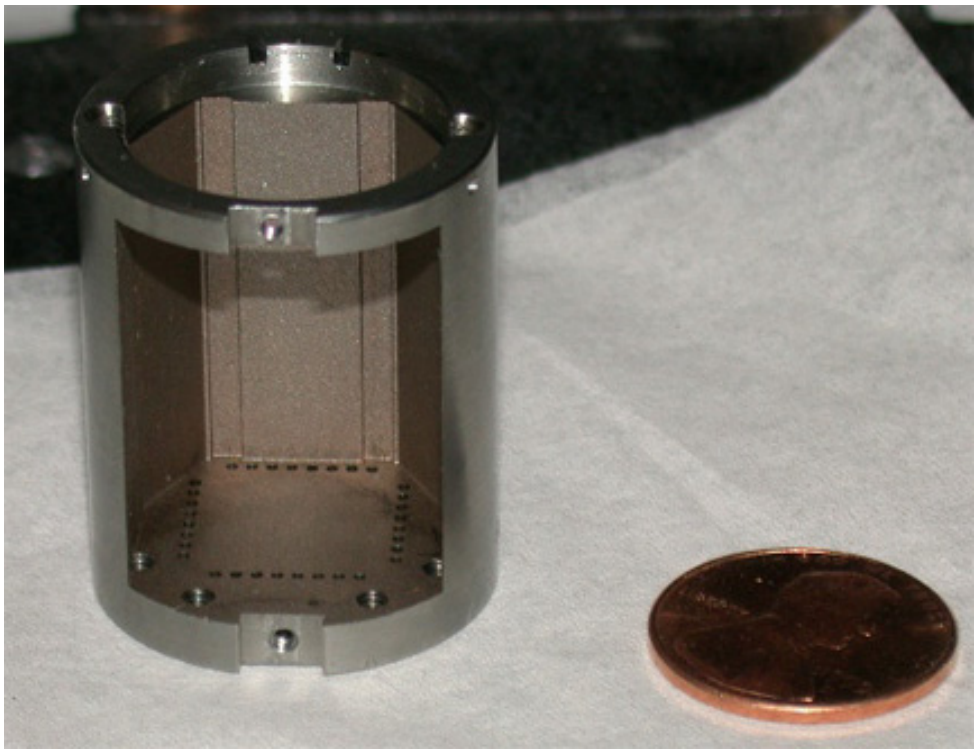

Figure 5.5. Molybdenum body for the Walker STM.

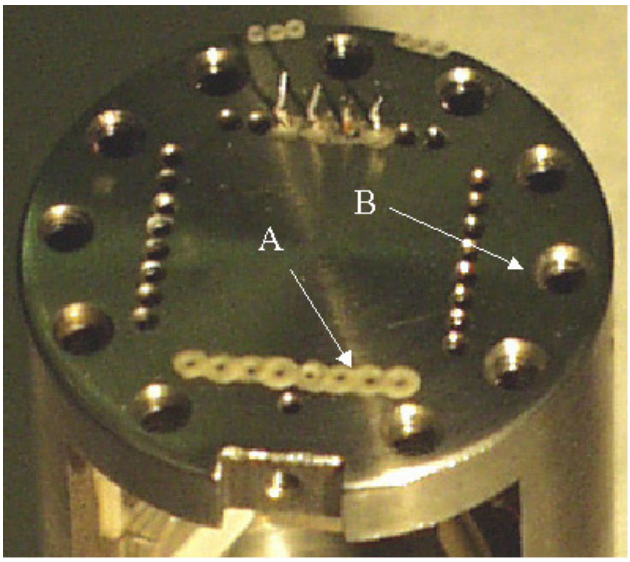

Figure 5.6. The top surface of the STM body contains a square formation of alumina-lined clearance holes (**A**) for wiring, and a ring of 2-56 tapped holes (**B**) for mounting the STM to the high pressure flow reactor cell.

Figure 5.7. Rear view of the STM body, now gold-plated, shows the alumina tubing inside the back trenches, before the trenches are electrically shielded with a covering gold foil.

The coarse approach mechanism of the Walker STM relies on the use of six shear piezoelectric legs upon the surface of a polished hexagonal sapphire prism that contains the scanning piezoelectrics, arranged in two sets of three legs in order to provide stable three-point contacts on the sapphire slider. Each shear leg consists of four square shear piezoelectric plate, of 5 mm long and 0.5 mm thick and with nickel-plated electrodes, glued together in a stack formation and in alternating direction by electrically conductive epoxy, to maximize the shear distance of each stack per voltage applied. Four shear stacks are glued in two columns within the STM body cavity (Figure 5.8), while another pair is secured onto an alumina plate (Figure 5.9). A polished alumina spacer is glued to the top surface of each stack to provide an equally smooth surface per stack for the sapphire slider to couple with. Referring to Figure 5.10, to power each shear piezoelectric leg, the central interface as well as the top and bottom surfaces of each stack are connected as electrical ground (which is connected to the STM body ground by electrically conductive glue), while the remaining two interfaces are designed as parallel high voltage. Relatively rigid Kapton-coated copper wires of 0.010” diameter are used to make connections for the shear legs to prevent accidental interference of the wires with the coarse approach mechanism, and the high voltage connections are guided along the inner walls of the body cavity in alumina tubing to exit through the small wiring openings at the top end of the body. Upon exiting the top surface, each wire is glued at the base of the wiring opening, and subsequently stripped and trimmed to 5 mm long as soldering points to be connected to the wiring junctions of the pressure cell (Subsection 5.3.1). Upon preparing all shear legs as described above, the hexagonal sapphire slider

containing the scanner can be placed among the six piezoelectric legs, with the pair of shear legs on the alumina plate placed on the slider at the front opening of the body, so that a pair of stacks will mate with every other surface of the prism. All six legs are pressed firmly against the prism surfaces by installing a CuBe spring plate, as mentioned briefly above and shown in Figure 5.11, over the alumina plate containing two of the shear piezoelectric stacks. Both the alumina and CuBe plates have a clearance hole of 0.015" diameter so that a glass ball of 1.5 mm diameter can be placed in-between as a stable ball point contact, as the CuBe plate is mounted down by 0-80 screws at the top and bottom ends of the body. Since the clearance seating hole on the CuBe plate is placed at different lengths from the ends, the pressure applied on the sapphire slider can be varied gradually by adjusting the 0-80 screw on the longer lever using the glass ball as a pivot point. Once secured, the scanner can approach in a "slip-stick" manner (Section 5.5), by initially shearing each of the piezoelectric legs in sequence while the other five remain stationary, and subsequently relaxing all shear stacks simultaneously for a net overall motion of the scanner. Figure 5.12 shows the reproducibility of the approach mechanism upon repeated approach and retraction of the scanner to the sample surface, revealing a steady decline most probably due to local thermal expansion and thus frictional change as a result of the slip-stick motion, since the approach step size usually fully recovers after idling overnight.

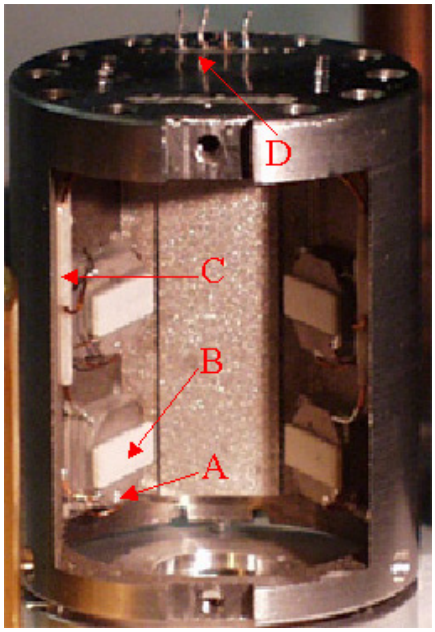

Figure 5.8. Four shear piezoelectric stacks (**A**) with their alumina spacers (**B**) are glued to the inner walls of the STM body. Kapton-coated copper wires are used to provide high voltage to the shear stacks, and are guided along the inner wall with alumina tubing (**C**), till they exit the top body surface where they are stripped, trimmed, and glued down as soldering junctions (**D**).

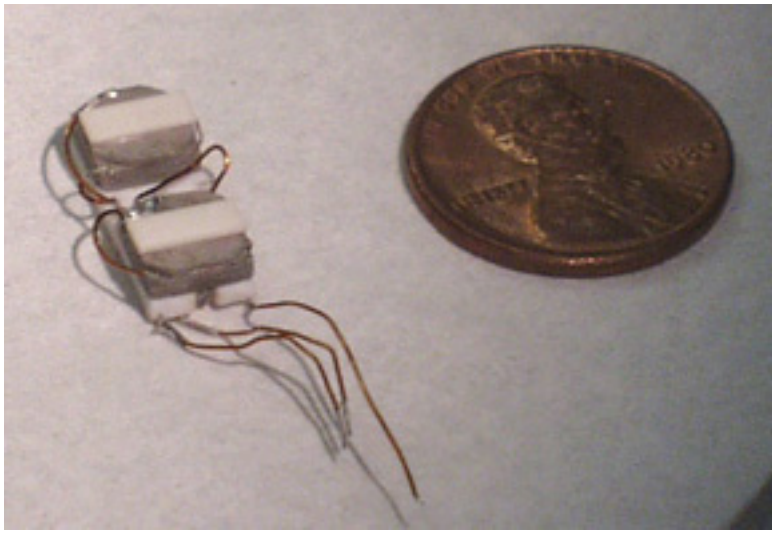

Figure 5.9. A pair of shear piezoelectric stacks on an alumina plate, for providing the coarse approach of the STM scanner in conjunction with the four shear stacks shown in Figure 5.8.

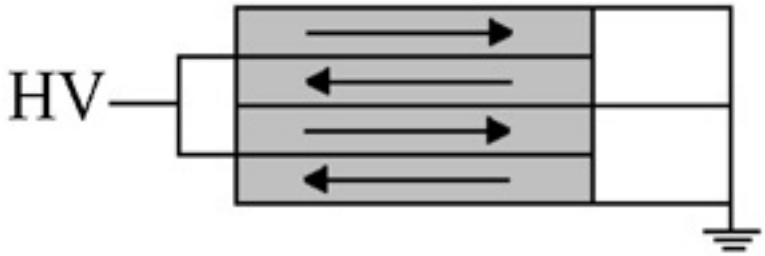

Figure 5.10. Schematic of the electrical connections for a shear piezoelectric stack.

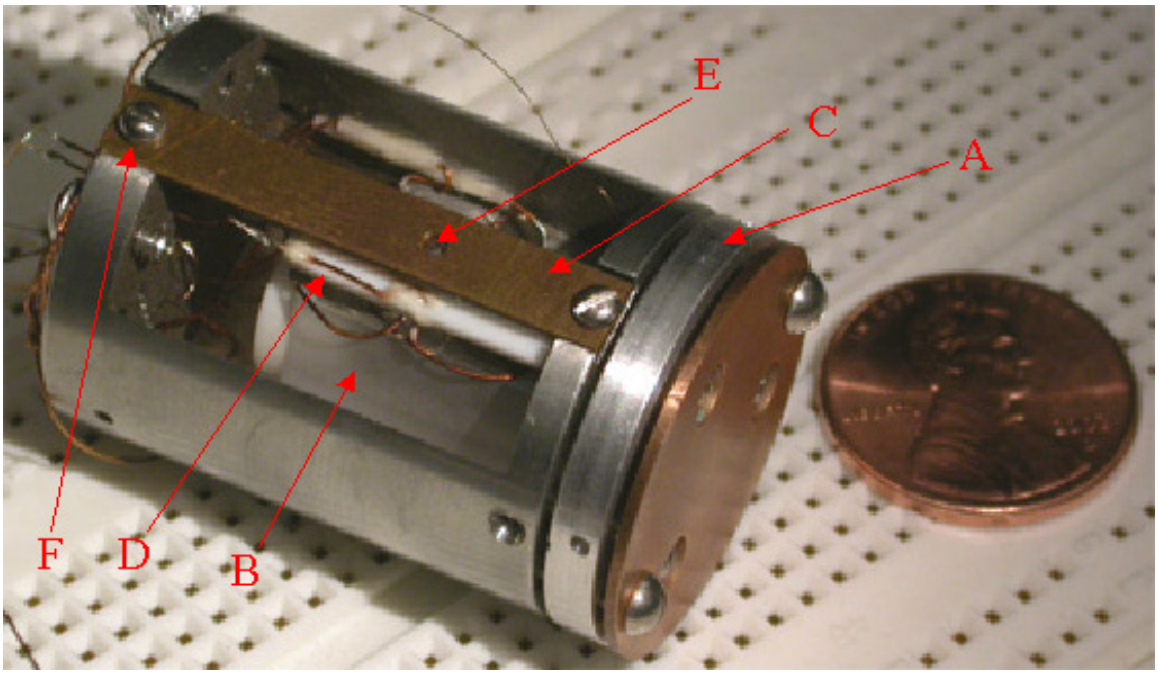

Figure 5.11. A fully assembled Walker STM with a mock sample holder (**A**) shows that the scanner (**B**) is pressed among the six shear piezoelectric stacks, by a copper beryllium spring plate (**C**) exerting pressure on the alumina plate (**D**) containing two of the shear stacks through a glass ball (**E**). The applied pressure can be adjusted by a 0-80 screw (**F**).

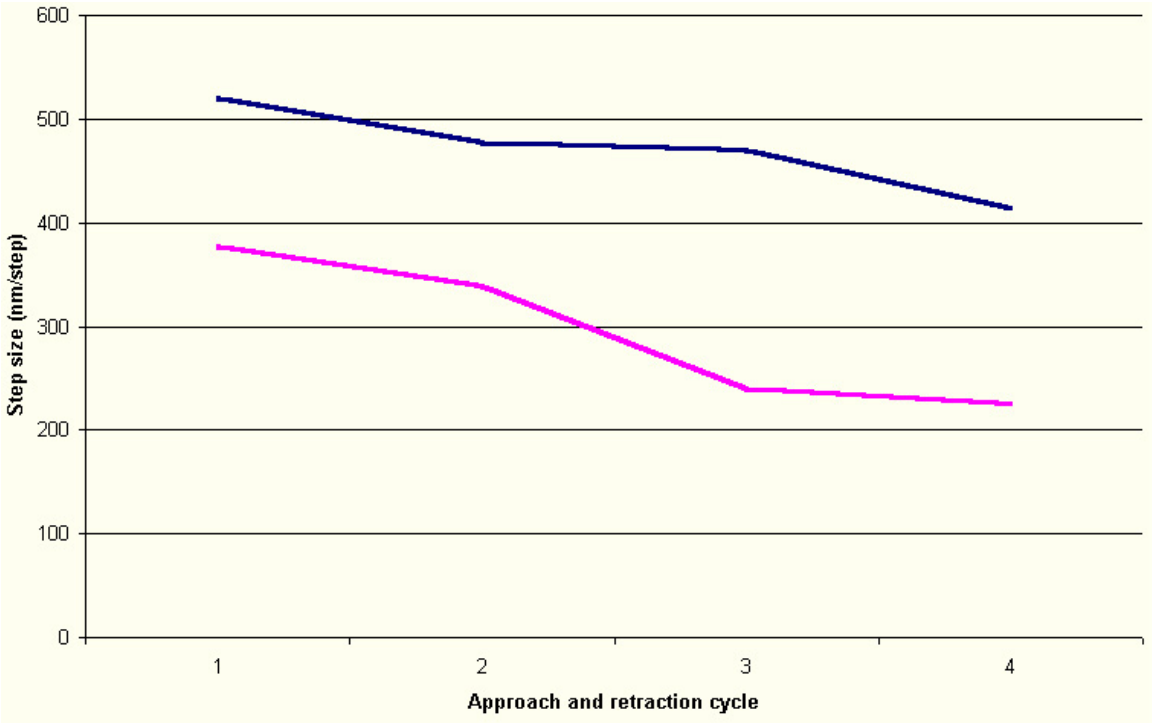

Figure 5.12. Successive cycles of approach and retraction show a gradual decrease in step size at 120 V. This is most probably due to local thermal expansion and increase in friction, which recover upon idling overnight.

The scanner portion of the STM motor consists of a Macor base plate, a PZT-5A scanning piezoelectric tube (0.250" diameter x 0.500" long x 0.020" thick) with the tip receptacle, and a hexagonal sapphire prism with an internal cylindrical cavity. (Figure 5.13) Since there is no coarse lateral offset mechanism in the Walker STM, the scanner serves as a scanning transducer with a limited but fine lateral adjustment. The Macor base plate contains two appropriately sized and concentrically placed columns, so that the inner cavities of the prism and the piezoelectric transducer can be glued securely onto the base plate and concentrically with each other, with the other end surfaces of the sapphire and piezoelectric components nearly level with each other. The exterior of the sapphire prism has been polished to two different smoothness, with the six faces alternating in the

two roughness so that the prism can be rotated to provide different frictional surfaces in addition to the freedom of adjusting the pressure exerted by the shear piezoelectric contacts. The interior hollow space of the sapphire slider is machined to be much considerably larger than the OD of the scan tube, so that a slight misalignment of the piezoelectric transducer on the Macor plate will not lead to direct mechanical contact and coupling to the sapphire. Soft Kapton-coated copper wires of 0.003" diameter are used to electrically connect the four exterior quadrant electrodes and the inner electrode of the scan tube to the wiring junctions present at the top end of the STM body, and the wires are routed out of the scanner through clearance holes fashioned at the Macor base plate. The wiring junctions at the top of the microscope body are in the form of gluing down segments of 0.010" diameter copper wires at the alumina-lined clearance holes, serving as soldering points for both external and internal portion of the STM body, a motif that is used again for the high pressure electrical connection of the reactor cell (Subsection 5.3.1) as well as modular wiring connection of the docking scaffold for the pressure cell (Subsection 5.3.2).

The end of scan tube can be equipped with a tip exchange mechanism for *in vacuo* manipulation as will be described in Subsection 5.2.4, or a simple tip receptacle consisting of a 0.020" thick Macor disk with a concentrically mounted gauge 22 needle for retaining and electrically connecting a tip.

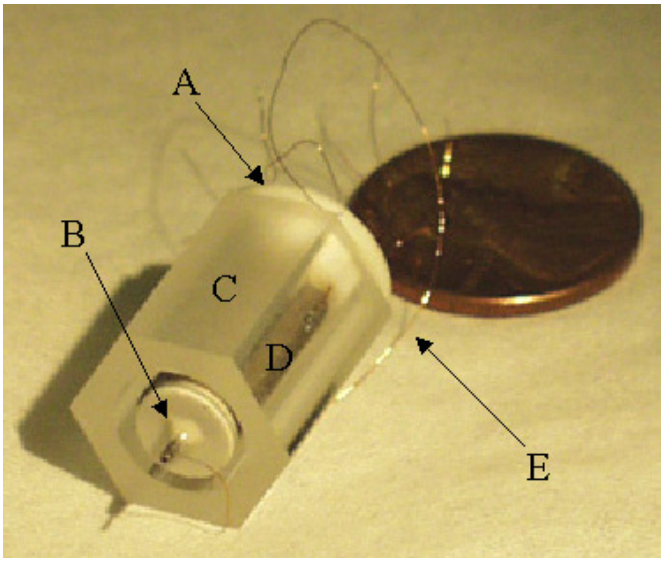

Figure 5.13. The scanner of the Walker STM consists of a Macor base plate (**A**), which is glued to a scan tube with a tip holder (**B**), and a hexagonal sapphire prism slider that is polished to two different grains (**C** & **D**). The electrodes of the scan tube are routed out by thin Kapton-coated copper wires (**E**) through the Macor base plate.

5.2.2 Sample Stage

The design of the sample stage revolves around two important interactions with both the STM motor and the sample holder: strong mechanical coupling and sound thermal isolation. Mechanical stability is important to ensure external vibration excitation does not vary the tip-sample separation distance beyond the compensation of the feedback control loop during imaging, while the secure design must remain modular to allow removal of sample stage from motor for individual inspection when necessary, as well as to permit exchange of tip and sample holders into the stage *in vacuo*. At the same time, thermally insulated design allows reduced heat transfer between the sample on stage and the STM motor while maintaining the rigid mechanical design, and thus ensures the thermal load is small and equilibrium is quickly reached during variable

temperature experiments. At the same time, the performance of the piezoelectric transducers within the motor is not compromised during thermal studies.

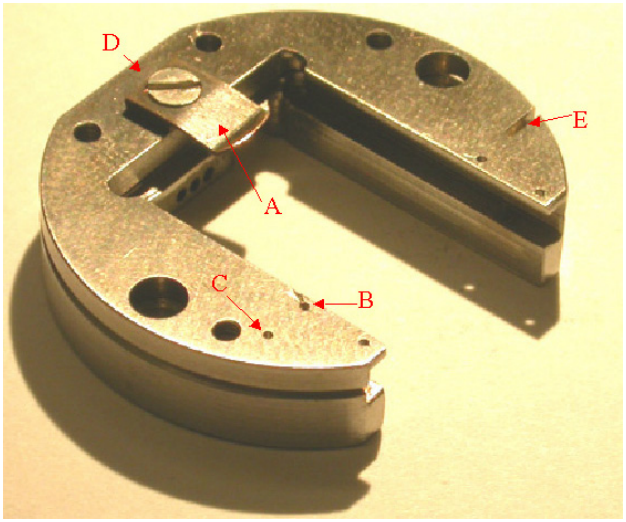

Figure 5.14. The sample stage contains a system of a leaf spring (**A**) and two wire springs that are each formed by a stainless steel loop to be placed through two clearance holes (**B**), for the purpose of mounting a removable sample holder. Both the top and bottom surfaces of the sample stage each contain a set of "point-blank-slot" (**C**, **D** & **E**) motif for mounting to the STM body by kinematic contact.

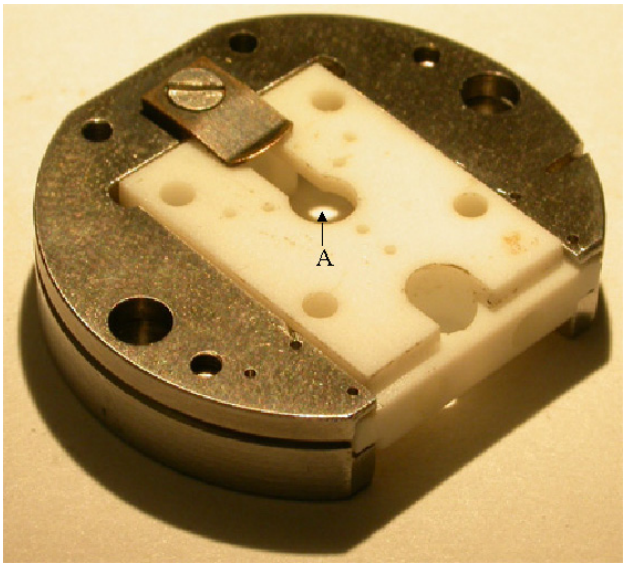

Figure 5.15. Sample stage with a mock removable sample holder inserted. **A** indicates where the sample surface will exposed to a scanning STM tip.

The stainless steel sample stage (Figure 5.14) has been constructed in two pieces due to the fact that some of the geometry required cannot be fashioned using conventional machining tools. The sample stage has been designed to allow exchange of a custom made sample holder (Subsection 5.2.3) or tip exchanger (Subsection 5.2.4) to facilitate the necessary *in vacuo* manipulation for tip and sample introduction. Upon the insertion of the sample holder, the sample is positioned in the center within the overall combined circular design of sample stage (Figure 5.15) and holder to minimize lateral drift in the tip-sample interaction as a result of thermal variation, while the sample holder is rigidly mounted and thermally isolated through a joint system of leaf spring and wire springs on glass ball contacts. Referring to Figure 5.16, the fitted recession of the sample stage for the placement of a holder have two cylindrical depressions of 0.5 mm diameter and 0.375" deep placed on either side of the entry, and one additional depression of the same size placed in the center of the ledge at the end of the recess. These three depressions allow three glass balls of 0.5 mm to be embedded at the bottom side of the recession to serve as a three-point contact for the holder to be seated on. In order to apply adequate force on the sample holder to maintain the kinematic contact on the glass balls, above each of the glass balls situated on either side of the entryway is two clearance holes of 0.25 mm diameter for secure placement of a stainless steel wire loop to act as a wire spring, and an adjacent recessed 2-56 tapped hole near the rear glass ball allows the addition of a stainless steel leaf spring. The combined mounting system of glass balls and springs provide not only the necessary mechanical stability for a rigid coupling loop between sample and tip, but also the reduced thermal transfer between sample and the

rest of the microscope by the use of insulating materials as well as fine contact points of high asperity.

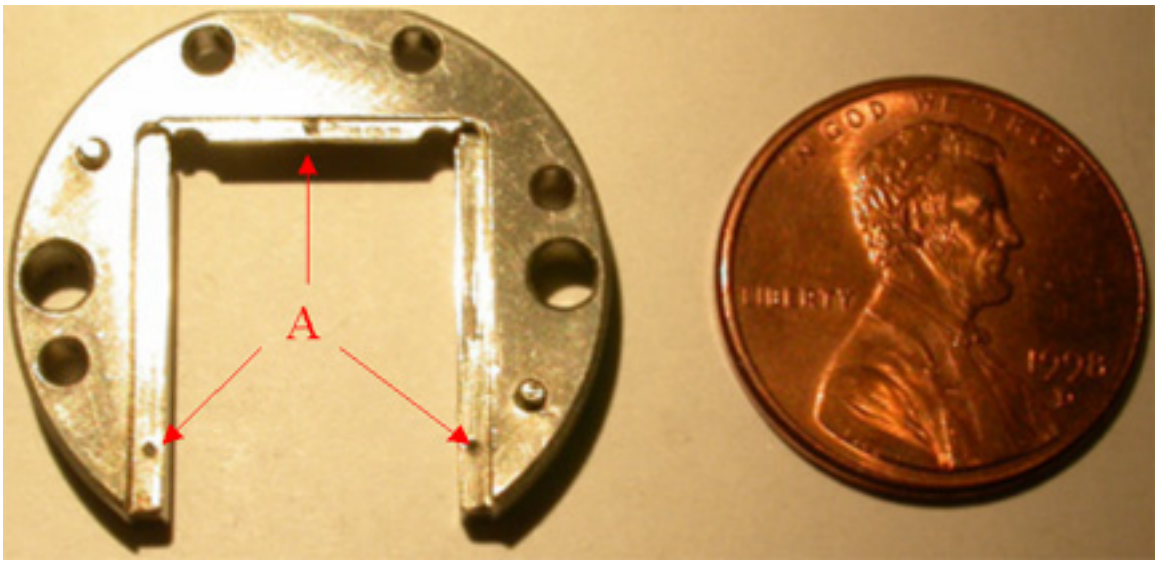

Figure 5.16. Top view of bottom section of the sample stage reveals three depressions (**A**) for fashioning 0.5 mm diameter glass ball contacts.

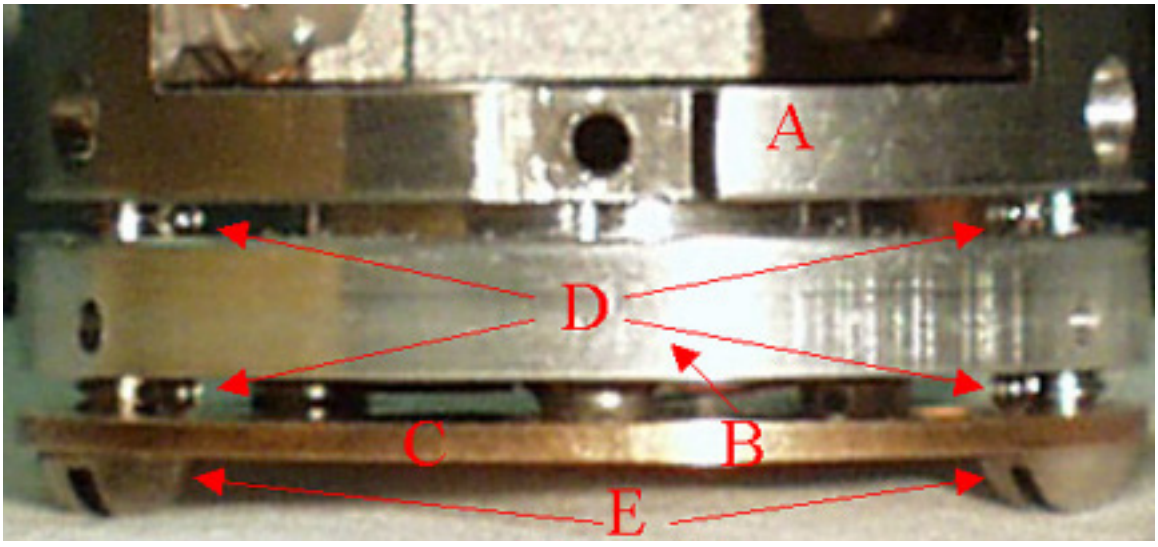

Figure 5.17. Kinematic contact is formed between STM body (**A**) and mock sample stage (**B**) by bracing them with a copper beryllium press plate (**C**) through two sets of glass balls (**D**) on the "point-blank-slot" motifs, by the use of two 2-56 screws (**E**).

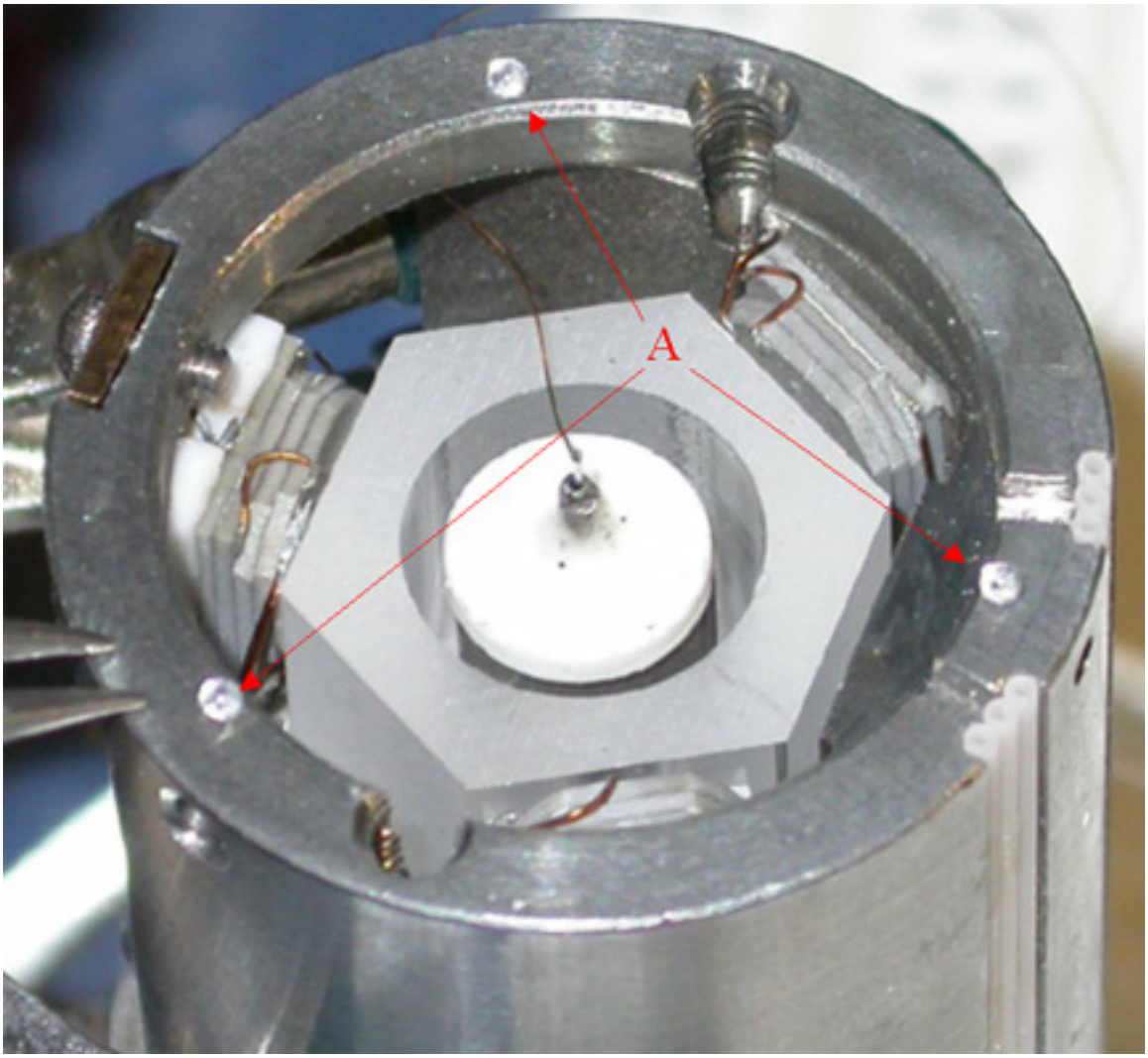

Figure 5.18. Glass ball contacts (**A**) placed at the three holes on the bottom of the Walker STM body.

The combined mechanical rigidity and thermal decoupling between the sample stage and the STM motor is achieved through the use of kinematic three-point glass ball contact. (Figure 5.17) The sample stage is pressed against and mounted to the STM motor with a circular CuBe pressure plate and three glass balls of 1 mm diameter in-between each pair of participants by two 2-56 screws. The top side of the sample stage contains a

set of appropriately placed “point-blank-slot” trio features, so that an adjustable contact can be made once the glass balls are placed into the three 0.020” holes at the bottom of the STM body. (Figure 5.18) Similar system is built into the bottom surface of the sample stage to be used with the CuBe press plate. Once the two sets of three glass balls are placed between the three components, two 2-56 screws can be inserted to mount the press plate tightly against the STM motor sandwiching the sample stage in-between. The 2-56 clearance holes on the sample stage have been fashioned larger than conventional size to prevent contact between the screws and the stage, ensuring further thermal isolation between the motor and the stage, and electrical insulation between those so that a bias voltage can be applied during imaging.

Three types of electrical connection need to be made to the exchangeable sample holder while insulated from the rest of the system: bias voltage, thermocouple, and high voltage supply for the button sample heater (as outlined later in the next subsection). Due to the extreme lack of space within the sample holder as evidenced in Subsection 5.2.3 and the similar situation on the sample stage, bias voltage for the current microscope has been designed to be applied through chromel wire of the type K thermocouple connection, while a special temperature display is used to read the potential difference between the thermocouple pair of wires to allow constant temperature monitoring even when a bias potential is being applied. Four rectangularly-arranged clearance holes of 0.022” diameter are placed at the back surface of the recess on the stage, so that they can be electrically insulated by alumina tubing of 0.020” OD and 0.012” ID for insertion of the two type K thermocouple wires of 0.010” diameter through the top holes and looping

to return through the lower holes in a top-down direction. The back surface of the recess is thinly coated with cured insulating epoxy, and the wire formations thus created are pushed firmly against the epoxy to allow a streamlined geometry while remaining electrically isolated from the stage. The thermocouple wires from the sample stage are routed along the back of the STM body in electrically shielded alumina tubing to the top of the body and subsequently to the external surface of the pressure cell. The vertical formation of the thermocouple is designed to couple mechanically and electrically with the horizontal arrangement of the thermocouple on the sample holder (as described in the next subsection), upon full insertion and engagement of the holder within the stage. The 90° out-of-phase arrangement of the mating contacts ensures a good electrical contact is always made upon mechanical stress on the contact system.

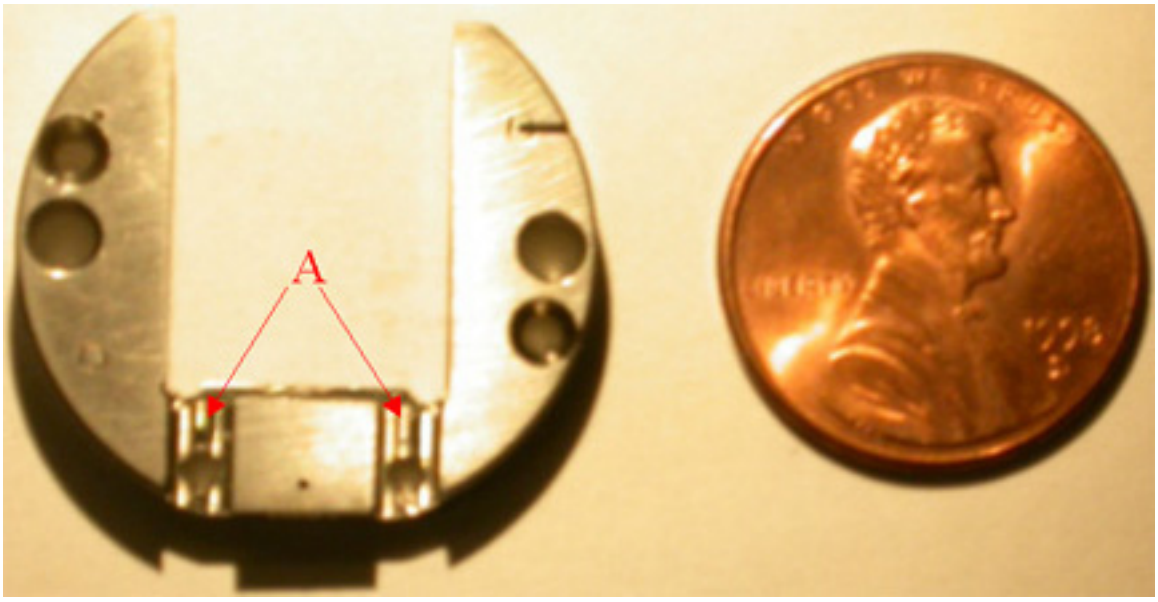

Figure 5.19. Bottom view of bottom section of the sample stage reveals two depressions with 2-56 tapped holes for fashioning leaf spring electrical contacts for the button sample heater in the sample holder.

Electrical connection between the sample stage and holder for the button heater has been implemented in the form of leaf springs and spring taps. The bottom of the sample stage features two depressions (Figure 5.19) containing two copper leaf springs that are electrically isolated by 0.5 mm thick Macor spacers and 2-56 alumina screws, which serve as high voltage supply electrodes to mate and ensure good contact with the spring taps extending from electrodes of the custom button heater embedded in the sample holder, upon full engagement of the sample holder within the sample stage. Similar design has been made for the sample preparation stage within the UHV analysis chamber of the system, to allow utilization of the button heater for sample annealing. Electrical connection between the leaf springs on the sample stage and external electrical contacts can be fashioned, though not currently implemented, through the installation of an electrical feedthrough at the back of the pressure cell bottom section.

5.2.3 Sample Holder

The sample holder has proven to be a critical component that strongly influences the thermal behavior and mechanical stability of the system. Since the sample remains fixed in the sample holder at all times, the UHV-compatible and chemically resistant materials used to construct the sample holder must withstand temperature extremes from room temperature to 1000 °C. In addition, the thermal conductivity and geometry of the parts of the sample holder must be chosen to balance the demands of heating and counter-cooling (as in the case of annealing) so that the sample temperature can be varied effectively. The optimal design combines high thermal impedance to the room

temperature sample stage with high thermal conductance between the sample and the heating element. Low heat capacity, achieved by compact construction, allows quick temperature variations with minimum heat flow, while thermal shielding of the sample with highly insulating materials ensures a low base temperature for rest of the microscope.

In order to meet the extreme thermal requirement as well as the robust physical properties necessary for the mechanical stress during manipulation and mounting, the sample holder for the current system is designed to be constructed out of fused silica, due to the material's low thermal conductivity and expansion coefficient at high working temperature, as well as strong mechanical characteristics. A fused silica sample holder, which is designed to enclose most of the sample except the limited scanned area needed for the new STM motor, enables thermal shielding of the hot sample from the rest of the microscope setup that should be near ambient temperature during variable temperature studies. However, it should be noted that fused silica is a material both difficult and expensive to machine with, and thus for the initial ambient temperature testing of the STM system, stainless steel and aluminum are chosen as the materials of choice.

While the sample holder is thermally insulating, it remains imperative to keep the thermal load on the miniature button heater at a minimum by maintaining a compact design for the sample holder. In contrast to the separate necks in the two-level design of the sample holder for the high pressure STM system as outlined in Chapter 3, the size of the sample holder can be reduced dramatically if it can be designed to allow interaction of two separate manipulation means on the level simultaneously. This design proves to be

essential in the complementary design of the sample preparation stage, which remains to be a dual fork interaction (Subsection 5.4.3) during manipulation with the transfer arm, while the wobble stick (Subsection 5.4.4) has evolved from a simple fork to a grabber design that allows stronger interaction and security in all lateral directions. As a result, the sample holder has been designed to simultaneously interact with a four-finger sample preparation stage) and a three-finger (transfer arm fork) forks with a minimal need in thickness, while providing necessary recess for a wobble stick to grip onto firmly.

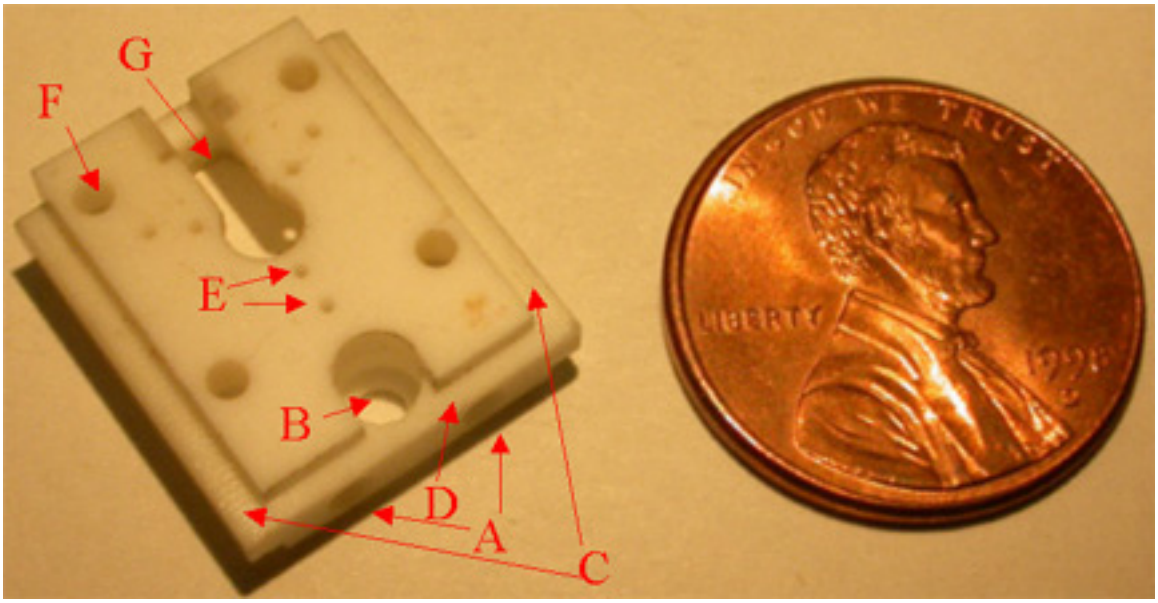

Figure 5.20. Top view of a mock Macor sample holder shows two alignment holes (**A**) for wobble stick manipulation and a clearance hole (**B**) for it to grip onto. The holder contains two "wings" (**C**) to slide into a four-finger fork, and a rear ledge (**D**) and a front cavity (not shown) for a simultaneous interaction with a three-finger fork. The top surface shows two circular sets of holes (**E**) for mounting sample from the back side with glass ball contacts by four 2-56 screws (**F**). A cutaway in the top surface (**G**) allows holder manipulation within the STM without significant tip retraction.

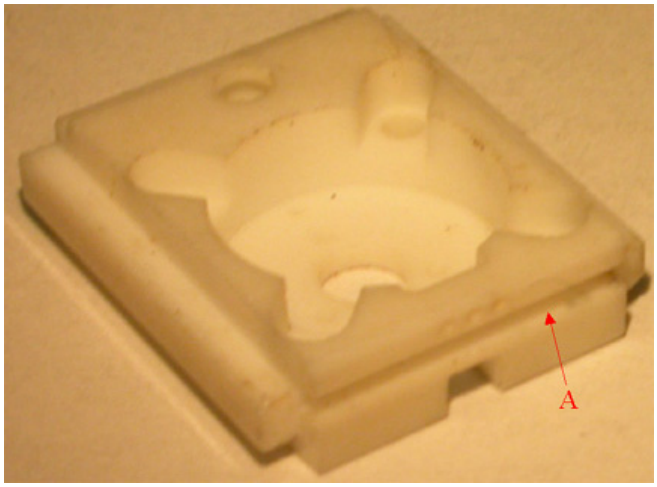

Figure 5.21. Front view of the mock sample holder reveals the square cavity for the three-finger fork manipulation.

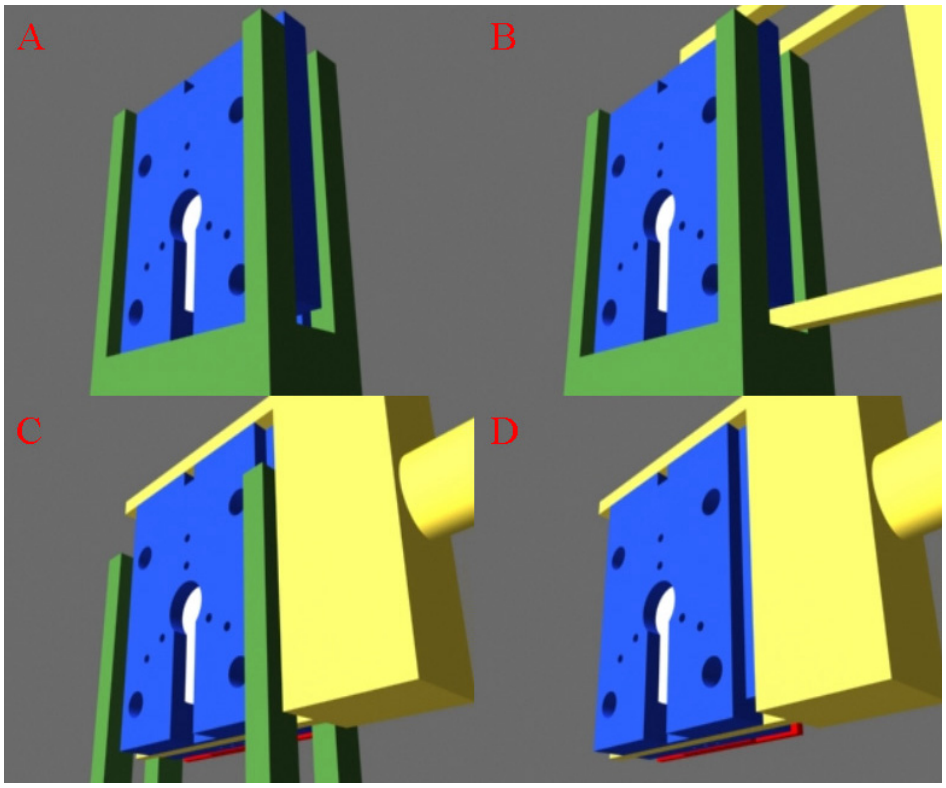

Figure 5.22. The four-finger fork on the sample preparation stage (green) engages the sample holder (blue) by the wings. The transfer arm three-finger fork (yellow) can engage the holder orthogonally. Subsequently, the transfer can be completed by lowering of the stage.

Referring to Figure 5.20, the sample holder contains two holes of 2 mm diameter at one end (which is designated as the back surface) with a vertically aligned clearance hole that is position nearby. This collection of cavities forms the motif, which reappears again in both the tip exchanger and the field emission plate, allows manipulation by a wobble stick through alignment with the two depressions at the back with pins while a maneuverable finger of the wobble stick engage or disengage with the vertical clearance hole. The back surface also contains 1 mm wide ledge that is formed from a 1 mm depression of the top surface and a 0.5 mm depression of the bottom, while the front surface contains a 1 mm square cavity (Figure 5.21). Together, they form the two necessary mating features for the engagement of a three-finger fork at the end of the magnetically coupled transfer arm. Referring to Figure 5.22, the two sides of the sample holder contain a pair of "wings" that are ledges of 1.5 mm wide and 2 mm thick, that can be interacted with and secured by the four-finger fork structure on the sample preparation stage, in a manner similar to that between the STM sample stage and the sample holder. The two different forks can interact with the sample holder at orthogonal axes at the same time, and disengage from each other when the sample holder is secured on one fork, by simply creating a necessary recess in the sample preparation stage for the transfer arm fork to enter when depositing or extracting the sample holder.

The top surface of the 4.5 mm thick sample holder is only 1 mm in thickness, as there is a central circular cavity within the sample holder to allow insertion of a sample and the button heater from the bottom. The front end of the sample holder top surface has a 2 mm wide cut-away, to minimize the tip retraction necessary in a spatially already

restricted design before manipulating the sample holder. The top surface contains two circular sets of 0.020" diameter clearance holes of two different radial lengths, for mounting a sample of various size (up to 10 mm in diameter) from the bottom side of the sample holder. Three glass balls of 1 mm diameter can be placed on one of the sets of clearance holes for the sample surface to be braced against in a kinematic three-point contact for mechanical stability and thermal isolation, while ensuring the sample surface is flat in relation to the scanning direction to minimize the slope compensation necessary during imaging. Subsequently, in the simpler case of a mock sample holder, the sample can be mounted down at the back side by four leaf springs extending from the four 2-56 tapped holes surrounding the central cavity.

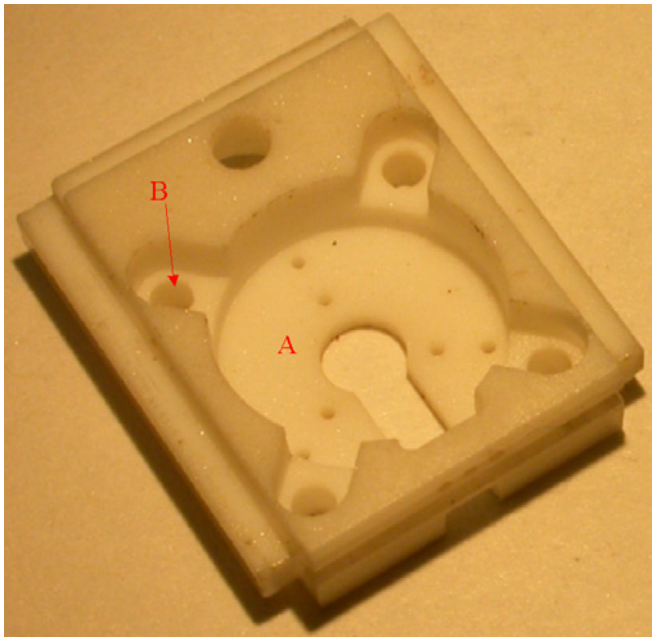

Figure 5.23. Bottom view of the mock sample holder reveals the central circular cavity (**A**) for placing the sample, as well as the dog-ear recessions for placing the button heater afterwards.

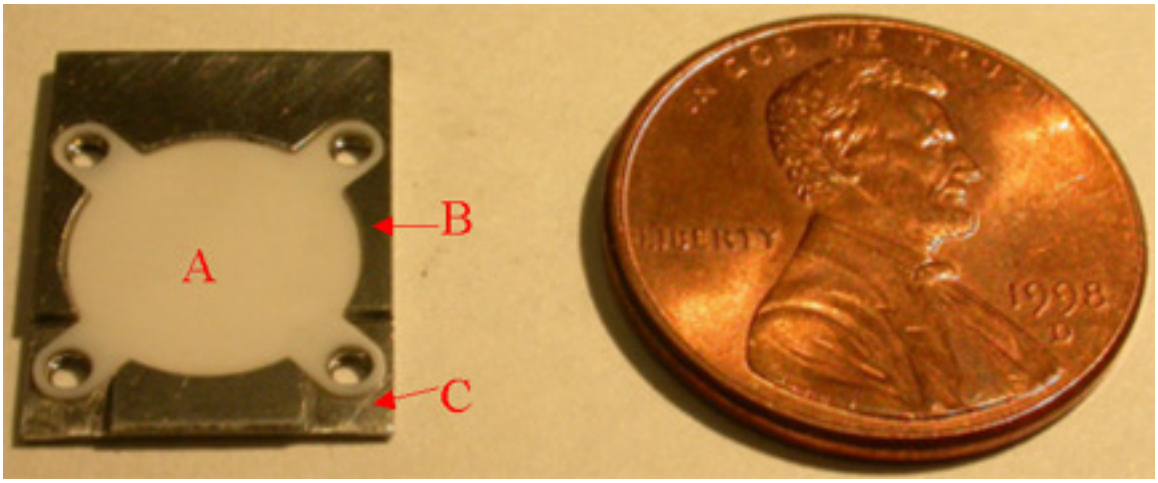

Figure 5.24. The Macor spacer (**A**) and the bottom press plate (**B**) for the button heater. The cutaways (**C**) in the front allow installation of spring electrodes to couple with the leaf springs on the STM sample stage.

In the case of the actual fused silica sample holder that is designed for use with the button heater, the back surface of the sample needs to be cut and polished in parallel to the front surface, in order to provide a smooth surface for mechanical contact of the button heater from the back. The mechanical and thermal contact between the sample and the heater is enhanced by plating the top surface of the button heater with gold. The button heater is circular and 2 mm thick in design with four dog-ear wings, two of which serve as electrodes for power supply to the heater. Similar dog-ear features have been made in the central cavity of the sample holder to allow the insertion of the sample heater. (Figure 5.23) The sample heater is placed in the holder in such a fashion that the two dog-ear electrodes will be pointing towards the front end of the sample holder. Upon insertion of the button heater, a 0.25 mm thick Macor spacer (for electrical insulation from the rest of the system) of the same shape as the heater and a stainless steel heater press plate with the necessary dog-ear depression for fitting are placed at the back of the

button heater. (Figure 5.24) The front end of the dog-ear depression on the press plate have been machined away, to allow the insertion of two spring taps to extend forward the electrical connections of the heater electrodes. The sample holder and the heater press plate are subsequently mounted together, sandwiching all components tightly in-between, by four 2-56 screws. The forwardly exposed spring taps as a result allow electrical contacts with the leaf spring system on the STM sample stage and the UHV sample preparation stage to supply power to the button heater.

Thermal measurement and bias voltage application of the sample are performed through a pair of type K thermocouple wires of 0.010" diameter that are spot-welded onto the side of the sample. The wires are subsequently routed out of the sample holder through the sue of the four 0.012" clearance holes situated at the front end of the sample holder, where each wire is channeled through an outer hole and wrapped around to enter the adjacent hole in a sideway manner. This horizontal arrangement of thermocouple wires is fashioned to be mechanically and electrically coupled with the vertical arrangement of wires on the sample stages in the STM (Subsection 5.2.2) and UHV (Subsection 5.4.3) compartments.

5.2.4 Tip Holder and Exchanger

The inclusion of an *in vacuo* tip exchange mechanism, as evidenced from Chapter 3, is vastly useful due to the high tip degradation rate during *in situ* high pressure studies, while it can also be a liability to mechanical stability if the removable tip holder is heavy, or not coupled strongly to the scan tube once installed. The task of designing a suitable

tip exchange mechanism for the new microscope is further complicated by the limited ability to manipulate the physically isolated STM setup. As a result, a extremely compact tip holder must be devised to both minimize the decrease in resonance frequency due to the added mass, as well as the size while maintaining a relative ease for *in vacuo* manipulation.

The tip exchange mechanism for the new microscope consists of three parts: a tube plate that is glued to the end of the scan tube to provide the necessary means to achieve a stable three-point contact with the tip holder, a removable tip holder that can be magnetically coupled to the tube plate, and a tip exchanger that serves as a carriage to shuttle the tip holder within the system as well as a means to decouple the tip holder from the tube plate during exchange.

Figure 5.25. The tube plate of the tip exchange mechanism contains a central hole for mounting of a samarium cobalt magnet to attract the iron tip holder, and three depressions for installing stainless steel ball contacts for stable coupling.

The tube plate is made out of aluminum due to its low density and thus light weight, and is affixed to the end of the scan tube with UHV-compatible epoxy with an alumina ring spacer in-between, to minimize leakage current detected at the tip as a result of the high voltage applied to the electrodes on the scanning piezoelectrics. The bare end of a Kapton-coated copper wire of 0.003" diameter is glued to the edge of the tube plate as the tunneling current wire using electrically conductive epoxy. The wire is anchored at the end surface of the sapphire slider to prevent dangling and consequently capacitance coupling with bias wires to the sample and and shear piezoelectric stacks nearby. Subsequently, the wire is routed out along the back of the STM body within an electrically shielded alumina tubing to the top of the body, similar to the wiring method of the thermocouple. Referring to Figure 5.25, the tube plate has a central clearance hole to house a samarium cobalt magnet of 1 mm diameter and 1.5 mm thick, that serves as a source of magnetic force necessary for coupling the tip holder. Samarium cobalt is chosen due to its extremely high magnetic properties (which allows for minimal size and mass given the required magnetic force), outstanding thermal stability, and excellent corrosion resistance, all of which are common characteristics of rare earth magnets. A radial arrangement of three circular depressions of 0.5 mm diameter and 0.25 mm deep permits the subsequently attachment of three stainless steel balls of 0.5 mm diameter, to provide the stable three-point contact and electrical connection with the tip holder.

The iron tip holder geometrically contains two discs connected by a short tube in-between. (Figure 5.26) The larger disc serves as the attachment side of the tip holder to the magnetic tube plate, and has a chamfered plateau in the middle to minimize the

distance and thus maximize the magnetic force exerted from the magnet, once the tip holder is attracted and attached to the tube plate by the three-point contact onto the outer area of the large disc. The lower disc, as its role will be described in detail later, serves as an anchor point for the tip exchanger to catch onto during removal of the tip holder from the scan tube. The tube connecting in-between is a gauge 22 needle that allows the insertion of a tip of diameter between 0.0130" and 0.0135".

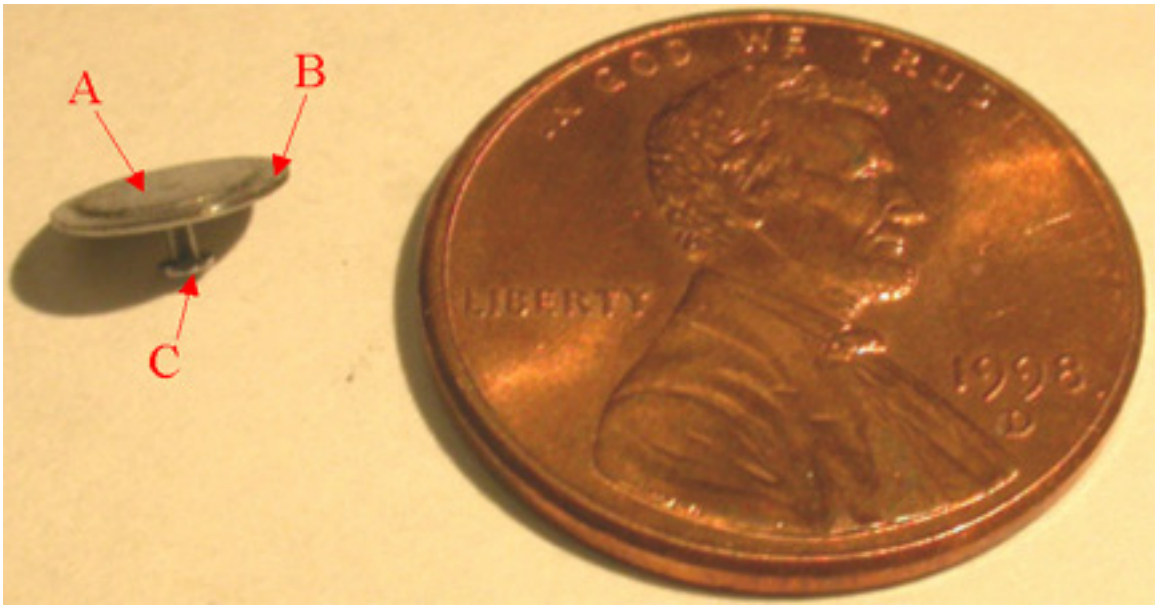

Figure 5.26. The top of the iron tip holder contains a plateau (**A**) to reduce the distance for the magnet in the tube plate to attract, while the outer ring (**B**) allows the three ball contacts to rest on. The small disk (**C**) at the bottom latches onto the tip exchanger during tip retraction during a tip removal manipulation.

The tip exchanger is very similar in design to the sample holder structurally, to allow analogous manipulation as well as insertion into the STM sample stage. There remains a central cavity on the bottom side of the tip exchanger and, while the top surface has a 0.4 mm deep depression to allow the seating of the tip holder, as well as a small requirement to elevate the holder before the tip exchanger can be safely and horizontally

extracted. At the same time, the front end has a similar cut away as in the sample holder to further reduce the tip retraction distance need before disengaging the tip exchanger. A spring-action lever, mounted by a 0-80 screw nearby, is used to secure the tip holder during transfer, and will disengaged upon insertion of the tip exchanger into the sample stage.

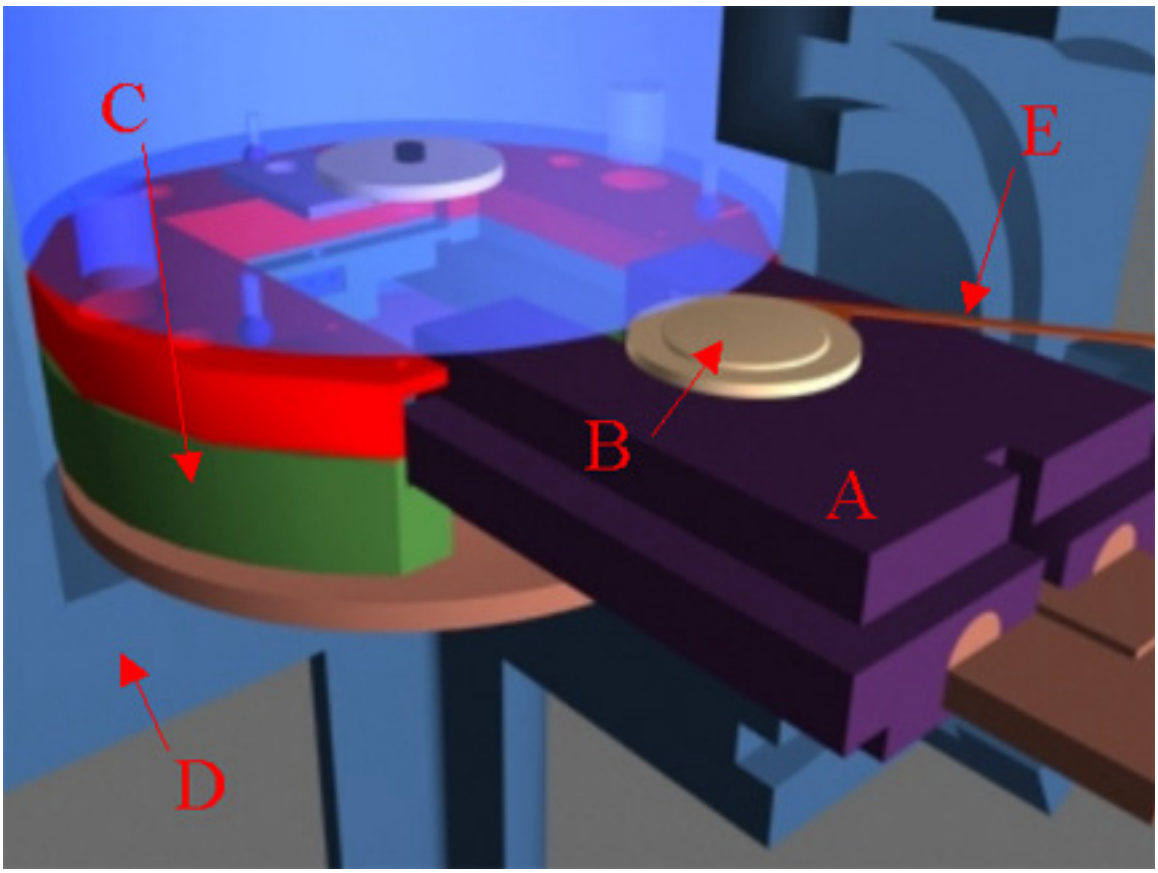

Figure 5.27. The tip exchanger (**A**) containing the tip holder (**B**) is deposited onto the sample stage (**C**) in the pressure cell (**D**). During entry, the spring lever (**E**) on the exchanger is disengaged from securing the tip holder, by the pressure cell access port due to the length of the lever.

Referring to Figure 5.27, in order to install a new tip onto the microscope, the tip exchanger containing the tip holder, secured by the spring lever, is inserted into the

sample stage of the STM setup. The spring lever, being longer than the pressure cell access port can allow, will disengage from securing the tip holder, as the tip exchanger is being inserted and the spring lever is pivoted around its 0-80 mount by the edge of the access port. Once the tip exchanger is deposited inside, the tip holder will be concentrically placed underneath the scan tube, and the tube plate can then be moved closer to the tip holder by the coarse approach mechanism of the microscope. (Figure 5.28) Eventually, the tube plate will be magnetically and electrically coupled to the tip holder on the three-point contact established by the stainless steel balls. Then, the scan tube can be retracted until the large disc is no longer in physical contact with the tip exchanger, which can be easily verified by the lack of electrical connection between the tunneling current wire and the sample temperature/bias wire(s). Afterwards, the tip exchanger can be safely removed with the tip holder remained secure on the scan tube.

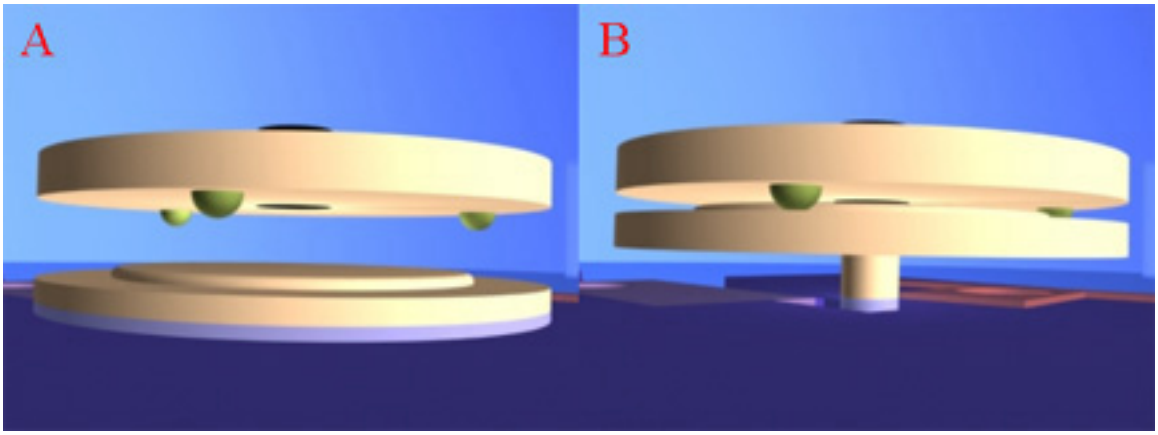

Figure 5.28. While the tip holder is resting on the tip exchanger, the tube plate can approach by the coarse approach mechanism of the STM. Eventually, the magnet (black) will attract and couple to the tip holder by the three-point contact (yellow). Retraction of the scanner lifts the tip holder from contacting the tip exchanger.

In the case of removing the tip holder for exchange, the scanner can be continually retracted, until the lower and smaller disc of the tip holder is caught by the tip exchange. Subsequently , the magnetic coupling between the tip holder and the tube plate will be broken, if the retraction of the scanner is continued. In this case, the tip holder drops back into the tip exchanger, which can then be removed from the sample stage, as the spring lever secures the tip holder once again upon exit.

5.3 Pressure Cell Design

5.3.1 Pressure Cell

The relation between surface structure at high pressure and temperature and the catalytic activity can be fully investigated, if structural observations by STM are combined with analysis of the reaction products in kinetic flow-reactor experiments. However, in order to reach a detectable product concentration from a catalytic reaction on a relatively small single crystal surface (in comparison to industrial high surface area supported catalysts), and avoid diffusion-limited mixing problems as demonstrated in previous with the existing high pressure and temperature STM system, the reactor volume needs to be sufficient small to allow correlation of structural changes and intermediate formation on the catalyst surface with reactivity that is on the time scale of seconds. Furthermore, reducing the reactor volume minimizes the resident time of reaction gas and thus impurities while maintaining a low flow rate to allow steady lamellar flow, as well as decreasing the amount of product adsorption onto reactor walls. For a typical surface consisting of 10^{15} atoms/cm^2 and a single crystal catalyst surface of

1 cm^2, 10^{13} molecules of product material are produced for a standard conversion rate of 10^{-2} molecules/site/s. For a detection limit of 1 ppm, the flow rate needs to be as low as on the order of 1 mL/s. At the same time, in order to achieve good time resolution of the gas composition analysis, the refresh rate of the reactor volume should be on the order of a few seconds. Thus, it becomes imperative to maintain the reactor volume on the order of few mL, which is significantly smaller than the size of a typical STM.

High pressure STM systems of reduce volume have been designed for atomically resolved imaging at up to atmospheric pressure. [7] However, although both batch [8] and flow [9] reactor STM systems for *in situ* studies at even higher pressure have been constructed, imaging quality for those systems is poor and lacks true atomic resolution in general for various reasons: mechanical coupling to external environment due to obligatory gas connection, flow-induced vibration (especially at the tip), and membrane separation of reactive gas from piezoelectric elements causing mechanical instability at the body or the tip. In order to address these issues with the current flow reactor STM system presented in this system, the pressure cell has been designed to be inclusive of the entire STM that is gold-plated for chemical resistivity to avoid the use of a soft separation membrane, while the flow direction of the reactive gases is along the length of the tip as well as the length of the cylindrical STM body to minimize any mechanical vibrations induced by flow turbulence as a result of jagged flow geometry. Lastly, soft polymer high performance liquid chromatography (HPLC) tubing with vibration damping by silicone sleeves and o-rings is used to direct high pressure reactive gases, and minimize mechanical excitation conducted along the length of gas inlet to the reactor cell, while the

STM body is mounted rigidly to the vibrationally damped pressure cell for mechanical stability under flow. In addition to all these precautions, the pressure cell is also designed to allow access to the STM for sample and tip exchange *in vacuo* when necessary.

Structurally, the pressure cell is constructed entirely out of stainless steel and subsequently plated of 1 μm thick gold for chemical passivation, and is divided mainly into three sections: a cell lid that contains both gas and electrical connections as well as a mounting mechanism that contributes to the necessary mechanical rigidity and precision during sample and tip transfer, a cell middle section that serves as a mounting platform for rigid coupling of the STM as well as an access panel to the interior of the STM for repairs, and a cell bottom section that contains both the second gas connection and the airtight access point for sample and tip introduction as well as electrical access point for the button sample heater if necessary.

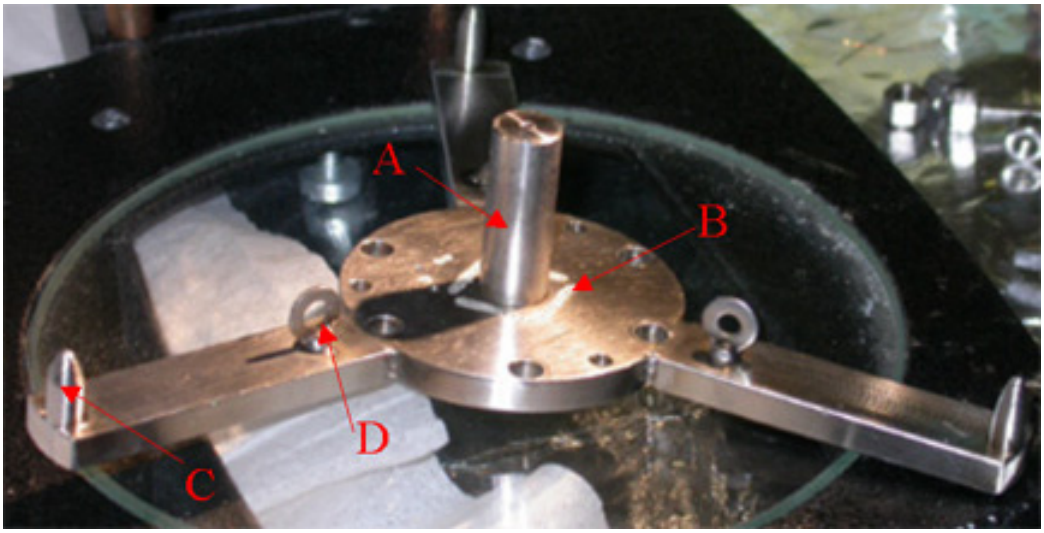

Figure 5.29. The cell lid contains a gas inlet (**A**) from introducing reactive gases, and small alumina-lined clearance holes (**B**) for wiring purposes. Three levers radially extend from the lid, each of which contain a chamfered pin (**C**) for mechanical mounting of the cell for manipulation, and a ring (**D**) as an attachment point for a vibrationally damping suspension spring.

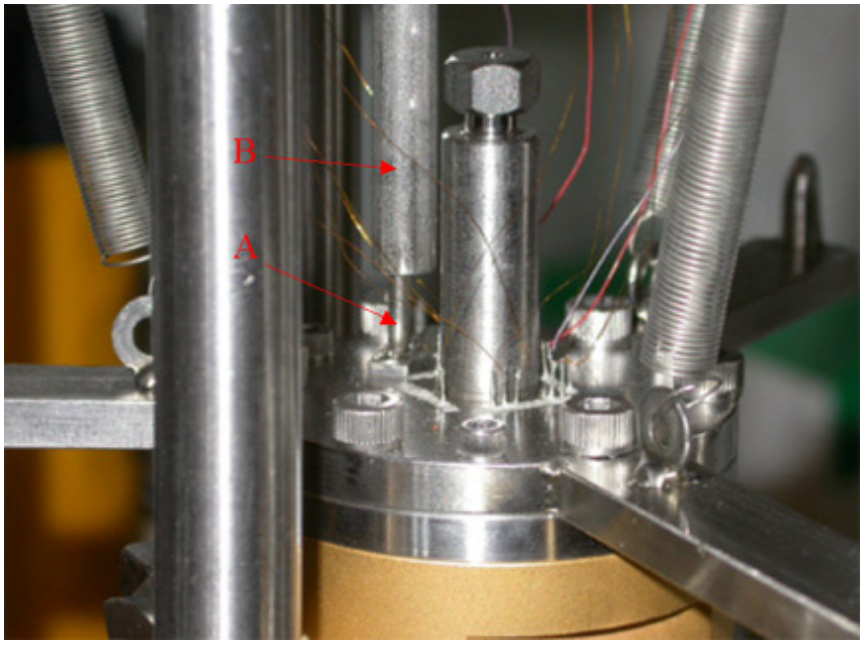

Figure 5.30. The removable external electrical shielding of the tunneling current wire (**A**) on the pressure cell has a small overlap with the shielding from the docking scaffold (**B**) for the pressure cell during imaging, to ensure continue shielding.

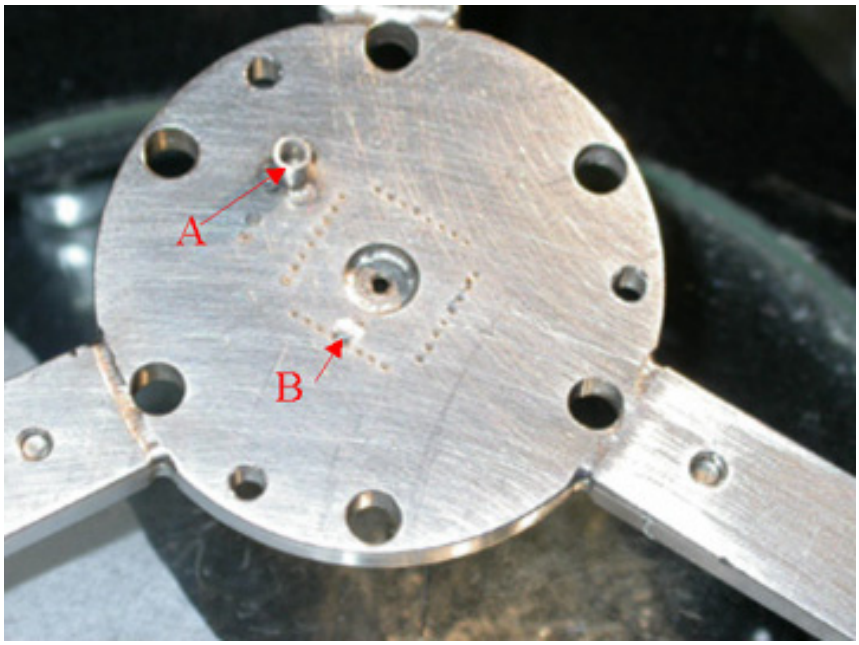

Figure 5.31. Bottom view of the pressure cell lid shows the internal shield for the tunneling wire (**A**) and the thermocouple for measuring the reaction gas mixture temperature (**B**).

Referring to Figure 5.29, the cell lid contains a concentrically placed 25mm long pipe of 0.375" outside diameter OD and 0.0625" ID for gas introduction. Surrounding the gas inlet, thirty two clearance holes of 0.032" diameter are machined into the lid in a square formation that is identical in dimension to the same set of clearance holes on the molybdenum STM body. These clearance holes are for electrical connections between the STM and the wiring external to the pressure cell. They are each lined with alumina tubing of 0.030" OD and 0.020" ID for electrical insulation. Afterwards, a 10 mm long platinum wire (or wire of appropriate material in case of thermocouple wiring) of 0.010" diameter is glued in place to each clearance hole with exposed wire on both sides of the opening to serve as soldering points for wiring connection, and the external side of the clearance hole is completely enclosed in UHV-compatible epoxy to provide a high pressure seal for the wiring. This wiring method for high pressure has been chosen over the conventional wiring connector due to both the limited space of the small pressure cell as well as the ease to improvise the current method with little machining. Since pressure is proportional to force applied and inversely so to area, it can be assumed that force applied to the each clearance hole opening under high pressure is small and not exceeding the bonding strength of the epoxy chosen. The internal side of each platinum wire secured thus is soldered to on one end of a Kapton-coated copper coil of 0.003" diameter, while the other end is subsequently connected to an exposed wiring on the STM body for electrical connection. For the tunneling current wire, special precaution in electrical shielding is made in form of a removable 0.0625" alumina-lined stainless steel tubing of 6 mm in length, which can be mounted and grounded to the pressure cell to enclose the external

side of the exposed tunneling current wire after connection, is made. (Figure 5.30) Similar design, though not removable, has also been made for the internal side of the tunneling current connection. (Figure 5.31) Lastly, the pressure cell lid contains three structurally robust levers radially and evenly extending from the plane of the lid, each of which contains a chamfered pin of 3 mm diameter at the end to be used in the mounting mechanism as outlined in Subsection 5.3.3, and a vertically placed ring for attachment of a suspension spring in physically supporting and vibrationally damped the pressure cell during imaging.

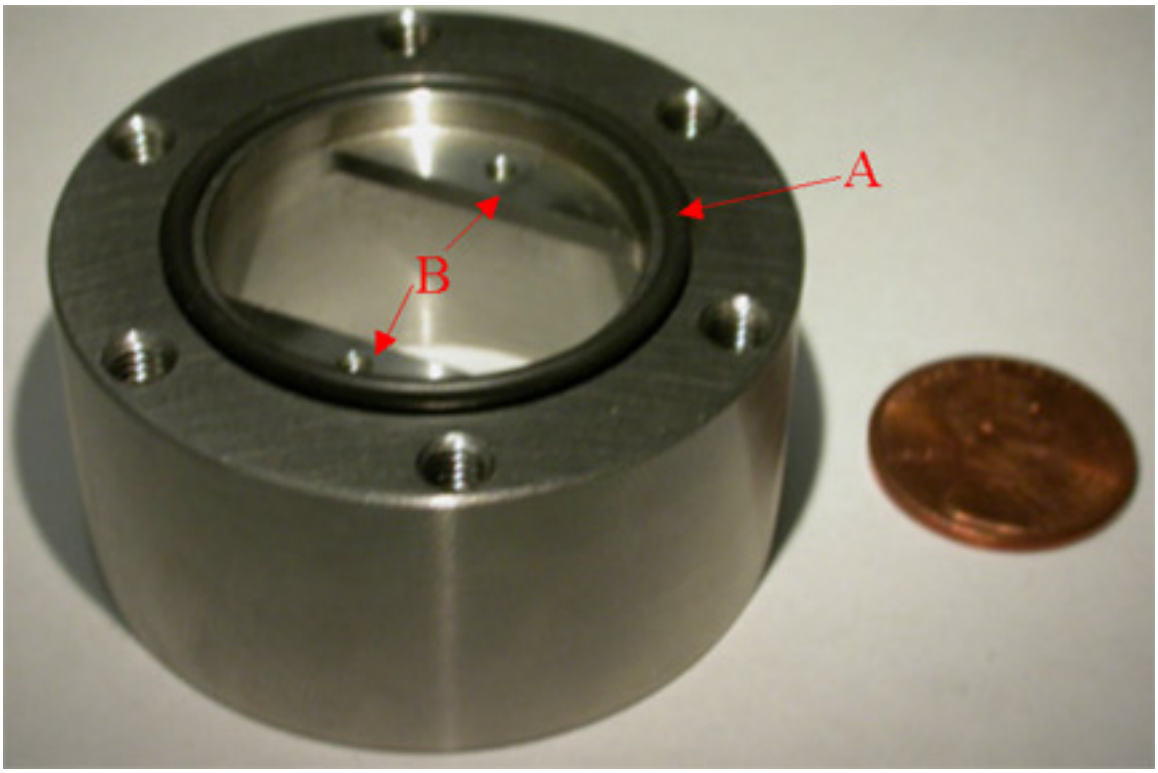

Figure 5.32. The middle section of the pressure cell contains o-ring seals (**A**) for coupling with the other two pressure cell sections, and two ledge-like leaflets (**B**) for mounting the microscope by two 2-56 screws.

The cell middle section contains the necessary depressions for effective 2-025 polymer o-ring seals needed in assembly of the pressure cell, as well as an internal ledge that allows mounting of the microscope through two of the 2-56 tap holes on top of the STM body. (Figure 5.32) The ledge consists of two 2 mm thick leaflets, each of which contains a single 2-56 clearance hole. The contact between the STM body and each leaflet is vibrationally damped by a 0.0625" thick Viton washer, while the 2-56 screw secures the connection as well as provides electrical connection between the pressure cell and STM bodies. The metal leaflets are designed to not interfere with exposed wires at the top of the STM body upon mounting of the microscope, and allow convenient access for soldering connection between the STM and the copper coils extending from the cell lid. To provide for easy access to the interiors of the microscope as well as for adjustment of the CuBe spring plate that is used to maintain good contacts between the shear piezoelectric stacks and the sapphire slider, the cell bottom section is subsequently divided into two sections, by cleaving the original part into two at the bottom plane of the leaflets. The lower part of the cell middle section can thus be conveniently removed to expose the entire STM body for repair and adjustment if the need arises.

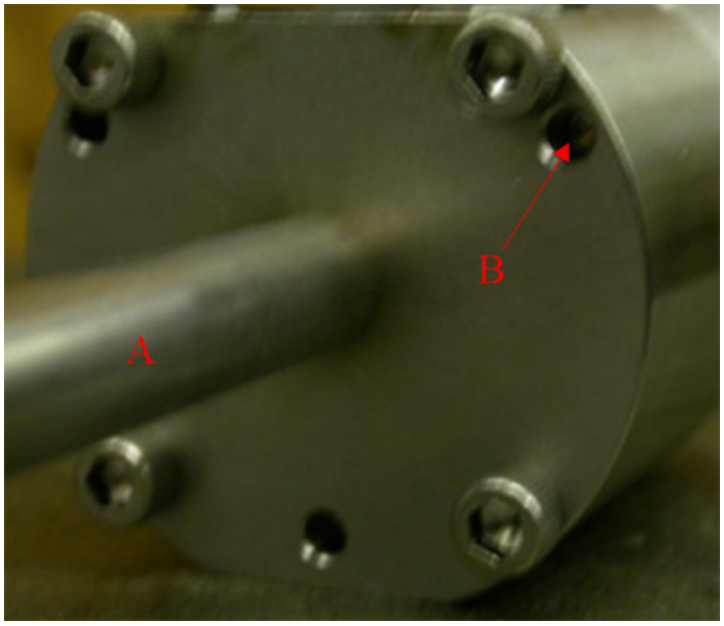

Figure 5.33. Bottom view of the bottom section of the pressure cell reveals a gas outlet (**A**) similar to that on the cell lid, and three holes (**B**) for coupling with the pins on the docking scaffold in a mounting mechanism necessary for manipulation.

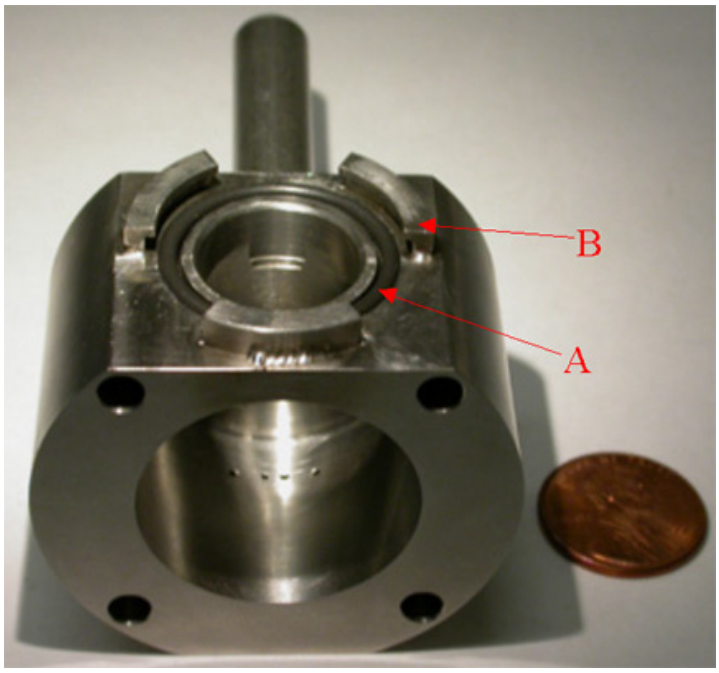

Figure 5.34. The bayonet-sealed access port is sealed by applying pressure on an o-ring (**A**) through placing the bayonet seal under the three "lips" (**B**) of the mechanism.

The cell bottom section contains a concentrically placed gas outlet that is identical to that is situated on the cell lid, three holes of 4 mm diameter at the bottom surface to secure with the three corresponding pins on the docking scaffold (Subsection 5.3.2) as a part of the mounting mechanism (Subsection 5.3.3) during sample and tip transfer (Figure 5.33), and a bayonet-sealed access for introduction of sample and tip (Figure 5.34). The bottom part of the pressure cell is connected to the rest of the body by only four 8-32 screws due to space limitation, and the hex caps of the screws serve as stable resting points for the pressure cell on the docking scaffold. However, the two screws on the side of the bayonet-sealed access have to be recessed into the body due to their interference with the pins-and-holes alignment of the pressure cell with the docking scaffold, and a single metal stud is placed directly under the access port as a replacement of the two resting points. Electrical access points, similar to the platinum wiring junctions on the pressure cell lid, can be established on the cell bottom section for the eventual wiring connection to the electrical leaf springs on the STM sample stage. A dynamic sealing mechanism is constructed on the cell bottom section to allow *in vacuo* access to the STM sample and tip, while still provides an adequate airtight seal under pressure upon manipulation. within the pressure cell While the use of a bayonet sealing mechanism has been used before in the design of a high pressure STM [10], the current bayonet seal must balance between providing adequate access to tip and sample manipulation for a pressure cell that is already miniature in size, and minimizing the size of the port to still provide an effortless *in vacuo* airtight seal in response to the increased demand in pressure requirement. By designing a small sample holder and tip exchanger, as well as a robust

guided mechanical manipulation, the bayonet-sealed access port has been designed to be 16 mm in diameter (which is 1 mm wider than the holders) for proven successful sample and tip transfer. The access port is surrounded by a depression specially designed for a 2-018 Kalrez o-ring seal, and subsequently surrounded by three radially arranged "lips" for securing the bayonet and applying mounting pressure on the polymer seal. Each lip extends 60° circularly in structure and is spaced 60° apart from each of its counterpart. The lip protrudes 5.25 mm from the flat front surface of the cell bottom section, and extends 1 mm radially inward with a 3 mm thick ledge to secure onto the bayonet seal.

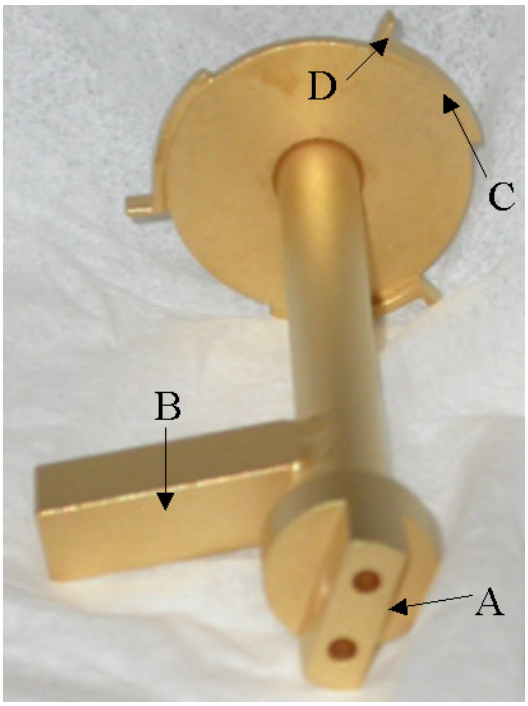

Figure 5.35. The bayonet seal contains the same manipulation motif (**A**) as the sample holder to allow interaction with a wobble stick. By applying pressure on the torque handle (**B**) when in the access port, seal is achieved by increasing pressure on the ramps (**C**) and consequently on the o-ring seal, until the mechanical stop (**D**) is reached.

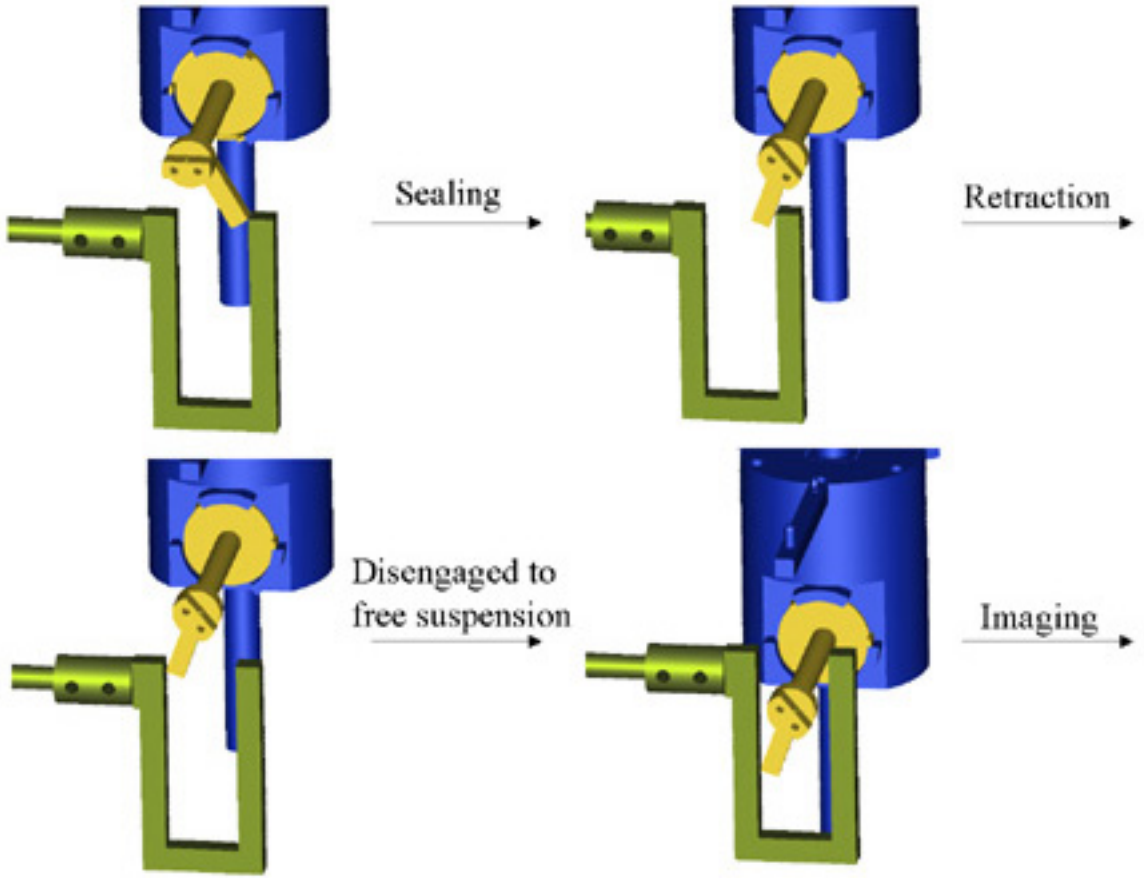

Figure 5.36. The U-shaped motif on the linear manipulator engages the torque handle when the pressure cell is secured. Once the access port is sealed, the linear manipulator retrace its steps so that it no longer is in contact with the bayonet seal. The pressure cell is then released and suspended on springs for imaging.

The bayonet seal is designed similarly in size to be fitted on top of the access port, and contains a vertically extended rod that is concentrically placed and has a mechanical manipulation motif that is similar for manipulation the sample holder or the tip exchanger, to provide access to the wobble stick as described in Subsection 5.4.4. Referring to Figure 5.35, the seal contains three ramps near the edge, each of which extends 60° circularly in structure and spacing. Each ramp extends over 1 mm in height over a 50° arc, and contains an elevated plateau at the end that extends over a 10° arc to

provide for a mechanical stop during sealing. In order to seal the access port, the pressure cell is rigidly secured as described in Subsection 5.3.3, and a wobble stick is used to insert the bayonet seal with the ramps 60° out of phase from the ledges surrounding the access port, and subsequently engage the bayonet by rotating clockwise the first 20°. The vertically extended rod on the bayonet contains a torque handle that extends downward 20° counter-clockwise from normal, which can be engaged by a linear manipulator to provide additional torque necessary in completing the pressure seal. The linear manipulator contains a U-shaped motif, where the cavity provides space for the insertion of the torque handle and subsequent contact-free lowering of the handle during imaging and suspension of the pressure cell. In addition, the two vertical bars of U-shaped motif provide the necessary torque to engage and disengage the bayonet seal, as the linear manipulator is translated horizontally. Upon the initial 20° engagement of the bayonet, the wobble stick can be removed while the seal remained secure to the ledges of the access port. Referring to Figure 5.36, the linear manipulator can then be translated horizontally to engage the torque handle with the U-shaped motif, and steadily apply increasing pressure onto the o-ring seal by engaging the bayonet ramps under the access port ledges, until the mechanical stops on the seal are reached. Then the linear manipulator is translated in the reverse direction to mechanically decouple from the bayonet.

All pressure cell parts can be assembled together, with the STM mounted inside, by 8-32 screws and 4-40 screws with Kalrez o-rings providing the necessary chemically resistant pressure seals (Figure 5.37). The body of the pressure cell is suspended and

electrically grounded on three precision springs hanging during imaging from a rotationally adjustable ring on an 8”-to-6” reduction nipple (Figure 5.38), at where a XYZΘ manipulator is situated, as described in the next subsection. The pressure cell has been leak tested in atmosphere up to 55 atm of internal pressure, and rated for 30 atm of continual use for safety and prevention of possible rupture due to thermal runaways during high pressure and temperature studies.

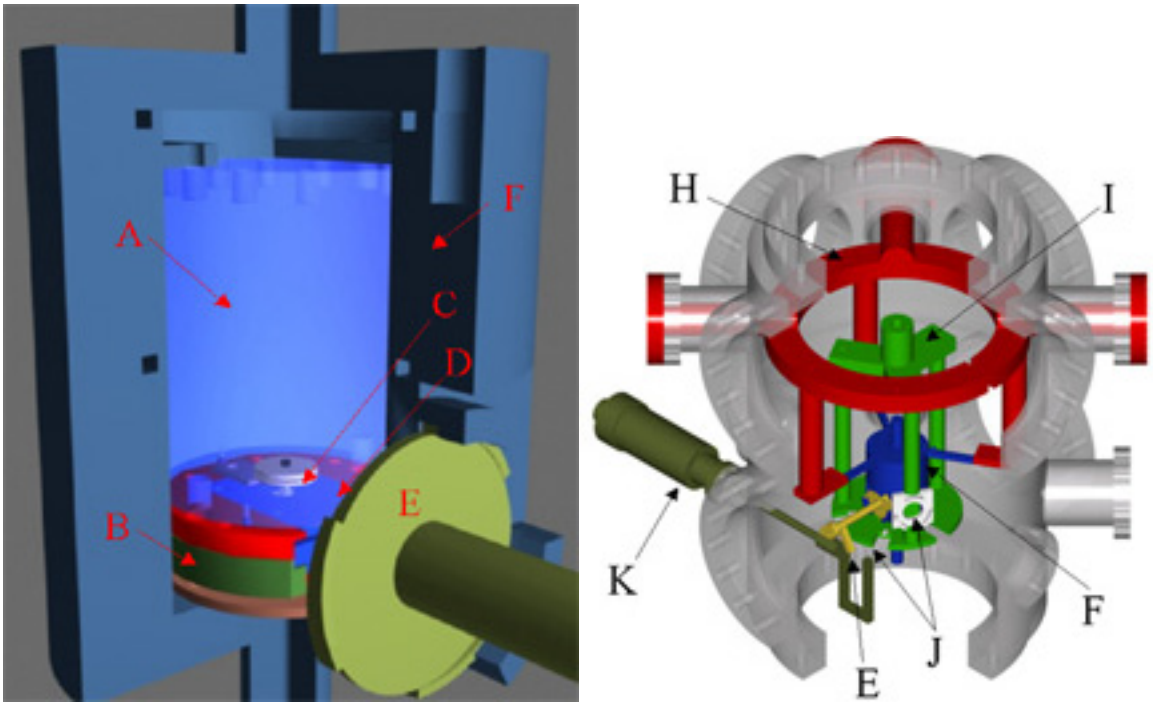

Figure 5.37. The fully assembled STM (**A**, Subsection 5.2.1) setup with the sample stage (**B**, Subsection 5.2.2), which contains removable tip (**C**, Subsection 5.2.4) and sample (**D**, Subsection 5.2.3) holders that are accessible through a bayonet-sealed (**E**, Subsection 5.3.1) opening in the cell, can be secured to the pressure cell (**F**, Subsection 5.3.1) by two 2-56 screws. The pressure cell can be secured by a mounting framework (**G**, Subsection 5.3.3) and a docking scaffold (**H**, Subsection 5.3.2) during manipulation within the STM compartment, the latter of which contains storage stations (**I**, Subsection 5.3.2) for tip, sample, and bayonet seal. The bayonet seal can be locked into the cell through torque applied by a linear manipulator (**J**, Subsection 5.3.2).

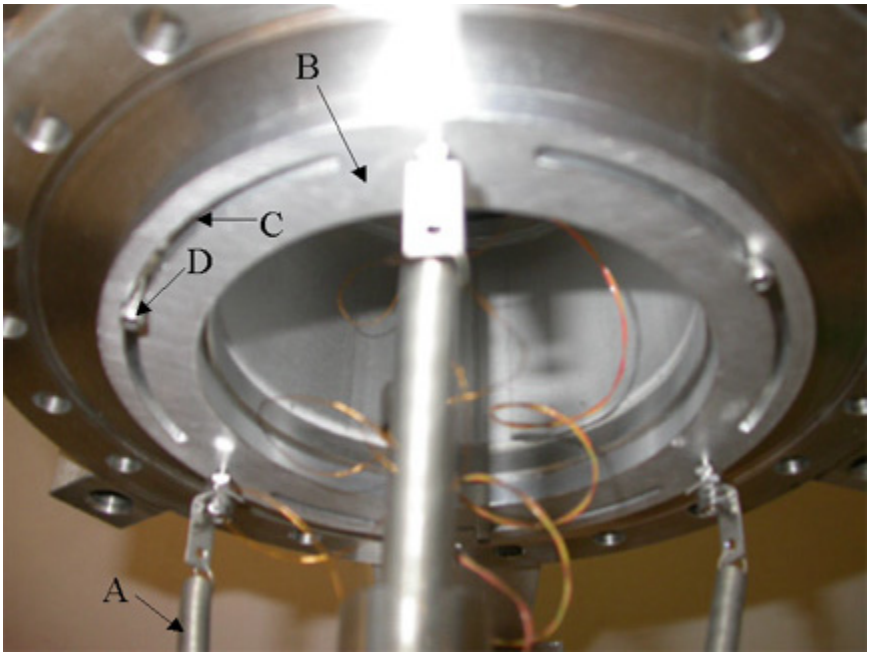

Figure 5.38. Suspension springs (**A**) from the pressure cell are hanged on a rotatable anchor (**B**) that can be adjusted by rotating along the tracks (**C**) and securing down using three 4-40 screws (**D**).

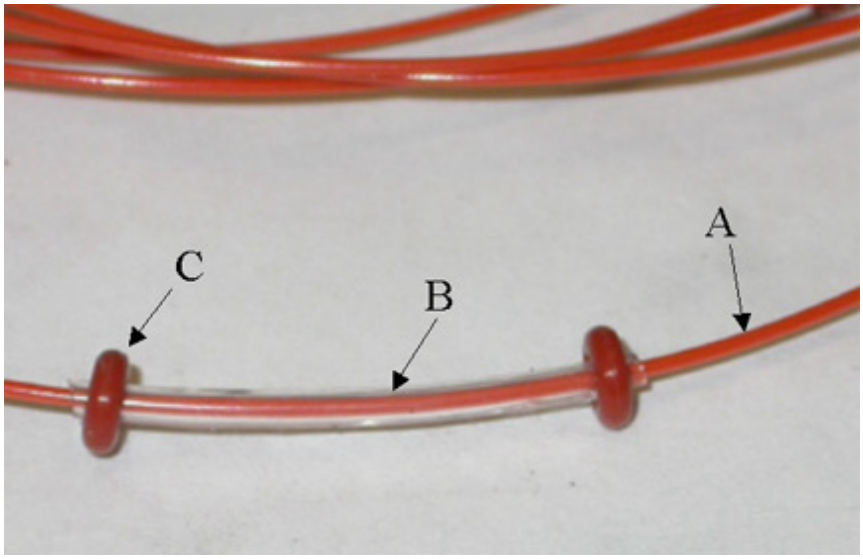

Figure 5.39. The PEEK gas tubing (**A**) is vibrationally damped by silicone sleeves (**B**) that are secured by silicone o-rings (**C**) at the ends of each segment.

The gas volume within the pressure cell is calculated to be 11.7 mL, excluding the volume of the STM setup contained within. The gas flow to pressure cell is introduced through two coils of 1/32" polyaryletherketone (PEEK) tubing of 0.015" thick wall, connecting between a 1.375" gas introduction flange on the manipulator and the two gas connections on the pressure cell through HPLC flangeless fittings. The flow direction of the reactive gases is from the cell lid to the cell bottom section, in order to carry any heated gas around the sample away from the piezoelectric transducers and out of the pressure cell. PEEK is a chemically resistant polymer that has high wear resistivity against wear under high pressure and velocity conditions, and is considerably more elastic to regular stainless steel tubing of same diameter and wall thickness. The coils of PEEK tubing are tailored to avoid mechanical contacts with surroundings to minimize vibrations conducted through, and to minimize the spring constants of the coils to ensure the pressure cell is supported entirely by suspension springs during imaging. As seen in Figure 5.39, sections of each coil are enfolded in silicone sleeves that are secured by silicone o-rings, in order to provide damping for the mechanical vibrations conducted along the length of the coils while minimizing the amount of additional weight incurred on the spring coils by the damping system.

External gas introduction to the system contains a gas manifold for mixing reactive gases and pressure regulation, which is connected to the 1.375" flange on the manipulator as mentioned above by PEEK tubing to minimize vibrations conducted to the system. This recirculation loop also contains a cold finger region for active cooling, a sampling valve for analysis by mass spectrometry or gas chromatography, and an

evacuation outlet that is connected to turbo molecular and mechanical pumps. (Figure 5.40)

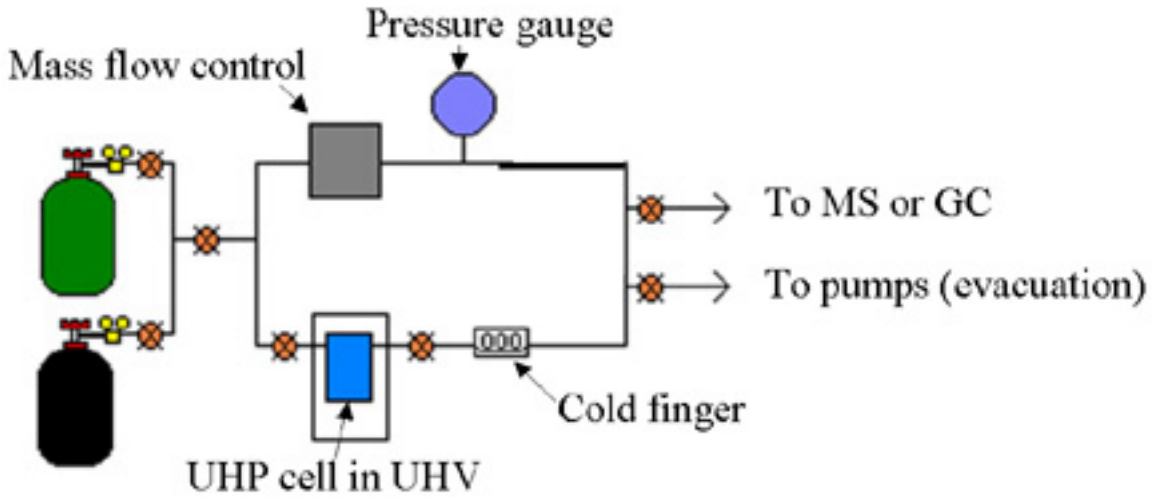

Figure 5.40. Schematic of external reaction gas loop.

5.3.2 Docking Scaffold

The purpose of the docking scaffold is threefold: to provide a mechanically rigid and stable resting point of the pressure cell when not imaging, to provide various docking stations for removable components such as holders and bayonet seal when not in use, and to provide wiring transition for the pressure cell so that the microscope can be safely removed from the rest of the system in a modular fashion in case of modification and repair.

The design of the docking scaffold is conceptually simple. Structurally, it is a tripod affixed at the bottom by a metal disk. Referring to Figure 5.41, the bottom disk contains three chamfered pins of 4 mm diameter and 5 mm in length, to be mated with the three alignment holes at the bottom surface of the pressure cell when the STM is not

imaging and the cell is not suspended, as mentioned in the previous subsection. A rectangular clearance is machined into the bottom plate to allow the penetration of the bottom gas connection as the pressure cell is resting on the plate, as well as to permit a reduced distance in the routing of bottom gas outlet to the proper manipulator flange.

Figure 5.41. The docking scaffold (before incorporation of storage stations) contains three chamfered pins (**A**) to be mated with the corresponding holes under the pressure cell. A rectangular notch (**B**) allows routing of gas from the lower connection of the pressure cell. The scaffold can be mounted onto a XYZΘ manipulator by two 4-40 set screws (**C**).

In addition, three docking stations, spaced 45° apart from each other, are fashioned into the metal disk for storage of the sample holder, the tip exchanger, and the field emission stage (which can be inserted into the STM stage as a sample holder to provide a potentially biased sacrificial plate for tip conditioning at both field emission

and tunneling ranges), where each docking station contains the same receiving motif as the STM sample stage and each holder is secured by a single leaf spring. (Figure 5.42) For the tip exchanger storage, a Teflon bottom plate is mounted at the bottom, with a centrally mounted 4-40 stainless steel screw that extends 3 mm from the top surface of the Teflon plate. Upon insertion of the tip exchanger, the tip contained therein can be conditioned by field emission through application of a high voltage onto the 4-40 screw. Lastly, the receptacle for the bayonet seal (which has the same motif as the pressure cell access port save the polymer o-ring seal), due to the increased size and length of the bayonet, is secured by a 8-32 screw in a radially more inward position on the bottom metal plate. (Figure 5.43)

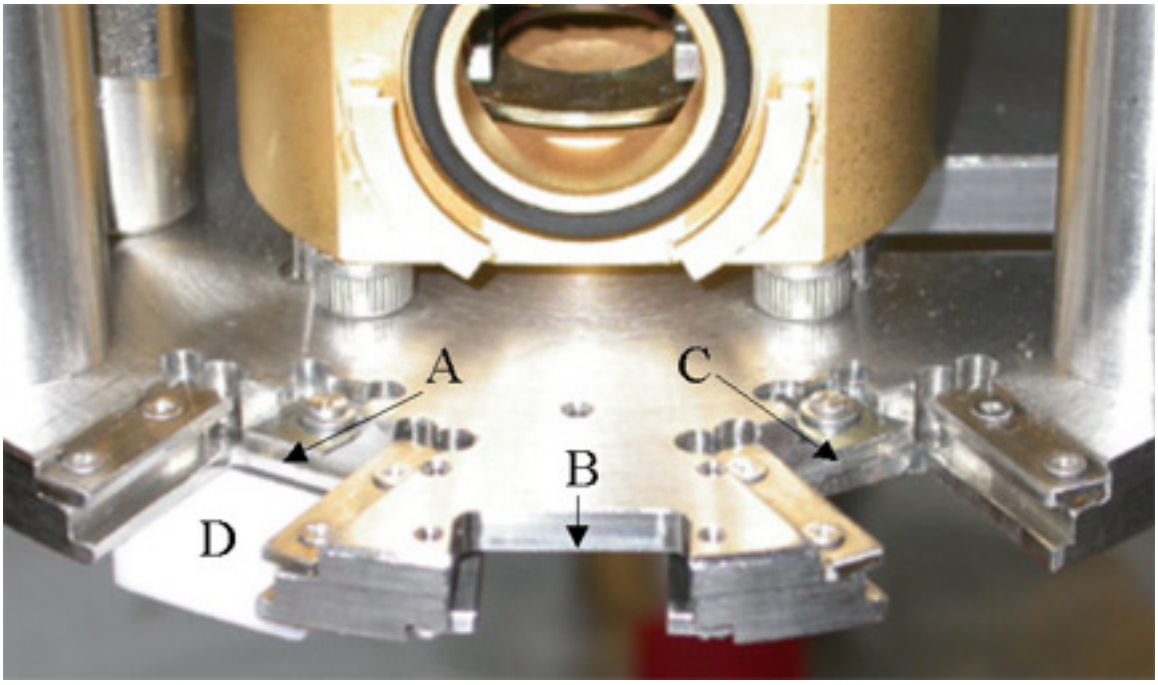

Figure 5.42. Storage stations of the docking scaffold for housing tip exchanger (**A**), field emission plate (**B**), and sample holder (**C**). A 4-40 screw linked to a high voltage supply can be placed into the Teflon bottom plate (**D**) for field emission of a tip when in storage.

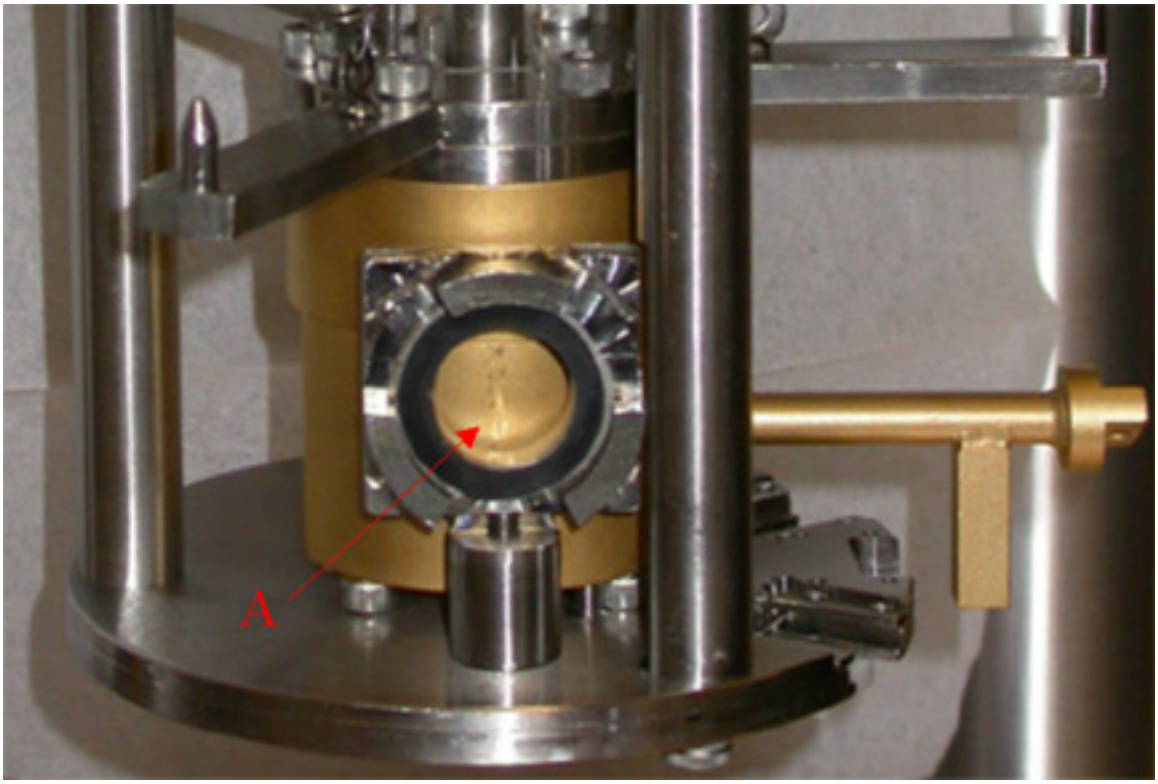

Figure 5.43. Docking station (**A**) for the bayonet seal of the pressure cell.

The tripod section of the scaffold is mounted rigidly through three 8-32 screws onto the structurally robust legs of 0.5" diameter. The tripod design is especially necessary for the top section of the scaffold, in order to avoid interference with the levers extending from the pressure cell lid and consequently with the suspension springs extending thereof, by having the tripod 60° out of phase from the pressure cell levers and suspension springs. The docking scaffold can be mounted at the top to the rod of a custom XYZΘ manipulator stage by the use of two 4-40 set screws, so that the position of the scaffold can be adjusted to provide wobble stick access to different docking stations, to secure pressure cell for manipulation, and to release pressure cell to be suspended on springs during imaging. The manipulator stage is designed to have 14" in

vertical travel for maneuvering the scaffold and the pressure cell over the entire length of the STM chamber, and interfaces on a 6” conflat flange, and is mounted to an 8”-to-6” reduction nipple fitting in order to place on top of the chamber. The 8” flange of the reduction fitting has three radially extended levers for securing on a tripod and subsequent extraction by a pulley, should the manipulator containing the scaffold and the pressure cell needs to be removed from the STM system for modification or repair. (Figure 5.44)

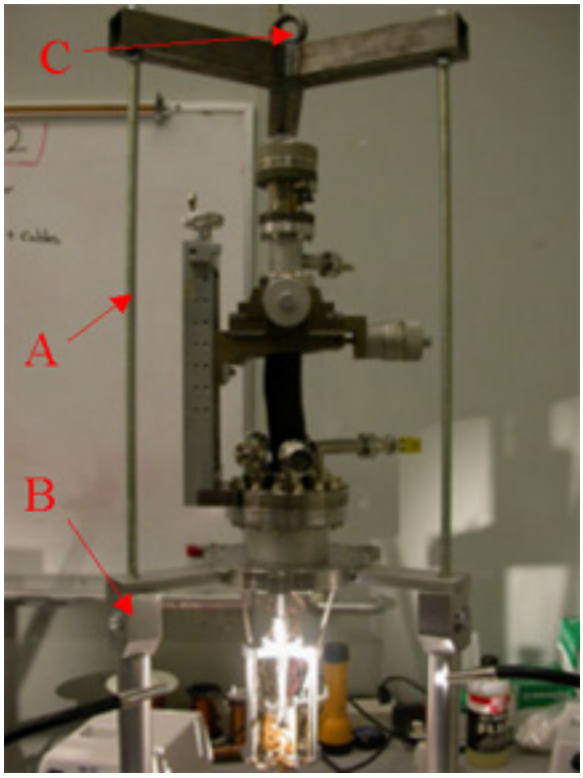

Figure 5.44. The STM manipulator flange can be mounted on to a tripod carrier (**A**) through three spacer blacks (**B**) that allow simultaneous engagement of the carrier and the inverted tripod stage. The STM setup can be lifted from the stage by a pulley attached at the centrally aligned ring (**C**).

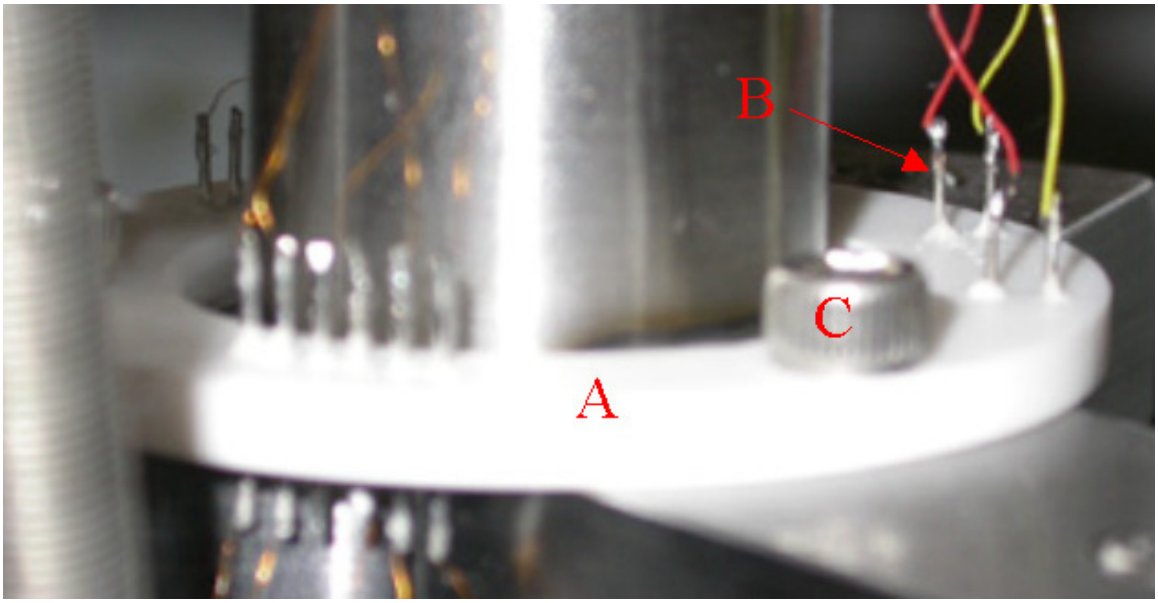

Figure 5.45. The Macor wire connector (**A**) with the platinum wiring junctions (**B**) can be mounted onto the docking scaffold by three 4-40 screws (**C**).

The top of the docking scaffold features a Macor wiring connector that is built and functions similarly to the pressure cell lid using wires of a more robust 0.015" diameter, due to anticipation of more frequent wiring at this junction. (Figure 5.45) Wiring connections between the pressure cell and the Macor connector are made using Kapton-coated or Teflon-coated wires of 0.003" diameter for maximal flexibility and minimal vibration conduction. Wiring connections between the instrumental and thermocouple feedthroughs and the Macor connector are made with the same types of wires, but they are twisted and bundled together to increase strength of the wires by functional category: shear piezoelectrics, scanning piezoelectrics, sample temperature/bias, and gas temperature. The twisted wire bundles are each coiled into a spring of 1" diameter before making wiring connection on either ends, so that the wire

bundles will coil and be undone over a predictability small area in lateral direction during the long vertical travel of the scaffold. (Figure 5.38)

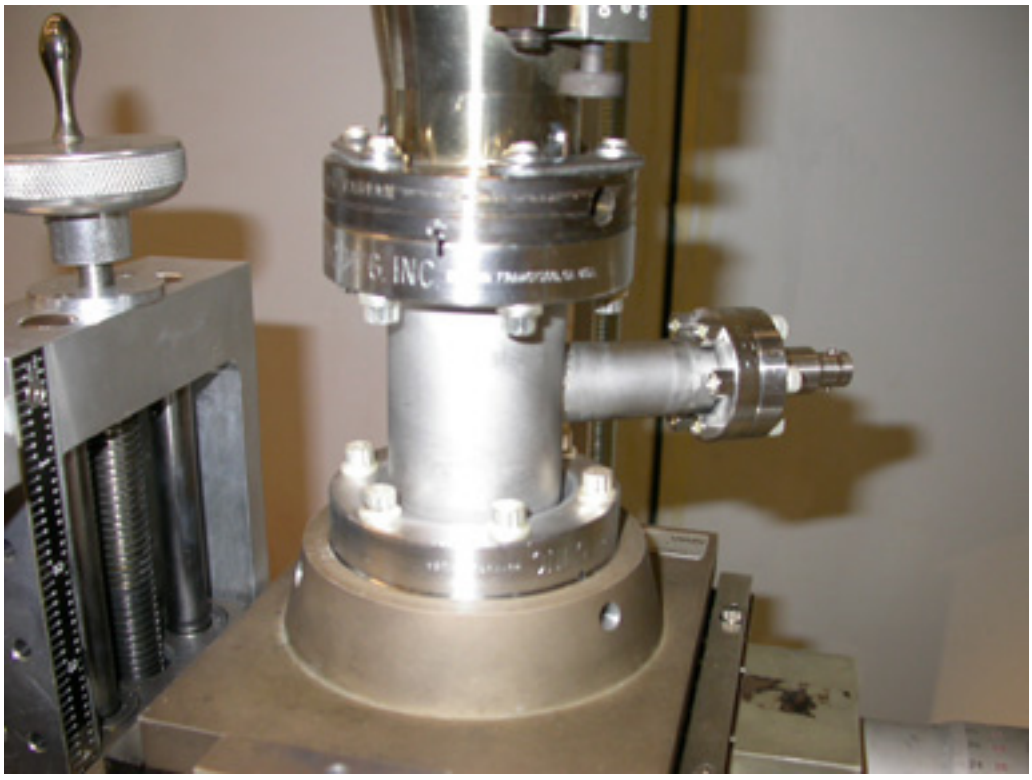

Figure 5.46. Electrical feedthrough for tunneling current signal is located away from the rest of the electrical feedthroughs for shielding of the output.

Similar to the case for the pressure cell, the tunneling current wire must be electrically shielded properly along the docking scaffold as well as along the manipulator. A 3/16” stainless steel tubing is welded vertically into the docking scaffold, so that the end is 10 mm above the surface of pressure cell lid and concentrically positioned to the removable 0.0625” shielding tubing mounted on the cell. This design allows a small overlap in shielding without mechanical contact between that on the pressure cell and that on the docking scaffold, upon the lowering of the scaffold to enable a mechanical

decoupling of the pressure for imaging. (Figure 5.30) The 3/16" shielding tubing extends along and beyond the length of the scaffold, and ends in another shielding overlap with a 3/32" shielding tubing welded to the side of the XYZΘ manipulator rod, which itself ends near the top of the manipulator at a reduction tee fitting, well removed in distance from all other electrical feedthroughs on the manipulator, to allow tunneling current output via an electrical feedthrough on a 1.375" conflat flange. (Figure 5.46) The tunneling current wire connection between the feedthrough and the pressure cell is made with a coiled 0.003" Kapton-coated copper wire, to maximize flexibility necessary for the large manipulator travel range and to minimize the vibrations conducted through the wire.

5.3.3 Mounting Framework

A vibrationally well-insulated STM with a highly rigid sample mounting scheme requires the microscope itself to be freely suspended and vibrationally damped during imaging, but also secured rigidly during manipulation of the sample. Due to the miniature size of the sample holder and the tip exchanger and small entry into the pressure cell, as well as the large lateral force required to provide enough torque for sealing the bayonet access port, the pressure cell must be firmly fixed in a highly reproducible position in order for successful transfer to occur. The description of the pressure cell mounting scheme is outlined in this subsection, while the details of the transfer process as a result of the design will be discussed later in Subsection 5.4.4.

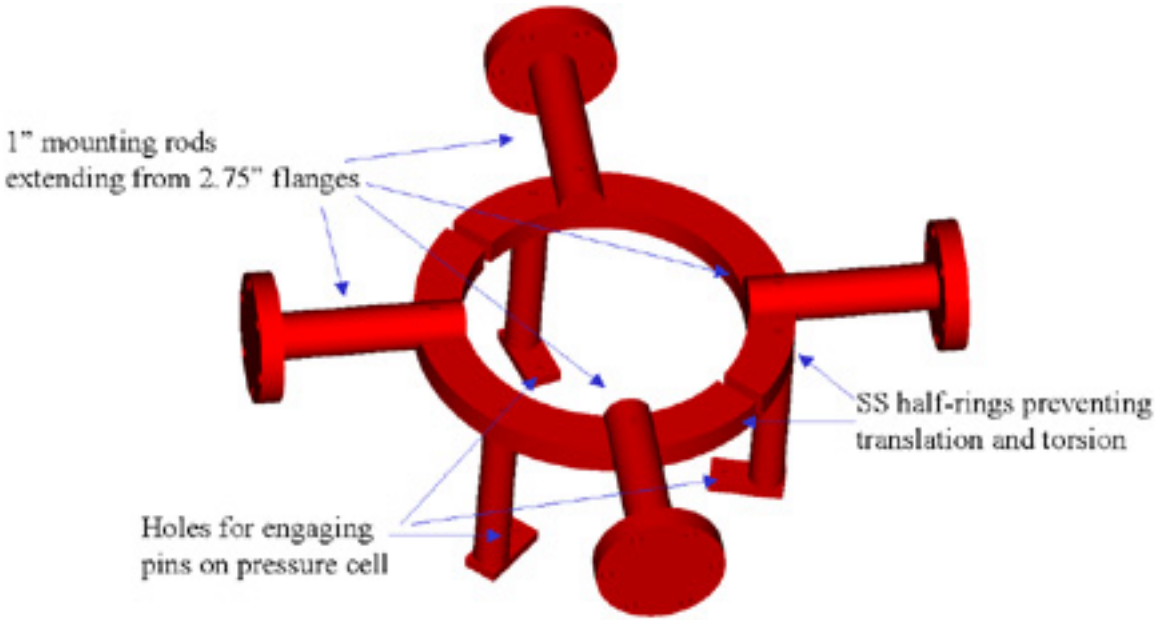

Figure 5.47. Schematic of the mounting framework for securing the pressure cell.

In order to maintain the pressure cell in a precise and repeatable position that has the access port of the reactor concentrically aligned to the 6" conflat flange that serves as the wobble stick entry, the overall mounting framework must be robust in structure that is also highly resistant against any sort of considerable translational and rotational stress that may come with sample and tip exchange as well as reactor cell sealing and opening. Referring to Figure 5.47, the mounting framework designed for the current system makes use of four radially arranged 2.75" flanges on the STM chamber to provide rigid support through stainless steel rods of 1" diameter extending from the flanges. The framework itself includes two semicircular structures of 0.625" thick and 1" in radial depth, each of which is mounted to two of the stainless steel rods extending from 2.75" flanges by 8-32 screws. Three pillars of 0.75" diameter are welded onto the bottom surfaces of the semicircular structures, at the end of each of which has a 0.25" thick rectangular plate,

extending radially inward, with a clearance hole of 3 mm diameter to mate with each of the chamfered pins on the pressure cell levers, as described in Subsection 5.3.1, in a pins-and-holes alignment system, similar to that designed for the alignment of the pressure cell bottom section with the docking scaffold in the previous subsection. The pillar structures are constructed in a way so that only the rectangular plates at the end can interact with the pressure cell levers. The robust dimensions of the entire mounting framework thus described are to ensure absolute resistance against all translational and torsional strain that comes with preparation of the reactor STM for high pressure and temperature *in situ* imaging.

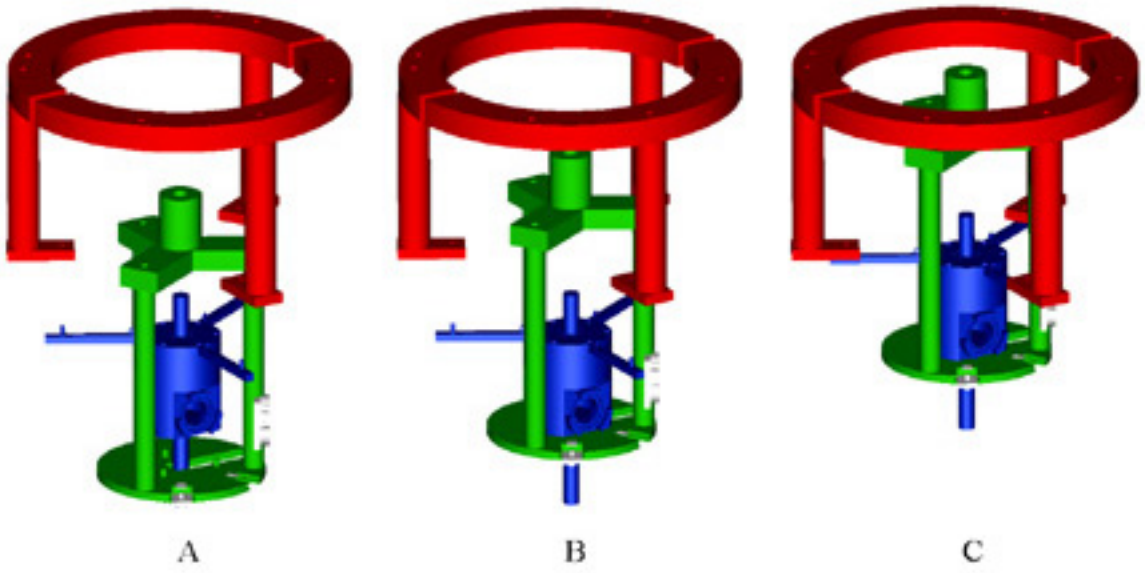

Figure 5.48. In order to secure the pressure cell from its suspension state (**A**), the docking scaffold is raised to first engaged the pins-and-holes system at the bottom of the pressure cell (**B**) and subsequently at the top (**C**).

Referring to Figure 5.48, assuming the pressure cell is in the free suspension position, in order to bring the pressure in a rigid mounting position for transfer or

bayonet-sealing, the docking scaffold can be raised by using the manipulator to engage the pins on the scaffold bottom plate with the holes aligned at the bottom of the pressure cell. Once engaged, the scaffold can be raised and adjusted along with the pressure cell, and bring the pins at the end of the levers extending from the pressure cell lids in alignment and to couple with the corresponding holes on the pillar structures of the mounting framework. Once coupled with the mounting framework, the scaffold can be continually raised, until the pins-and-holes systems at both the top and bottom of the pressure cell are fully engaged, and the pressure cell cannot be raised further. The overall mounting scheme has been constructed to assure that once the fully engaged state of mounted transfer position is reached, the pressure cell access port is concentrically aligned with the wobble stick access flange for manipulation, and the bayonet seal is ready for sealing by the linear manipulator once inserted. The robust dimensions of all parts involved in the mounting mechanism make certain that repeated use and occasional over-engaging of the pressure cell will not seriously compromise the structural integrity and precision of the procedure.

For access to the docking stations located at the bottom plate of the scaffold, as well as for elevating the pressure cell out of the path of the magnetically coupled transfer arm, the docking scaffold with the reactor STM can be lower to disengage from the mounting framework, and subsequently rotated 30° in either direction to maneuver the pressure cell levers away from the framework pillars while preventing the suspension springs from overextending from equilibrium positions. Then, the docking scaffold can be raised above the mounting plates on the framework pillars, and either be rotated to

allow access to different docking stations or continue to be elevated to allow transfer between system compartments.

5.4 System design

5.4.1 Overall Schematic

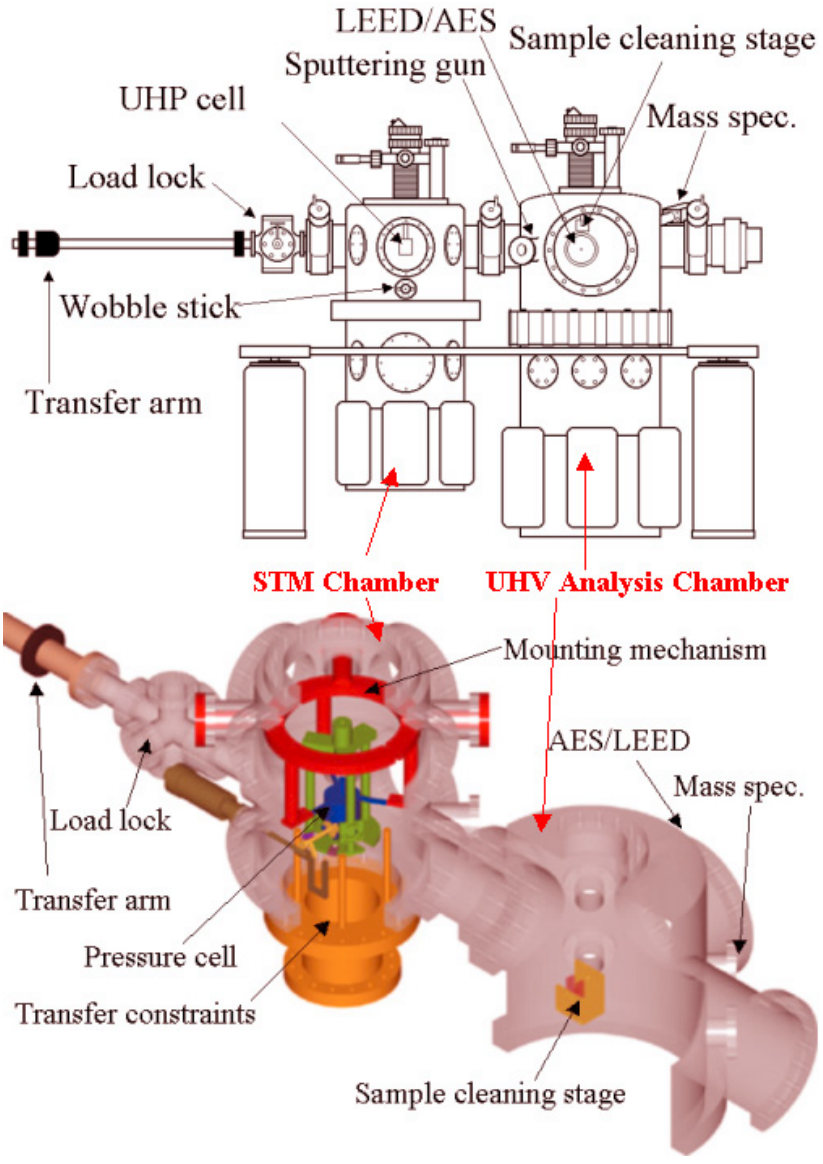

Figure 5.49. Schematic of the ultra high pressure, high temperature STM system.

The new ultra high pressure, high temperature scanning tunneling microscope system (Figure 5.49), similar to the high pressure and high temperature STM system described in Chapter 3, is divided functionally into three sections: a load lock for sample and tip introduction, a STM chamber to house the high pressure reactor cell containing the Walker STM motor and serve as a protective barrier to provide enough evacuated volume to prevent an explosion in case of pressure cell rupture, and a UHV analysis chamber for surface preparation and analysis by common surface science methods prior to and after high pressure *in situ* reaction studies. A 48" long magnetically coupled linear rotary transfer arm with a custom fork, specially designed to handle the new sample holder and tip exchanger, allows relocation of sample and tip between compartments. However, there are major improvements added to this latest system based on the shortcomings of the current high pressure system, as outlined in this and following subsections.

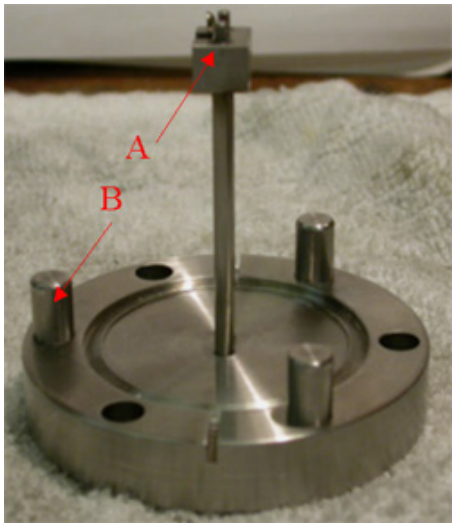

Figure 5.50. The loading flange for the load lock has a pins-and-leaf-spring system (**A**) for securing sample holders or tip exchangers, and three alignment posts (**B**) for engaging the load lock to ensure accurate placement for the transfer arm fork to intercept.

As in the previous system, the load lock is a six-way cross with 2.75” conflat flanges to minimize evacuation volume after each introduction and exchange of sample and tip. In contrast to the load lock manipulation in the previous system that requires much finesse on the part of the user, for this new system sample and tip introduction to the fork on the magnetically coupled transfer arm can be easily performed by the use of a loading flange (Figure 5.50), which consists of a tailored leaf spring fork for securing holders with a snap-on mechanism, which is welded to the center of a 2.75” blank flange with three alignment pins that match three specially adapted holes on the venting flange of the load lock. Transfer of a holder entails securing the holder onto the manipulation fork, inserting the loading flange squarely onto the load lock to automatically align the holder for the transfer arm fork to engage, and removal of the loading flange upon engagement of the transfer arm fork on the holder. Alternatively, the user can also choose to use a manual loading fork to perform transfer as in the previous system. In order to improve the evacuation time and the cleanliness of the load lock, a 60 L/s turbo molecular is installed below and dedicated for evacuation of the load lock, which is in turn backed by the system mechanical pump. During evacuation and normal operation, both the load lock and the attached magnetically coupled transfer arm are maintained by the said turbo molecular and system mechanical pumps, while isolated from the rest of the system by a 2.75” gate valve. The gate valve is open only when transfer between system compartments is needed, to minimize contamination from the load lock, which can usually proceed upon evacuation of the load lock from atmospheric pressure for fewer than 3 hours.

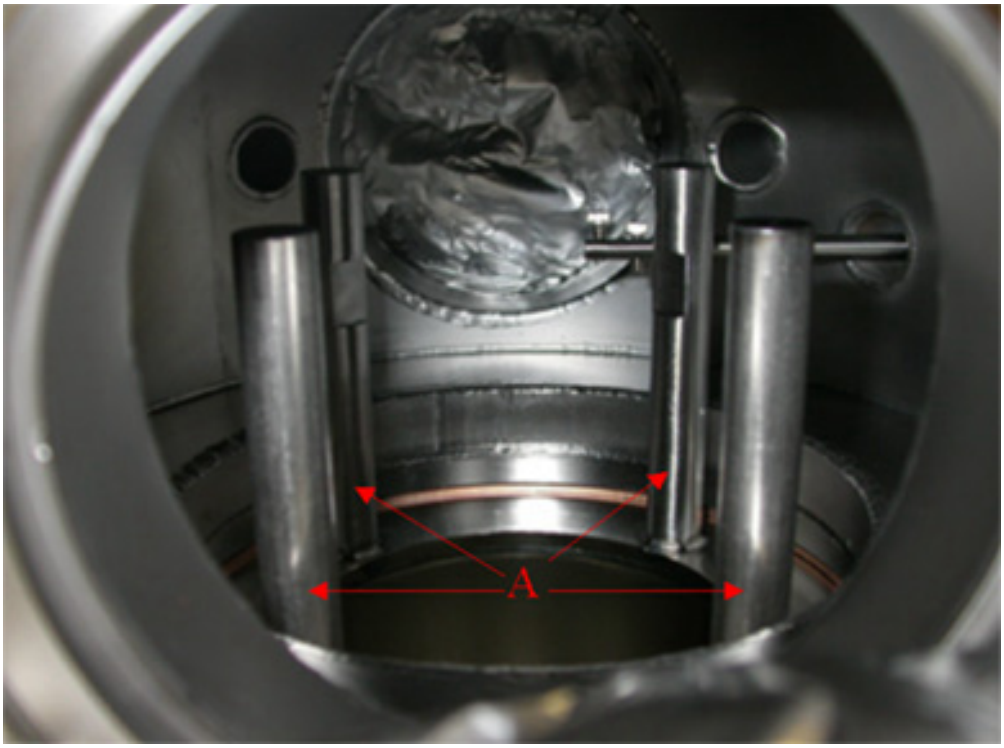

Figure 5.51. Constraints for transfer into and out of storage stations on the docking scaffold consist of four stainless steel posts (**A**) extending from the bottom of the chamber.

The STM section contains a UHV chamber of 10 L volume, which houses the high pressure reactor cell containing the STM and its associated mounting and transfer mechanisms, the latter of which will be discussed in detail in Subsection 5.4.4. The chamber is cylindrical in dimensions with two rows of flanges on its side and 8” flange access on both ends. The top row of radially arranged flanges contains evenly spaced and alternating array of four 6” flanges and four 2.75” flanges. The former flange type serve as view ports to provide ambient lighting as well as visual access by eye and charge-coupled device (CCD) cameras during manipulation, while the latter allows fastening of the mounting framework as described in Subsection 5.3.3. The lower row of flanges is

similar in arrangement, with two 2.75” flanges on the side of wobble stick access flange (same system side as the introduction flange on the load lock) replaced by three specially placed 1.375” flanges as described later in this subsection, and one 6” conflat flange replaced by a 2.75” flange. The two opposite 6” and 2.75” flanges in this row serve as gated access ports for the transfer to and from the two other compartments of the system, while the remaining two 6” flanges function as a view port and a wobble stick access port, the mechanism of which will be detailed in Subsection 5.4.4. One of the 2.65” flanges in this row provides electrical access for the internal lighting system on the mounting framework as described below, while the other acts as an access point for various vacuum gauges. The XYZΘ manipulator containing the pressure cell and STM setup is installed onto the top 8” flange of the chamber, while the lower 8” flange access of the chamber leads to an 8”-to-6” nipple followed by a 6” conflat tee junction to provide gated access to the 340 L/s system turbo molecular pump or a 60 L/s ion pump on either remaining flanges. Four evenly spaced rods of 0.375” diameter and 112 mm long are situated on a bolt circle of 116 mm diameter extending from the 8” side of the nipple to the interior of the STM chamber (Figure 5.51), to provide the necessary security for the bottom of the STM docking scaffold during the transfer of holders and bayonet seal to and from the docking stations, and to minimize the swaying motion of the elongated manipulator setup when the scaffold is not in mounting position. Due to the precision required in manipulation of the sample and the tip, adequate lighting within the STM compartment is warranted in form of three 42 Candelas halogen light bulbs, each of which is mounted onto each support pillar on the mounting framework. In addition, two

1.375” flanges are fashioned near the wobble stick access flange into the STM chamber so that the center lines converge onto the pressure cell entrance when the cell is in the mounted transfer position. Two inverted metal-to-glass domes on 1.375” flanges are installed in those position to allow insertion of guided lighting from an fiber optics illuminator (variable up to 350,000 Candelas). (Figure 5.52) One additional 1.375” flange is also machined nearby in the chamber for a linear manipulator access to provide the necessary torque for the bayonet sealing action as described in Subsection 5.3.1.

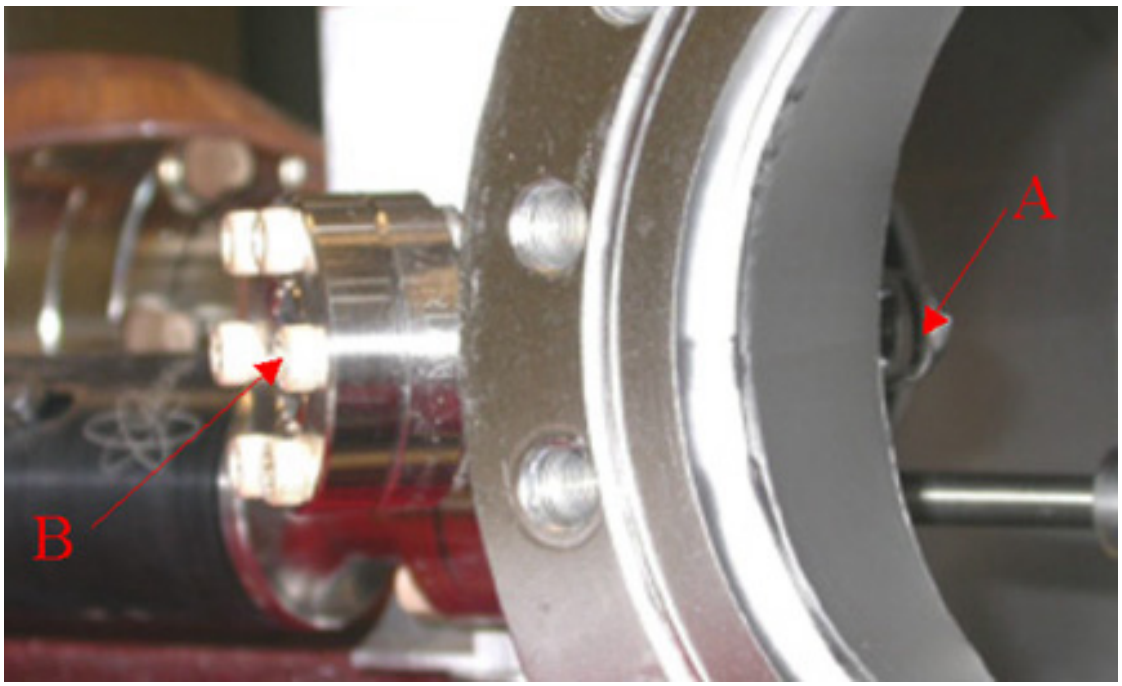

Figure 5.52. Each of the illumination view ports contains an inverted glass dome (**A**) that can be accessed by a fiber optic through an entry on the 1.375” flange (**B**).

The UHV chamber is a Varian surface analysis chamber equipped horizontally with a collection of surface science equipment for treatment and analysis before and after *in situ* STM studies: cylindrical mirror analyzer (CMA) for Auger electron spectroscopy, low energy electron diffractometer for qualitative surface analysis after sample

preparation, mass spectrometer for residual gas analysis and chemical analysis concurrent with *in situ* STM studies, sputtering gun for argon ion bombardment to vigorously remove surface contaminants, and electron beam bombardment heater for annealing sample. The chamber is adjoined to the STM chamber through a gated 6"to 8" fitting. Unlike the system described in Chapter 3, the major view port for visualizing the sample is on a different side compared to the wobble stick access and the introduction flange of the STM chamber and the load lock, due to the asymmetric transfer arm fork and the lack of circular symmetry in the sample holder and tip exchanger. Vacuum gauges are set up on the system to provide pressure readings between 1 x 10^{-10} Torr and 1000 Torr. Like in the high pressure STM system, the sample preparation stage, as detailed later in Subsection 5.4.3, is mounted on a XYZΘ manipulator to allow repositioning of the sample for access by different surface analysis and preparation techniques, and leak valves are installed to allow introduction of argon and oxygen for sputtering and annealing as well as gas sampling from the pressure cell and the STM chamber. A 2.75" conflat flange provides gated access to a conversion tee that connects to both the system turbo molecular pump and the 6" tee below the STM chamber. Normally, the UHV analysis chamber is maintained by a gated 200 L/s ion pump after initial evacuation by the system turbo molecular and mechanical pumps. A titanium sublimation pump (TSP) is available to reduce chamber pressure further to reduce the amount of residual gases before sample cleaning. During ion bombardment or oxygen annealing treatment of the

sample, the chamber is differentially pumped by the system pumps to minimize contamination.

5.4.2 Vibration Isolation

As mentioned in Section 5.2, a STM can be viewed as a mechanical system that has a collection of coupled resonance frequencies. These resonance frequencies are excited both by the surroundings and by the scanning piezoeletrics within the STM. The effect of the scanning piezoeletrics can be minimized through careful design, but it cannot be eliminated. The microscope, however, can be isolated from the vibrations present in the surrounding. The vibration isolation setup of the new system is introduced as follow, and the analysis of its design and performance will be presented later in Subsection 5.7.1.

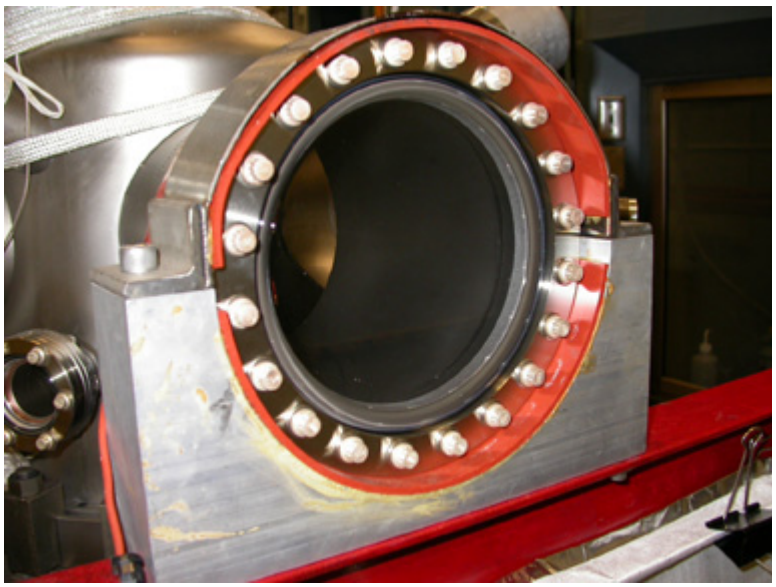

Figure 5.53. The system is secured onto the carbon steel framed through a series of silicone-lined ring clamps, each mounted onto a flange on the transfer arm axis.

In addition to the vibration damping provided by the carefully-chosen suspension springs of the pressure cell and the built-in high resonance frequency of the system through rigidity and compactness of the design, the vibration damping ability of the system depends heavily on the careful design of the support frame. Instead of the wooden frame as installed on the previous system, the new system is supported securely on a carbon steel frame that encloses the system below the transfer arm axis. The system is supported and mounted down at flanges located at endpoints of each compartment and the transfer arm along the transfer axis, to increase stability by lowering the center of gravity in relation to the support axis. The flanges are secured in ring clamps that have 0.125" silicone lining (Figure 5.53), for damping vibration transmitted between the frame and the system. The frame is mostly built out of 2.5" carbon steel square tubes, which are filled to 80% interior volume with play sand to act as a sandbox for providing a large damping factor for the rigid frame of otherwise high resonance frequency, and several steel I-beams in spatially restricted area. One of the ends along the length of the system contains a detachable I-beam, which can be removed to allow easy access and extraction of the UHV analysis chamber, the heaviest compartment, from the system. The system frame is maneuverable on four 5.625" high heavy duty caster wheels installed at the four lower corners during relocation of the system. The frame also provides four access points for easy coupling to the pistons of four 28" high pneumatic isolators if necessary, which provides heavy damping on all excitation except very low frequency. While the frame is equipped with the caster wheels resting upon a flat surface, the four access points (which are four depressions for the pneumatic pistons to engage into) are 0.125" above the

pistons. By pressurizing the pneumatic isolators with air and positioning the pistons directly under the access points on the frame, the pistons will engage the access points that are designed to allocate the asymmetric weight distribution of the system evenly on the four isolators, and elevate the entire frame off the floor thus allowing removal of the caster wheels and subsequent relaxing the weight of the entire system on the four pneumatic isolators.

Altogether, the system frame on pneumatic isolators serve as a mass-spring system that has a very low intrinsic resonance frequency and a large damping factor, while the silicone lining between the system and the support and the suspension springs of the pressure cell serve as secondary low pass filters. In this manner, only excitation of very low frequency and amplitude will be able to reach the microscope, but too far removed from its intrinsic resonance to couple and excite significantly.

5.4.3 Sample Preparation Stage

The oxygen free high conductivity (OFHC) copper sample preparation/cleaning stage is mounted onto a commercial XYZΘ manipulator through a collection of stainless steel plates that serve both as extension of the manipulator and as part of the necessary manipulation system within the UHV analysis chamber for securing the sample holder within the stage. Referring to Figure 5.54, the stage has a fork-like structure of four fingers that together act to confine the sample holder, upon deposition from the transfer arm fork through a vertical motion of the manipulator. Upon insertion of the sample holder, a stainless steel spring-loaded clamp can be lowered to secure the holder within

the stage, through the use of the extension rod within the manipulator setup and a pivot-and-lever system. This allows the sample holder to remain stationary during manipulation of the stage as well as the extraction and insertion of the transfer arm fork. At the same time, the clamp ensures good mating contacts between the pairs of type K thermocouple wires on the sample holder and the stage (with each pair 90° rotationally out of phase from the other to ensure a secure contact). Another set of type K thermocouple wires is connected to measure the temperature of the stainless steel manipulator plates at ambience as well as during sample annealing as well as system bake-out.

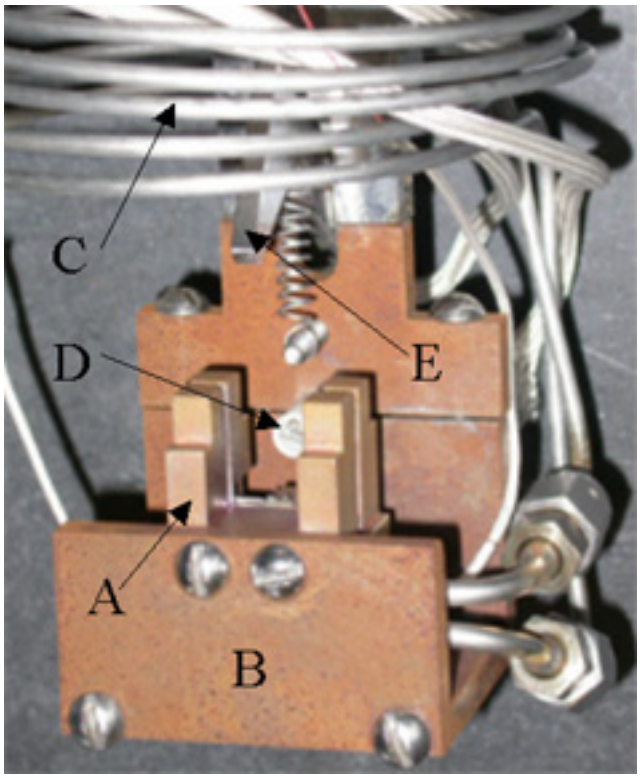

Figure 5.54. The sample stage (**A**) is mounted onto the XYZΘ through a collection of stainless steel plates (**B**), and has an internal cooling reservoir accessible externally through a cooling coil (**C**). Behind the stage is an electron bombardment heater (**D**), and above it is a maneuverable metal clamp (**E**) that can be used to secure a sample holder within the stage.

The back of the sample stage features two copper leaf springs that are electrically isolated by 0.5 mm thick Macor spacers and 2-56 alumina screws from the rest of the setup, which serve as high voltage supply electrodes to mate and ensure good contact with the spring taps extending from electrodes of the custom button heater embedded in the sample holder. The leaf spring are connected to two high voltage feedthrough flanges on the manipulator through copper coils of 0.5 mm diameter.

In addition to the button heater, the stainless steel manipulator plates contain a ring clamp section that allows installation of a ceramic tube containing a thoriated tungsten filament of 0.010" diameter for heating of the sample by electron bombardment, should the button heater be removed from the sample holder. The electron beam heater is positioned to within 4 mm of the backside of the sample, to minimize heating of the surroundings while still allow sample holder insertion when the button heater is present inside the holder.

In order to improve the cooling ability of the sample preparation stage over the existing design in the high pressure STM system to compensate for the thermally insulating material used for the construction of the sample holder, the copper stage contains an internal circuit of 0.0625" diameter, which are connected to a stainless steel coil of the same diameter to allow direct cooling of the stage with an external introduction of liquid nitrogen or chilled inert gas, while minimizing the thermal load as well as the resistance between the coolant reservoir and the sample.

5.4.4 Transfer Mechanism

The overall transfer mechanism of the system consists of a magnetically coupled linear rotary transfer arm for relocation of sample holder or tip exchanger between the three system compartments, a wobble stick on the STM section that provides the necessary precision and agility in exchanging sample and tip within the severely confined space of the pressure cell, and the intelligent use of the XYZΘ manipulators in both STM and UHV analysis chambers to maneuver receptacles into accessible and secured positions. While the transfer process between the transfer arm fork and the manipulator stage in the UHV analysis chamber has been sufficiently described, details of the relatively more complicated transfer process within the STM chamber are outlined within this subsection.

The stainless steel transfer arm fork features three fingers, with one finger being a thin plate to mate with the front cavity of the sample holder or the tip exchanger, while the other two being L-shaped angled plates with one arm of each "L" engaging the ledge on the opposite end of the holder. (Figure 5.55) The arm gripping the underside of the ledge (if the sample surface and back define the front and rear axis) has a 1.5 mm depression across 14 mm from the end, to allow insertion of the wobble stick finger (as described later) and the spring leaf on the introduction flange for the load lock, and to permit subsequent disengagement of the transfer arm fork after engagement of the manipulating counterpart is achieved. The purpose of the L-shaped angled plates is to provide alignment during insertion and removal of the sample at the sample preparation stage in the UHV analysis chamber, through mating with the top of the four fingers on

the stage for guided lateral movement. The fork can be removed from the transfer arm by disengaging two 2-56 set screws.

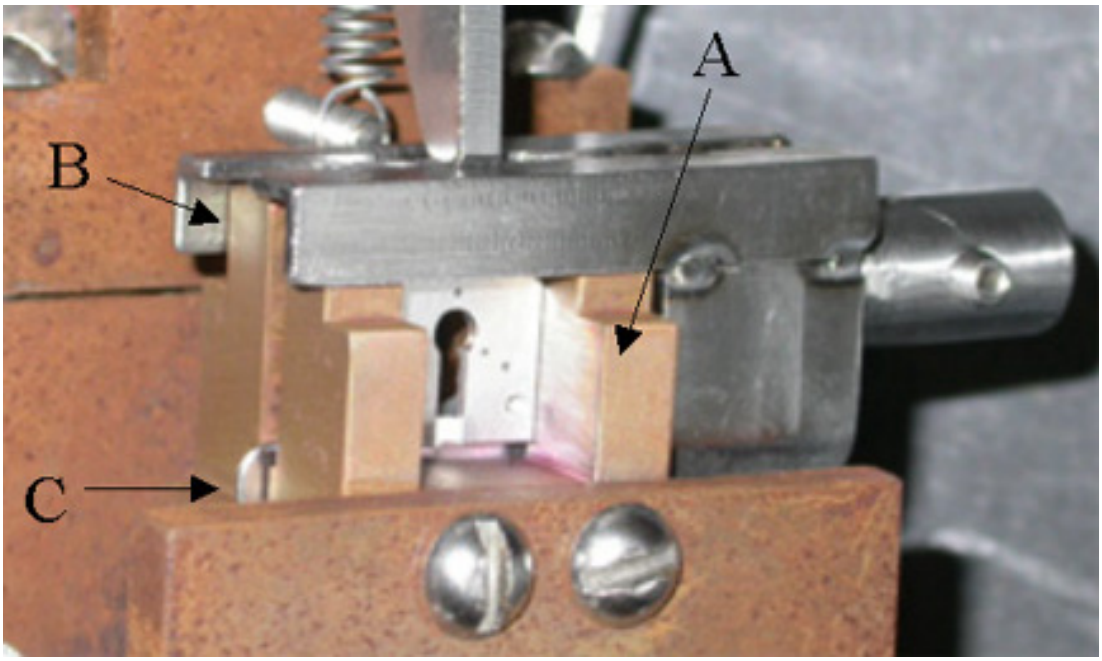

Figure 5.55. The sample preparation stage (**A**) provides guided movement to the transfer arm form by its four-finger structure (**B**), and contains a suitable recess for the insertion of the third finger (**C**).

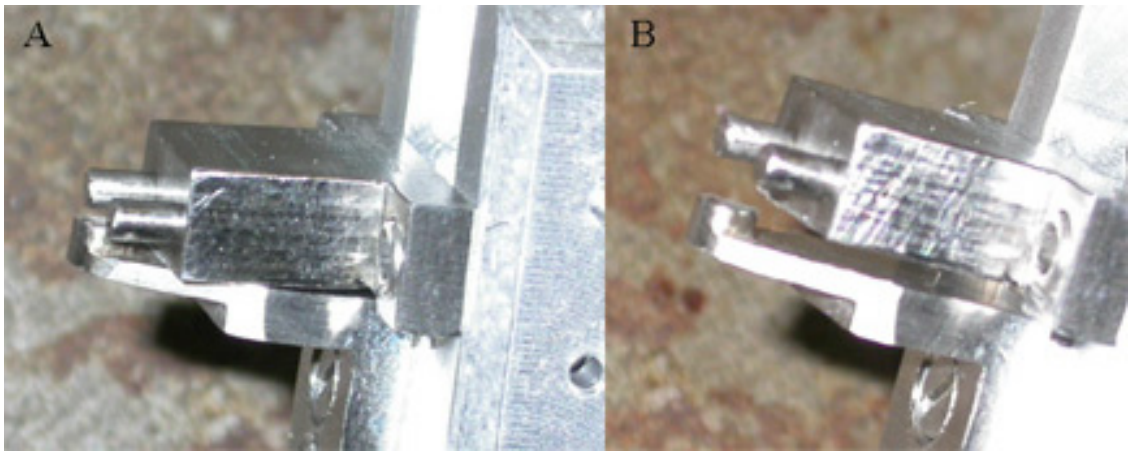

Figure 5.56. The wobble stick hand contains two alignment rods and one maneuverable finger that grips onto the sample holder at rest (**A**) and releases when an external lever is pressed (**B**).

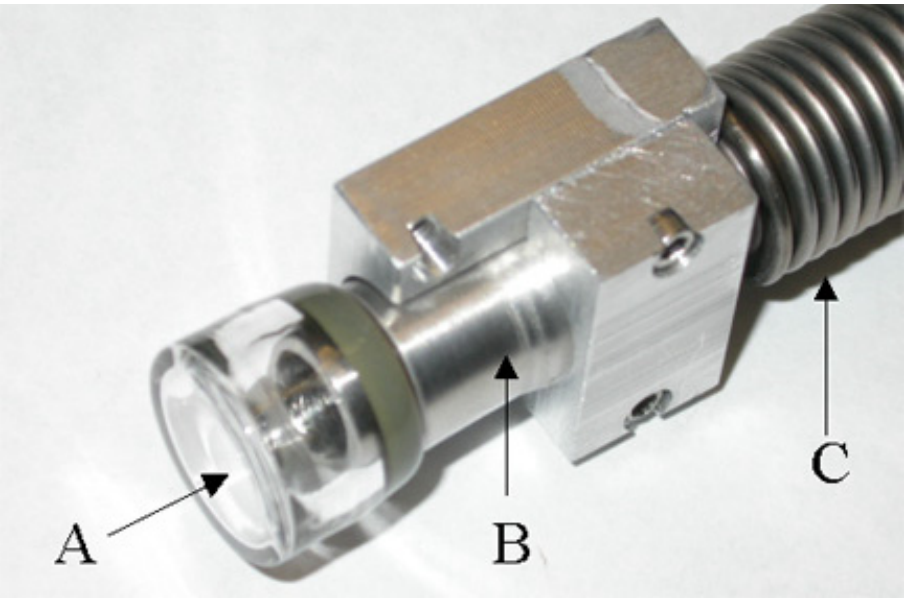

Figure 5.57. The miniature view port for the wobble stick contains an optically flat glass port (**A**), and a robust metal tube (**B**) for connection to a bellow system (**C**) and mounting onto the wobble stick. The tube also prevents over-insertion of the fiberscope.

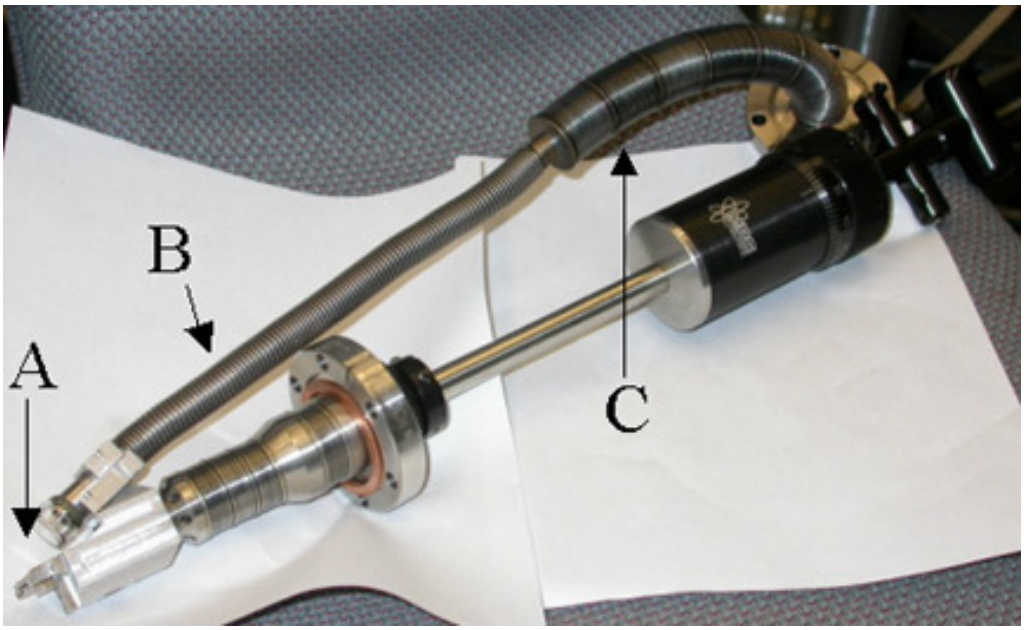

Figure 5.58. The miniature view port is mounted to the wobble stick at an angle to give a full view of the manipulation process (**A**). The bellow system for the view port contains a standard bellow section (**B**) for mechanical robustness against abrasion and a welded bellow section (**C**) for flexibility necessary for transfer.

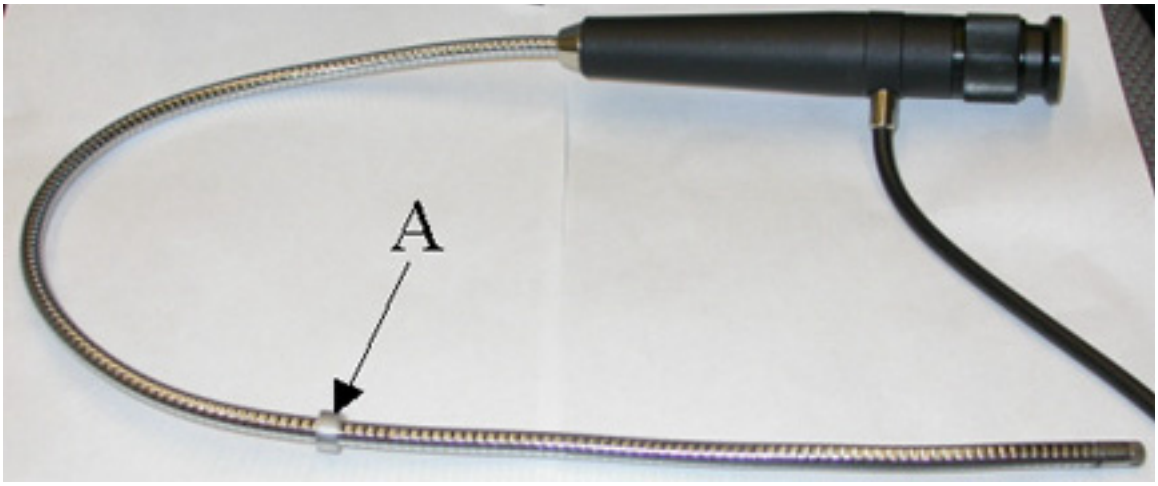

Figure 5.59. Fiberscope with adjustable metal stop collar (**A**) to work with the metal tube in the miniature view port system and prevent over-insertion.

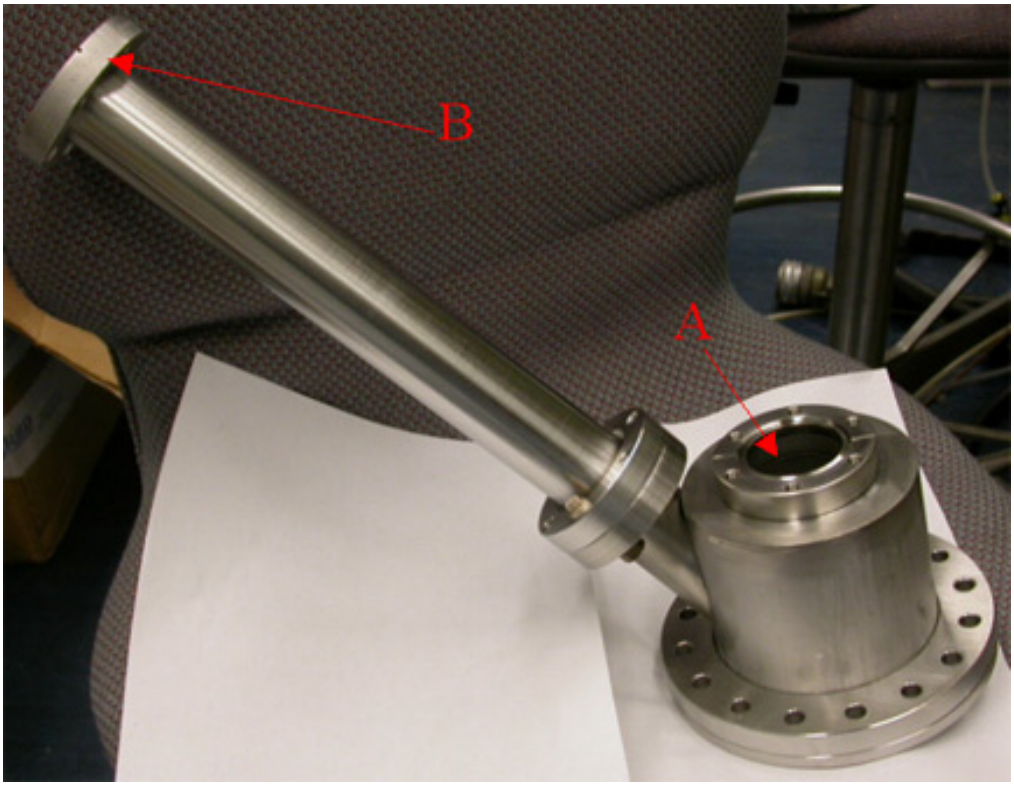

Figure 5.60. The custom allows the wobble stick to be mounted (**A**) concentrically to the 6" access port on the STM compartment, and the miniature view port system to be secured at an angle (**B**).

Transfer process in the STM compartment requires active manipulation by transfer arm fork and wobble stick, along with positioning by the XYZΘ stage to proper transfer position of the pressure cell and the docking scaffold. The pressure cell and scaffold can be elevated to allow the introduction of the transfer arm into the STM chamber, and subsequently either continual proceeding of the arm into the adjacent UHV analysis chamber or manipulation of sample holder or tip exchanger by the wobble stick in the STM chamber. In the latter case, a custom-designed wobble stick is used to extract or deposit sample holder or tip exchange to and from the transfer arm fork. The wobble stick features both linear and rotary manipulation, and contain a specially designed hand at the end that can mate and grip onto a holder by adjusting an external lever on the wobble stick, with the holder fully engaged by the wobble stick hand at the rest position of the lever. As seen in Figure 5.56, the wobble stick hand consists of two small straight rods for alignment with the two end circular holes on the sample holder and the tip exchanger (as well as the field emission plate and the bayonet seal), and a maneuverable finger that can grip onto the adjacent hole on the holder in a vertical motion through the use of the wobble stick lever. Mounted by a custom ring clamp to the wobble stick hand is a miniature glass-to-metal view port that contains an optically flat view port (Figure 5.57), which is sealed to a 8” long standard bellow and subsequently a 6” long welded bellow and a 2.75” flange. (Figure 5.58) This optical setup is positioned at an angle to the end of the wobble stick, and allows the insertion of a fiberscope externally to permit monitoring of the wobble stick hand and the surrounding space during transfer. A CCD camera is attached at the end of the fiberscope so that the image can be viewed easily on

a monitor. The miniature view port contains a short rigid metal tube between the glass and the standard bellow that is mounted firmly to prevent individual movement during travel of the wobble stick, and the metal tube also prevents the fiberscope from pushing onto the optical glass from over-insertion with the use of a custom collar on the fiberscope to provide a stop at the metal tube. (Figure 5.59) The two-staged bellow setup is necessary because the standard bellow provides the necessary mechanical durability against abrasion during manipulation by structures inside the chamber, and the more receded welded bellow allows the translational and rotational agility necessary for manipulation. The entire wobble stick along with the optical setup is installed onto the STM chamber on a 6" conflat flange as indicated previous, through the use of a custom mounting fitting that provides two angled 2.75" flanges for mounting the wobble stick and the optical setup, as well as allows complete recession of the wobble stick setup from the chamber when idle. (Figure 5.60)

After removing the sample holder, for example, from the transfer arm by the use of the wobble stick, both the transfer arm and the wobble stick can be retracted from the chamber, and the pressure cell can be lowered for access by the wobble stick by the use of XYZΘ stage. Subsequently, the pressure cell and the docking stations on the scaffold can be reached by adjusting the manipulator stage to appropriate positions.

In the case of the delicate handling of sample and tip within the pressure cell, the pressure cell is secured rigidly so that the bayonet-sealed opening is aligned concentrically with the wobble stick access flange in the mounted transfer position, by the use of the pins-and-holes system on the pressure cell with the mounting framework

and docking scaffold, as described in Subsections 5.3.2 and 5.3.3. The concentric arrangement is essential for accurate introduction of the sample holder and the similar by the wobble stick, since any angle of engagement introduced by otherwise can impede insertion or even cause breakage due to the small bayonet-sealed opening and, more importantly, the minute size of the holders. Once aligned and secured, the sample holder can be introduced simply by inserting it through the bayonet-sealed opening onto the sample stage, with visualization of the transfer by CCD cameras mounted on the fiberscope as well as 6" view ports on the STM chamber. Since the pressure cell is mounted rigidly, the wobble stick can be used to push the sample holder firmly in place to ensure engagement by the leaf spring and the wire springs on the sample stage without concern of breakage, as long as no torsional stress is applied. Once the holder is deposited, the wobble stick finger can be disengaged from the holder and the manipulation hand can be retracted.

Similarly, when the pressure cell is in the mounted transfer position, the manipulation hand on the wobble stick can be used to engage the bayonet seal onto the pressure cell by depositing and turning the seal to connect into the lips of the closing mechanism, followed by disengagement of the wobble stick and subsequent torque action provided by the linear manipulator to complete the pressure seal.

For deposition of sample holder, tip exchanger, and field emission plate into storage at the bottom plate of the docking scaffold, as well as placement of the bayonet seal into the docking station mounted on the scaffold, the pressure cell can be rotated and maneuvered into free transfer positions for such tasks. While in free transfer positions,

the pressure cell is only engaged by the three pins of the scaffold mainly for support, and the docking scaffold is prevented from swaying excessively during the deposition and extraction of various holders at the storage through the restricted movement of the lower scaffold plate imposed by the four stainless steel posts at the bottom of the STM chamber, as described in Subsection 5.4.1. The process of using the wobble stick for manipulation during free transfer positions is the same as stated in the case of mounted position.

5.5 Electronics Design

Since the mechanical control of the scanning piezoelectric transducer is inherently similar for most scanning tunneling microscopes, a commercial SPM imaging control electronics (SPM-1000HV) with an integrated digital signal processor (DSP) and the associated software (STiMage), for loading the DSP control and serving as the user interface to the STM, are obtained from RHK Technology, Inc. The control software acquired has been modified to control an external input/output card on a computer to output a transistor-transistor logic (TTL) clock signal for controlling a custom approach electronics of the Walker STM motor.

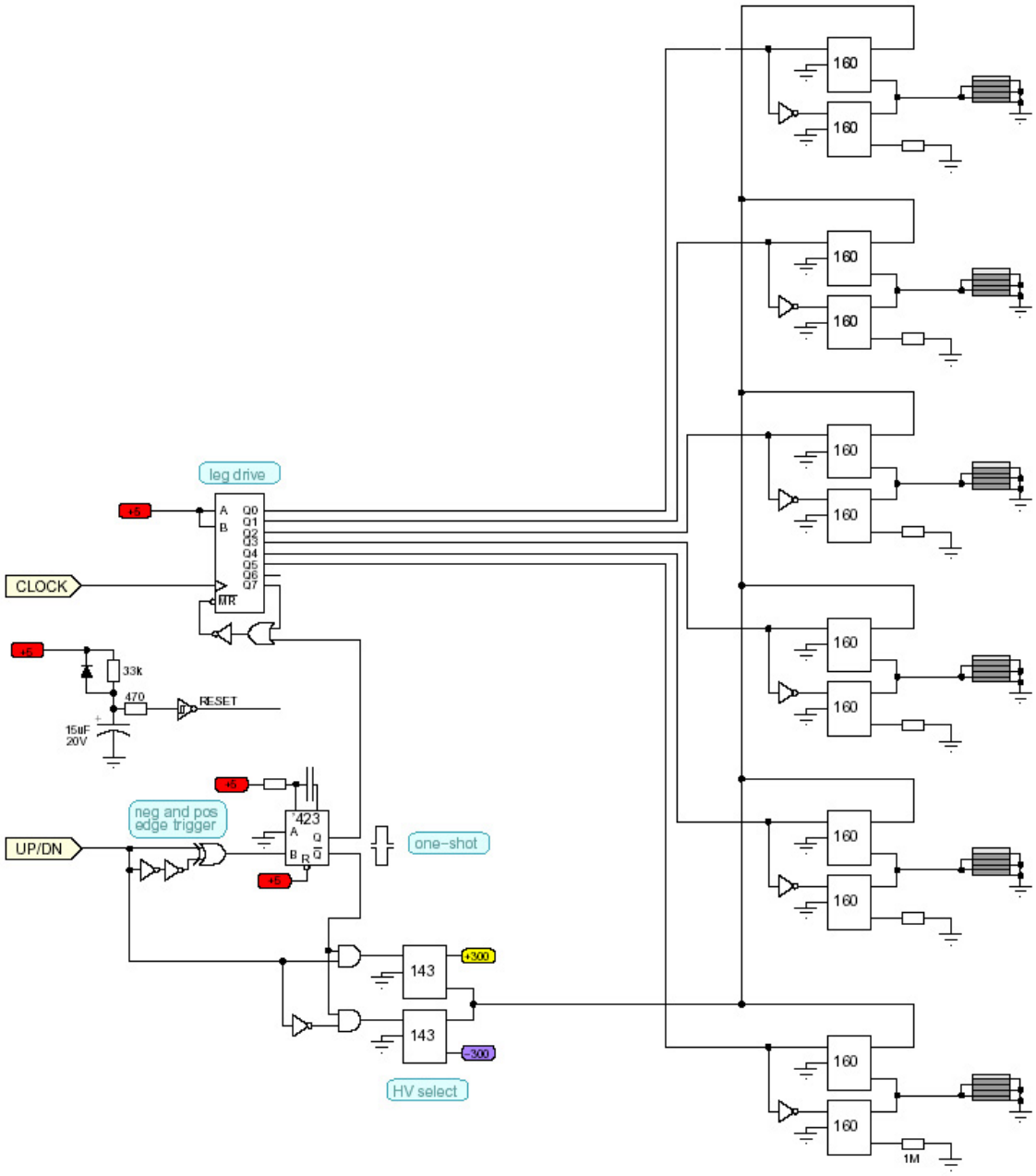

Figure 5.61. Schematic of approach electronics for the Walker STM.

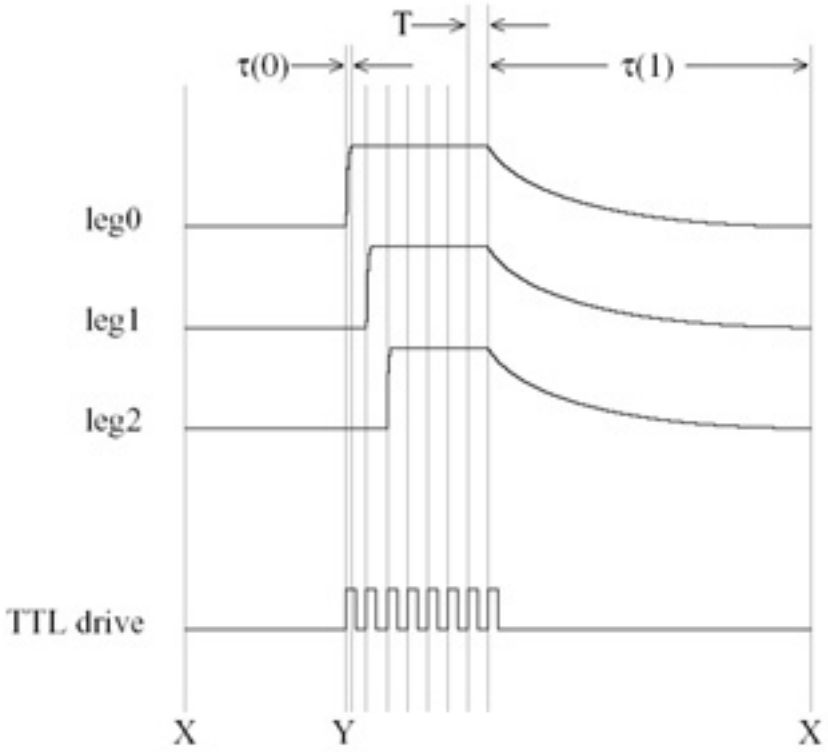

Figure 5.62. The timing graph of the Walker STM electronics, show the shear legs are sequentially charged up and eventually simultaneously discharged, all set on the TTL drive signal of a drive period **T** that is greater than the charging time. The charging time **τ(0)** depends on the shear piezoelectric capacitance, and the discharging time **τ(1)** depends on the relay speed and the discharge resistor. The wait time **XY** between steps is dependent on the existence of tunneling current check in-between.

The initial approach electronics, used in Subsections 5.6.1 and 5.6.2 and schematically shown in Figure 5.61 and Figure 5.62, consists of three sections: a 2-serial-in 8-parallel-out shift register (Motorola SN54/74LS164) for sequential movement of the six shear piezoelectric legs for tip approach (or retraction), six pairs of quad 2-input AND gates (Fairchild DM74LS08) for charging and discharging of the shear stacks, and an up/down control that determines net movement direction as well as resetting sequence counter and piezoelectric stacks at the end of each approach step. Operationally, the TTL

clock signal from the computer of a user-determined frequency (or alternatively, a square pulse clock signal of 1 V_{pp} from a function generator will suffice if manual control of triggering is desired) is sent to the shift register to set the rate of moving each shear piezoelectric leg within each step. 5 V DC signals of opposite polarity serve as the two input signals controlled by the shift register, and one is sent successively and maintained in each of the 8 gated output, in synchrony with the rising transition of each clock pulse. The polarity of the 5 V signal transmitted is determined by the up/down control, and has the same polarity as the high voltage output (up to 250 V) that is sent as input to the first of each pair of AND gate logic chips. The 5 V signal serves as a switch input to each pair of AND gate chips, with the polarity inverted for the signal sent to the second of each pair. Upon receiving the 5 V signal sequentially in each of the first chips in the six AND gate pairs, the high voltage signal (through a Schmitt trigger to decrease the rise time of the signal) is successively sent to and maintained at each shear piezoelectric leg to cause a sudden shear movement to allow the slipping motion of the shear stack on the sapphire slider surface, while the other five static shear stacks provide enough frictional force to maintain the slider in stasis. After triggering the first six of eight gated outputs on the shift register, the seventh gated output is intentionally grounded on the circuit to allow equilibrating time for all six shear legs before relaxation, which commences upon the triggering of the last gate that is linked to the master reset of the shift register. Resetting the shift register causes all eight gates to output and maintain simultaneously a 5 V signal that is of opposite polarity to the previous output. Once again, the 5 V signal is sent to both AND gate chips for each shear piezoelectrics. The signal, now of opposite polarity,

causes the first chip to cease supplying high voltage to each shear leg, while at the same time causes an output (or discharge) of the stored potential in the piezoelectrics to a 1 MΩ resistor by the gated output of the second AND gate chip in the pair. The resistor is necessary for a slow discharge, in comparison to the quick 5 μs charging (a function of capacitance of each shear stack), of the shear leg to allow a translational motion with the shear stacks remaining in contact (or sticking) with the sapphire slider. The use of a 1 MΩ resistor per shear leg allows an adequately slow relaxation time of 20 μs. As a result, all six shear piezoelectric legs are relaxed simultaneously to "drag" the sapphire slider in motion. Upon triggering of the last gate in the shift register, the computer proceeds to extend slowly the scan tube in an attempt to detect tunneling current. If no current is detected, the scan tube (and thus the tip) is quickly retracted and the next set of TTL clock signals is then sent to trigger the next user-determined number of approach steps.

Apparently, decreasing the discharge resistance below 1 MΩ and thus increasing the discharge rate causes a minor increase in approach speed initially and no improvement after that, probably due to the fact that rapid relaxation causes at least partial slipping of the shear stack surfaces on the sapphire slider and thus decreasing step size. Furthermore, it should be noted that the discharge time relies on both the discharge resistance and the relay time set by the second AND gate chip of each pair. Likewise, increasing the clock speed above 120 Hz causes inadequate relaxation time between steps and thus reduced step size. As a result with the initial electronic setup, each step (a complete cycle of six shear stack sequentially charging and simultaneously discharging) requires a minimum of 58 ms.

The principles behind the approach electronics used in Subsections 5.6.3 and 5.6.4 remain essentially unchanged, with the major change from a voltage-controlled AND gate pair for each shear stack to a current-controlled triac triggered by the peak of a 60 Hz 10 V line on a static shunt load of 10 kΩ. As a result of this modification, the present approach electronics allows a shorter approach time of 25 ms per step if no check for tunneling current is performed.

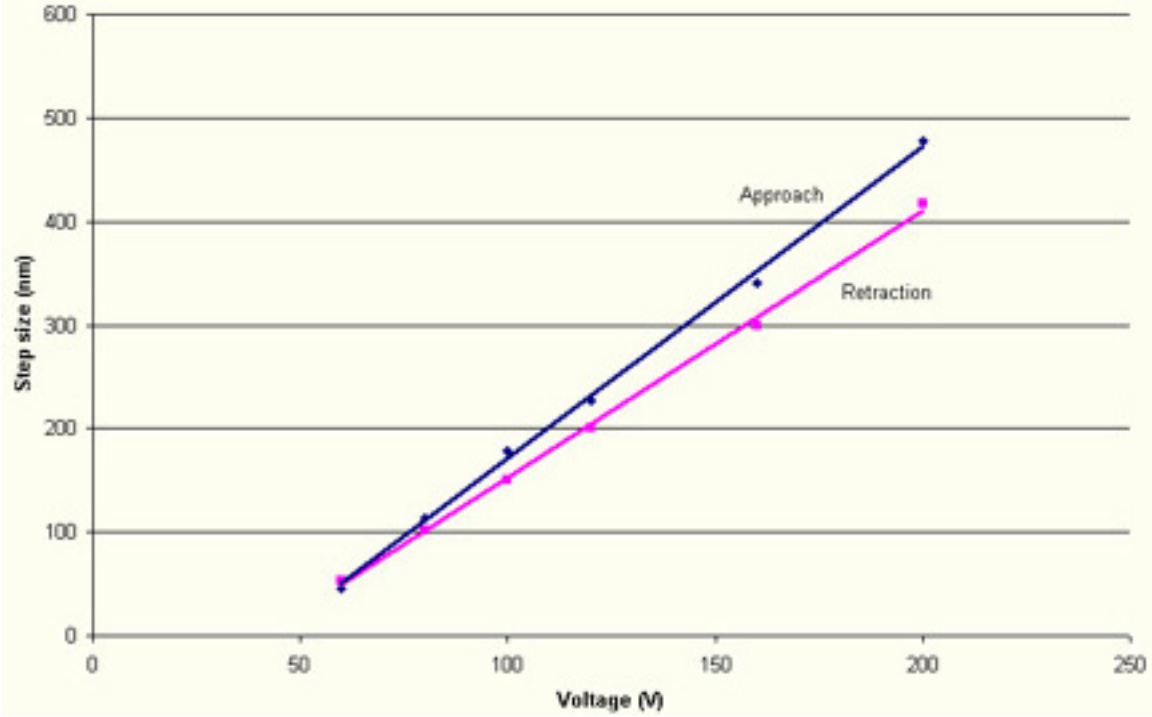

Figure 5.63. Step size of the approach mechanism as a function of voltage applied.

Figure 5.63 shows the relation between step size of the STM motor and the voltage applied using the more recent electronic setup, which is linear in the step distance range of interest. The step size can be modified further by adjusting the bracing pressure of the shear legs through the adjustment screw of the CuBe spring plate on the

microscope, or by using the alternate set of sapphire prism surfaces for the shear stacks to rest on.

5.6 Performance in Air

In order to assess the performance of the Walker STM motor, surface imaging of gold deposited on glass and highly ordered pyrolytic graphite is attempted, due to the high resistance of these samples against contaminants after initial preparation. The XYZ ranges of the motor has not been calibrated during these tests, and the dimensions in the three directions for imaging have been approximated through known atomic distances (atomic lattice of graphite for XY ranges and atomic step height of Au(111) for Z direction). In all performance tests recorded in the following subsections, imaging in air along with using only a cut tip (made of oxidatively resistant platinum alloy with 10% rhodium), instead of imaging in a well-isolated environment with a carefully assembled setup similar to Subsection 5.6.4, introduces many fundamental noise problems, both mechanically and electrically. Mechanical stability is considerably compromised due to acoustic transmission, physical induction by convection, and a structurally weak and poorly defined tip. While most of these problems can be eliminated by carefully isolating the motor and making appropriate preparation before testing, the minimally mechanically isolated setup serves two important purposes: a comparison of mechanical stability between the Walker STM and the current Beetle STM, and a preliminary test of susceptibility to vibrational excitation of the new motor in order to predict future performance under mechanical stresses such as vibrations from gas flow and tubing

connection. Electrically, interference from nearby devices such as power sources, electronic modules for STM imaging as well as sweeping frequency of computer monitor is apparent during the initial tests due to the lack of a grounded housing (normally in the form of a UHV chamber in a system), and should be typically eliminated after the motor is introduced into the system and the routing of signals to and from the motor are properly designed and shielded.

5.6.1 Unannealed Gold on Glass - Microscope only

The Walker STM, complete with exchangeable tip and sample installed and sample stage rigidly coupled by the use of the CuBe press plate, is mounted onto a vibrationally undamped optical table. The optical table is chosen to mount the STM firmly through the body with the use of a micro clamp, due to the fact that its dynamic and static rigidity, along with the lack of surface and side wall resonances, allows for the accurate simulation of securing the microscope directly onto a desktop.

The sample is prepared by electron beam deposition from a gold source onto the surface of a glass disc of 10 mm diameter and 1 mm thick, at a rate of 500 nm per minute to 1 μm thickness. The sample is mounted onto the metallic mock sample holder with the use of four tantalum leaf springs and three stainless steel balls of 1 mm diameter, instead of the usual glass balls, to provide electrical connection between sample and holder for application of the bias voltage.

Electrical connections are made by 0.003” thick Kapton-coated copper wires between the microscope and an electrical breadboard, which is secured onto the optical

table and allows conversion to BNC connections to the approach and imaging electronics. The BNC cables are secured firmly to a hook shortly away from the breadboard to protect the connection and minimize vibrations conducted to the optical table. While an attempt to shield the microscope from external electrical noises by surrounding with a grounded aluminum foil cage, interference as a result of capacitance coupling between the tunneling current wire and other microscope lines is still present in the form of a strong 60 Hz peak in the tunneling current noise spectrum.

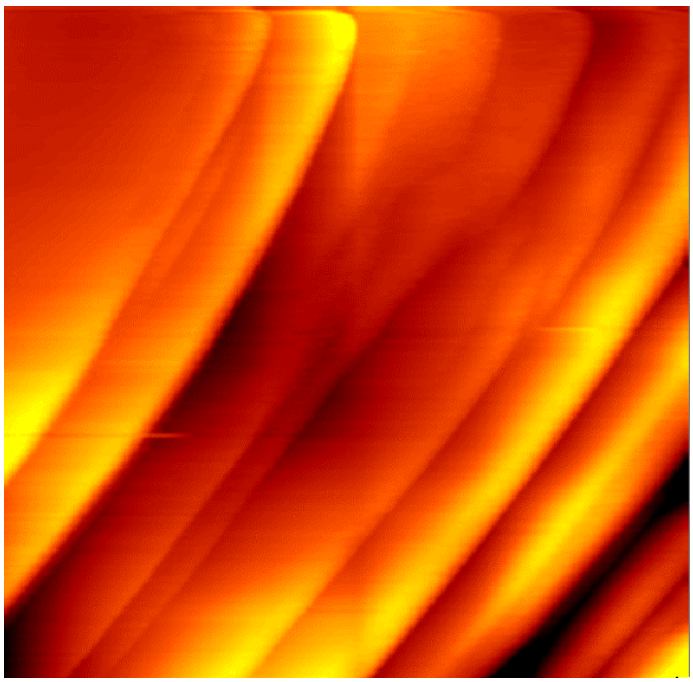

Figure 5.64. (2000 x 2000) $Å^2$ image of gold deposited on glass with no vibration damping reveal step edges with clarity, but smaller scans are unable to resolve individual gold atoms. (V = 225 mV, I = 0.51 nA)

Initial imaging of the gold sample proves difficult due to the mechanically unreliable nature of the tip as a result of the fashioning method as well as the relatively soft Pt alloy, and due to the often amorphous structures on the surface as a result of high

deposition rate (even after annealing by hydrogen flame post-deposition). However, images of granular structures on the amorphous surface can still be obtained with the vibrationally undamped setup. In the case of several well-prepared gold on glass samples, step edges between flat terraces can be imaged clearly (Figure 5.64), in sharp contrast to the need of the current Beetle STM for extensive vibration damping and an atomically sharp tip to image atomic step edges. No tunneling current noise spectrum is taken due to the lack of such ability in the initial electronic setup, but fast Fourier transformation reveals a medium response at 35 Hz that is known to be the vibration frequency from the laboratory building, in addition to dominant peaks at 60 Hz and 120 Hz, probably as a result of external power sources nearby despite shielding with an aluminum cage. The noise level in the vertical direction in the images obtained is calculated to be 0.17 ± 0.03 Å, which explains the lack of atomic resolution in the attempt to observe the Au(111) lattice. No measurable drifts in XY ranges are observed during as small as $(700\ Å)^2$ imaging of step edges.

5.6.2 Graphite(0001) - Microscope Only

Identical setup is used for imaging HOPG surfaces, due to the lack of consistency in preparing well-structured gold surfaces for imaging. The graphite sample is glued to a copper disk of 10 mm diameter and 3 mm thick by conductive epoxy for eventual electrical connection to the sample holder. Before immediate imaging of the surface, the graphite sample is stripped by scotch tape to reveal a new layer and subsequently

mounted to the holder by four tantalum spring leafs and three glass balls of 1 mm diameter.

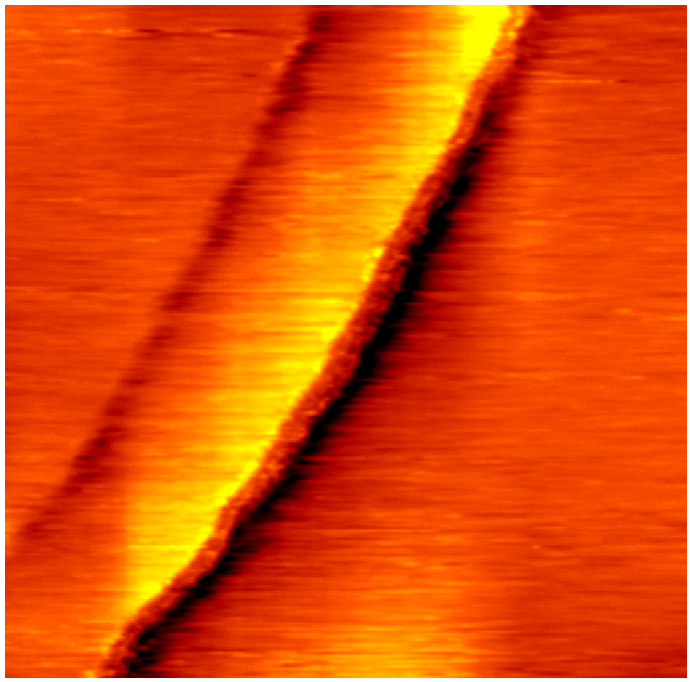

Figure 5.65. The Walker STM under no vibration damping does not resolve individual atoms on fine scan ranges, but shows step edges on HOPG clearly in an (800 x 800) $Å^2$ image. (V = 1000 mV, I = 1.97 nA)

Step edges between graphite terraces can be imaged but individual atoms cannot be atomically resolved (Figure 5.65), as in the case of the unannealed gold on glass sample. Subsequently, the microscope is evenly suspended on three rubber bands from a plate supported on a tripod with pinpoint contacts to minimize vibration transmission from the support surface, in an attempt to damp mechanical noises conducted to the microscope. After the modification, low frequency noises in the images can still be observed but the graphite lattice can be atomically resolved (Figure 5.66), with the noise level vertical resolution being 0.07 ± 0.02 Å. Fast Fourier transformation of the tunneling

current no longer shows observable excitation near 35 Hz, but still reveals strong responses at 60 Hz and 120 Hz. By assuming each carbon atom observed in the lattice to be a perfect circle and measuring the distortion of the atom in comparing the X and Y directions, the drift rate in the slow scan direction is found to be less than 1 Å per minute.

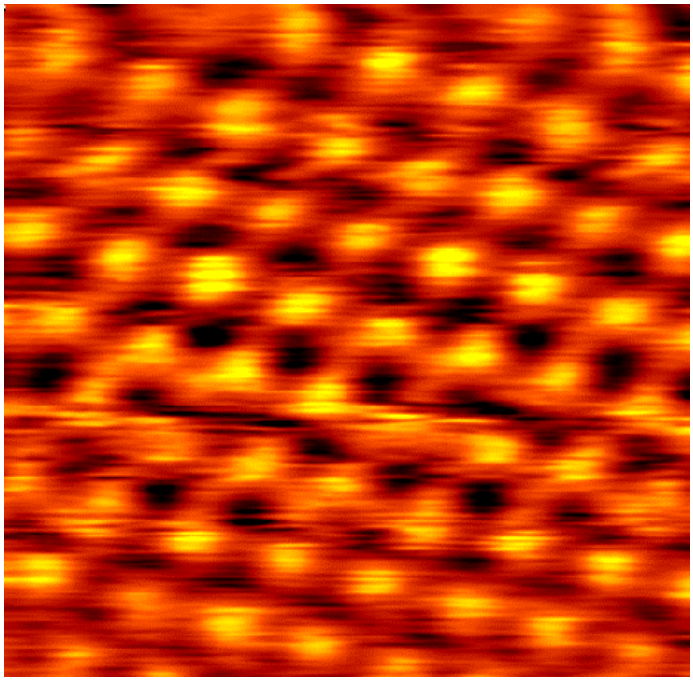

Figure 5.66. (20 x 20) $Å^2$ image of HOPG by the Walker STM suspending on rubber bands resolves atomically. (V = 149 mV, I = 6.45 nA)

5.6.3 Graphite(0001) - Microscope in Pressure Cell

The STM is installed inside the pressure cell, which is subsequently connected to the XYZΘ manipulator (temporarily and currently without installing the high pressure gas tubing coils) for future operation within the system designed. During this test, the entire manipulator setup is secured on an inverted tripod to be placed on a desktop for operation. (Figure 5.37) During operation, the pressure cell initially is decoupled from the

support scaffold and damped by three suspension springs as designed, but silicone spacers are inserted periodically within each spring subsequently so that any excitation inducted can be more quickly damped compared to using springs alone (< 3 minutes compared to 10 minutes). Throughout the test, the pressure cell is closed up in atmosphere by the bayonet seal to simulate the final operation condition inside the system as well as to minimize the amount of convection and acoustic excitation inducted directly on the microscope. Also, the inverted tripod with the entire manipulator setup is enclosed in electrically grounded aluminum foil to minimize electrical noises as well excitation of the setup by convection.

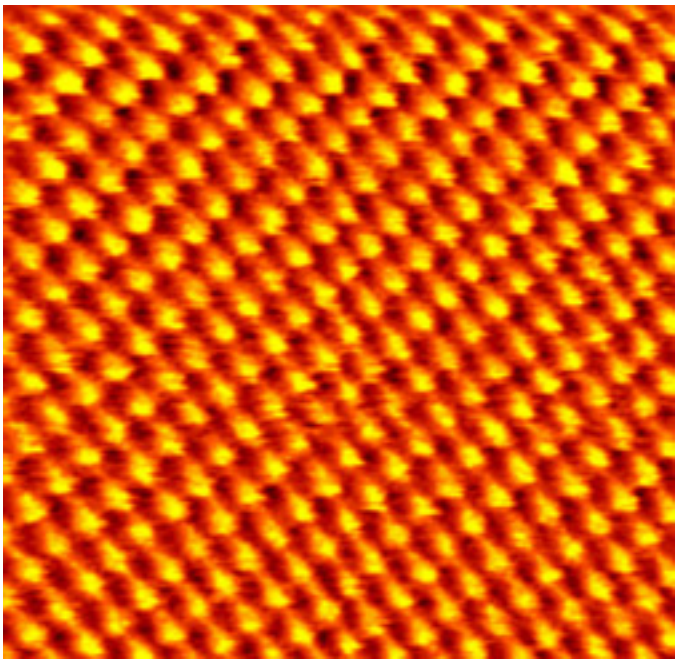

Figure 5.67. (45 x 45) $Å^2$ image of HOPG with Walker STM in the pressure cell suspended by precision springs on desktop shows clear atomic resolution. (V = 333 mV, I = 2.86 nA)

Imaging of HOPG surfaces reveal similar drift rate (< 1 Å per minute) and noise level (0.07 Å ± 0.03 Å) as in previous cases (Figure 5.67), but images show considerably smaller amount of low frequency excitation and electrical interference in the setup, proving the carefully chosen springs of defined low resonance and the meticulous shielding of the tunneling current signal are crucial contributors in minimizing noise within the system. The nevertheless high noise level in the vertical resolution remains despite the improved setup, and the tunneling current noise spectrum reveals strong response and low damping at low frequency (< 10 Hz) upon excitation externally or internally (such as after repositioning of the tip position by the scan tube). This most likely is due to the low damping performance of the suspension springs currently chosen, even when mitigated by the installation of the silicone spacers; while the springs are well defined low pass filter with a narrow bandwidth, its high excitation response at resonance requires a low equilibration time. It is assumed that when the manipulator setup is secured inside the system, the added rigidity and damping of the system by the pneumatic legs and the custom-designed support frame, as well as the eventual evacuation of the system to reduce acoustic conduction and convective excitation, will eliminate the high excitation and low damping problem and reduce the noise level to a more acceptable level. Aside from the low damping situation, the tunneling noise spectrum shows the lowest observable mechanical excitation frequency, as identified by a broadened response, is a pair of resonance peaks at 14.8 kHz and 15.3 kHz. This shows that the introduction of the microscope into the multi-part pressure cell does not compromise the

performance of the STM, and the mounting and wiring mechanisms of the STM inside the pressure cell as designed are mechanically stable.

Meanwhile, no observable signals as in previous cases can be seen at 60 Hz and 120 Hz, but a sharp response at 3.1 kHz of unknown origin is observed in the noise spectrum, which most likely is a result of electrical induction on the system. This can be a result of ineffectual shielding of the setup by the aluminum foil, which can not be confirmed until the current setup is placed inside the grounded system as planned.

5.6.4 Graphite(0001) - Microscope in System

The manipulator setup as described in the previous subsection is placed inside the system as described within this chapter, and imaging is once again performed in air with additional damping of the microscope by pneumatic legs and steel support frame. (Figure 5.68) Drift rate in the lateral directions remains small (< 1 Å per minute), while the noise level in the vertical resolution improves slightly (0.04 Å ± 0.01 Å). Mechanically and electrically induced signals within the tunneling current remain essentially unchanged in frequency but mildly diminished, with mechanical resonances at 15 kHz and electrical excitation at 3.1 kHz, while the damping performance of the feedback loop below 10 Hz improves with help of the added damping. While acoustic and convective excitation can still be responsible for moderately compromising the mechanical performance of the microscope, the cause for low frequency electrical noise within an electrically shielded system remains unidentified but most likely a result of capacitance coupling between

wires within either the pressure cell or the manipulator, as similar noise has not been observed prior to the installation of the microscope into the cell or the manipulator.

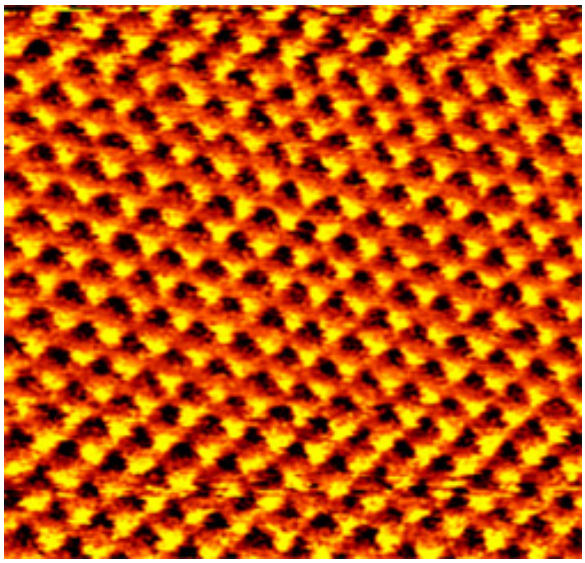

Figure 5.68. (38 x 38) $Å^2$ image of HOPG with the Walker STM in pressure cell and suspended on precision springs within the STM compartment engaging on pneumatic legs. (V = 249 mV, I = 3.65 nA)

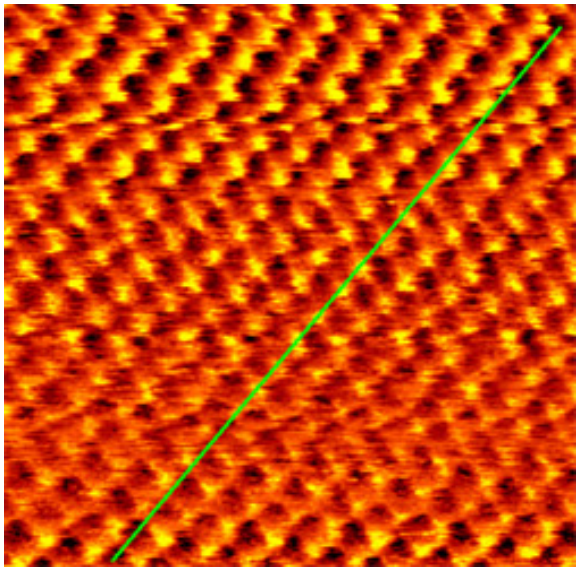

Figure 5.69. (40 x 40) $Å^2$ tunneling image of HOPG under varying sample bias between 250 mV and 600 mV and current set point of 3.00 nA shows a change in tunneling probability of the atomic row as indicated by the green line.

For proper testing, it is essential to verify that the tunnel barrier represents true vacuum (or atmosphere, in this case) and is free of material that can provide additional mechanical stability to the junction and create a false impression of the intrinsic mechanical properties of the system. Such material often results in "abnormal" tunnel barriers that are considerably smaller than the work functions of the tip and surface. In order to ascertain whether the images obtained thus far on HOPG surfaces by the Walker STM motor are a result of true tunneling or tip profiling of the surface similar to contact mode in atomic force microscopy (AFM), imaging response to altering either bias voltage or tunneling current set point is observed. This information is crucial because true tunneling mode of imaging indicates the microscope is mechanically stable enough, within the correction range of the feedback response, for maintaining a constant tip-surface distance and performing STM studies. Furthermore, this will validate the excitation response of the microscope during STM imaging performed on HOPG surfaces so far, as the mechanical reaction will certainly be very different if the tip is in contact with the sample surface. By decreasing bias voltage applied when maintaining the same tunneling current set point, for example, the tip can be brought closer to the surface. If the tip is not in contact with the surface, decreasing the tip-sample distance changes the tunneling barrier potential and thus tunneling contribution between different energy states and different layers of the HOPG surface, which in turn results in a noticeable change of contrast in the images. If the tip is in contact with the surface already when decreasing bias, the change in the absolute tip height is smaller and thus the contribution to the

current remains almost identical. As a result, the contrast change in imaging from altering bias is nearly negligible. Through varying either bias or current set point during imaging HOPG with the new microscope, images show that contrast varies with changing parameters, as conductive (brightly contrasted) atomic features change to less conductive (darkly contrasted) areas and then back to conductive state again. (Figure 5.69) Thus, it is apparent that the images obtained are from tunneling mode instead of contact mode of scanning on the surface.

5.7 Vibrational Analysis

A carefully designed STM system minimizes vibrational excitation through maintaining high resonance frequency of the STM motor and rigid coupling between motor and sample, as described previously in Section 5.2. At the same time, the system must provide an effectively damped low pass filtering system between the STM and the environment, so that any vibrations conducted will be of small amplitudes and as far removed from the resonance frequency of the motor to couple and excite effectively. The first subsection outlines both known and calculated theoretical frequencies of the damping system designed, as well as the theoretical intrinsic resonance values of the microscope. The second subsection presents the measured responses of the scanning piezoelectric transducer as well as tunneling current noise spectra under mechanical excitation and normal operation, in order to assess the damping efficiency of the constructed system and the accuracy of the design and theoretical expectation.

5.7.1 Theory

As presented in Subsection 5.4.2, the low pass filtering and damping setup in the system presented in this chapter consists of a mass-spring system created by pneumatic legs and carbon steel system support frame (that also serves as a sandbox), the silicone lining to further damp vibrations conducted between the system and the support frame, and the suspension springs for the high pressure flow reactor cell. While the silicone lining typically provides a high damping factor for high frequency modes (> 20 Hz), effective filtering of high frequency excitation of the system in both vertical and horizontal modes comes from the use of pneumatic legs, which have low settling time (1.5 s) for both vertical (> 1 Hz) and horizontal (> 1.5 Hz) frequencies (Figure 5.70), in junction with the rigid carbon steel frame that provides added damping and further low pass filtering, by creating profuse amount of vibration coupling junctions through its role as a sandbox, and by its added weight (2500 lbs in addition the system's inherent 1000 lbs). As seen in Subsection 3.3.3, bending modes of an object (through approximated consideration as a well-behaved tubular structure) are in general of much lower frequency than stretching modes. Using a rigid steel frame that extends over the entire dimensions of the system with proper intermediate support points allows minimized excitation of the low frequency bending modes (and stretching modes). In addition, by using a stiffer (or of larger Young's modulus) such as steel, the inherent resonance of the frame is much lower than the wooden support formerly built for the existing high pressure STM system.

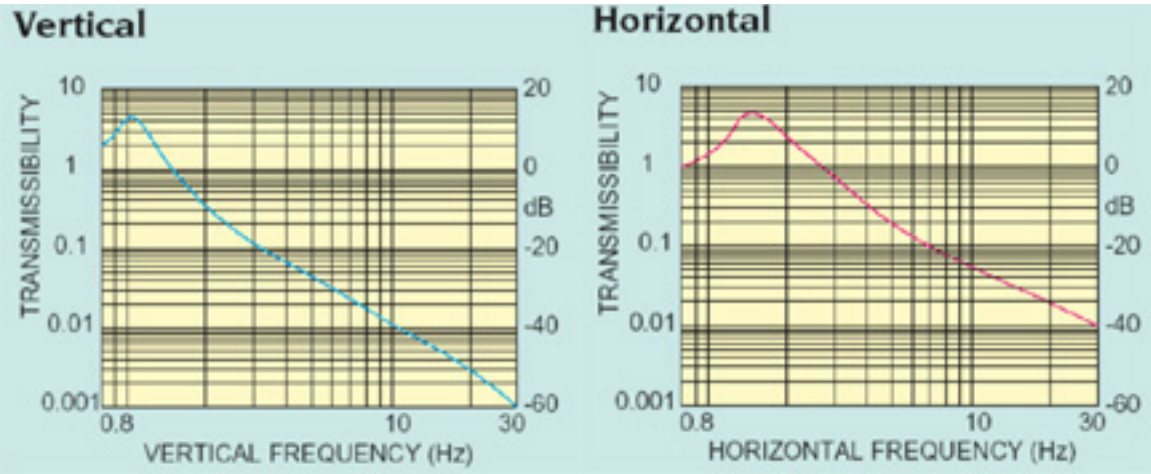

Figure 5.70. Response of pneumatic legs to horizontal and vertical excitation reveals vertical resonance of 1 Hz and horizontal resonance of 1.5 Hz with very small settling time.

Catalog #	Spring constant (lb/in)	Coils/inch	ΔL (mm)	frequency (Hz)	L (mm)
9665K51	30.8	76.9	32.12	2.78	211.22
9665K81	53.3	66.7	16.10	3.93	227.24
9665K12	82.4	58.8	9.18	5.20	234.16
9665K42	170	50	3.78	8.10	239.56
9665K53	13.3	66.7	64.52	1.96	178.82
9665K83	23.5	58.8	32.19	2.78	211.15
9665K54	40	50	16.08	3.93	227.26
9665K15	138.5	38.5	3.58	8.33	239.76
9665K84	5.3	66.7	161.90	1.24	81.44
9665K16	8.2	58.8	92.25	1.64	151.09
9665K57	20	50	32.16	2.78	211.18
9665K85	53.8	38.5	9.21	5.19	234.13
9665K18	125	31.3	3.22	8.78	240.12
9665K19	8	50	80.40	1.76	162.94
9665K21	23.1	38.5	21.44	3.40	221.90
9665K22	62.5	31.3	6.44	6.21	236.90
9665K23	175.6	24.4	1.79	11.78	241.55

Table 5.4. Resonance frequencies of various commercial precision spring from McMaster-Carr Supply Company.

The suspension springs for the pressure cell serves as the final stage of low pass filtering and damping, and are chosen among a variety of miniature precision springs that are commercially available. The resonance frequency of a spring can be related to its extension under stress as the following:

$$f = \frac{1}{2\pi}\sqrt{\frac{g}{\Delta l}}$$

where f is the resonance frequency of the spring, g gravity and Δl the increase in length under load. Thus, it is apparent that the low pass filtering can be made more effective by increasing the extension of the spring under the same load, or simply by using a spring with lower spring constant, without exceeding into the inelastic regime of the spring. Table 5.4 outlines the properties and calculated resonance frequencies, under the weight of the pressure cell setup and given the maximal desired length of 243.34 mm as restricted by the length of the chamber and structures therein, of various commercially available stainless steel precision springs. It is important to note that the frequencies thus calculated represent original elastic conditions of the springs, and the resonance frequencies can be expected to be lower when the springs are loaded under thermal stress, for example, in the case of system bake-out. Thus, it is imperative to put springs under simultaneous physical and thermal loads before introduction to attain accurate performance. Spring 9665K16 (1.6 Hz) is ultimately used in place of Spring 9665K84 (1.2 Hz) for the new system, even though it has a slightly higher resonance frequency, due to the latter spring extends into inelasticity under load after thermal treatment. The suspension spring system serves as an excellent low pass filtering system, as the precision

springs have well defined resonance frequency. However, this also leads to a heightened response and low damping factor near resonance, as a result of narrow response bandwidth imposed by the well defined resonance. In order to increase the damping ability of the suspension spring system, 0.125" thick silicone spacers are periodically inserted into the coils of each spring. Though the resonance frequency of the spring system is evidently not as well defined as a result, the settling time improves noticeably.

	Bending resonance (kHz)	Stretching resonance (kHz)
Scan tube	18.46	62.74
Scan tube + tip holder	16.61	56.47
Sapphire slider	21.66	49.87
Sapphire slider + base plate	17.54	40.39
STM body	19.59	46.76
Body + Stage + Press Plate	18.78	44.83
Fully assembled STM	15.85	37.84

Table 5.5. Resonance frequencies calculated for various Walker STM parts.

The intrinsic bending and stretching responses of the Walker STM motor can be calculated as previously done for the Beetle STM, using the equations outlined in Chapter 3. The components calculated are assumed to be perfect tubular structures with evenly distributed mass along its length, and with any attached mass at the end considered as point mass. Furthermore, all structures are considered affixed at one end as a result of

attachment of the tubular structure to a much heavier fixture, such as the placement of a Macor base plate at the end of the scan tube and the sapphire slider, or the attachment of the motor to the pressure cell, moving the nodal plane of the bending mode from the center to the end of the tube. Table 5.5 contains the theoretical calculation for the basic bending and stretching frequencies of various components within the STM setup. Vibration modes of the pressure cell are assumed to be negligible contributions due to the damped coupling between the STM setup and the pressure cell in form of silicone spacers at the mounting points. The theoretical calculation shows that the intrinsic bending response of the new STM setup is higher in frequency compared to the Beetle STM, with a calculated excitation frequency of 18.46 kHz versus 12.92 kHz for the scan tube without the attached mass of tip receptacle.

Since the sapphire slider containing the scan tube and the tip receptacle are mounted rigidly by two sets of three-point contact maintained through the six shear piezoelectric stacks, additional vibrational modes can be introduced by shearing motion of the flexible contact between the shear piezoelectric stacks and the molybdenum body due to gluing. By assuming the contacts between the piezoelectric stacks and the sapphire slider to be perfectly rigid, the characteristics of the shearing action introduced by the epoxy contacts can be calculated by the following equations:

$$f = \frac{1}{2\pi}\sqrt{\frac{K}{M_{scanner} + 6 \cdot M_{shear}}} \quad \text{where} \quad K = 6(\frac{E \cdot A}{t})$$

where f is the resonance frequency introduced by the weakened contacts, K the effective spring constant, $M_{scanner}$ and M_{shear} the weights of the scanner (that includes sapphire

slider, Macor base plate, scan tube, and tip receptacle) and each of the shear piezoelectrics, respectively, E the Young's modulus for the epoxy after curing (492 MPa), A the total contact area between each stack and the molybdenum body, and t the thickness of the epoxy applied (assumed to be between 10 and 100 μm). The thus calculated resonance response is between 3.45 kHz and 10.9 kHz, which indicates that in general application of epoxy in constructing a STM must be judicious: While it is essential to apply enough to ensure good mechanical rigidity upon curing, the epoxy applied must be as thin as possible to prevent introduction of weak contact points in the microscope.

Lastly, the effect of the length of the cone/tapered section of the STM tip to inherent bending mode of the probe is also explored. Assuming the tip end to be a pyramid with a square cross section rigidly mounted to the rest of the length of the tip, and the physical properties of the materials are equal to the proportional sum of those of the components, the bending vibrational mode of a tip that is exposed outside of the tip holder can calculated by using the following equations:

$$f_{\perp} = \frac{1}{2\pi}\sqrt{\frac{K_{\perp}}{M}} \qquad \text{where} \quad K_{\perp} = \frac{3\pi}{64}\frac{E \cdot d^4}{l^3}$$

where $f_{\perp}$ is the bending frequency of the tip, $K_{\perp}$ the associated spring constant, M the effective mass of the tip (which is a third of the overall mass, assuming even mass distribution along the length), E the effective Young's modulus (according to the above assumption, 210.8 GPa for Pt-40%-Rh composition), d the dimension of the square cross section of the tip cone (assumed to be 50 μm), and l the length of the tip cone. The

calculated resonance frequencies are 23.8 kHz and 5.9 kHz for 0.5 mm and 1.0 mm long tapered tip respectively. Thus, it is important to reduce the tip taper during etching or other type of fashioning of the type, as a macroscopically small difference in length can lead to a much worsened vibrational response of the scanning probe during studies.

5.7.2 Analysis of Measured Responses

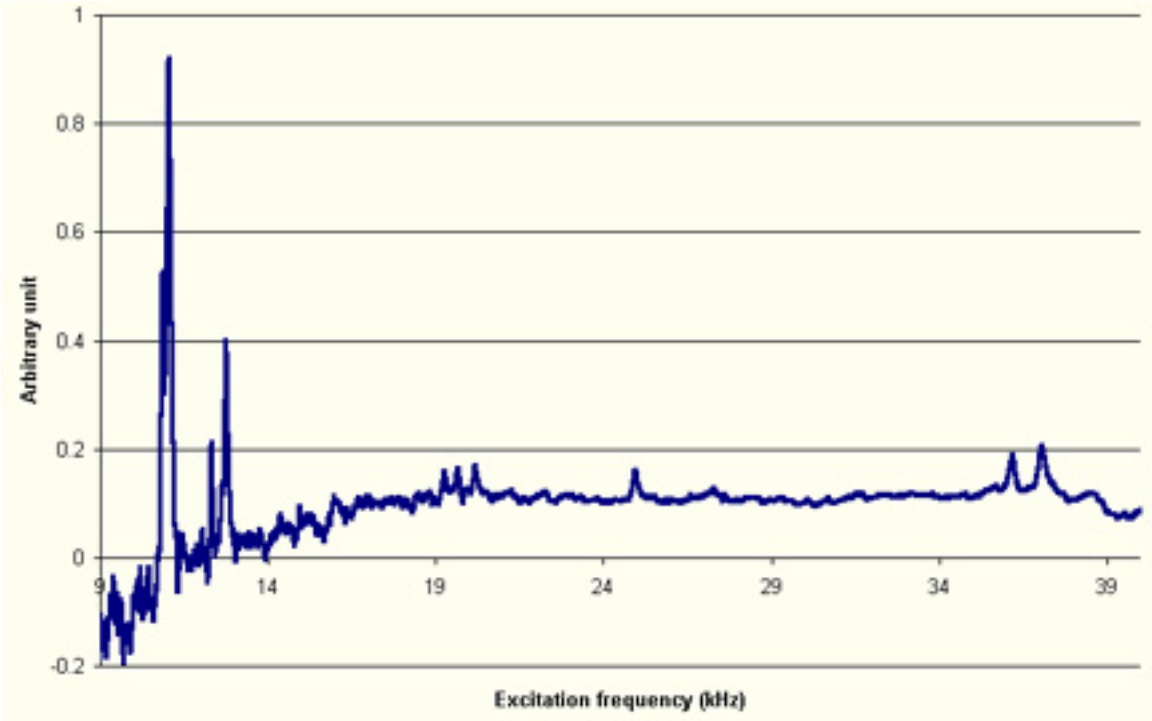

Figure 5.71. Vibrational response in the bending mode of the Walker STM shows strong response in 10-13 kHz, and mild responses in 19-21 kHz, 24.9 kHz, and 35-38 kHz regions. Weak response in 14-16 kHz range is also observed (as shown in Figure 5.75).

Using the setup as described in Subsection 3.3.3 to excite the shear and scanning piezoelectric transducers, with the STM mounted to an optical table without the pressure cell as described in Subsection 5.6.1, we can measure the vibrational susceptibility of the

microscope by detecting excitation response at the scan tube and compare the measured responses to the calculated values. Excitation of the scanning piezoelectrics reveals similar responses in the detection of both bending (Figure 5.71) and stretching (Figure 5.72) modes, showing strong responses between 10 kHz and 13 kHz, and mild responses at regions between 19 kHz and 21 kHz, 24.9 kHz, and between 35 kHz and 38 kHz.

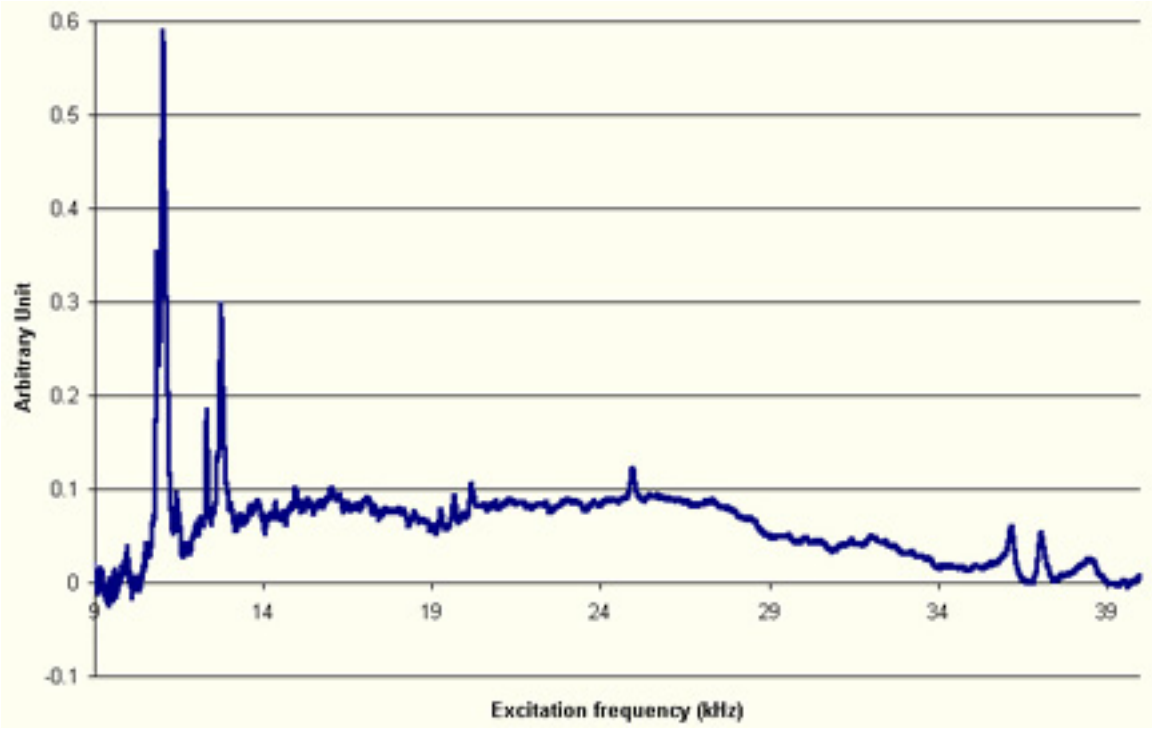

Figure 5.72. Vibrational response in the stretching mode of the Walker STM reveals similar responses as in the case of the bending mode.

While measuring the excitation of the scan tube in response to vibrations induced by the shear piezoelectric stacks are not relevant as the shear stacks are immobile and used only to mount down the scanner during imaging, excitation response of the shear stacks itself is useful in identifying additional source of vibration frequencies within the mechanical response spectra of the scan tube. By exciting a shear piezoelectric stack to

provide enough mechanical disturbance in the rigid system while measuring another stack, strong excitation modes are found in regions between 19 kHz and 22 kHz and between 26 kHz and 32 kHz. (Figure 5.73) Additional vibrational modes can be found between 69 kHz and 75 kHz, which are most likely the higher harmonics of vibrational modes. By comparing to the expected vibration regime as a result of weak gluing junctions between the shear stacks and the molybdenum body as calculated in the previous section, the lack of response below 12 kHz in the shear stack response spectra indicates the shear stacks are firmly attached to the STM body.

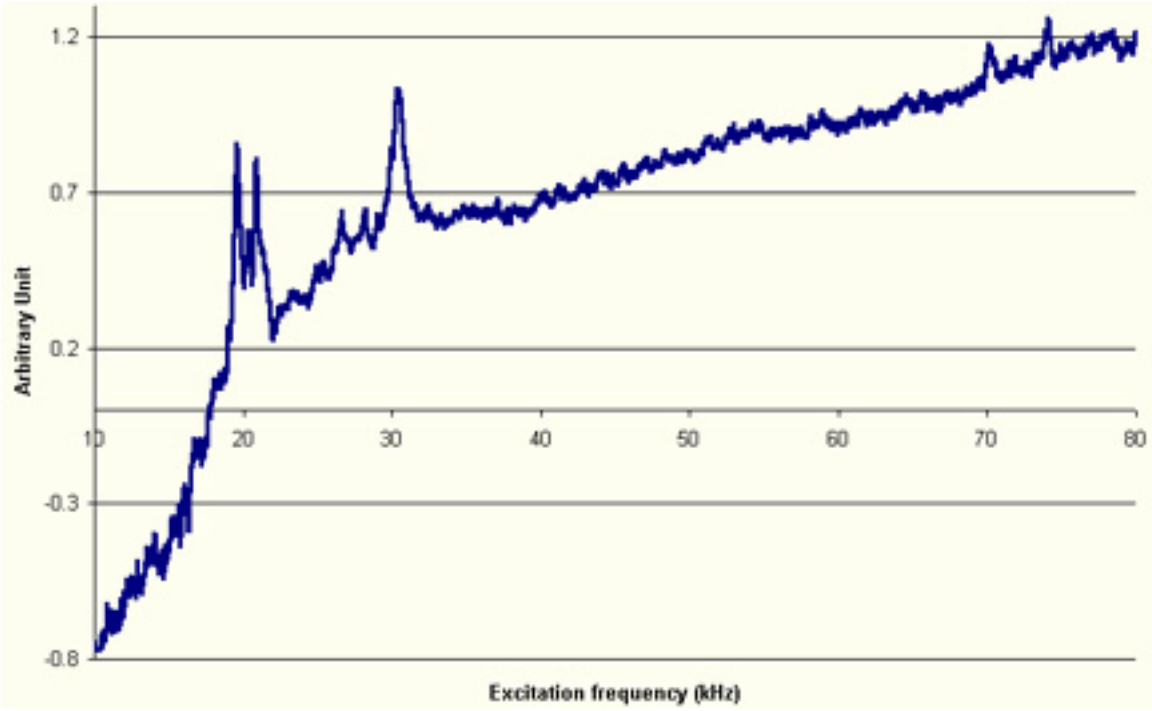

Figure 5.73. Vibrational response in the shear piezoelectric stack of the Walker STM upon excitation reveals strong responses in the 19-22 kHz, 26-32 kHz, and 69-75 kHz regions.

By comparing the excitation spectra of the scan tube to those of the shear stacks, the resonance frequencies detected between 19 kHz and 21 kHz for the scan tube cannot

be an intrinsic response of the scanning piezoelectrics. Most likely, it is a result of excitation modes of the shear stacks or the bending responses of the STM body. While the peak at 24.9 kHz on the excitation spectra of the scan tube cannot be attributed with certainty to any calculated response, the resonance frequencies detected between 35 kHz and 38 kHz can be attributed to the stretching modes of the scanner, the molybdenum body, and the entire STM setup (which includes the motor, sample stage and holder, and the CuBe press plate). The four strong vibration peaks detected at the lower frequency (10.8 kHz, 11.0 kHz, 12.3 KHz, and 12.7 kHz) are unique to vibration detection at the scan tube during excitation of the scan tube or the shear stacks, and are thus assigned to be the various bending modes related to the scanning piezoelectric transducer.

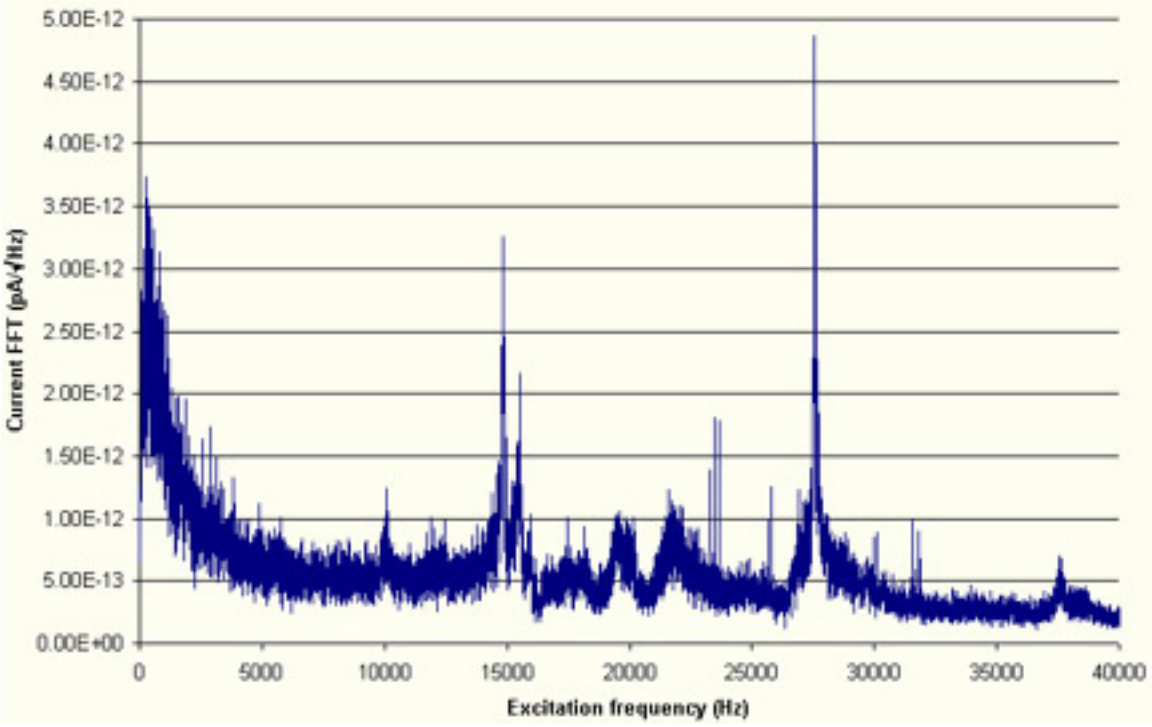

Figure 5.74. Tunneling current noise spectrum of the Walker STM, upon physical agitation of the system, shows strong mechanical response between 14 kHz and 38 kHz.

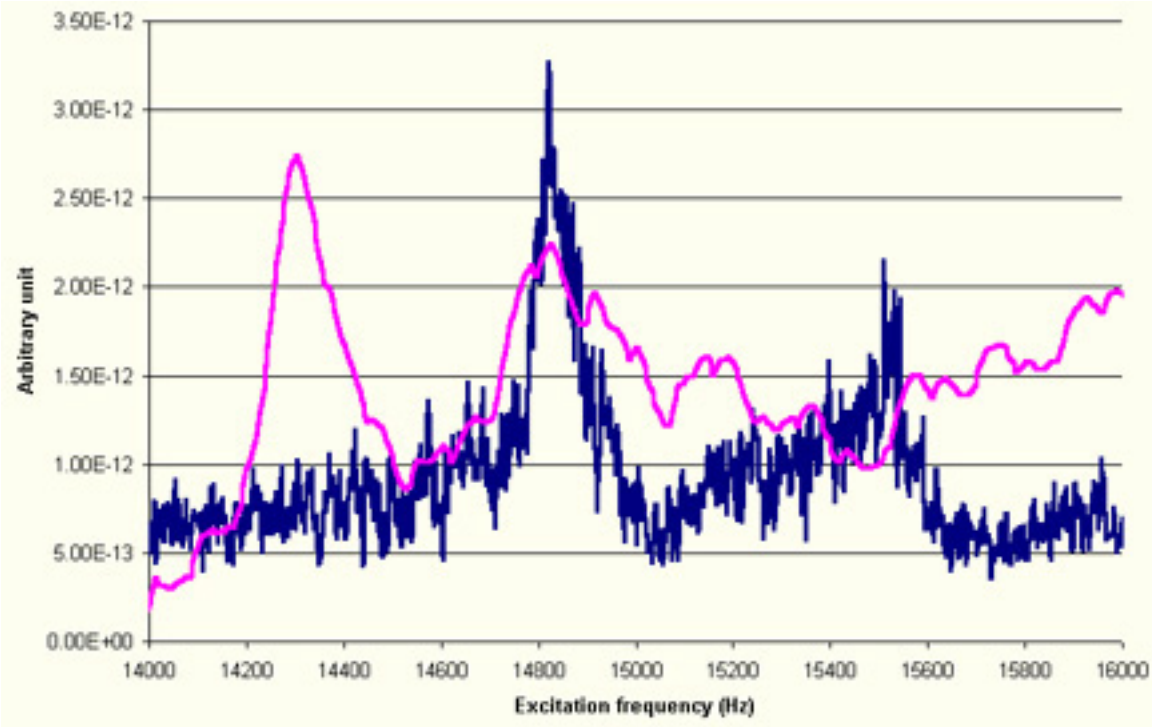

Figure 5.75. Current noise (blue) and vibrational response (magenta) spectra of Walker STM both show additional mechanical response between 14 kHz and 16 kHz, previously too weak to be detected under physical detection. The shift in peaks between two methods is due to non-linearity of mechanical driving amplitude inherent in setup.

Under tunneling condition with the pressure cell containing the STM vibrationally damped by only suspension springs with silicone spacers, noise spectra of the tunneling current have been taken to show that mechanical vibrations between 19 kHz and 38 kHz remain noticeable during physical excitation of the pressure cell. (Figure 5.74) In addition to the mechanical responses indicated above, weak resonance responses can be detected at the scan tube between 14 kHz and 16 kHz during physical excitation as well as at tunneling current noise spectra. (Figure 5.75) Thus, it confirms the mechanical vibration modes detected earlier are intrinsic to the STM.

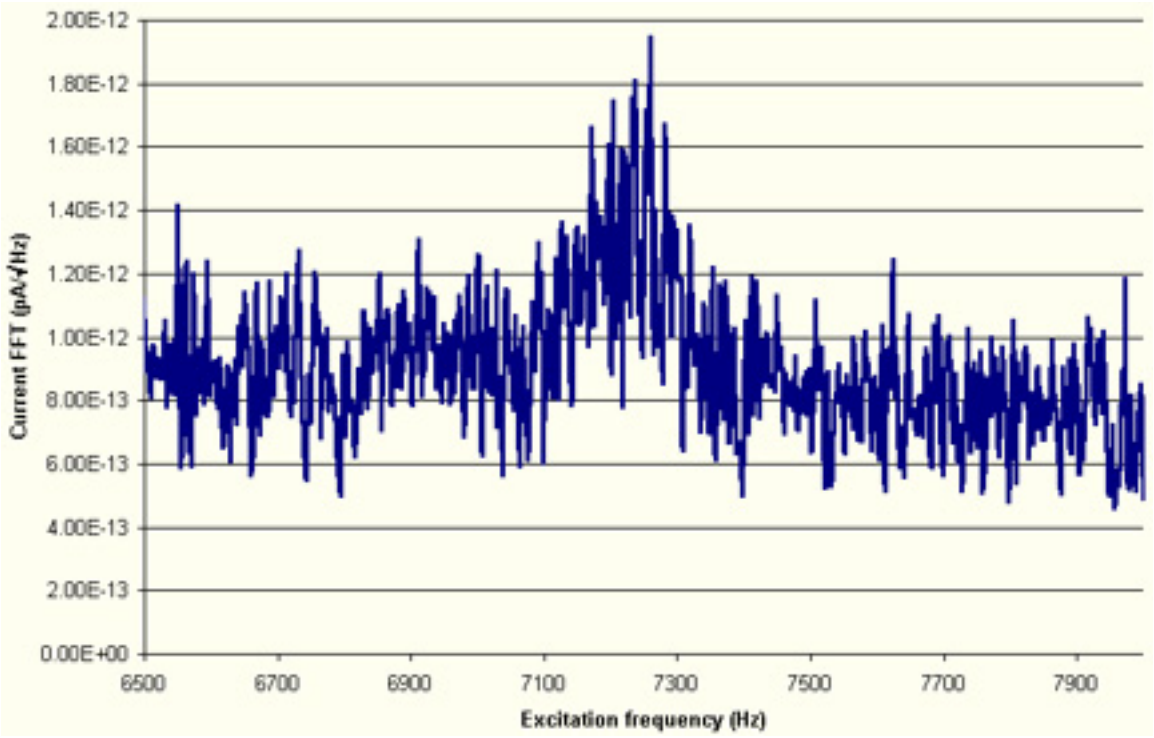

Figure 5.76. Transient low frequency resonance of the Walker STM at 7.2 kHz appears and disappears upon the introduction of different tips.

A transient and weak mechanical response is sometimes detected at 7.2 kHz during tunneling (Figure 5.76), and varies upon tip exchange. This frequency can either be attributed to a tip-induced effect on the tunneling junction, or a possible and occasional mechanical instability in the magnetic attachment of the tip holder to the tip plate at the end of the scan tube. Since no other mechanical responses are detected within the tunneling current noise spectra between 0 and 74 kHz, it thus has been shown that the complex inclusion of the STM into the pressure cell and subsequently to the custom XYZΘ manipulator stage does not incur any noticeable mechanical compromises during imaging.

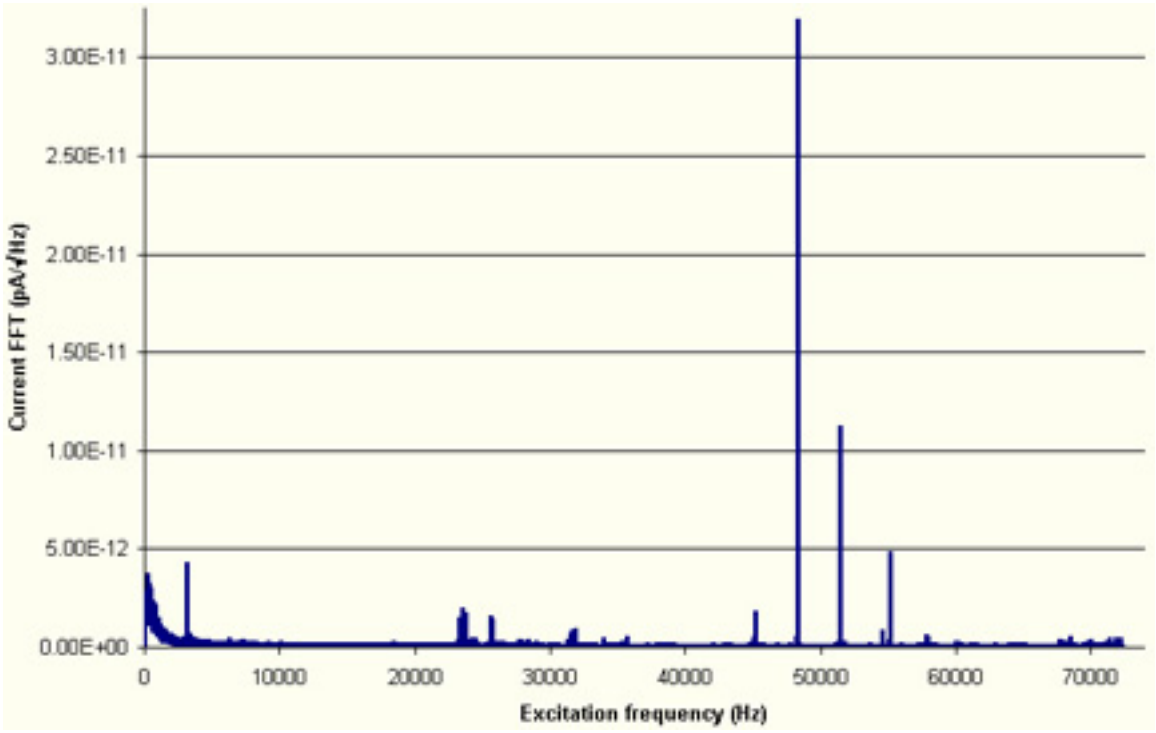

Figure 5.77. Well-defined electrically-induced noise frequencies are left, once mechanical resonances are damped.

In addition to mechanical responses, electrical noises of well defined frequencies are found at 3.1 kHz, 23.3 kHz, 23.5 kHz, 23.7 kHz, 31.7 kHz, 31.8 kHz, 31.9 kHz and above 40 kHz within the tunneling noise spectra. (Figure 5.77) Only the 3.1 kHz electrical response poses a significant concern to imaging, as the other frequencies observed are too far removed to couple with the frequency of interest (< 1 kHz). Since the test setup lacks proper electrical shielding, further tests need to be conducted in order to isolate and identify the source for the 3.1 kHz electrical noise.

5.8 Challenges and Limitations

Despite various mechanical and thermal precautions displayed in the design of the new STM system, and excellent mechanical performance presented thus far by the associated STM motor, a variety of potential problems within the current design, especially the thermal aspect, remains to be examined and elucidated within vacuum and under operating pressure range. While foreseeable limitations such as the reduced scan range of the microscope as imposed by the rigid design and the low cooling rate of the sample during annealing as a result of the highly insulating material chosen for the sample holder are as expected and can be resolved by alternate means as physically reinserting the sample and increasing thermal dissipation rate on the preparation stage, various thermal and mechanical issues remain to be addressed.

First and foremost is the thermal performance of the STM design, which remains largely unexplored thus far. While the actual sample holder is built out of fused silica for low thermal conductivity in order to compensate for the high power needed for the button heater as a result of high annealing temperature in vacuum and elevated thermal performance needed under increased pressure, the insulating ability of the geometry and material chosen and the actual thermal load under pressure remain to be tested. While the ability to assume as a flow reactor alleviate the potential thermal depolarization of the piezoelectric transducers in form of an external active cooling in the gas loop, an optimal flow range must be found to effectively remove heated gas from the pressure cell, while maintaining a low enough rate to minimize turbulence within the cell as well as to maximize external cooling. At the same time, it is important to identify the thermal effect

on the mechanical stability of the microscope, in form of drift rate as well as performance of the leaf spring and wire spring in securing the sample holder as well as additional electrical connections under thermal stress.

Mechanical stability of the microscope during experiments has been extensively tested, and *in vacuo* manipulation, especially relating to transfer mechanism within the STM chamber, remains unexamined under vacuum, where friction is considerably higher due to the lack of carbonaceous lubrication normally present in ambient environment. The precise fit in the pins-and-holes system within the mounting mechanism for the pressure cell can be more difficult under vacuum, and necessary modification must be made accordingly as any sudden mechanical movement or stress may cause breakage of wiring as well as system components that will require considerable amount of repair time due to their compact assembly.

The delicateness of manipulation and the associated compactness and fragility of the parts involved requires a high demand of caution as well as finesse, which has from time to time proved to be problematic when visualization has to be done by and limited to secondary means of CCD cameras, due to the requirement of the wobble stick entry has to be concentric to the limited access of the pressure cell. To complicate the matter further, the resolution of the fiberscope image is low and limited by the number of optical bundles within the scope. While an alternate fiberscope of higher resolution and magnification can be highly beneficial, it is financially more feasible to introduce additional view ports, especially onto the custom mounting fitting for the wobble stick setup, to allow additional direct and secondary visualization means.

The tip exchange mechanism, which includes securing the tip holder during transfer and precise coupling of the tip holder to the magnetic tip plate at the end of the scan tube, still requires additional modification and adjustment to function reliably to prevent occasional weak coupling that gives rise to the weak mechanical response at 7.1 kHz. The amount of retraction necessary, once the tip holder is magnetically coupled, before the extraction of the tip exchanger can be predicted more effectively if a capacitance measurement of distance can be performed. The capacitance measurement can be installed as simply as partially plating one side of the sapphire slider, and measuring its capacitance with respect to ground as the slider is motored along.

Further challenges lie in the pressurization of the flow reactor cell. While the potential problem of gas leakage from the pressure cell is most likely through wiring junctions and can be simply corrected by judicious use of sealing epoxy, the problem of mechanical vibration conducted through the polymer gas line, though damped by silicone sleeves and o-rings, still needs to be tested and most likely remains to be resolved. The gas line must be fashioned long enough to create a relaxed spring so that the pressure cell is rested and damped entirely on suspension springs, while it has to be short and light enough (along with the added weight of damping sleeves and o-rings) to minimize reaction volume and surface area as well as to prevent slumping of the gas line onto the docking scaffold thus making mechanical loops for vibration conduction.

Lastly, electrically induced interferences such as that induced at 3.1 kHz remain to be identified and resolved. Additional shielding as well as twisting of inverted signals

(such as the Y+ and Y- signals for the scanning piezoelectrics and similarly for the X+ and X- signals) to minimize inductive coupling effects may be required.

5.9 References and Notes

[1] Curtis, R.; Mitsui, T.; Ganz, E. *Rev. Sci. Instrum.* **1997**, *68*, 2790.

[2] Kuipers, L.; Loos, R. W. M.; Neerings, H.; Horst, J.; Suwiel, G. J.; de Longh, A. P.; Frenken, J. W. M. *Rev. Sci. Instrum.* **1995**, *66*, 4557.

[3] Hoogeman, M. S.; van Loon, D. G.; Loos, R. W. M.; Ficke, H. G. ; de Hass, E.; van der Linden, J. J.; Zeijlemaker, H.; Kuipers, L.; Chang, M. F.; Klik, M. A. J.; Frenken, J. W. M. *Rev. Sci. Instrum.* **1998**, *69*, 2072.

[4] Pohl, D. W. *Surf. Sci.* **1987**, *181*, 174.

[5] Frohn, J.; Wolf, J. F.; Besocke, K.; Teske, M. *Rev. Sci. Instrum.* **1989**, *60*, 1200.

[6] Pan, S. H.; Hudson, E. W.; Davis. J. C. *Rev. Sci. Instrum.* **1999**, *70*, 1459.

[7] Besenbacher, F. *Rep. Prog. Phys.* **1996**, *59*, 1737.

[8] Weeks, B. L.; Durkan, C.; Kuramochi, H.; Welland, M. E.; Rayment, Trevor. *Rev. Sci. Instrum.* **2000**, *71*, 3777.

[9] Rasmussen, P. B.; Hendriksen, B. L. M.; Zeijlemaker, J.; Ficke, H. G.; Frenken, J. W. M. *Rev. Sci. Instrum.* **1998**, *69*, 3879.

[10] Petersen, L.; Schunack, M.; Schzefer, B.; Linderoth, T. R.; Rasmussen, P. B.; Sprunger, P. T.; Laegsgaard, E.; Stensgaard, I.; Besenbacher, F. *Rev. Sci. Instrum.* **2001**, *72*, 1438.

Chapter 6

Conclusions

6.1 Summary of Results

The aim of the work presented therein is to take advantage of scanning tunneling microscope's (STM) capability for operation under a variety of environments under real time and at atomic resolution to monitor adsorbate structures and mobility under high pressures, as well as to design a new generation of STM systems that allow imaging *in situ* at both higher pressures (35 atm) and temperatures (350 °C).

The design of a high pressure, high temperature scanning tunneling microscope system, that is capable of monitoring reactions *in situ* at conditions from UHV and ambient temperature up to 1 atm and 250 °C, is briefly presented along with vibrational and thermal analysis, as this system serves as a template to improve upon during the design of the new ultra high pressure, high temperature STM.

Using this existing high pressure scanning tunneling microscope we monitored the co-adsorption of hydrogen, ethylene and carbon dioxide on platinum (111) and rhodium (111) crystal faces in the mTorr pressure range at 300 K in equilibrium with the gas phase. During the catalytic hydrogenation of ethylene to ethane in the absence of CO the metal surfaces are covered by an adsorbate layer that is very mobile on the time scale of STM imaging. We found that the addition of CO poisons the hydrogenation reaction and induces ordered structures on the single crystal surfaces. Several ordered structures were observed upon CO addition to the surfaces pre-covered with hydrogen and ethylene: a rotated ($\sqrt{19}$ x $\sqrt{19}$)R23.4° on Pt(111), and domains of c(4 x 2)-CO+C_2H_3, previously unobserved (4 x 2)-CO+3C_2H_3, and (2 x 2)-3CO on Rh(111). A mechanism for CO poisoning of ethylene hydrogenation on the metal single crystals was proposed, in which CO blocks surface metal sites and reduces adsorbate mobility to limit adsorption and reaction rate of ethylene and hydrogen.

In order to observe heterogeneous catalytic reactions that occur well above ambient pressure and temperature, a custom STM motor has been designed and constructed in-house. The new STM design features a much reduced size and a rigid coupling to the sample, and has been tested to show considerably higher resonance frequency than conventional tripod designs, providing the ability to image faster and yielding smaller susceptibility to noise. A flow reactor cell of much reduced volume for pressures up to 35 atmospheres has also been designed and constructed to house the new STM. The small volume reduces gas consumption and sensitivity to impurities in high pressure gases, as well as maximizes product concentration and reduces response time.

The ability to flow reactant gases also allows for continuous monitoring of reaction mixture by mass spectrometry or gas chromatography, and permits correlation of structural information from STM and reaction kinetics. The reactor cell containing the STM is placed inside an UHV system to allow cleaning and characterization of sample before and after experiments, as well as continuous monitoring by mass spectrometry or gas chromatography through a leak valve. The new ultra high pressure system also allows *in vacuo* sample and tip exchange through a load lock, without exposing the system to impurities in air. This new ultra high pressure, high temperature STM system has been shown to perform with major improvements over the existing high pressure, high temperature STM system. Unlike the older system which requires extensive vibration damping setup in order to operate, the new system is shown to be less susceptible to noise, and be able to image atomic steps with no vibration isolation and atomically resolve highly ordered pyrolytic graphite with only spring suspension and a cut tip. Extensive vibrational analysis of the new system is presented, as well as an appendix of AutoCAD-generated design schematics for the major components of the system is included at the end.

6.2 Future Direction

The ability of scanning tunneling microscopy to resolve surface structures at atomic resolution and the potential capability to measure dynamic studies at a more refined time scale need to be explored and fully taken advantage of, due to this technique's unique capacity to obtain real time and space measurement. While it is

difficult to construct a STM that has temporal resolution that is comparable to ultra fast spectroscopy on the femtosecond or better time scale due to the limited response time of piezoelectric motors, more mechanically stable and faster STM motors can still offer a temporal resolution of microsecond timescale. Given the author's experience in both the design and application of STM, it is the author's opinion that the most foremost problem of using STM in reaction studies lies in thermal control to reduce both thermal drift during image and thermal excitation of electrons at the tip, both of which can affect physical and electronic resolutions. As STM becomes more rigid and compact to enhance mechanical stability, careful plans must be in isolating thermal input to avoid unnecessary thermal load that can both reduce thermal control and stability of the piezoelectrics in the STM motor. Lastly, the enhanced daily difficulty of obtaining an atomically sharp enough tip for imaging under high pressure and temperature requires a focused effort to find ways to create and condition reliable tips, as tips tend to degrade quickly under these harsh conditions while conditioning also becomes less controllable and dependable.

Appendix

Collection of AutoCAD Drawings for UHP-STM

This section includes alphabetically the detailed design schematics for all major custom components constructed during the creation of the ultra high pressure, high temperature scanning tunneling microscope (STM) system. While the dimensions recorded herein are precisely representative of the functional modules as they have been constructed, care must be taken in recreation as minor modifications such as chamfering and filleting are not indicated in the drawings. It is the author's hope that the reader will find the designs appended here highly informative for both reproduction of the system as well as improvement to create the next generation of *in situ* reactor STM systems.

I – Bayonet Plug

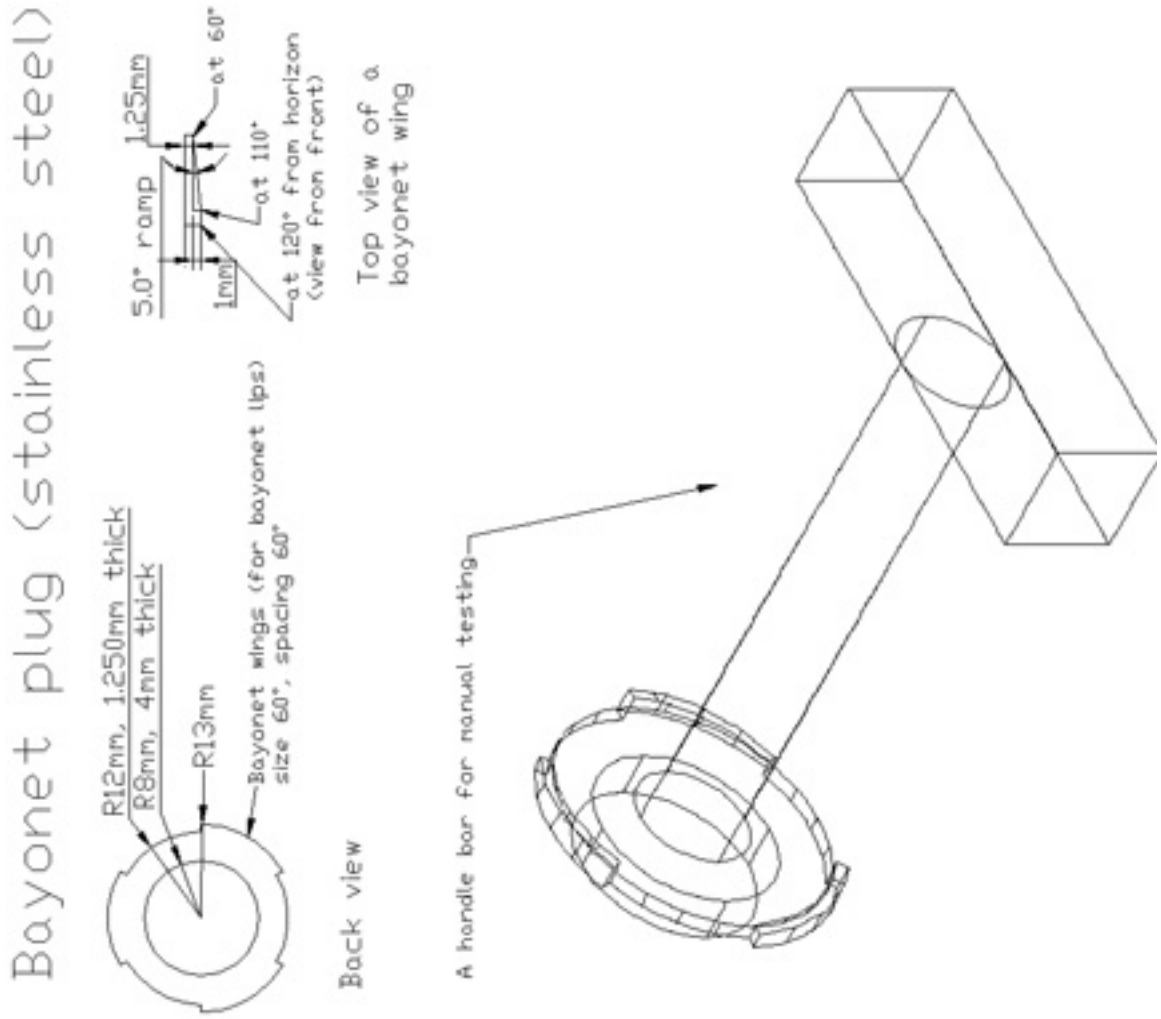

II – Cell Bottom

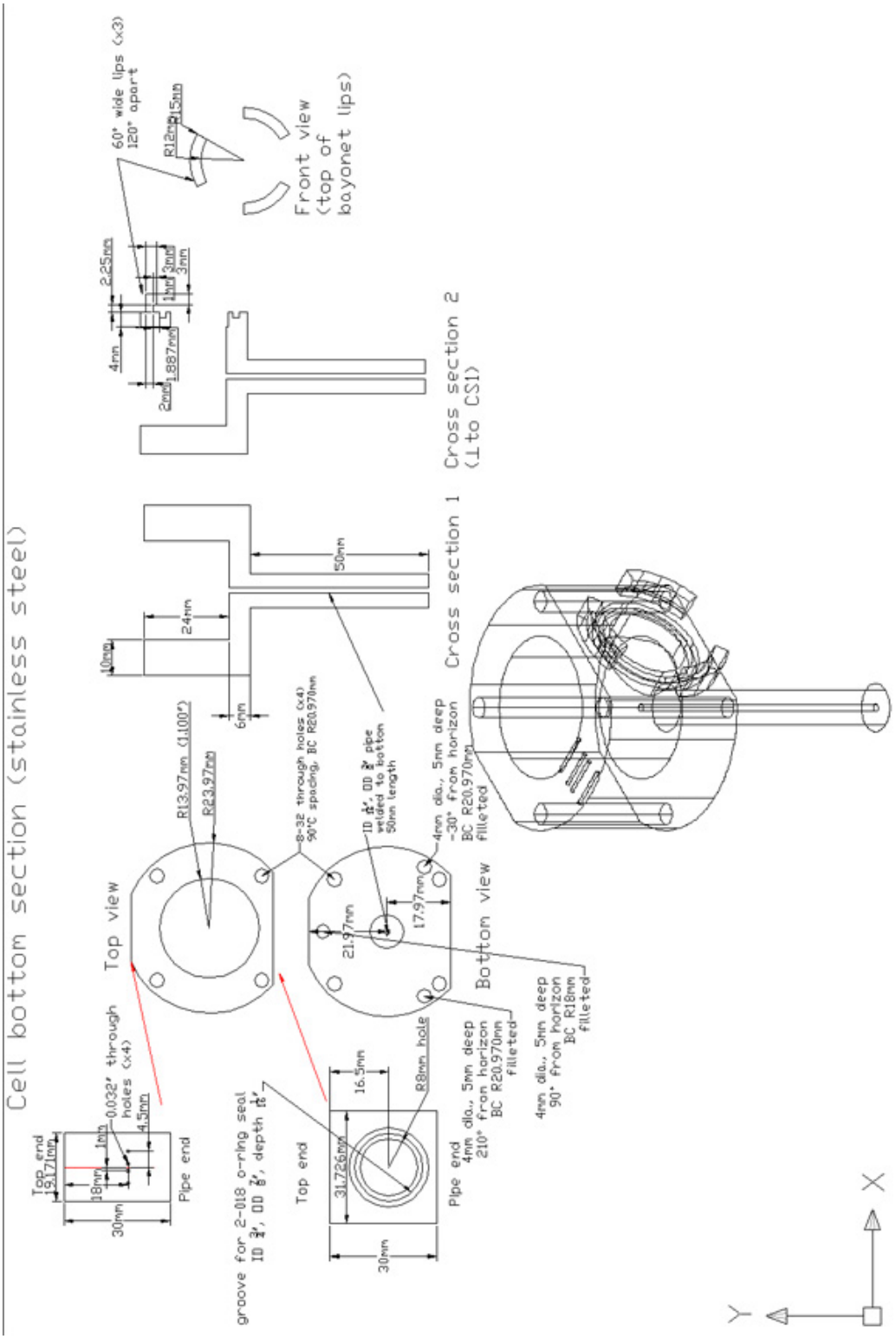

III – Cell Lids

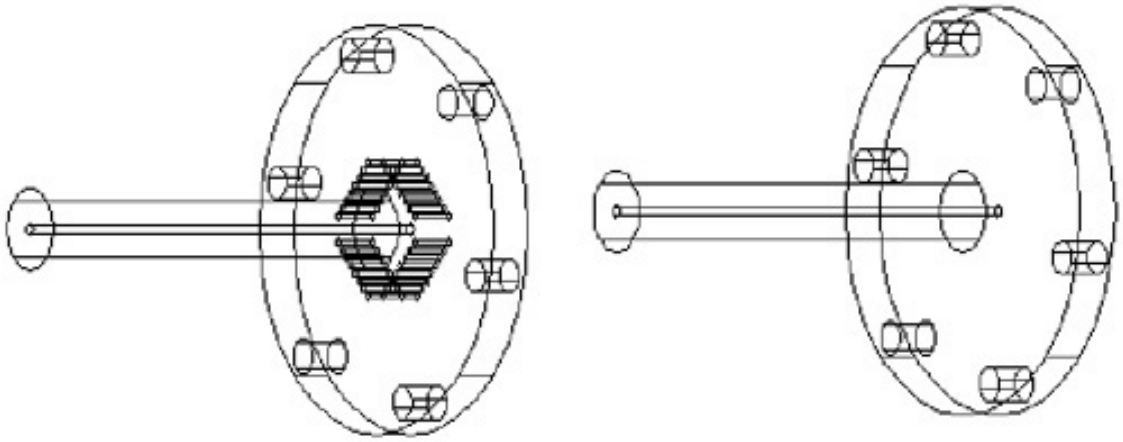

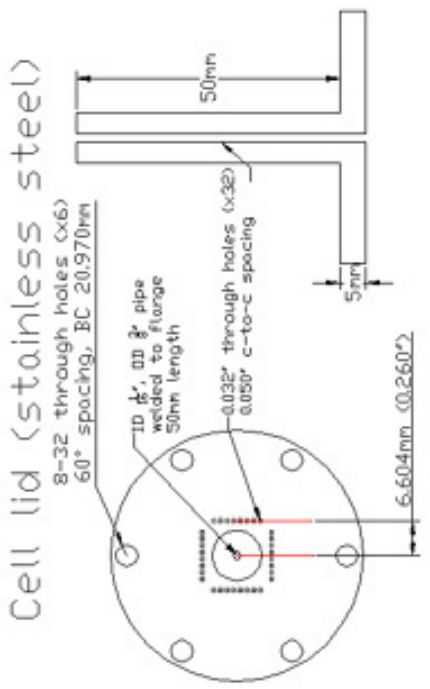

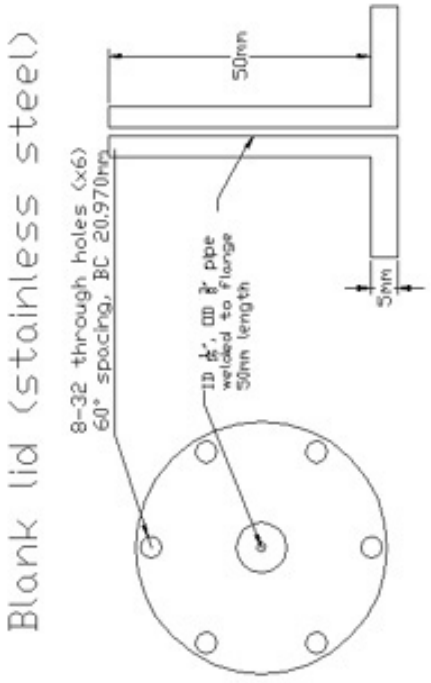

IV – Cell Middle

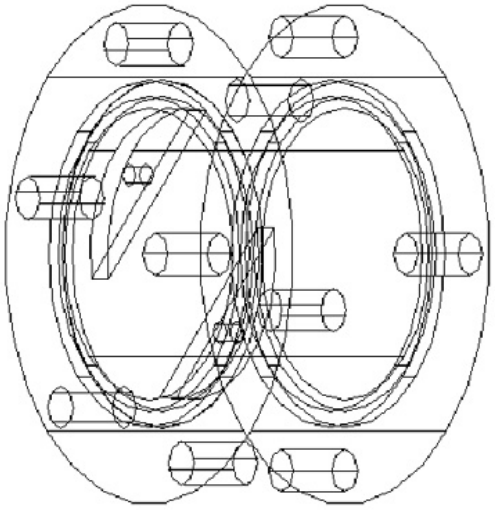

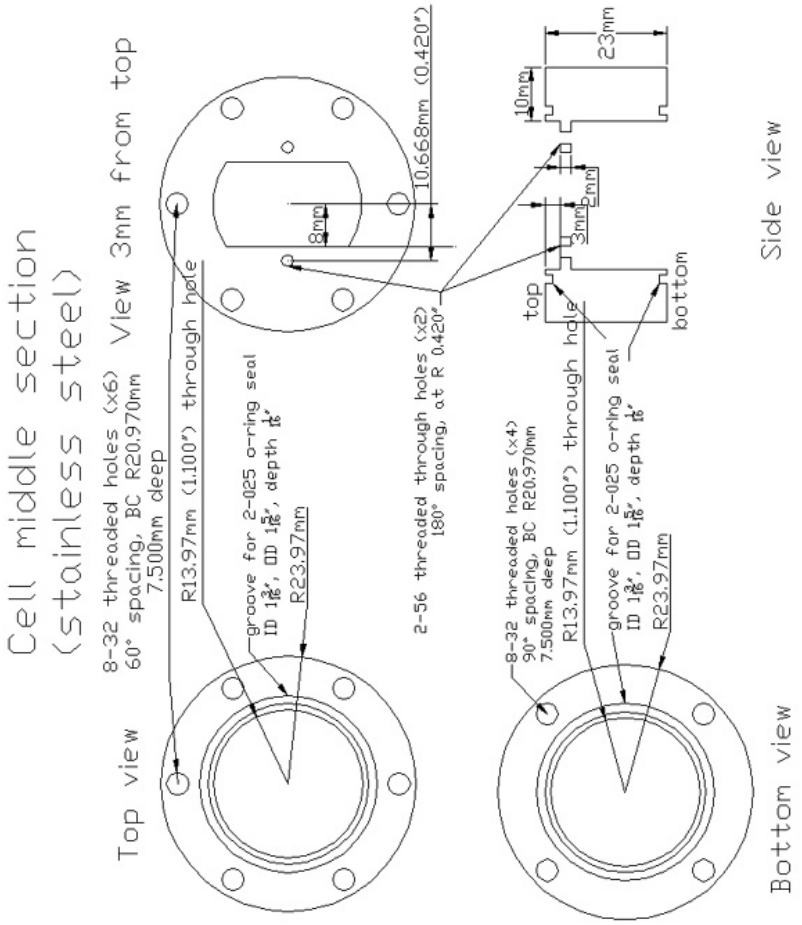

V – Cell Restraint Bottom Plate

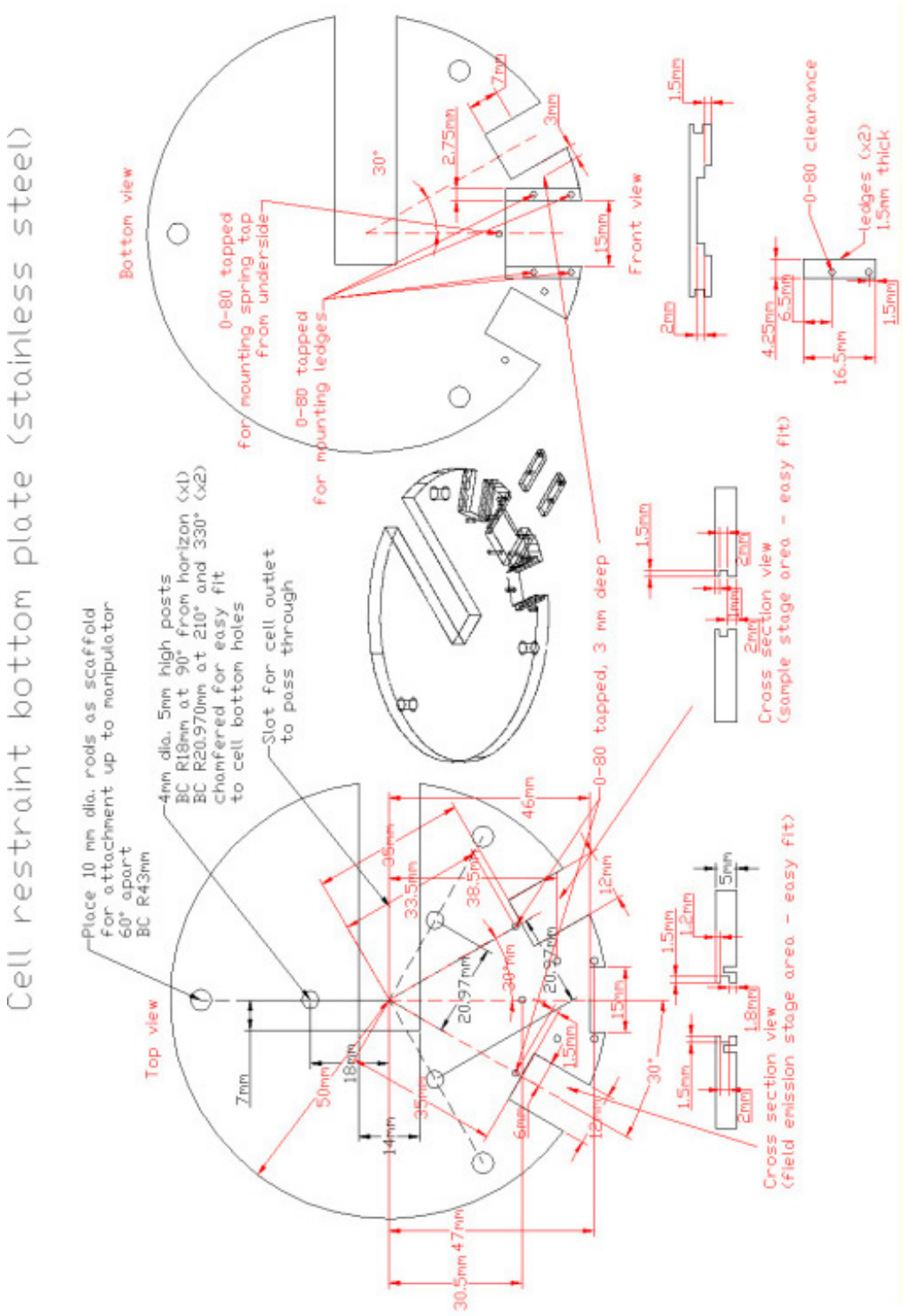

VI – Cleaning Stage Plates

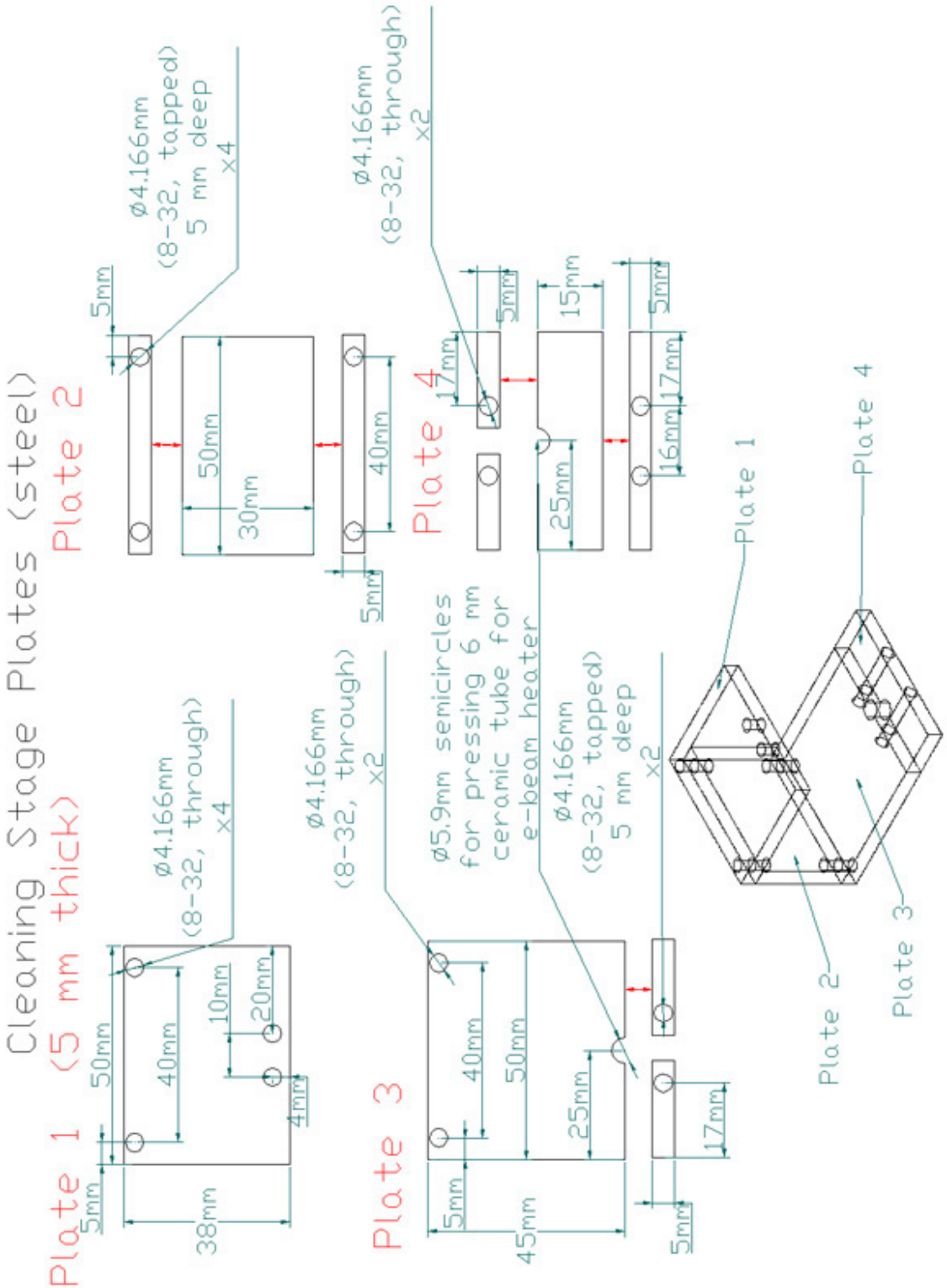

VII – Cleaning Stage

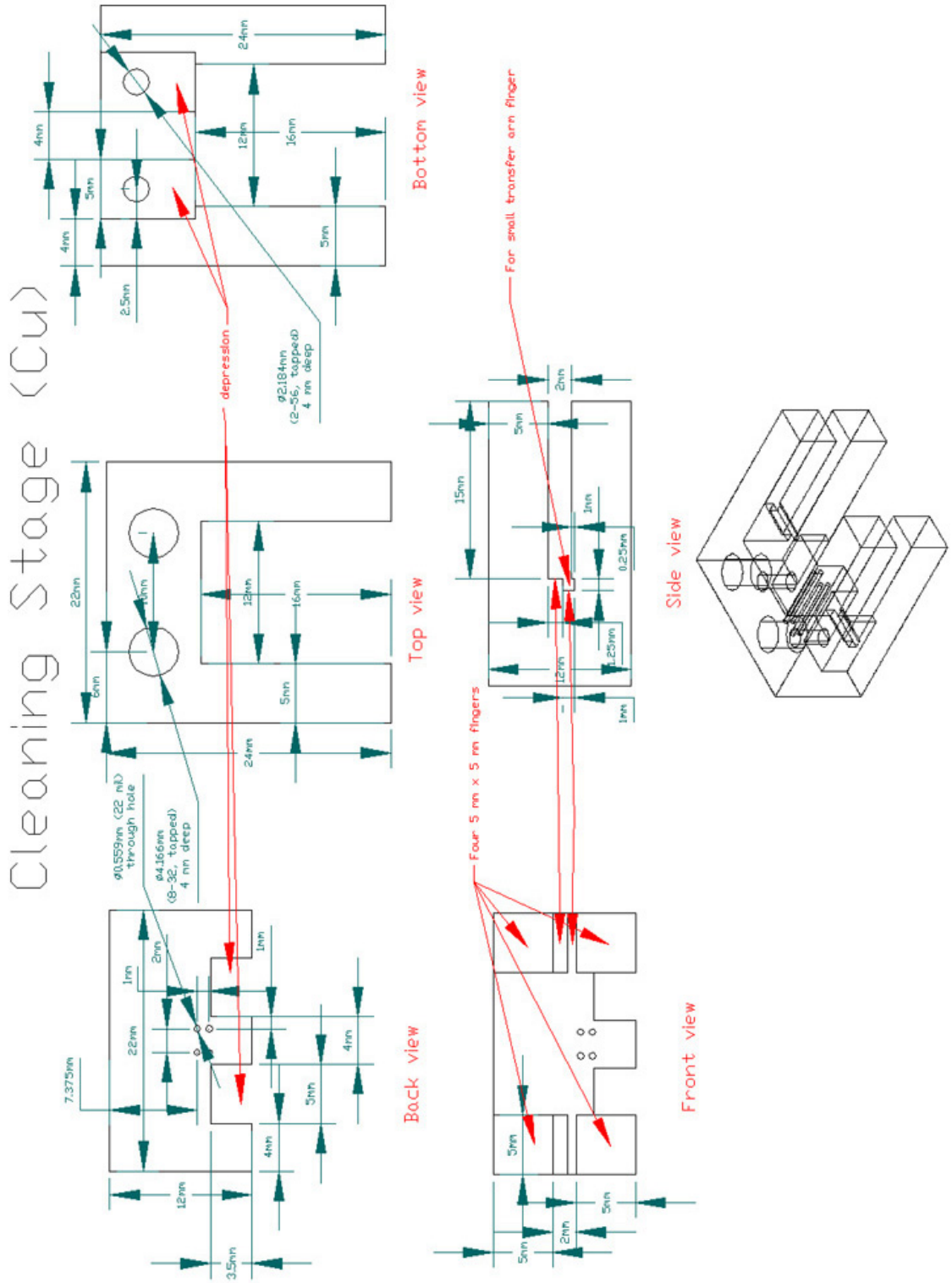

VIII – CuBe Press Plate (for STM)

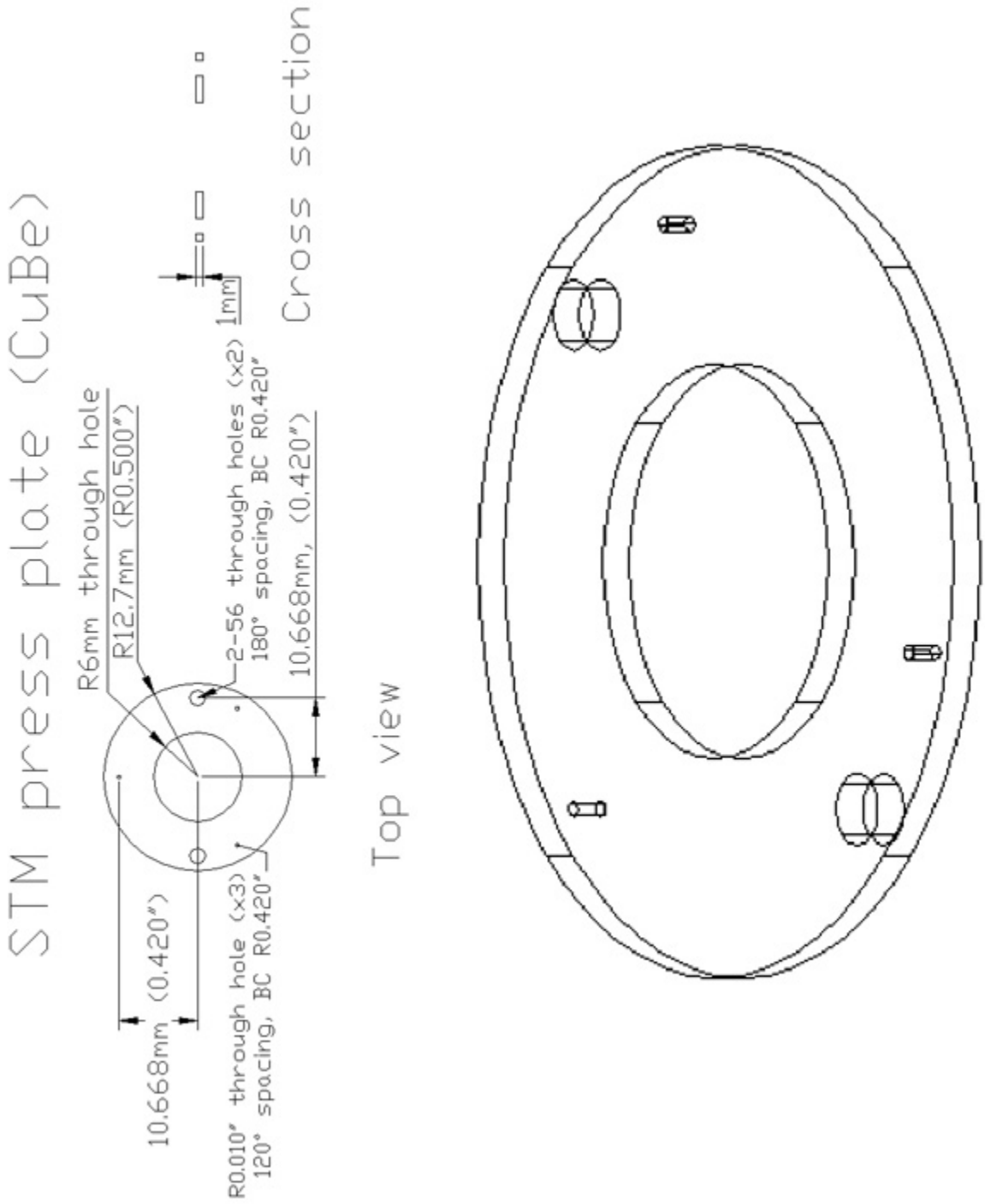

IX – Docking Station

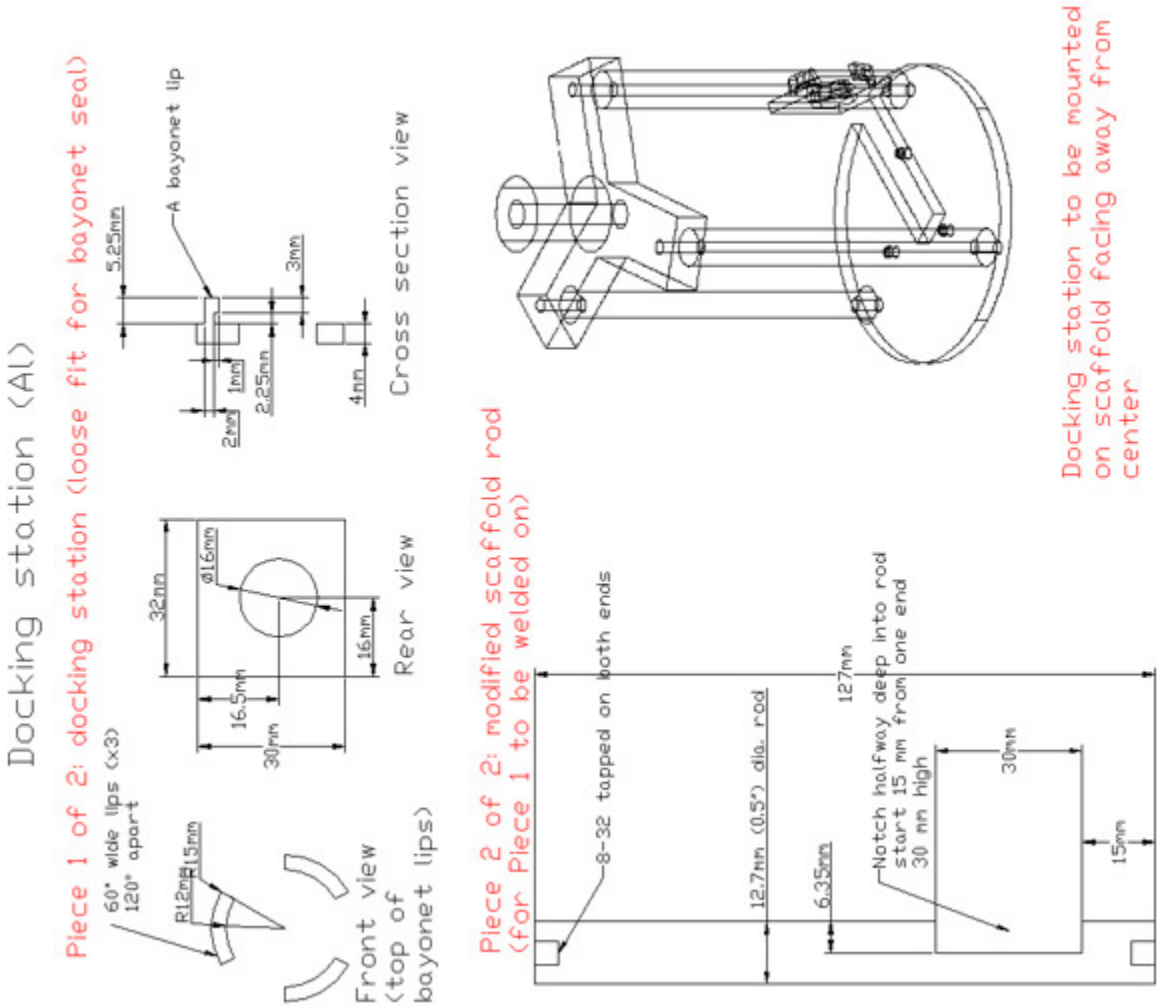

X – Emission Stage Accessories

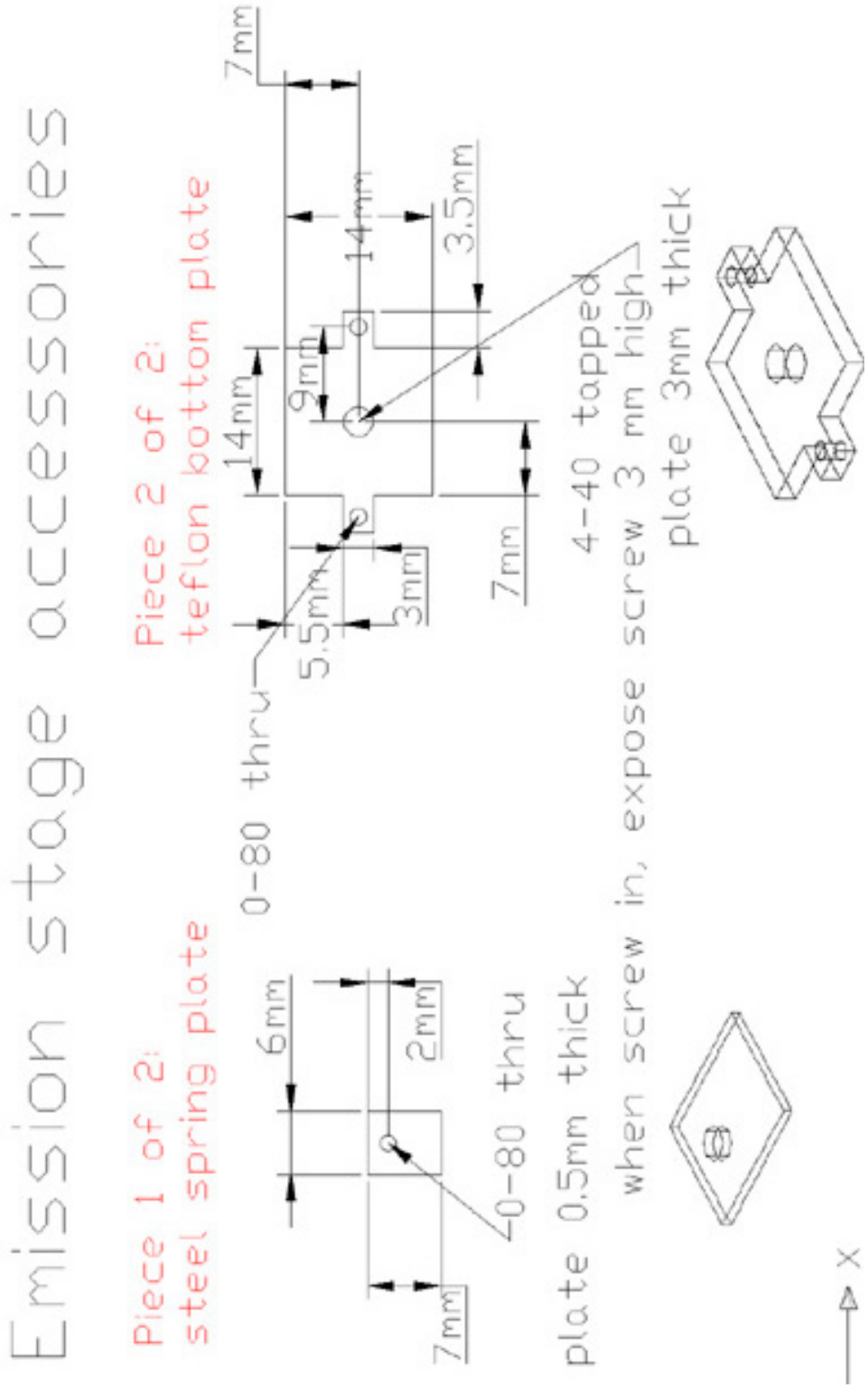

XI – Field Emission Plate

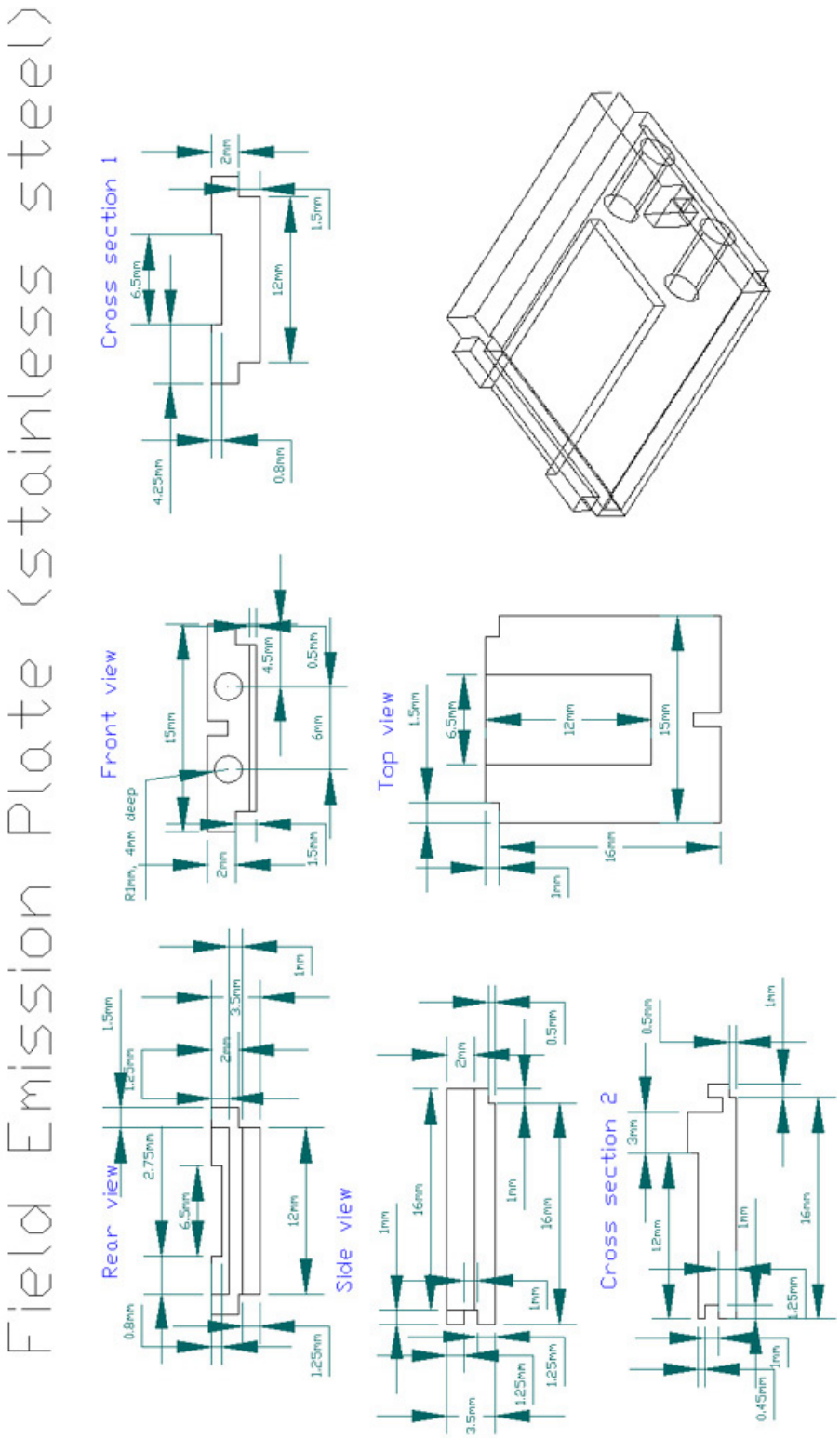

XII – Heater Press Plate

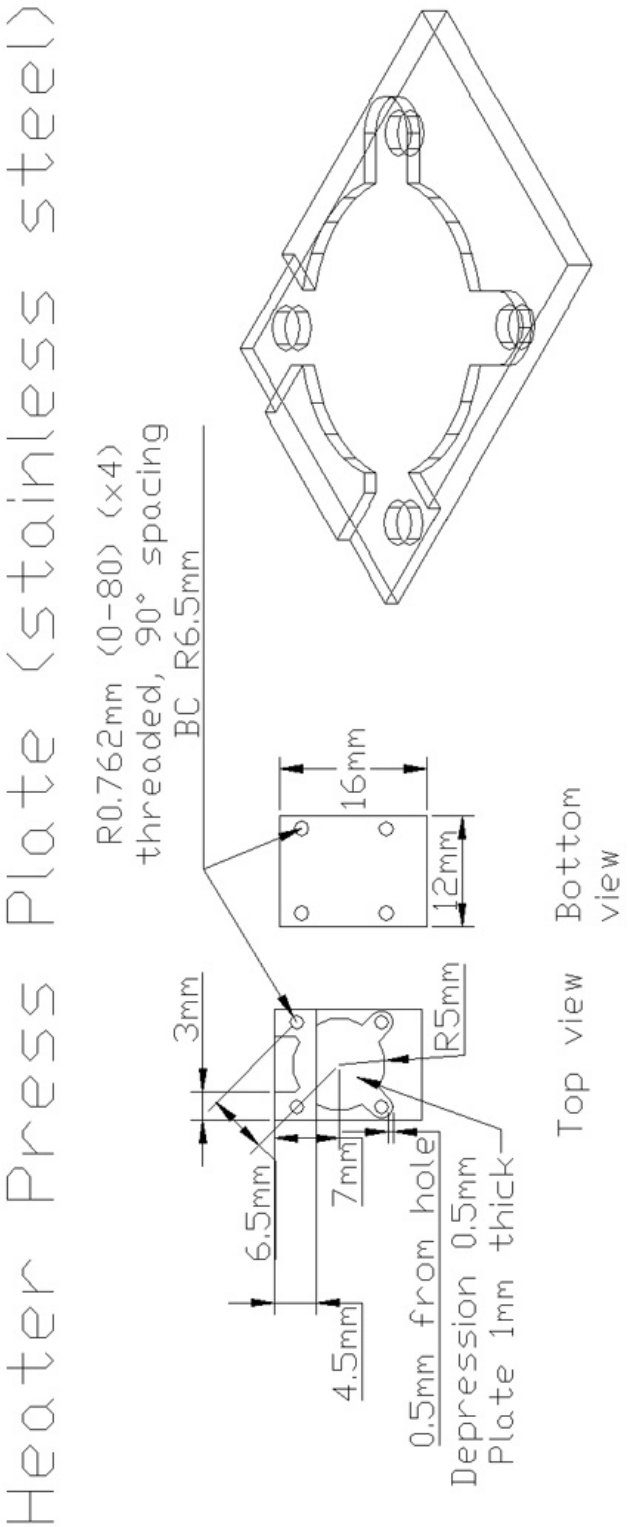

XIII – Heater Spacer

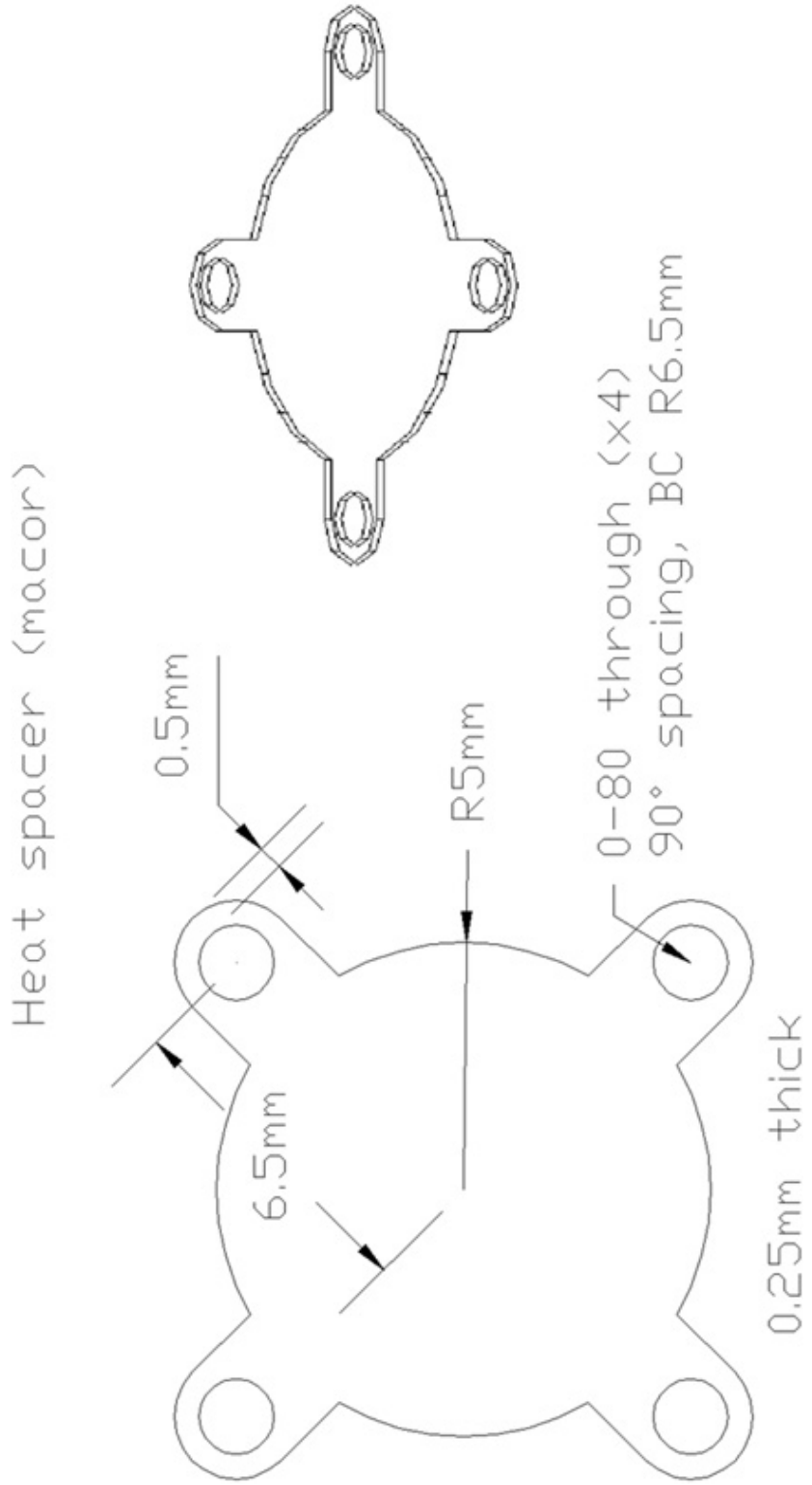

XIV – Sample Holder (Mock Version)

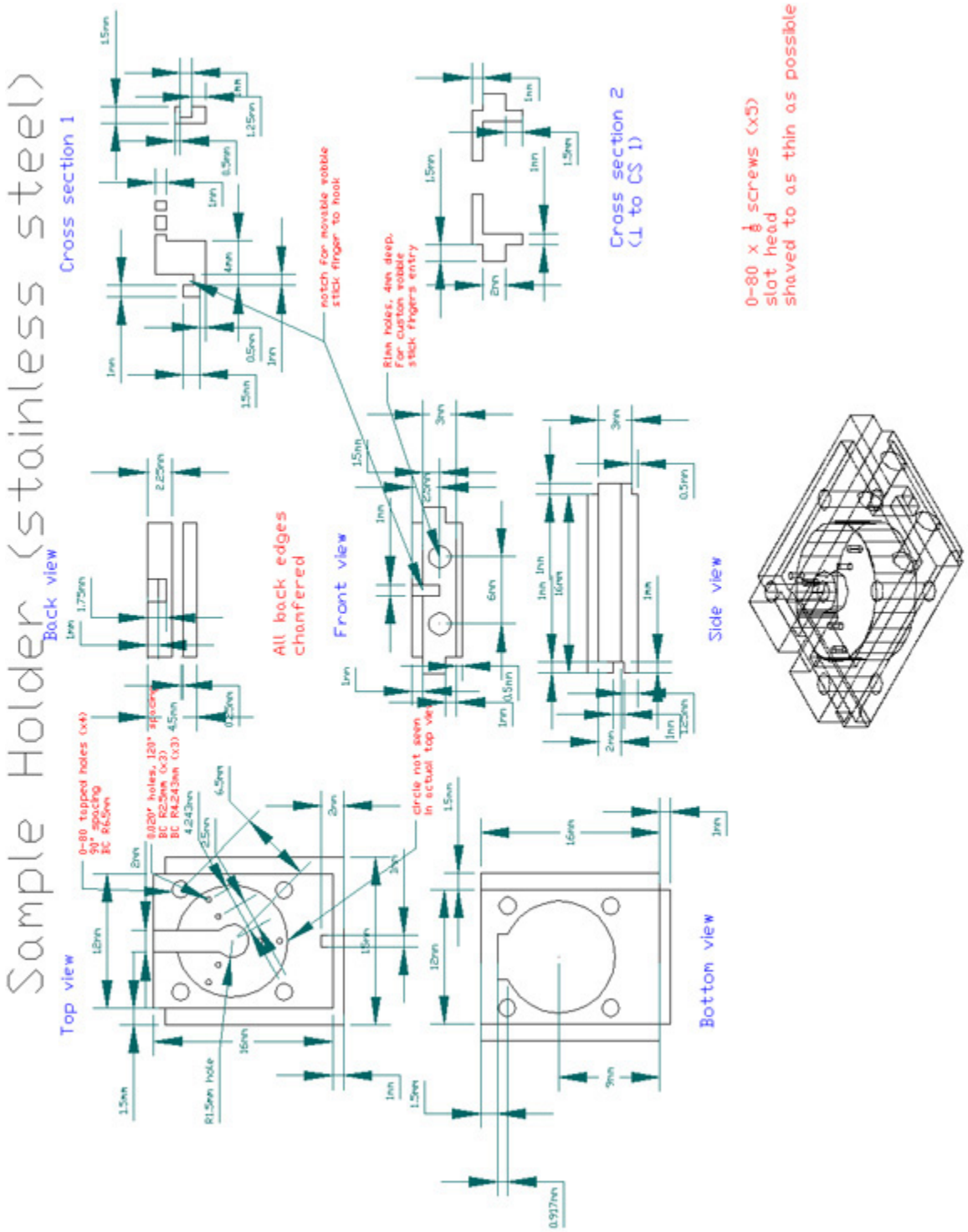

XV – Sample Holder

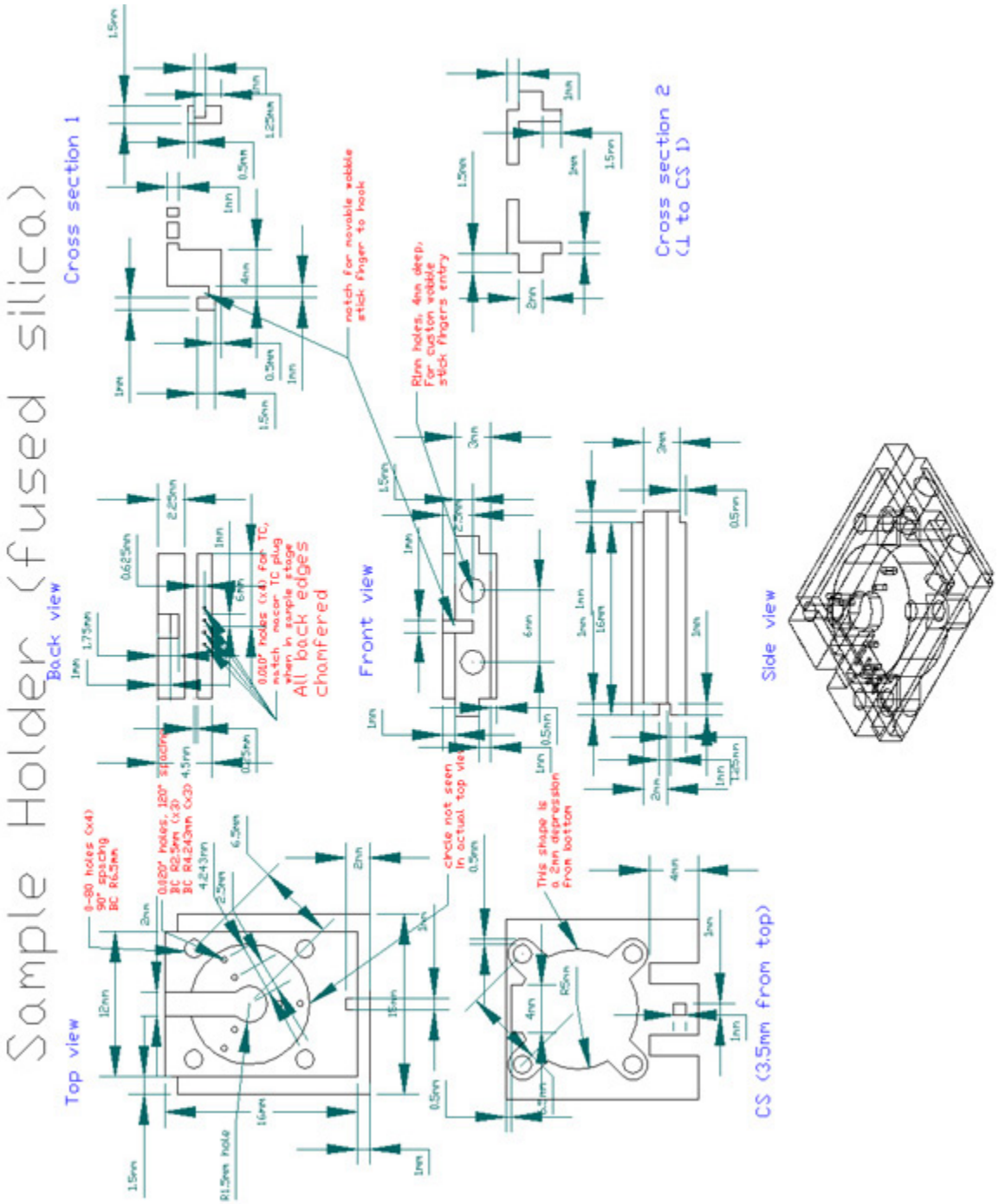

XVI – Sample Stage Bottom Piece

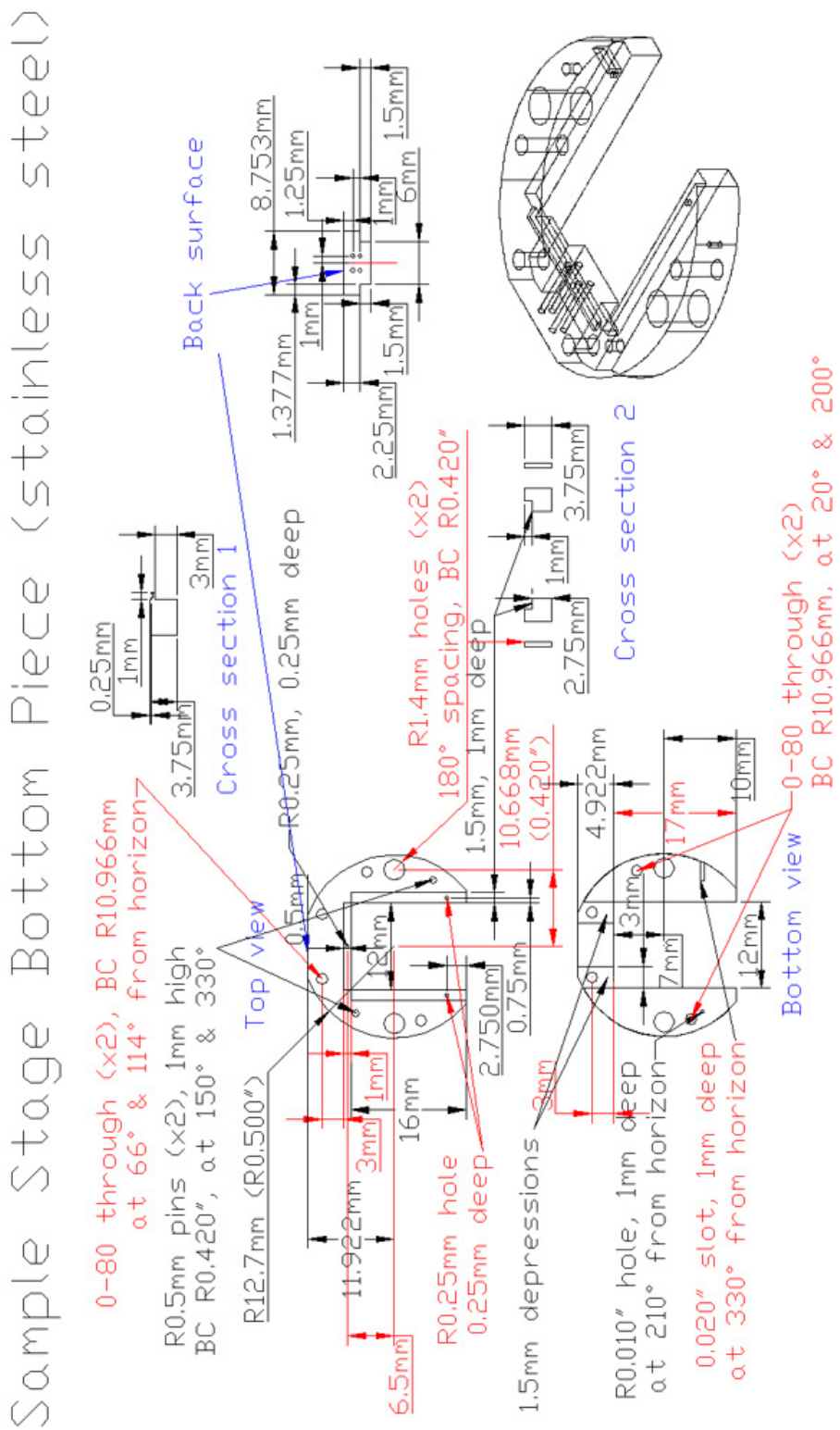

XVII – Sample Stage Top Piece

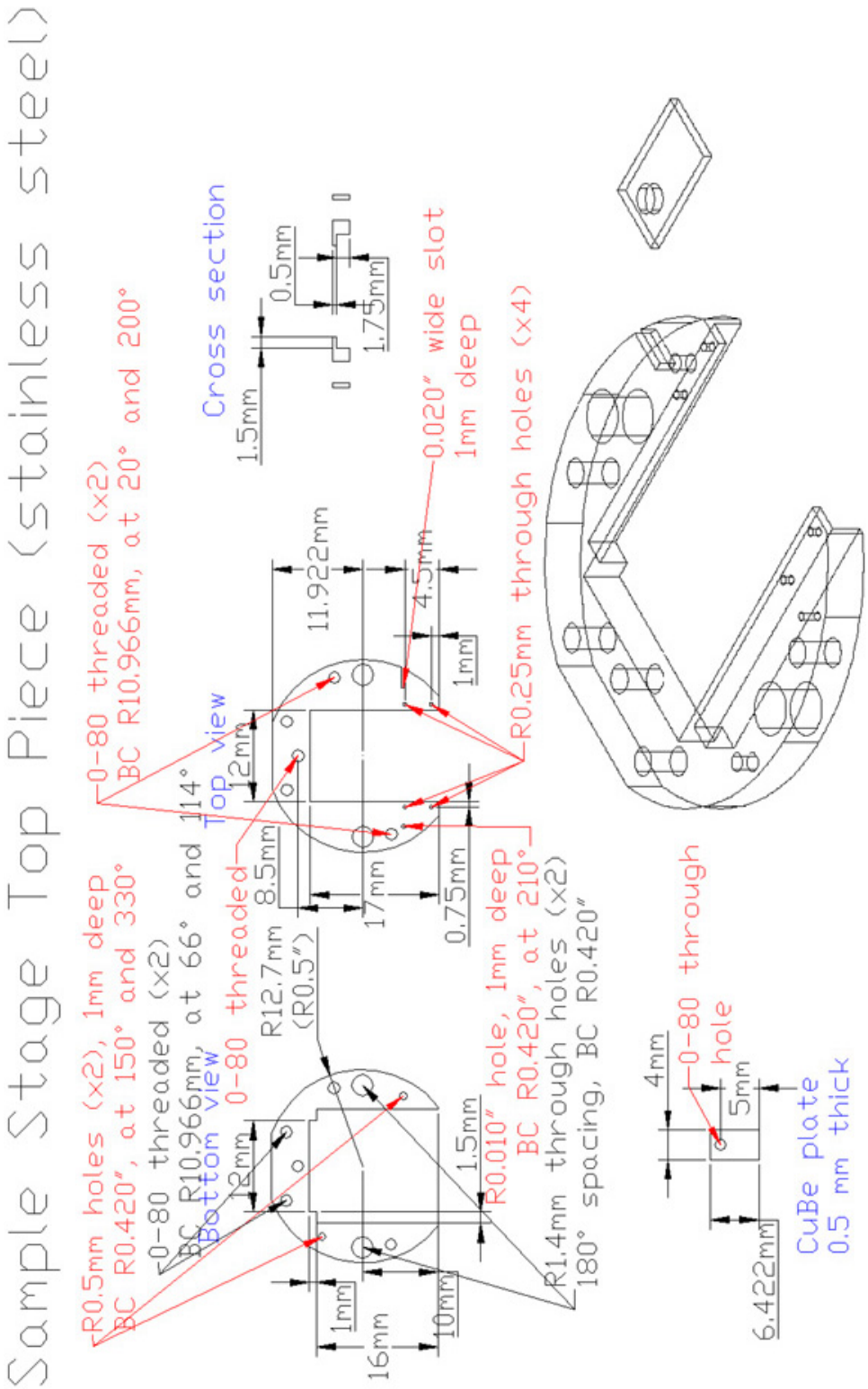

XVIII – Sapphire Slider

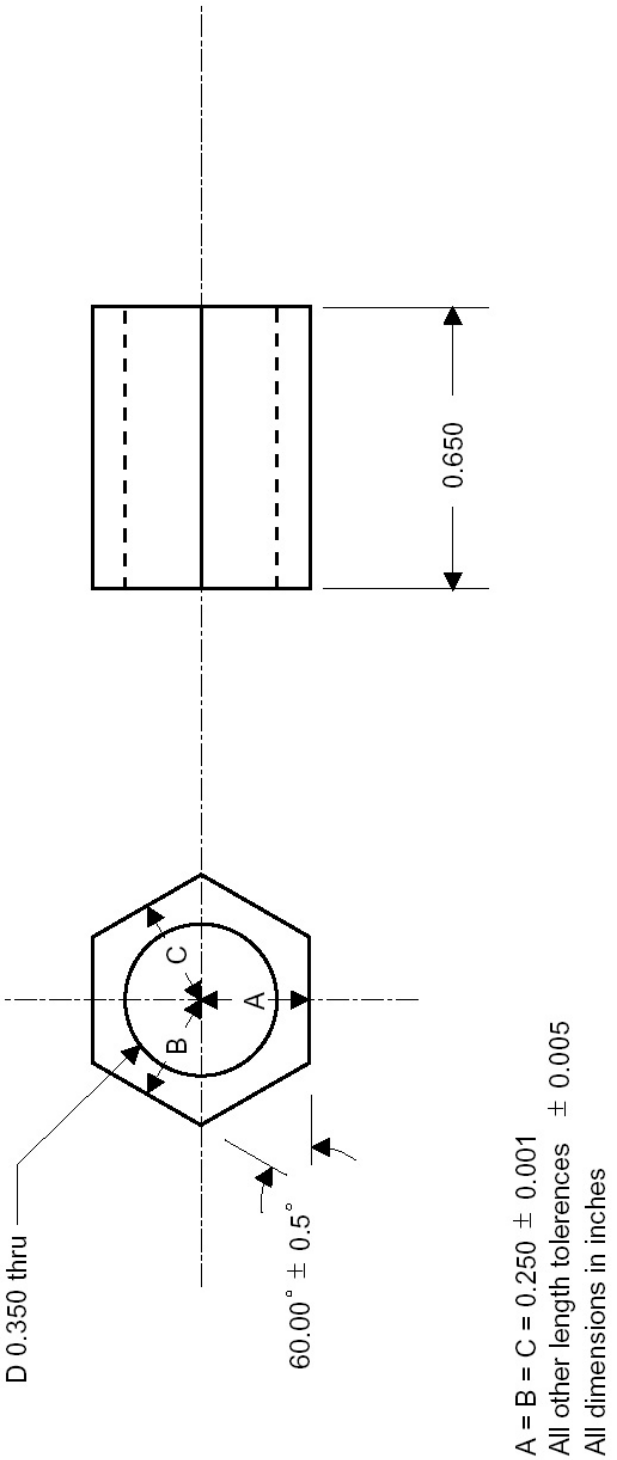

XIX – Scaffold Wiring Connector

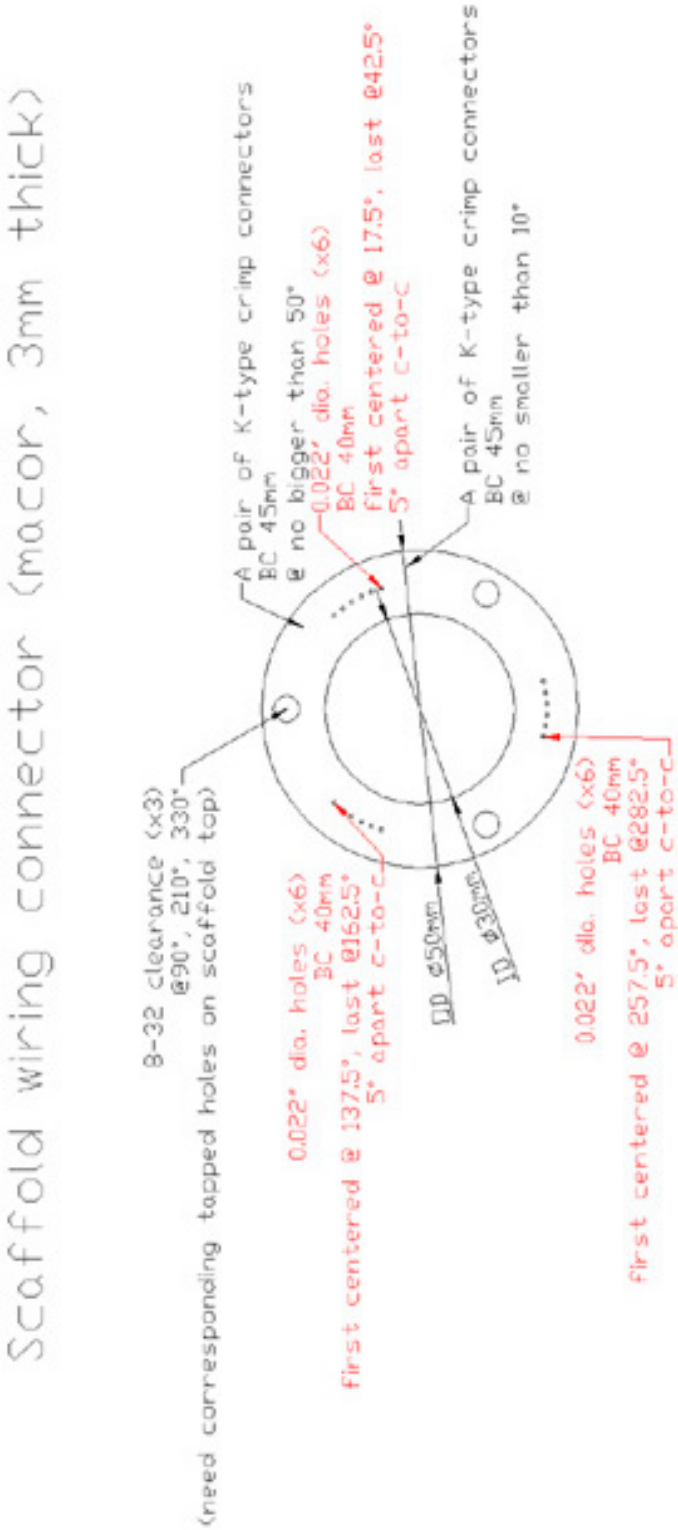

XX – STM Body

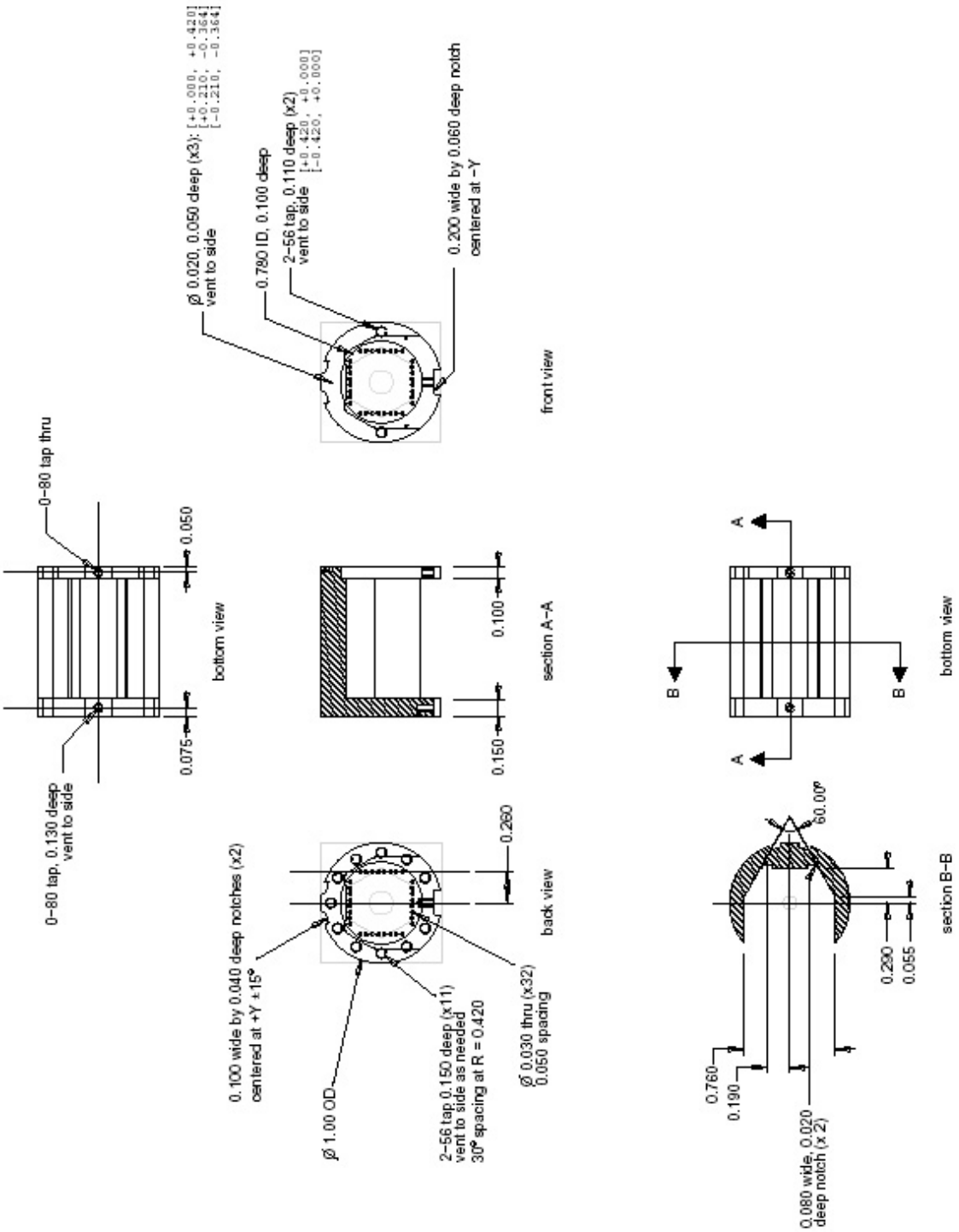
Ø 0.020, 0.050 deep (x3): [+0.000, +0.420]
[+0.210, -0.364]
[-0.210, -0.364]
vent to side
0.780 ID, 0.100 deep
2-56 tap, 0.110 deep (x2)
vent to side [+0.420, +0.000]
[-0.420, +0.000]
0.200 wide by 0.060 deep notch
centered at -Y
front view
0-80 tap thru
0.050
0.075
0-80 tap, 0.130 deep
vent to side
bottom view
0.100
0.150
section A-A
0.260
0.100 wide by 0.040 deep notches (x2)
centered at +Y ±15°
Ø 1.00 OD
2-56 tap, 0.150 deep (x11)
vent to side as needed
30° spacing at R = 0.420
Ø 0.030 thru (x32)
0.050 spacing
back view
A
B
B
A
bottom view
60.0°
0.290
0.055
section B-B
0.760
0.190
0.080 wide, 0.020
deep notch (x 2)

XXI – Tip Exchanger

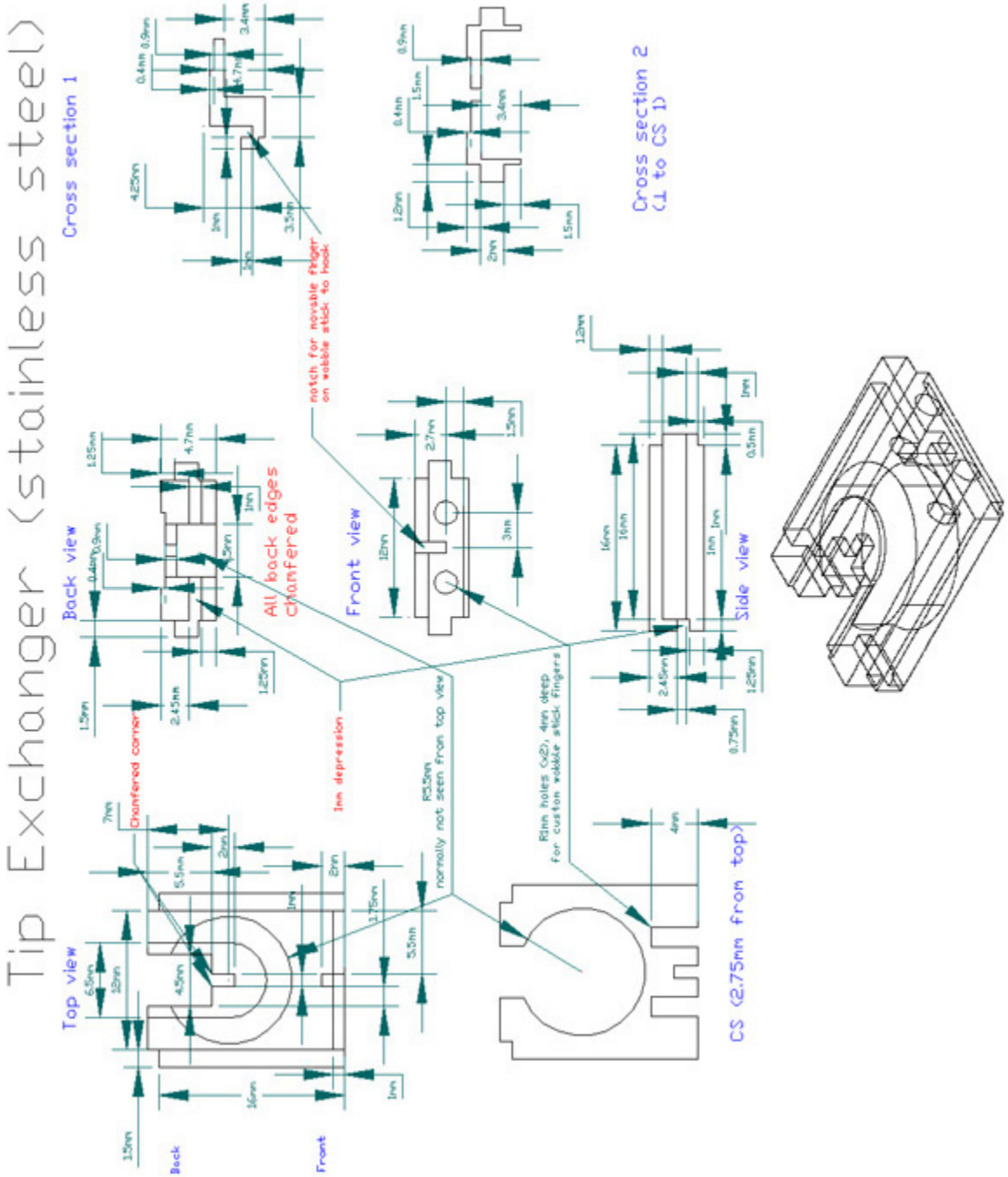

XXII – Tip Holder and Tube Plate

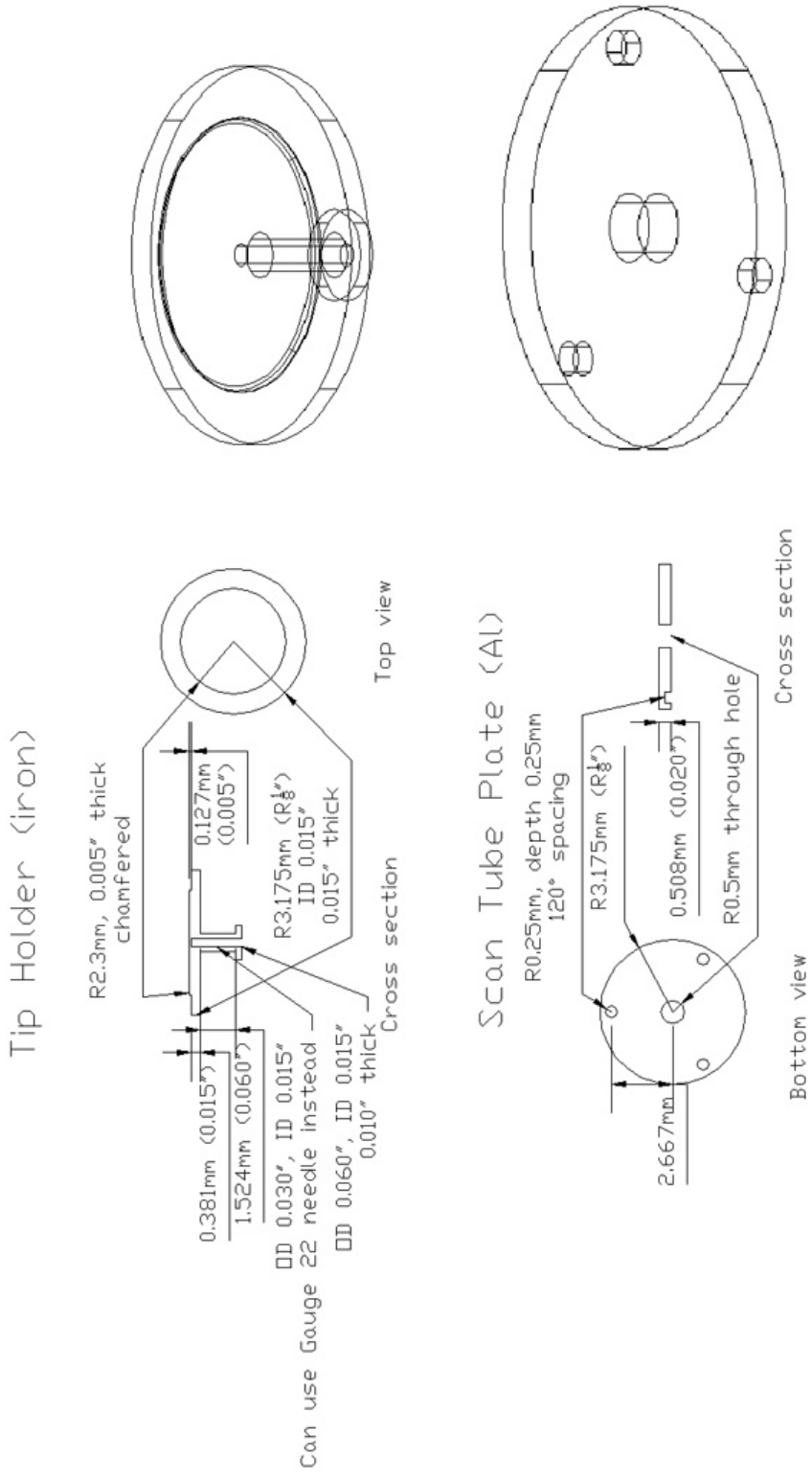

XXIII – Transfer Arm Fork

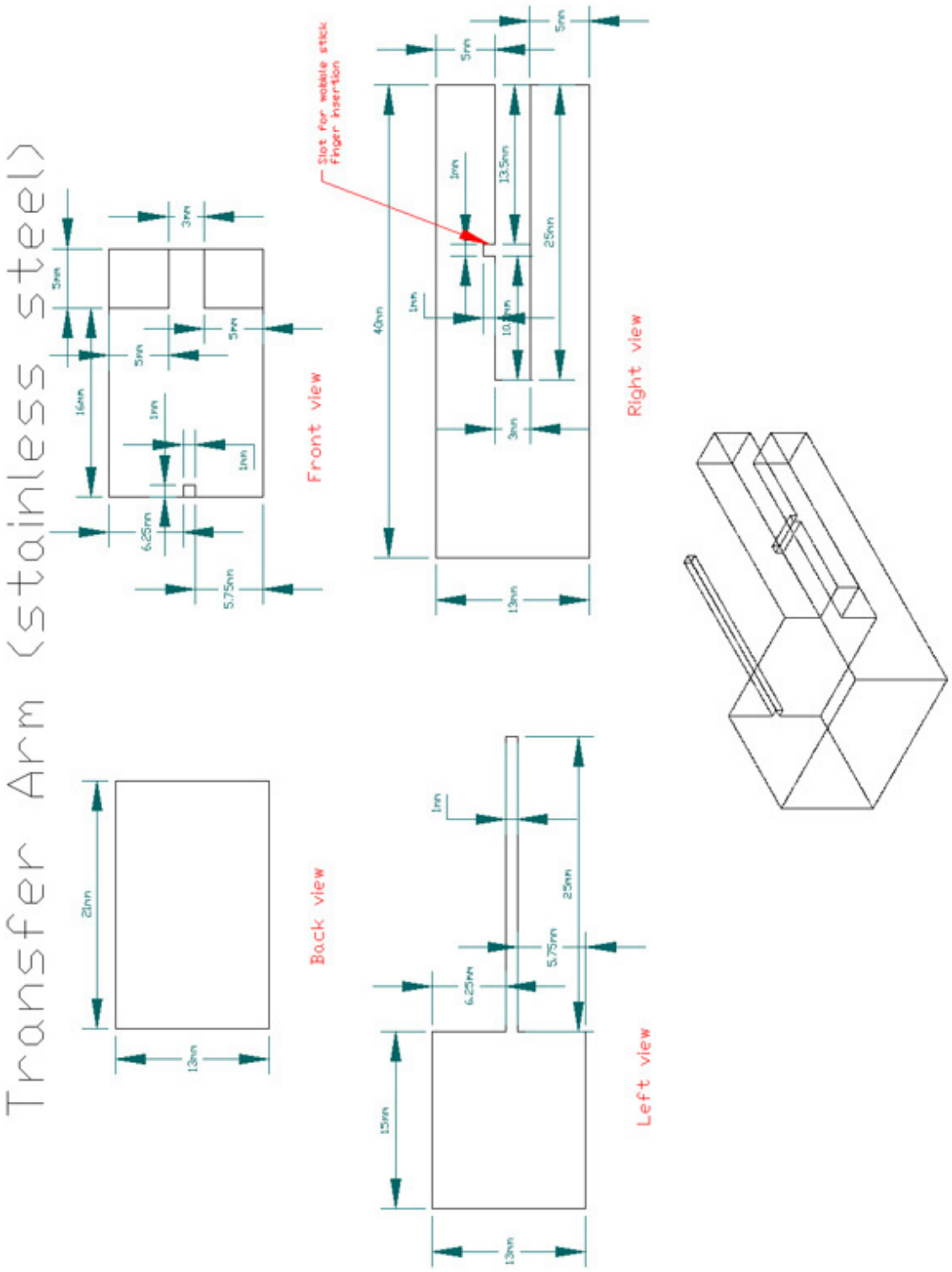

XXIV – Wobble Stick Attachment

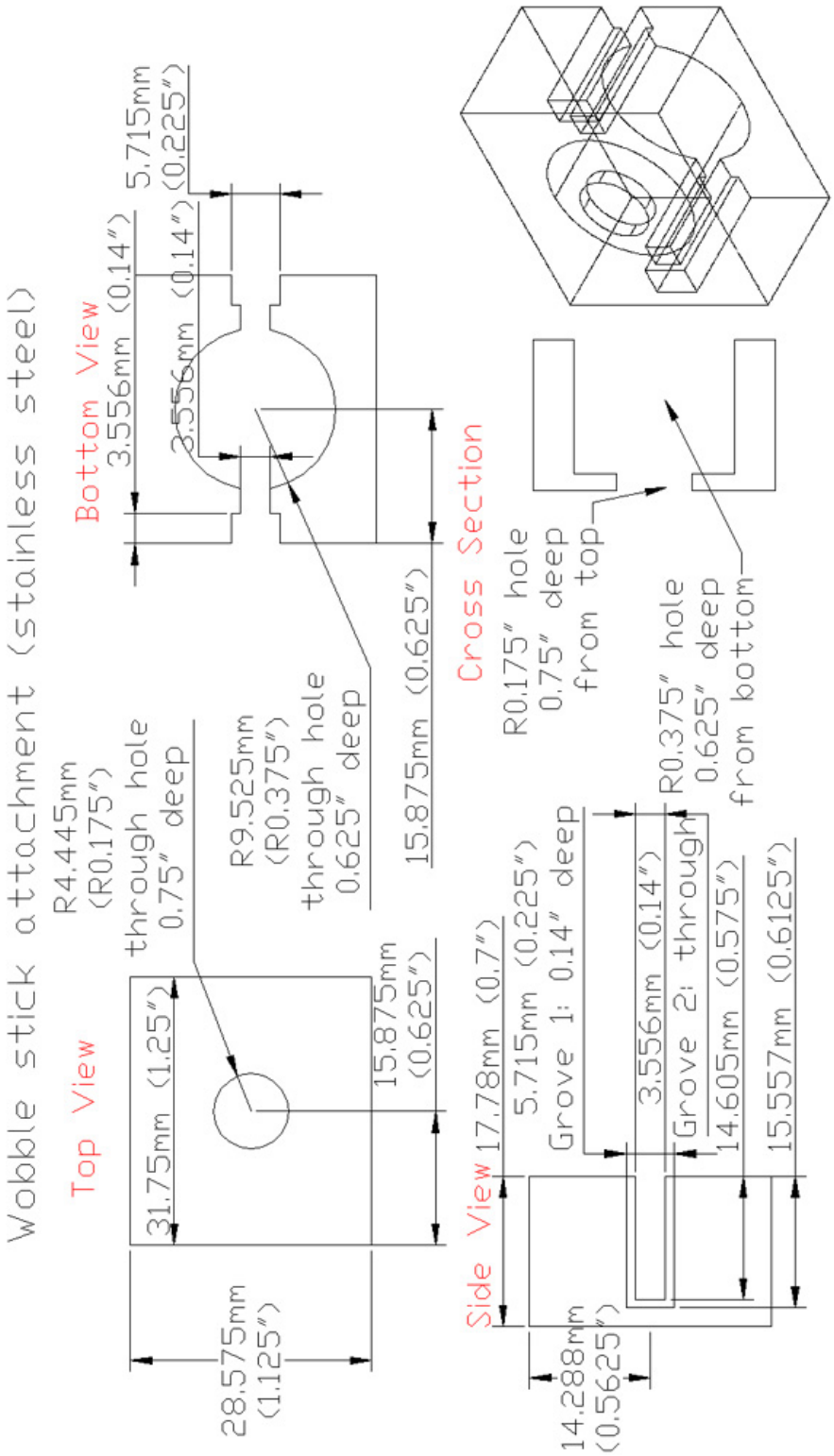

XXV – Wobble Stick Fork